Spring 1993

Navier-Stokes Simulation of Quasi-Axisymmetric and Three-Dimensional Supersonic Vortex Breakdown

Hamdy A. Kandil
Old Dominion University

NAVIER–STOKES SIMULATION OF QUASI-AXISYMMETRIC AND THREE-DIMENSIONAL SUPERSONIC VORTEX BREAKDOWN

by

Hamdy A. Kandil

B.Sc. May 1981, Alexandria University, Egypt

M.Sc. March 1987, Alexandria University, Egypt

A Dissertation submitted to the Faculty of Old Dominion University

in Partial Fulfillment of the Requirement for the Degree of

DOCTOR OF PHILOSOPHY

MECHANICAL ENGINEERING

OLD DOMINION UNIVERSITY

May 1993

Approved by:

Osama A. Kandil (Director)

Robert L. Ash

Oktay Baysal

Chen-Huei Liu (NASA LaRC)

Dennis M. Bushnell (NASA LaRC)

ABSTRACT

NAVIER–STOKES SIMULATION OF QUASI-AXISYMMETRIC AND THREE-DIMENSIONAL SUPERSONIC VORTEX BREAKDOWN

Hamdy A. Kandil

Old Dominion University, 1993

Director: Dr. Osama A. Kandil

Computational simulation of supersonic vortex breakdown is considered for internal and external flow applications. The interaction of a supersonic swirling flow with a shock wave in bounded and unbounded domains is studied. The problem is formulated using the unsteady, compressible, full Navier-Stokes equations which are solved using an implicit, flux-difference splitting, finite-volume scheme. Solutions are obtained for quasi-axisymmetric and three-dimensional flows. The quasi-axisymmetric solutions are obtained by forcing the components of the flowfield vector to be equal on two axial planes, which are in close proximity to each other. For the flow in a bounded domain, a supersonic swirling flow is introduced into a configured circular duct. The duct is designed such that a shock wave intersects with the incoming swirling flow in the inlet portion. For the quasi-axisymmetric flow problem, a parametric study is performed which includes the effects of the Reynolds number, Mach number, swirl ratio and the type of exit-boundary conditions on the development and behavior of vortex breakdown. The effect of the duct wall boundary-layer flow on the vortex breakdown is also investigated. For the same duct geometry, three-dimensional effects are studied along with the effect of the duct wall boundary-layer flow. For the external flow application, a supersonic swirling

jet is issued from a nozzle into a uniform supersonic flow of lower Mach number. For the quasi-axisymmetric flow problem, the effects of the Reynolds number and the type of downstream-boundary conditions are studied. For the three-dimensional flow problem, the effects of the grid fineness, grid-point distribution, grid shape and swirl ratio on the vortex breakdown are studied.

The results show several modes of vortex breakdown such as no-breakdown, transient single-bubble breakdown, transient multi-bubble breakdown, periodic multi-bubble multi-frequency breakdown and helical spiral breakdown.

In another application, a subsonic steady quasi-axisymmetric flow of an isolated slender vortex core is considered. The solution is obtained using a simple set of parabolic equations. The results are in excellent agreement with those of the full Navier-Stokes equations.

ACKNOWLEDGMENTS

Praise and thanks be to GOD to WHOM I owe everything.

I would like to express my sincere appreciation and deepest gratitude to my advisor, Prof. Osama A. Kandil for his technical guidance, encouragement and continuous support. His knowledge, guidance and generous input made this research possible.

Thanks are extended to the members of my dissertation committee, Prof. Robert L. Ash, Prof. Oktay Baysal, Dr. Chen-Huei Liu and Mr. Dennis M. Bushnell, for reviewing this dissertation.

This research work has been supported by the Computational Aerodynamics Branch and the Theoretical Flow Physics Branch of NASA Langley research Center under NASA Grant No. NAS-1–994, monitored by Dr. Chen-Huei Liu. Special thanks are due to Dr. James L. Thomas, head of the Computational Aerodynamics Branch, and to Dr. Ajay Kumar, head of the Theoretical Flow Physics Branch, for their support of this research. Some support has also been received from the Air Force Office for Scientific Research under Major Daniel Fant, Manager of the Unsteady Aerodynamics Program. Special thanks are also due to Mr. Dennis M. Dushnell, associate chief of the Fluid Mechanics Division of NASA Langley Research Center, for initially proposing the problem.

I would like also to acknowledge the substantial computational resources provided by NASA Langley Research Center and the Numerical Aerodynamics Simulation Program (NAS) at NASA Ames Research Center.

I would like to express my love, gratitude and appreciation to my parents, my wife, Hoda, and my daughters, Noha and Nada, for their endless love, encourage and patience.

TABLE OF CONTENTS

ACKNOWLEDGMENTS ii

LIST OF FIGURES viii

LIST OF SYMBOLS xv

CHAPTER 1 INTRODUCTION 1

1.1 Motivation 1

1.2 Present Work 2

CHAPTER 2 LITERATURE REVIEW 6

2.1 Understanding the Vortex-Breakdown Phenomenon 7

2.1.1 Early Observations 7

2.1.2 Theories 8

2.2 Incompressible Vortex Breakdown 12

2.2.1 Experimental Studies 12

2.2.2 Theoretical and Computational Analysis 15

2.2.2.1 Steady Axisymmetric Equations 15

2.2.2.2 Unsteady Quasi-Axisymmetric Equations 18

2.2.2.3 Three-Dimensional Equations 19

2.3 Compressible Vortex Breakdown and Vortex/Shock Interaction 21

2.3.1 Experimental Work 21

2.3.2 Numerical Studies 25

CHAPTER 3 FORMULATION 29

3.1 Introduction 29

3.2 Three-Dimensional Navier-Stokes Equations 30

3.3 Slender Quasi-Axisymmetric Formulation 34

3.3.1 Inflow and Boundary Conditions 36

CHAPTER 4 COMPUTATIONAL SCHEMES FOR THREE-DIMENSIONAL NAVIER-STOKES EQUATIONS 39
4.1 Introduction 39
4.2 Implicit Upwind Schemes 41
4.2.1 Semi-Discrete Finite-Volume Formulation 41
4.2.1.1 Time Integration 43
4.2.2 Higher Order Spatial Differencing of the Inviscid Fluxes 45
4.3 Flux-Difference Splitting 47
4.4 Discretization of the Viscous Fluxes 50
4.5 Initial and Boundary Conditions 53
4.5.1 Initial Conditions 53
4.5.2 Wall Boundary Conditions 53
4.5.3 Exit Boundary Conditions 53

CHAPTER 5 COMPRESSIBLE QUASI-AXISYMMETRIC SLENDER-VORTEX FLOW AND BREAKDOWN 56
5.1 Introduction 56
5.2 Effects of Initial Mach Number on the Vortex-Breakdown Length . . . 57
5.3 Effects of the External Axial Pressure Gradient on the Vortex Breakdown Length 58
5.4 Effects of the Initial Swirl Ratio on the Vortex Breakdown Length . . . 58
5.5 Radial Profiles for M = 0.5 and M = 0.75 59
5.6 Comparison of the Slender-Vortex-Equation Results and Navier-Stokes Results 60
5.7 Conclusion 60

CHAPTER 6 QUASI-AXISYMMETRIC SUPERSONIC VORTEX BREAKDOWN IN A CIRCULAR DUCT 70
6.1 Introduction 70
6.2 Duct Geometry and Computational Domain 71
6.3 Boundary and Initial Conditions 72
6.4 Computational Results 73
6.4.1 Effects of Reynolds Number 73
6.4.1.1 Case 1: R_e = 2,000 74
6.4.1.2 Case 2: R_e = 4,000 74
6.4.1.3 Case 3: R_e = 10,000 74

6.4.1.4 Case 4: R_e = 20,000 76
6.4.1.5 Case 5: R_e = 100,000 77
6.4.1.6 Case 6: Inviscid Flow 78
6.4.2 Effects of the Exit-Boundary Conditions 79
6.4.2.1 Extrapolation from Interior Cell Centers 79
6.4.2.2 Riemann-Invariant Type Boundary Conditions with $p_b = p_\infty$. 80
6.4.2.3 Riemann-Invariant Type Boundary Conditions with $p_b = 2p_\infty$. 81
6.4.2.4 Extrapolating the Pressure Gradient, $\frac{\partial p}{\partial x} = constant$ 81
6.4.2.5 Placing a Disk of r = 0.33 at the Exit Section 82
6.4.3 Effects of the Inlet Swirl Ratio 83
6.4.3.1 Swirling Flow with R_e = 10,000 and β = 0.26 83
6.4.3.2 Swirling Flow with R_e = 10,000 and β = 0.28 84
6.4.3.3 Swirling Flow with R_e = 10,000 and β = 0.3 85
6.4.3.4 Swirling Flow with R_e = 100,000 and β = 0.15 86
6.4.3.5 Swirling Flow with R_e = 100,000 and β = 0.20 86
6.4.3.6 Swirling Flow with R_e = 100,000 and β = 0.38 87
6.4.3.7 Swirling Flow with R_e = 100,000 and β = 0.44 87
6.4.4 Effects of the Inlet Mach Number 88
6.4.4.1 Swirling Flow with M_∞ = 1.75, R_e = 10,000 and β = 0.32. . . 88
6.4.4.2 Swirling Flow with M_∞ = 2.00, R_e = 10,000 and β = 0.32. . . 88
6.4.4.3 Swirling Flow with M_∞ = 2.25, R_e = 10,000 and β = 0.32. . . 89
6.4.5 Swirling Flow in a Duct with an Inviscid Wall 89
6.4.5.1 Flow Case with R_e = 10,000 90
6.4.5.2 Flow Case with R_e = 100,000 90
6.4.6 Interaction of a Supersonic Vortex Flow with an Oblique Shock Wave. 91
6.4.6.1 Supersonic Vortex Flow in a Duct with a 6°Wedge. 91
6.4.6.2 Supersonic Vortex Flow in a Duct with a 10°Wedge. 93
6.5 Summary and Discussion 93
6.5.1 Internal Structure of Vortex-Breakdown Bubbles in View of the Available Experimental Results. 95

CHAPTER 7 INTERACTION OF A SUPERSONIC SWIRLING JET AND A SHOCK WAVE 128

7.1 Introduction 128
7.1.1 The Computational Domain 128
7.2 Initial and Boundary Conditions 129
7.2.1 Initial Conditions 129
7.2.2 Boundary Conditions 129

7.3 Computational Results 131
7.4 Effects of the Downstream Boundary Conditions 134
7.5 Effects of Reynolds Numbers 136
7.6 Summary and Discussion 138

CHAPTER 8 THREE-DIMENSIONAL SUPERSONIC VORTEX BREAKDOWN IN A CIRCULAR DUCT 155

8.1 Introduction 155
8.2 Computational Domain and Grid Description 156
8.3 Computational Results 156
8.3.1 Vortex-Breakdown Evolution 156
8.3.2 Effect of the Duct-Wall Boundary-Layer Flow 160
8.4 Summary and Discussion 161

CHAPTER 9 THREE-DIMENSIONAL VORTEX BREAKDOWN OF A SUPERSONIC SWIRLING JET 174

9.1 Introduction 174
9.2 Boundary and Initial Conditions 175
9.2.1 Inflow Boundary Conditions 175
9.2.2 Outflow Boundary Conditions 176
9.2.3 Initial Conditions 176
9.3 Computational Domain and Types of Computational Grids 176
9.4 Effects of Grid-Point Distributions 177
9.4.1 Grid Number 1; Coarse Rectangular Grid 177
9.4.2 Grid Number 2, Fine Grid in the Cross-Flow Plane and Coarse in the Axial Plane 179
9.4.3 Grid Number 3, Fine Grid in All Directions 181
9.4.4 Grid Number 4, Circular Grid 182
9.4.5 Topological Study of the Sectional Streamlines on a Horizontal Plane. 183
9.5 Summary and Discussion 184

CHAPTER 10 CONCLUDING REMARKS AND RECOMMENDATIONS FOR FUTURE WORK 210

10.1 Concluding Remarks 210
10.2 Recommendations for Future Work 214

REFERENCES 217

Appendix A COMPATIBILITY EQUATION 226

LIST OF FIGURES

Figure 4.1 Finite-volume discretization 55

Figure 4.2 Schematic representation of the waves at a cell interface 55

Figure 5.1 Slender quasi-axisymmetric flow solutions for the effect of the initial Mach number on the vortex-breakdown length. 62

Figure 5.2 Slender quasi-axisymmetric flow solutions for the effect of the initial Mach number on the vortex-breakdown length. 63

Figure 5.3 Slender quasi-axisymmetric flow solutions for the effect of the external axial pressure gradient on the vortex-breakdown length, $M = 0.5$. 64

Figure 5.4 Slender quasi-axisymmetric flow solutions for the effect of the external axial pressure gradient on the vortex-breakdown length, $M = 0.75$. 64

Figure 5.5 Slender quasi-axisymmetric flow solutions for the effect of the initial swirl ratio, β, on the vortex-breakdown length, $M = 0.5$. . 65

Figure 5.6 Slender quasi-axisymmetric flow solutions for the effect of the initial swirl ratio, β, on the vortex-breakdown length, $M = 0.75$. . 65

Figure 5.7 Flow profiles for slender quasi-axisymmetric flow solutions at $M = 0.5$, $\beta = 0.4$ and $dp/dx)_e = 0.25$. 66

Figure 5.8 Flow profiles for slender quasi-axisymmetric flow solutions at $M = 0.75$, $\beta = 0.4$ and $dp/dx)_e = 0.25$. 67

Figure 5.9 Flow profiles for slender quasi-axisymmetric stable vortex flow using the present method, $M = 0.5$, $\beta = 0.6$ and $dp/dx)_e = 0.0$. . 68

Figure 5.10 Flow profiles for slender quasi-axisymmetric stable vortex flow using a full Navier-Stokes solver, $M = 0.5$, $\beta = 0.6$ and $dp/dx)_e = 0.0$. 69

Figure 6.1 Typical grid for the configured circular duct, 221x51x2 grid points. 98

Figure 6.2 Quasi-axisymmetric flow profiles at x = 0.0 for a supersonic swirling flow with $M_\infty = 1.75$, $\beta = 0.32$. 99

Figure 6.3 Streamlines and Mach contours for a swirling flow without breakdown, $M_\infty = 1.75$, $\beta = 0.32$ and $R_e = 2,000$. 100

Figure 6.4 Streamlines and Mach contours for a swirling flow with a transient single-bubble breakdown, $M_\infty = 1.75$, $\beta = 0.32$ and $R_e = 4,000$. 100

Figure 6.5 Streamlines and Mach contours for a swirling flow with a transient multi-bubble breakdown, $M_\infty = 1.75$, $\beta = 0.32$, $R_e = 10,000$ and $\Delta t = 0.0025$. 101

Figure 6.6 Streamlines and Mach contours for a swirling flow with a transient multi-bubble breakdown, $M_\infty = 1.75$, $\beta = 0.32$, $R_e = 10,000$ and $\Delta t = 0.00125$. 102

Figure 6.7 Streamlines and Mach contours for a swirling flow with a transient multi-bubble breakdown, $M_\infty = 1.75$, $\beta = 0.32$ and $R_e = 20,000$. 103

Figure 6.8 Streamlines for a swirling flow with unsteady multi-frequency multi-bubble breakdown, $M_\infty = 1.75$, $\beta = 0.32$ and $R_e = 100,000$. . . 104

Figure 6.9 Mach contours for a swirling flow with unsteady multi-frequency multi-bubble breakdown, $M_\infty = 1.75$, $\beta = 0.32$ and $R_e = 100,000$. 106

Figure 6.10 Streamlines and Mach contours for a swirling flow using Euler equations, $M_\infty = 1.75$ and $\beta = 0.32$. 107

Figure 6.11 Streamlines and Mach contours for a swirling flow with transient multi-bubble breakdown, $p_b = p_\infty$, Riemann-invariant exit-boundary conditions. 108

Figure 6.12 Streamlines and Mach contours for a swirling flow with transient multi-bubble breakdown, $p_b = 2p_\infty$, Riemann-invariant downstream boundary conditions. 109

Figure 6.13 Streamlines and Mach contours for a swirling flow with transient multi-bubble breakdown, $\frac{\partial p}{\partial x} = constant$, downstream boundary conditions. 110

Figure 6.14 Streamlines and Mach contours for a swirling flow with quasi—steady multi-bubble breakdown, downstream disk of $r = 0.333$. 111

Figure 6.15 Streamlines and Mach contours for a swirling flow without breakdown, $M_\infty = 1.75$, $\beta = 0.26$ and $R_e = 10,000$. 112

Figure 6.16 Velocity vectors and axial distributions for a swirling flow without breakdown, $M_\infty = 1.75$, $\beta = 0.26$ and $R_e = 10,000$. 112

Figure 6.17 Streamlines and Mach contours for a swirling flow with a transient single-bubble breakdown, $M_\infty = 1.75$, $\beta = 0.28$ and $R_e = 10,000$. 113

Figure 6.18 Streamlines and Mach contours for a swirling flow with a transient multi-bubble breakdown, $M_\infty = 1.75$, $\beta = 0.30$ and $R_e = 10,000$. 114

Figure 6.19 Streamlines and Mach contours for a swirling flow with unsteady multi-bubble breakdowns, $M_\infty = 1.75$, $\beta = 0.15$ and $R_e = 100,000$. 115

Figure 6.20 Streamlines and Mach contours for a swirling flow with unsteady multi-bubble breakdowns, $M_\infty = 1.75$, $\beta = 0.2$ and $R_e = 100,000$. 116

Figure 6.21 Streamlines and Mach contours for a swirling flow with multi-bubble breakdowns, $M_\infty = 1.75$, $\beta = 0.38$ and $R_e = 100,000$. . 117

Figure 6.22 Streamlines and Mach contours for a swirling flow with multi-bubble breakdowns, $M_\infty = 1.75$, $\beta = 0.44$ and $R_e = 100,000$. . 118

Figure 6.23 Streamlines and Mach contours for a swirling flow with a transient single-bubble breakdown, $M_\infty = 2.0$, $\beta = 0.26$ and $R_e = 10,000$. 119

Figure 6.24 Streamlines and Mach contours for a swirling flow with a transient multi-bubble breakdown, $M_\infty = 2.25$, $\beta = 0.26$ and $R_e = 10,000$. 120

Figure 6.25 Streamlines and Mach contours for a swirling flow in a duct with an inviscid-wall, $M_\infty = 1.75$, $\beta = 0.32$ and $R_e = 10,000$. 121

Figure 6.26 Streamlines and Mach contours for a swirling flow in a duct with an inviscid-wall, $M_\infty = 1.75$, $\beta = 0.32$ and $R_e = 100,000$. 122

Figure 6.27 Streamlines and Mach contours for a swirling flow with a transient single-bubble breakdown, $M_\infty = 1.75$, $\beta = 0.32$ and $R_e = 100,000$ with a wedge angle of 6°. 123

Figure 6.28 Streamlines and Mach contours for a swirling flow with a transient single-bubble breakdown, $M_\infty = 1.75$, $\beta = 0.32$ and $R_e = 100,000$ with a wedge angle of 10°. 124

Figure 6.29 The mean experimental streamline pattern inside the breakdown. The C's denote the centers of the recirculation cells, ... 125

Figure 6.30 The computational streamline pattern inside the breakdown for the flow case of R_e = 100,000, M = 1.75 and β = 0.32 at t = 125. 125

Figure 6.31 Photograph and Schematic representation of axisymmetric (bubble) vortex breakdown, ... 126

Figure 6.32 Computational streamline patterns for quasi-axisymmetric flow cases with stable vortex-breakdown structures. 127

Figure 7.1 Typical grid for supersonic swirling jet from a nozzle, 221x51x2 grid points. 139

Figure 7.2 Quasi-axisymmetric flow profiles at x = 0.0 for supersonic swirling jet from a nozzle $M_j = 3.0$, $\beta = 0.22$. 140

Figure 7.3 Streamlines and Mach contours for supersonic swirling jet from a nozzle with almost single-bubble vortex breakdown, extrapolation downstream boundary conditions. 141

Figure 7.4 Axial distributions of the flow variables, ρ, u and p, along the vortex axis, $r = 0$, for supersonic swirling jet from a nozzle, extrapolation downstream boundary conditions. 144

Figure 7.5 Streamlines and Mach contours for supersonic swirling jet from a nozzle with almost single-bubble vortex breakdown, Riemann–invariant downstream boundary conditions. 145

Figure 7.6 Axial distributions of the flow variables, ρ, u and p, along the vortex axis, $r = 0$, for supersonic swirling jet from a nozzle, Riemann–invariant downstream boundary conditions. 146

Figure 7.7 Streamlines for supersonic swirling jet from a nozzle with almost single-bubble vortex breakdown using Riemann–invariant and extrapolation downstream boundary conditions. 147

Figure 7.8 Mach contours for supersonic swirling jet from a nozzle with almost single-bubble vortex breakdown using Riemann–invariant and extrapolation downstream boundary conditions. 148

Figure 7.9 Axial variations of the flow variables, ρ, u and p, along the vortex axis, $r = 0$, for supersonic swirling jet from a nozzle using Riemann–invariant and extrapolation downstream boundary conditions. 150

Figure 7.10 Streamlines and Mach contours for supersonic swirling jet from a nozzle with almost single-bubble vortex breakdown, $R_e = 100,000$. 152

Figure 7.11 Axial distributions of the flow variables, ρ, u and p, along the vortex axis, $r = 0$, for supersonic swirling jet from a nozzle, $R_e = 100,000$. 154

Figure 8.1 Configured-circular-duct computational domain and grid, 200x51x49 grid points in the axial, radial and wrap-around directions, respectively. 163

Figure 8.2 Streamlines and Mach contours in a horizontal plane for a supersonic swirling flow in a circular duct, $M_\infty = 1.75$, $\beta = 0.32$ and $R_e = 100,000$. 164

Figure 8.3 Experimental results of an incompressible swirling flow in a circular duct, from reference 165

Figure 8.4 Streamlines and Mach contours in a horizontal plane for a supersonic swirling flow in a circular duct, $M_\infty = 1.75$, $\beta = 0.32$ and $R_e = 100,000$. 166

Figure 8.5 Axial distributions of the axial velocity, u, density, ρ and pressure, p, for a supersonic swirling flow in a circular duct, $M_\infty = 1.75$, $\beta = 0.32$ and $R_e = 100,000$. 167

Figure 8.6 Streamlines and Mach contours in a horizontal plane for a supersonic swirling flow in a circular duct, $M_\infty = 1.75$, $\beta = 0.32$ and $R_e = 100,000$. 168

Figure 8.7 Streamlines and Mach contours in a horizontal plane for a supersonic swirling flow in a circular duct, $M_\infty = 1.75$, $\beta = 0.32$ and $R_e = 100,000$. 169

Figure 8.8 Streamlines and Mach contours in a horizontal plane for a supersonic swirling flow in a circular duct, $M_\infty = 1.75$, $\beta = 0.32$ and $R_e = 100,000$ using inviscid-wall boundary conditions. . . . 171

Figure 8.9 Streamlines and Mach contours in a horizontal plane for a supersonic swirling flow in a circular duct, $M_\infty = 1.75$, $\beta = 0.32$ and $R_e = 100,000$ using inviscid-wall boundary conditions. . . . 172

Figure 8.10 Experimental results of an incompressible swirling flow in a circular duct, from reference 173

Figure 8.11 Streamlines on a horizontal plane for the flow case of $M_\infty = 1.75$, $\beta = 0.32$ and $R_e = 100,000$ at t = 38.5. 173

Figure 9.1 Experimental measurements at the nozzle exit for a supersonic swirling jet in uniform wind-tunnel conditions, $M_j = 3.0$, $M_\infty = 2.0$ and $R_e = 296,000$. 186

Figure 9.2 Three-dimensional asymmetric inlet flow profiles at $x = 0.0$ for supersonic swirling jet from a nozzle, $M_j = 3.0$, $M_\infty = 2.0$ and $R_e = 296,000$. 187

Figure 9.3 Three-dimensional quasi-axisymmetric inlet flow profiles at $x = 0.0$ for supersonic swirling jet from a nozzle, $M_j = 3.0$,$M_\infty = 2.0$ and $R_e = 296,000$. 188

Figure 9.4 Grid number 1 (rectangular coarse grid in the cross-flow plane), 210x51x51 grid points in the axial and cross-flow plane, respectively. 189

Figure 9.5 Streamlines and Mach contours in a horizontal plane for a supersonic swirling jet using grid number 1, $M_j = 3.0$, $M_\infty = 2.0$ and $R_e = 296,000$. 190

Figure 9.6 Axial distributions of the axial velocity, u, density, ρ and pressure, p, for a supersonic swirling jet using grid number 1, $M_j = 3.0$,$M_\infty = 2.0$ and $R_e = 296,000$. 192

Figure 9.7 Grid number 2 (rectangular fine grid in the cross-flow plane), 145x61x61 grid points in the axial and cross-flow plane, respectively. 193

Figure 9.8 Streamlines and Mach contours in a horizontal plane for a supersonic swirling jet using grid number 2, $M_j = 3.0$, $M_\infty = 2.0$ and $R_e = 296,000$. 194

Figure 9.9 Axial distributions of the axial velocity, u, density, ρ and pressure, p, for a supersonic swirling jet using grid number 2, $M_j = 3.0$, $M_\infty = 2.0$ and $R_e = 296,000$. 197

Figure 9.10 Grid number 3 (rectangular fine grid), 145x61x61 grid points in the axial and cross-flow plane, respectively. 199

Figure 9.11 Streamlines and Mach contours in a horizontal plane for a supersonic swirling jet using grid number 3 with asymmetric inflow profiles, $M_j = 3.0$, $M_\infty = 2.0$ and $R_e = 296,000$. 200

Figure 9.12 Streamlines and Mach contours in a horizontal plane for a supersonic swirling jet using grid number 3, $M_j = 3.0$, $M_\infty = 2.0$ and $R_e = 296,000$. 201

Figure 9.13 Axial distributions of the axial velocity, u, density, ρ and pressure, p, for a supersonic swirling jet using grid number 3, $M_j = 3.0$, $M_\infty = 2.0$ and $R_e = 296,000$. 203

Figure 9.14 Grid number 4 (circular fine grid), 145x61x61 grid points in the axial and cross-flow plane, respectively. 204

Figure 9.15 Streamlines and Mach contours in a horizontal plane for a supersonic swirling jet using grid number 4 with asymmetric inflow profiles, $M_j = 3.0$, $M_\infty = 2.0$ and $R_e = 296,000$. 205

Figure 9.16 Streamlines and Mach contours in a horizontal plane for a supersonic swirling jet using grid number 4, $M_j = 3.0$, $M_\infty = 2.0$ and $R_e = 296,000$. 206

Figure 9.17 Axial distributions of the axial velocity, u, density, ρ and pressure, p, for a supersonic swirling jet using grid number 4, $M_j = 3.0$, $M_\infty = 2.0$ and $R_e = 296,000$. 208

Figure 9.18 Streamline patterns on a horizontal plane for a supersonic vortex breakdown (grid number 1) at t = 20, $M_j = 3.0$, $M_\infty = 2.0$ and $R_e = 296,000$. 209

Figure 9.19 Experimental streamline patterns on a vertical plane for an incompressible vortex breakdown on a delta wing at high angle of attack, ... 209

LIST OF SYMBOLS

a	local speed of sound
A	Inviscid Jacobian matrix $\frac{\partial E}{\partial Q}$
c	Sutherland's constant
C_+, C_-	Wave velocities (Benjamin's theory)
C_p	Specific heat at constant pressure
CFL	Courant-Friedrichs-Lewy number
e	Total energy per unit mass
E	Inviscid flux
E_v	Viscous flux
I	Identity matrix
J, J^{-1}	Jacobian and inverse Jacobian of coordinate transformations
k	Coefficient of thermal conductivity
L	Characteristic length or radius of the duct
M	Mach number
MSF	Modified shape factor (slender vortex)
N	Universal characteristic coefficient (Benjamin's theory)
p	Static pressure
P_r	Prandtl number
q	Heat-flux component
$\vec{q}$	Flowfield vector
$\vec{Q}$	Vector of conservative variables in body-fitted coordinates
R_e	Reynolds number
$\Re$	Integration domain and gas constant
R^+, R^-	Non-negative and non-positive Riemann invariants
r	Distance in the radial direction
t	Nondimensional time
T	Static temperature

u_1, u_2, u_3	Cartesian components of velocity
u, v, w	Velocity components in cylindrical coordinates (slender vortex)
$U_1,\ U_2,\ U_3$	Contravariant velocities
$x_1,\ x_2,\ x_3$	Cartesian coordinates
α	Angle of attack
β	Swirl ratio
γ	ratio of specific heats $\frac{C_p}{C_v}$
$\delta_i j$	Kronecker delta function
η	Transformed radial coordinate (slender vortex)
λ	Shape factor (slender vortex)
$\lambda_1,\ \lambda_2,\ \lambda_3$	Eigenvalues
Λ	Diagonal eigenvalue matrix
μ	Molecular viscosity
ξ	Tranformed axial coordinate (slender vortex)
ξ^1, ξ^2, ξ^3	Computational coordinates
ρ	Density
τ	Shear stress tensor
ϕ	Polar angle
∂	partial derivative
∇	Backward differencing operator or gradient
Δ	Forward differencing operator

Subscripts

a	Quantities at the vortex axis (slender vortex)
e	Quantities at the vortex outer edge (slender vortex)
L	Values obtained from the left side of a cell face
n	Normal
R	Values obtained from the right side of a cell face
x_1, x_2, x_3	With respect to the Cartesian coordinates
ξ^1, ξ^2, ξ^3	With respect to the computational coordinates
∞	Free-stream value

Superscripts

$n, n+1$	Time levels
$-$	Non-positive eigenvalues
$+$	Non-negative eigenvalues

CHAPTER 1
INTRODUCTION

1.1 Motivation

The interaction of a longitudinal vortex and a transverse shock is a very important flow phenomenon that usually develops in several external and internal flow applications. For external flows, the transonic flow around delta wings in the high-angle-of-attack range and the transonic and supersonic flows around strake-delta wing configurations in the moderate to high-angle-of-attack range are some of the applications. Under some flow conditions, vortex breakdown occurs behind the shock wave over the delta wing causing a loss of lift. The problem is of great importance for high-performance airplanes where the design emphasis has been on high-angle-of-attack maneuvering. In this application, vortex breakdown produces severe buffet and may lead to premature fatigue failure of the vertical tail. Such a breakdown is undesirable and flow control methods need to be developed to delay the occurrence of vortex breakdown. For internal flows, the supersonic inlet ingesting a vortex and the supersonic combustion chambers where fuel is injected in a swirling jet are some of the applications. Jet growth, entrainment and decay, flame size, shape and stability and combustion intensity are some of the large-scale effects of the swirl on the flow field in combustion chambers. At critical values of swirl and pressure gradients, vortex breakdown occurs with a recirculation zone behind the shock wave. The recirculation zone plays an important role in flame stabilization by providing a hot flow of recirculated combustion products and a reduced velocity region where flame speed and flow velocity can be matched resulting in efficient combustion. Vortex breakdown in

these application is desirable and hence its occurrence needs to be controlled for optimum performance of the combustion chamber. For such problems, computational schemes are needed to study, predict and control vortex-shock interaction including vortex breakdown. The problem of vortex-shock interaction for internal flows is very complicated since it includes several phenomena such as vortex breakdown, shock/boundary layer interaction and boundary-layer separation. Recently, the high-speed digital computers have made it possible to address these complex flow problems. Unfortunately, the literature lacks this type of analysis. Most of the available research work has been focused on incompressible flow problems with few exceptions.

1.2 Present Work

In the present study, the unsteady, compressible full Navier-Stokes equations are used to study compressible vortex breakdowns and vortex-shock-wave interaction problems both in bounded and unbounded computational domains. The present work is focused on the existence of vortex breakdown as a result of vortex-shock interaction. In studying the vortex-shock interaction, two applications are considered. The first problem is that of a supersonic swirling flow in a configured circular duct where a shock wave is formed at the entrance portion of the duct and the interaction of the formed shock with vortex may result in bursting of the vortex core. In this application, a parametric study is performed to consider the effects of the Reynolds number, Mach number, and swirl ratio on the development and behavior of the vortex breakdown. The second problem is that of a supersonic swirling jet issued from a convergent divergent nozzle into a uniform supersonic free-stream domain. In this application, the effects of the swirl ratio and grid on the development and behavior of the vortex breakdown are studied.

Because of the expensive computational resources required for solving three-dimensional flow problems, some of the computations in the present work have been performed using the quasi-axisymmetric flow assumption to reduce the cost of computations by solving only for two meridian planes. In this way, a larger number of computational applications could be addressed and extensive understanding of the flow physics could be gained. This assumption is widely used both for internal and external flow applications in the majority of the available literature on incompressible vortex breakdown. In another application, the full Navier-Stokes equations are reduced to a simple set of steady quasi-axisymmetric boundary-layer-like equations by assuming the flow to be steady and the vortex core to be slender. Selected flow cases are computed using the three-dimensional unsteady full Navier-Stokes equations for better simulation of the physical problem since the experimental studies show the vortex-breakdown problem to be an unsteady three-dimensional flow.

In Chapter 2, a literature survey of research work concerning the vortex breakdown problem is presented. Both experimental and computational works are reviewed where emphasis is placed on the early observations and understanding of the vortex breakdown phenomenon. Because the literature lacks the analysis of the supersonic vortex breakdown problem, the available work in incompressible vortex breakdown is reviewed in some detail.

In Chapter 3, the unsteady, compressible, three-dimensional Navier-Stokes equations are presented. The equations are then written in terms of time independent body-conformed coordinates. Next, the equations are simplified for the steady flow case of a slender vortex core.

In Chapter 4, the computational scheme used in the present study to solve the full Navier-Stokes equations is presented. The computational scheme is an implicit, upwind,

flux-difference splitting, finite volume scheme. It employs the flux-difference splitting scheme of Roe which is based on the solution of the approximate one-dimensional Riemann problem in each of the three directions. At the end of the Chapter, the initial and boundary conditions are presented.

Numerical results are presented in Chapters 5–9. In Chapter 5, the reduced form of the Navier-Stokes equations for the case of an isolated, subsonic, steady, slender vortex is solved using a type-differencing scheme. The results are compared with those of the full Navier-Stokes solver.

The results of the unsteady, full Navier-Stokes equations are presented in Chapters 6–9. Because of the unsteady nature of the vortex-breakdown flows, global time-integration technique is used in all the present computed cases. Global-time stepping is used to satisfy the stability of the computational scheme. Since the computational scheme is first-order accurate in time and third-order accurate in space, very small time steps are used to increase the accuracy in time without sacrificing of the computational efficiency.

In Chapter 6, the problem of a supersonic swirling flow in a configured circular duct is considered. A study was performed to select an optimum time step which satisfies computational accuracy and efficiency. A typical flow case of $M_\infty = 1.75$, $R_e = 10{,}000$ and $\beta = 0.32$ was computed using global time steps of 0.0025 and 0.00125 for the same computational grid. The results show negligible differences. Therefore, it was decided to use the higher value of time step since it increases the efficiency of the computations by saving one half of the computer time. Meanwhile, this value of time step maintains the accuracy of the computed results. The results of a parametric study which includes the effects of the Reynolds number, swirl ratio and Mach number on the development and behavior of vortex breakdown are presented. The critical effects of the duct-wall and

downstream boundary conditions on the vortex breakdown are addressed. The problem of the interaction of a supersonic swirling flow and an oblique shock wave is also presented.

In Chapter 7, the problem of a supersonic swirling jet interacting with a shock wave is solved. The effects of the Reynolds number and downstream boundary conditions on the vortex breakdown are studied.

In Chapters 8 and 9 some of the problems presented in Chapters 6 and 7 are computed using three-dimensional unsteady full Navier-Stokes equations. In Chapter 8, the effects of the grid fineness and distribution and the swirl ratio are addressed for the problem of a supersonic jet interacting with a shock wave. In Chapter 9, the supersonic swirling flow in a circular duct is solved using viscous and inviscid wall boundary conditions for the duct wall. The results show the formation of three-dimensional unsteady vortex-breakdown modes. Concluding remarks and recommendations for future work are presented in Chapter 10.

CHAPTER 2
LITERATURE REVIEW

In this Chapter, a literature review of analytical, experimental and computational works concerning vortex breakdown is presented. In general, the Chapter is divided into three sections. In the first section, the interest is focused on the physical understanding of the vortex-breakdown phenomenon where the important observations, definitions and theories are reviewed. In the second section, the previous work in the area of incompressible vortex breakdown is reviewed. Although the main interest in the present study is compressible vortex breakdown, it is very important to review the incompressible flow research work because most of the available literature has been focused on incompressible vortex breakdown. The literature lacks the compressible vortex-breakdown studies, and understanding the incompressible vortex-breakdown phenomenon could help in understanding the phenomenon of compressible vortex breakdown since the physics is similar in both applications, except for the compressibility effects. In the third section, the available literature in the area of compressible vortex breakdown and vortex-shock interaction is considered where emphasis is placed on research applications that may be compared with the present work.

Many comprehensive reviews on experimental, theoretical and computational aspects of vortex breakdown have been published by several authors. Among the important reviews are those presented by Hall [1], Leibovich [2, 3], Newsome and Kandil [4] and Escudier [5].

2.1 Understanding the Vortex-Breakdown Phenomenon

2.1.1 Early Observations

The first observation of vortex breakdown was documented by Peckham and Atkinson [6] on a Gothic wing of aspect ratio 1.0. They noticed that, at speeds greater than 150.0 ft/s and angles of attack between 20° and 30°, the decrease in temperature due to expansion in the low pressure cores of the vortex sheets was sufficient to cause water vapor condensation which revealed the path of the cores. As the incidence was increased, the length of the visible core decreased. The condensation trail appeared to "bell-out" before disappearing.

In 1958, Elle [7] noticed the same phenomenon on a thin delta wing at low speed and called it "vortex breakdown". He suggested that the breakdown may be due to the field of vorticity around the vortex developing in such a way that the downstream transport of fluid in the vortex core fails.

In 1960, Wérle [8] described how the free spiral vortices on delta wings suddenly expand if the incidence is increased beyond a critical value. He suggested that the phenomenon is due to transition from laminar to turbulent flow in the vortex.

In 1961, Lambourne and Bryer [9] conducted a general investigation of leading-edge vortex flow for better description and understanding of the vortex-breakdown phenomenon. They successfully captured two types of vortex breakdown, an axisymmetric bubble type and an asymmetric spiral type. The bubble type was characterized by a stagnation point along the vortex axis followed by a core enlargement and a limited region of re-circulation flow. This type was noticed to be highly unsteady along the core axis and it usually switched to the spiral-type. The spiral-type was characterized by a sudden deceleration of the fluid moving along the axis, followed by a kink, where the axial filament

was deflected to a spiral configuration. This structure was followed by a breakdown with large scale turbulence. They also studied the effects of external pressure gradients, the incidence angle and the Reynolds number on the formation and position of vortex breakdown. They suggested that the vortex breakdown or vortex (burst) may be due to the usual pressure recovery associated with a tailing edge. They also reported a vortex breakdown of an incompressible flow in a circular tube.

In 1962, Harvey [10] studied the vortex breakdown of a cylindrical vortex formed in a long water tube. His results showed that there was a critical value of swirl ratio beyond which a vortex breakdown occurred. It was noticed that, the vortex breakdown is characterized by a spherical bubble of stagnation fluid downstream of which conditions similar to those upstream of it are restored for a short distance until a second breakdown occurs.

In 1964, Lowson [11] conducted some water tunnel flow experiments on a slender delta wing. He found that the vortex breakdown is a non-axisymmetric instability. He suggested that the pressure gradient plays an important role in the phenomenon.

2.1.2 Theories

Following Hall [1] and Escudier [5, 12], the different approaches and theories of vortex breakdown can be categorized into three groups according to their principle ideas as follows:

1. The breakdown is a transition between two states, an upstream supercritical state and a downstream subcritical state.
2. The breakdown can occur as a consequence of some hydrodynamic instability.
3. The vortex breakdown is analogous to the two-dimensional boundary-layer separation.

The first approach was introduced originally by Squire in 1960. Motivated by the early observations of Elle [7], Werlé [8] and others, Squire [13] suggested the first theoretical model for the vortex breakdown. He suggested that, if standing waves were able to exist on a vortex core, then disturbances, which are generally present downstream, will spread forward along the vortex and cause breakdown. He considered only cylindrical vortices and symmetrical disturbances and assumed the flow to be inviscid and incompressible. For the three assumed forms of swirl distributions, it was found that the vortex breakdown may occur when the maximum swirl velocity is "rather larger" than the axial velocity. Squire's theory was supported by the experimental results obtained by Harvey [10]. The first criticism of Squire's theory came in 1971 when Sarpkaya [14] observed breakdowns in flows with adverse pressure gradients and swirl ratios less than unity.

Benjamin [15, 16, 17] proposed that vortex breakdown is a transition between two conjugate steady states of axisymmetric swirling flows. The transition is from a supercritical flow, which cannot support standing waves, to a subcritical flow, which can support standing waves. That is a direct analogy with the hydraulic jump in open-channel flow. A universal characteristic parameter, N, was defined which delineates the critical regions of the flow analogous to the Froude number for open-channel flow and Mach number for compressible flow. This parameter is the ratio of absolute phase velocities of long wavelength waves, which propagate along the vortex in the axial direction, where

$$N = \frac{C_+ + C_-}{C_+ - C_-} \tag{2.1}$$

and C_+ and C_- are the velocities at which waves of extreme length propagate with and against the flow direction, respectively. A flow is said to be supercritical if $N > 1$ and subcritical if $N < 1$. The computational results of Grabowsiky and Berger in 1976, [18], showed that it was possible to obtain vortex breakdown with subcritical upstream flow conditions.

Bossel [19] proposed that vortex breakdown is a necessary feature of supercritical flows having high swirl close to the critical state and some flow deceleration at and near the axis. He assumed the flows to be steady and axisymmetric. He solved the inviscid equations of motion using a prescribed rigid-body rotation at the upstream boundary. It was found that the breakdown depends very much on the form assumed for the downstream distribution of the stream function. Hall [1] suggested that a safer proposal would be that a necessary condition for breakdown is that the upstream flow is supercritical but near critical.

The second approach, which is the hydrodynamic instability, was introduced by Ludwieg [20]. He proposed that vortex breakdown, with a local stagnation of the axial flow, is a direct consequence of hydrodynamic instability with respect to spiral disturbances. He found the stability boundary for inviscid flow spiraling in a narrow annulus. He suggested that after the onset of the instability, spiral disturbances could amplify, induce an asymmetry in the vortex core and subsequently lead to stagnation. However, Leibovich and Stewartson [3] have pointed out that Ludwieg's application of his stability criterion to general vortex flows has no rational basis. It is also not expected to apply to the bubble type of vortex breakdown which is near-axisymmetric. Howard and Gupta [21] were able to derive a stability condition for non-dissipative swirling flows subjected to axisymmetric disturbances. Recently, In 1983 Leibovich and Stewartson [3] derived a sufficient condition for instability of unbounded columnar vortices. Some other studies concerning the hydrodynamic stability of swirling flows were carried out by Jones [22] and Lessen [23, 24].

The third approach was proposed by Hall [25, 26] who considered vortex breakdown to be analogous to the separation of a two-dimensional boundary layer. Hall was the first to show that the axial pressure gradient consists of the imposed external pressure

gradient plus the swirl contribution. He solved the quasi-cylindrical form of the equations of motion for an isolated slender vortex. The assumption of quasi-cylindrical flow was justified by the experimental observations that showed the axial gradients of the flow upstream of breakdown were small compared to the radial gradients and the stream surfaces were approximately cylindrical. In his study, the vortex breakdown was detected by the failure of the computations to converge. In 1967, Hall [26] attempted to reproduce numerically the behavior of a vortex core that was set up experimentally by Kirkpatrick [27] in a duct. He found a pronounced retardation of the flow along the axis, where the duct was converging, and was unable to proceed further because of the failure of his iterative computational scheme.

Similar approaches were used by Bossel [28], Mager [29], Kandil, et al. [30], Krause [31, 32], Menne and Liu [33] and most recently by Kandil and Kandil [34] for compressible vortex flows.

This method can be used to predict the occurrence and position of the abrupt change corresponding to the vortex breakdown. The boundary-layer-like equations used in this approach cannot be used to study the effects of the downstream boundary conditions since the equations are parabolic in space and the computational method is a marching-in-space technique. Therefore, there is no upstream influence and no description can be given of the flow field at/or downstream of the breakdown region.

Recently, Stuart [35] presented a critical review of vortex breakdown theories. He excluded the instability hypothesis and tried to unify the stagnation condition theory (the boundary-layer analogy) and the theory of conjugate conditions (the hydraulic jump analogy) in one theory. He considered the flow to be inviscid axisymmetric and incompressible . He showed that flows which exhibit a stagnation-like tendency on the axis evolve from a primary state A to another state B. If the state B is supercritical then

it will jump to another subcritical state. The supercritical and subcritical states were conjugate in Benjamin's sense. The supercritical state was defined as the one that cannot support very long waves while the subcritical state can support very long waves.

It is noticed that the phenomenon of vortex breakdown was first observed in 1957 and the first theoretical model was proposed in 1960 and then some other models followed but to date, there is still no general agreement regarding the essential nature of vortex breakdown regarding how and why it happens.

Next we review the experimental studies conducted to examine and validate the above theories. We start with the experimental work in the area of incompressible vortex breakdown.

2.2 Incompressible Vortex Breakdown

2.2.1 Experimental Studies

In the experiments conducted by Sarpkaya [14, 36, 37] in a water tube, three types of vortex breakdown were observed. These types are; mild (double helix) breakdown, spiral breakdown (followed by turbulent mixing), and axisymmetric breakdown (followed by a thicker vortex core, then a spiral breakdown, and finally by turbulent mixing). The type and location of the breakdown were found to be dependent upon the Reynolds number and circulation number of the flow. It was noticed in an axisymmetric breakdown that the bubble included an inclined vortex ring whose axis was rotating about the tube axis. It was shown that the axisymmetric breakdown may travel downstream responding to gradual and abrupt changes in the upstream or downstream flow conditions, in a manner analogous to the hydraulic jump in open-channel flows. In a later paper [37], it was shown that the adverse pressure gradient resulting from the axisymmetric tube convergence has a significant effect on the position of the vortex breakdown. Increasing the adverse

pressure gradient moves the breakdown position upstream as long as the boundary does not separate.

Faler and Leibovich [38] carried out a series of experiments and flow visualization to study the incompressible vortex breakdown. Their studies revealed six distinct modes of vortex breakdown depending on the values of Reynolds number and circulation. Among those modes are the three modes captured by Sarpkaya [14]. They found that the flow conditions upstream of bubble and spiral modes of breakdown were supercritical, in the sense of Benjamin's theory [15, 16, 17]. No axisymmetric disturbance patterns were observed and the authors concluded that the "axisymmetric" vortex breakdown is a misnomer that may lead to the over-emphasis of axial symmetry in theoretical work. In a later paper, Faler and Leibovich [39] presented the internal structure of the recirculation zone of the vortex breakdown. The time-averaged streamlines, in the interior of the bubble, showed a two-celled structure. The internal cells were rotating in opposite directions.

Garg and Leibovich [40] found, from experimental observations, that the bubble or spiral types of vortex breakdown act like solid bodies in changing an upstream jet-like flow into a wake-like flow. The wake regions were observed to be unstable to non-axisymmetric disturbances.

Uchida, et al. [41] conducted an experiment on a bubble-type vortex breakdown in a circular duct using air as the working fluid and LDV to measure the velocity components. The results showed the measured breakdown to have a positive axial velocity component around the center of the bubble. The flow was almost steady except for the flow downstream of the bubble. In 1987, Uchida, et al. [42] studied the spiral-type vortex breakdown in a pipe using water as the working fluid. The results showed the phenomenon to be completely unsteady.

The experimental studies showed the vortex-breakdown flow to be unsteady especially downstream of the breakdown region. The unsteady behavior was studied by Chanaud [43]. He studied the periodic motion that occurs in the vortex whistle and cyclone separators at high Reynolds numbers beyond a reversed flow region. He concluded that the motion can be described in terms of an oscillator which derives its energy from hydrodynamic instability of the fluid within a reversed-flow region on the swirl axis. Also, Cassidy and Falvey [44] presented observations and measurements made on the unsteady vortex flow developing at high axial Reynolds numbers in straight tubes. They concluded that the unsteady wall pressures, developed after vortex breakdown, are produced by a helical vortex processing about the tube axis.

No general rules can yet be given regarding the type of breakdown to be expected for any specified flow conditions. Under some conditions the forms can alternate randomly even though the imposed flow conditions do not change.

According to Lowson [11], the vortex-breakdown phenomenon, attendant to leading-edge vortices, always starts as a spiraling of the axial filament while the axisymmetric bubble form is a later development of the primary spiral form under certain transient conditions. On the other hand, It was shown by Lambourne [45] that the breakdown in a tube is initially axisymmetric but becomes transient and unstable and finally changes into the spiral form. He suggested that the spiral form should be regarded as arising from instability of the axisymmetric form. In another application, Granger [46] performed some experiments with a bathtub vortex. He described the development of the surge in details. At some instance in the development, a sphere with an inclined vortex ring inside was formed. Owing to pressure instabilities in the wake, the vortex ring was broken apart and the trapped fluid was shed downstream along the vortex filament. The bubble shape was then transformed to a single spiral filament.

The observations of Escudier and Zehnder [47] and Sarpkaya [37] showed also the random change of the vortex breakdown type.

It was also shown that the vortex breakdown has major effects on the performance of delta wings. Hummel and Srinivasan [48] carried out flow measurements and visualization of the vortex breakdown on two sharp-edged delta wings. Their results showed that the slopes of the coefficients of lift, drag and moment dropped markedly because of the vortex breakdown. Similar effects on the pitching moments of the tested delta wings were presented by Wentz and Kohlman [49].

2.2.2 Theoretical and Computational Analysis

2.2.2.1 Steady Axisymmetric Equations

Hall [50] studied a steady axisymmetric swirling flow of an incompressible fluid. He reduced the Navier-Stokes equations to a set of parabolic equations by assuming the viscous vortex core to be slender and applying boundary-layer type approximations. He used an implicit finite-difference method to solve the equations by marching in the axial direction. The method was used to solve for the vortex breakdown, Hall [25, 26]. The breakdown was detected by the failure of the computational iterative scheme to converge. The results of a sample vortex showed the failure of the computations occurred with a pronounced deceleration of the axial velocity, at a location close to the experimentally observed position for breakdown.

Bossel [19, 28] showed that the Navier-Stokes equations for viscous incompressible flow at high core Reynolds number can be reduced to three different systems. These systems are: a boundary-like parabolic set in regions of quasi-cylindrical flow; an inviscid elliptic equation where the vortex flow is expanding or contracting at or near the axis; and Stokes equations in a very small region surrounding a free stagnation point. He used

a Fourier-Bessel series to solve the inviscid set of equations in the vortex breakdown region. The scheme captured the vortex breakdown bubbles. It was concluded that vortex breakdown is a necessary feature of supercritical viscous vortex flows having high swirl close to the critical condition, with some flow retardation at and near the axis.

Lavan, et al. [51] studied the swirling viscous flow in a circular duct. They developed a linearized analytical solution which is valid for flows of large swirl ratios and small Reynolds numbers.

Torrance and Kopecky [52] and Kopecky and Torrance [53] numerically solved Navier-Stokes equations for axisymmetric incompressible flow of a rotating stream. An explicit finite-difference scheme was used and conditions for the formation of an isolated eddy were obtained. Results were presented for a range of Reynolds numbers and swirl ratios.

Mager [29] solved the quasi-cylindrical momentum-integral equations for the flow in the viscous core of a wing-tip vortex. Closed-form solutions with two separate branches were obtained. He suggested that the disturbance due to the beginning of the spiral breakdown causes the downstream asymmetric departure of the flow from its quasi-cylindrical behavior and the formation of the upstream axisymmetric bubble.

Grabowski and Berger [18] solved the steady axisymmetric Navier-Stokes equations for an unconfined viscous vortex for core Reynolds numbers up to 200. The method of artificial compressibility was used to solve the incompressible governing equations. Vortex breakdowns were obtained for subcritical upstream conditions, which is conflicting with Benjamin's theory. The results showed, for large values of swirl, a second axial flow retardation that could be considered as a spiral following the vortex breakdown bubble as observed in the experiments by Sarpkaya.

Narain [54] used an implicit finite-difference scheme to solve the axisymmetric viscous, incompressible Navier-Stokes equations for the flow case of a swirling jet in a cylindrical duct. He found that increasing swirl ratio and Reynolds number, decreasing surrounding stream velocity, and increasing the size of the tube enhanced the occurrence and size of vortex breakdown.

Hafez, Kuruvila and Salas [55] solved the axisymmetric steady Navier-Stokes equations and the Euler equations for the vortex breakdown. Their approach was restricted to low values of Reynolds numbers. Typical values of Reynolds numbers used were 100 and 200. The minimum grid-cell side was 1/16. The results showed the bubble size to be decreased by increasing the swirl ratio which contradicts the experimental observations.

Salas and Kuruvila [56] solved the axisymmetric steady Navier-Stokes equations in the stream function-vorticity formulation form using a second-order central-difference scheme. They were able to obtain steady solutions for a range of Reynolds numbers from 100 to 1800 by using direct matrix-inversion techniques. The minimum grid-cell side was 1/16. Increasing the Reynolds number and/or the swirl parameter revealed multi vortex-breakdown bubbles along the vortex axis.

Salas and Kuruvila [57] attempted to study the stability of their axisymmetric solutions to three-dimensional perturbations. Their results showed a small effect at low Reynolds numbers and a significant effect at higher Reynolds numbers.

The steady, axisymmetric Navier-Stokes and Euler equations were also used by Hafez, et al. [58] and Beran [59] to numerically simulate the vortex breakdown in an unbounded domain. The study was extended by Hafez and Ahmed [60] to cover both unbounded and bounded vortex-flow domains. In both studies, steady multiple-bubble solutions were obtained.

2.2.2.2 Unsteady Quasi-Axisymmetric Equations

Krause, Shi and Hartwich [31] presented the first attempt to solve the time-dependent axisymmetric Navier-Stokes equations for vortex-breakdown flows. The time-accurate solutions revealed a two-celled internal structure of the vortex breakdown bubble, that was observed experimentally by Faler and Leibovich [39]. Steady-state solutions were obtained only for the cases with no vortex breakdown.

Shi [61, 62] showed that the solution of the time-dependent axisymmetric Navier-Stokes equations did not depend on Reynolds number for low values of Reynolds number. The time-accurate results showed the evolution, merging and shedding of the vortex breakdown bubbles. He concluded that the flow appeared to be quasi-periodic. He suggested that the periodic inner cells flowing downstream could be representing the spiral tail behind a broken cell as observed in Sarpkaya's experiments.

Benay [63] studied the swirling flow in a cylinder using the unsteady, axisymmetric Navier-Stokes equations. A time-marching scheme was developed and used to obtain the steady-state solution. The effects of swirl ratio, Reynolds number and inflow profiles on the breakdown were studied.

Pagan and Benay [64] studied the effect of applying an adverse pressure gradient on the outer boundary of an incompressible swirling flow in an unbounded domain. They compared the results with their experimental results [65]. They concluded that pressure gradient effect on the vortex breakdown was not local and the magnitude of the pressure rise between inflow and exit sections played a major role. They carried out a parametric study of the axisymmetric vortex breakdown occurrence conditions [66] . The parameters included Reynolds number, velocities and pressure distribution on the outer boundary of the vortex. Steady state solutions were obtained for low and moderate values of Reynolds

numbers. For sufficiently large Reynolds numbers, pseudo-periodic unsteady solutions were obtained.

Menne [67] solved the axisymmetric Navier-Stokes equations for unsteady swirling flows. Cases of an isolated vortex and vortex flows in circular tubes were considered. Several finite-difference methods and inflow-boundary conditions were used. Steady and unsteady solutions were obtained depending on the type of inflow boundary conditions. The vortex-breakdown-bubbles' formation, merging and shedding were observed. Reynolds number of 200 was used in the study.

Recently, Wu and Hwang [68] solved the unsteady, axisymmetric Navier-Stokes equations for a confined swirling flow in a circular tube. A parametric study was performed to investigate the effects of inflow boundary conditions, wall boundary conditions and Reynolds number on the vortex breakdown structure. They concluded that the formation of steady, periodic or unsteady vortex breakdowns depends on the combination of the Reynolds number and boundary conditions. Reynolds numbers from 200 to 1000 were used in their study.

2.2.2.3 Three-Dimensional Equations

Nakamura, et al. [69, 70, 71] used the vortex-filament method to study the three-dimensional vortex breakdown phenomenon under the assumption of nonlinear, inviscid dynamics of vorticity. The method cannot take into account the viscous effects and the effects of Reynolds number. The breakdown was produced by introducing three-dimensional disturbances into the computational domain. The results showed the bubble-type breakdown to be followed by a kink or spiral-type breakdown.

Spall [72] presented the first attempt to solve the three-dimensional Navier-Stokes equations for incompressible vortex breakdown in an unbounded domain using a velocity-

vorticity formulation. Two flow cases were considered. In the first case, the vortex core was impeded in a uniform free-stream. In the second case, a pressure gradient was imposed on the free-stream boundary by decelerating the axial velocity component in the stream-wise direction. Typical Cartesian grids of 48x28x28 and 52x20x20 points were used in the study with a minimum cell thickness of 0.13. Bubble-type breakdowns were captured in both cases for a certain range of Rossby number. In a later paper, Spall, Gatski and Ash [73] presented the internal structure of the three-dimensional bubble-type vortex breakdown. The results showed the asymmetry and unsteadiness of the flow and the existence of multiple vortex rings inside the bubble. The effects of the free-stream axial velocity distribution on the position and type of vortex breakdown were studied by Spall and Gatski [74]. Bubble-type and spiral-type were produced depending on the imposed axial velocity deceleration.

Liu and Menne [75, 76] and Menne and Liu [77] studied the vortex flow in a slightly diverging tube using Navier-Stokes equations. The flow was assumed nearly axisymmetric and the non-axisymmetric influence was described by a Fourier decomposition in the circumferential direction. The results of the axisymmetric set showed only one vortex ring inside the bubble with no stagnation points on the vortex axis. The results of the non-axisymmetric set of equations showed a two-cell vortex breakdown bubble. In this case multi bubbles were observed along the axis.

Breuer and Hänel [78] used the concept of dual time-stepping to extend the classical numerical method of artificial compressibility to time-dependent applications. The problem of unsteady three-dimensional breakdown of an isolated vortex was considered. A Cartesian grid with 41x41x60 grid points was used in the study. The evolution and internal structure of the vortex breakdown bubble at Reynolds numbers of 200 and 2000 were presented. It was noticed that the solution became highly asymmetric after a large

computational time and a spiral type breakdown was developed. An axial pressure gradient was imposed on the vortex outer boundary to provoke the vortex breakdown.

Hsu, et al. [79] used a numerical method based on the concept of artificial compressibility to solve the unsteady three-dimensional vortex breakdown problem in an unbounded domain. Bubble-type vortex breakdowns were obtained for different flow and boundary conditions. The solutions approached steady-state conditions. There were no stagnation points or negative axial velocities along the vortex axis.

2.3 Compressible Vortex Breakdown and Vortex/Shock Interaction

2.3.1 Experimental Work

Elle [80] carried out an experimental investigation of vortex breakdown on a 60° delta wing at Mach numbers ranging from 0.7 to 1.03. For all the Mach numbers used except 1.03, the flow field was characterized by a shock wave followed by a vortex breakdown. The results showed that increasing the Mach number in the transonic zone had a stabilization effect on the vortex core. As the Mach number was increased, the position of the shock-vortex breakdown system moved downstream. At a Mach number of 1.03, no vortex breakdown was observed on the delta wing surface. The author rejected the idea that the vortex breakdown is a secondary effect of the shock wave-vortex interaction. Instead, he suggested that the shock wave is a direct consequence of the vortex breakdown.

Lambourne and Bryer [9] reported on the occurrence of a local region of supersonic flow which was terminated by a shock wave on a delta wing at a freestream Mach number of 0.9. The terminating shock wave intersected with the leading-edge vortex. It was observed that a vortex breakdown occurred immediately behind the shock wave. In their conclusion, it was suggested that the occurrence of the breakdown behind the

shock could be associated with the strong pressure rise across the shock. Increasing the freestream Mach number to 0.95 moved the shock-vortex breakdown system further downstream.

Craven and Alexander [81] carried out wind tunnel tests on a 75° swept delta wing at a Mach number of 2.0. It was found that the angle of attack at which vortex breakdown occurred was somewhat less than that at lower speeds. They observed the spiral-type vortex-breakdown region to be always bounded upstream by a conical shock wave.

Zatoloka, et al. [82] studied the interference of a compressible vortex filament at a freestream Mach number of 3.0 with a strong bow shock in front of a blunt body. It was noted that a stagnation zone with a conical shock was formed in front of the blunt body. In another experiment, an airfoil, as a vortex generator, was placed at an angle of attack ahead of an air-inlet-model entrance. The freestream Mach numbers were ranging from 1.4 to 1.95. It was observed that the interference of the vortex filament and the shock at the entrance resulted in the dissipation of the vortex and the formation of a conical shock with a stagnation point at the cone apex. It was concluded that the interaction caused a significant deterioration of the inlet performance.

An extensive study of the compressible vortex-normal shock interaction was reported by Delery and Horowitz [83]. In their study, the vortex produced using a half delta wing was intersected by a normal shock wave at the entrance of a Pitot tube. A parametric study was performed to obtain a swirl ratio limit, at each Mach number, beyond which the vortex breakdown will take place. The range of Mach number considered was from 1.7 to 2.8. For the breakdown cases, the measurements showed recirculation zones behind the interactions.

Schrader, et al. [84] studied the effects of Mach number and Reynolds number on leading-edge vortices on a delta wing of an aspect ratio of 2 at a high angle of attack.

The results showed the existence of supersonic pockets inside the primary vortices for transonic freestream Mach numbers. The supersonic pockets were terminated by a shock wave. At low-speed the vortex breakdown appeared as a slow decrease in the lift and it was coincident with the vortex-core lift-off. The high-speed lift-off revealed a sharp decrease in the lift coefficient and caused significant rolling moments. There was no clear evidence that the high-speed vortex breakdown was coincident with the lift-off.

Glotov [85] studied the interaction of a vortex core with a cone-cylinder body. It was reported that the limit for the breakdown to take place was the critical Mach number at which the oblique shock starts to detach. For Mach numbers greater than the critical value, unsteady conical detached shocks at the interaction were observed. For Mach numbers smaller than the critical value, the existence of a stagnation point and a reversed flow region was reported.

The experiments of Bannink [86] on a 65° delta wing showed that vortex breakdown at transonic speeds occurs more violently than at subsonic speeds. At an angle of attack of 20°, no vortex breakdown occurred at Mach numbers of 0.6 and 0.7 while breakdown occurred at Mach numbers of 0.75, 0.8 and 0.85. The position of the breakdown moved upstream with increasing Mach number. The results showed that the vortex breakdown was unsteady and asymmetric.

Erickson [87] studied the flow field of a 65° delta wing over a wide range of Mach numbers. At Mach numbers of 0.85 and 0.9 the leading-edge vortex interacted with a normal shock wave along the rear portion of the wing. The pressure distributions and total lift, drag and pitching-moment characteristics suggested that the vortex-shock interaction caused vortex breakdown over the wing at a slightly lower angle of attack.

Metwally, Settles and Horstman [88] presented the results of an experimental study of the interaction of a supersonic swirling jet with a normal shock wave. The swirling

jet was impeded in an inviscid freestream supersonic flow with a lower Mach number. Because of the mismatch of the static pressures of the freestream and the vortex, a normal shock was produced which intersected with the stream-wise vortex. In a typical case, the supersonic swirling jet Mach number was 3.0 while the freestream Mach number was 2.0. The intersection was characterized by the formation of a bubble shock with an apparent stagnation point at the cone apex on the vortex centerline. A recompression shock was observed downstream of interaction. A hypothetical model was suggested which assumed the occurrence of vortex breakdown and a recirculation zone behind the shock. However, their experiments did not support the hypothetical model.

The results of Cattafesta and Settles [89] supported the hypothetical model of Metwally, et al. The vortex core diverged rapidly as a result of a strong interaction of a swirling jet at a Mach number of 2.5 and a shock wave. The observations suggested the occurrence of a reversed flow region behind the shock. A supersonic vortex-breakdown curve, originally developed by Delery, et al. [90], was expanded to cover Mach numbers up to 4.0.

Cutler and Levy [91] studied the flow characteristics of a supersonic swirling jet. In the case of an overexpanded jet, a highly unsteady system of shocks was produced. The results suggested the occurrence of vortex breakdown. No qualitative or quantitative results were presented to support this suggestion.

The interaction of tip vortices and two-dimensional, conical and bow shock waves were studied by Kalkhoran, et al. [92]. No apparent vortex breakdown was reported as a result of vortex-oblique shock interaction. In a later paper, Kalkhoran, et al. [93] studied the influence of the vortex strength and vortex-airfoil vertical separation distance on the interaction. Unsteady detached shock waves were formed upstream of the airfoil leading edge.

2.3.2 Numerical Studies

Delery, et al. [90] were the first to consider compressible vortex breakdown problem. They assumed the flow to be steady, inviscid and axisymmetric. Furthermore, they assumed the stagnation enthalpy to be constant to avoid solving the energy equation. The Mach numbers varied from 1.4 to 2.2 with different swirl ratios. The results showed the dependency of the breakdown limit on the Mach number and swirl ratio.

Liu, Krause and Menne [94] studied the influence of compressibility on slender vortices. By assuming the vortex core to be slender, the full Navier-Stokes equations were reduced to a boundary-layer-like set of equations. Vortex breakdown was detected by the failure of their iterative scheme to converge. The results showed the shifting of the vortex breakdown position downstream with increasing Mach number. For Mach numbers greater than 0.7, no vortex breakdown was captured for the flow conditions considered.

Kandil and Kandil [34] presented the analysis and computation of a steady, compressible, quasi-axisymmetric flow of an isolated slender vortex. The compressible Navier-Stokes equations were reduced to a simpler set by using the slenderness and quasi-axisymmetry assumptions. The resulting set of equations, along with a compatibility equation, were transformed from the diverging physical domain to a rectangular computational domain. The governing equations were solved using a space marching type-differencing scheme. Vortex-breakdown location was detected by the failure of the scheme to converge. Computational examples included vortex flows at different Mach numbers, swirl ratios and external axial-pressure gradients. Good agreement was shown for a bench-mark case between the computed results using the slender-vortex equations and those of a full Navier-Stokes solver, which were also produced by the same authors. The results are presented in Chapter 5.

Copening and Anderson [95] solved the three-dimensional Euler equations for shock-vortex interactions at Mach numbers of 2.28 and 5.0. No vortex breakdown was obtained in both cases.

Metwally, et al. [88] solved the quasi-axisymmetric Navier-Stokes equations for the interaction of a supersonic swirling jet and a shock wave. The results showed a region of reversed flow behind the shock wave. These results supported the authors' hypothetical model. The only set of flow conditions considered was for a flow case of a jet Mach number of 3.0 and freestream Mach number of 2.0.

The first time-accurate Navier-Stokes solution for a supersonic vortex breakdown was developed by Kandil, et al. [96]. They considered a supersonic, quasi-axisymmetric vortex flow in a configured circular duct. The time-accurate solution of the unsteady, compressible, full Navier-Stokes equations was obtained using an implicit, upwind, flux-difference splitting finite-volume scheme. A shock wave was generated near the duct inlet and an unsteady vortex breakdown was predicted behind the shock. The predicted flow was characterized by the evolution, convection and shedding of vortex-breakdown bubbles. The Euler equations were also used to solve the same problem. The Euler solution showed increases in both the size and number of vortex-breakdown bubbles, in comparison with those of the Navier-Stokes solutions. Only one value of Reynolds number (10,000) was used in Ref. [96]. In a later paper [97], the study of this flow was expanded using time-accurate computations of the Navier-Stokes equations with a fine grid in the shock-vortex interaction region and for long computational times. Several issues were addressed in that study. First, they showed the effect of Reynolds number on the temporal evolution and persistence of vortex-breakdown bubbles behind the shock. In that stage of computations, the conditions at the downstream exit were obtained by extrapolating the components of the flowfield vector from the interior cell

centers. Although the flow was supersonic over a large portion of the duct exit, subsonic flow existed over a small portion of the exit around the duct centerline. Therefore, selected flow cases were computed using Riemann-invariant-type boundary conditions at subsonic points of the duct exit. Finally, the effect of swirl ratio at the duct inlet was investigated. The results of that study will be presented in Chapter 6. The critical effects of downstream-boundary conditions on supersonic vortex-breakdown were studied by Kandil, et al. [98] for both internal and external flows. For this purpose, the unsteady, compressible, full Navier-Stokes equations were used along with an implicit, upwind, flux-difference splitting, finite-volume scheme for time-accurate solutions. For the internal flow case, supersonic swirling flow in a configured duct is considered along with four types of downstream boundary conditions. Keeping the duct geometry and the upstream flow conditions fixed, the exit boundary conditions were varied. The four exit boundary conditions included extrapolation of all the five variables from the interior cell centers, specifying the downstream pressure by two methods and extrapolating the other flow conditions from the interior cell centers, and using a disk of specified radius at the exit section. For the external flow case, a supersonic swirling jet issued from a nozzle into a supersonic non-swirling flow of a lower Mach number. Two types of downstream boundary conditions were considered. In the first type, extrapolation of all five variables from the interior cell centers was used, while in the second type, the standard Riemann-invariant-type boundary condition was used. The results will be presented in Chapters 6 and 7.

Kandil, Kandil and Liu [99] expanded their study of supersonic vortex breakdown to include both quasi-axisymmetric and three-dimensional flow cases for both internal and external flows. For internal flow cases, they presented time-accurate solutions for the flow in a configured circular duct. For external flow cases, they presented

time-accurate solutions for the shock-vortex interaction problem using different types of grids. The results showed several modes of breakdown; e.g., no-breakdown, transient single-bubble breakdown, transient multi-bubble breakdown, periodic multi-bubble multi-frequency breakdown and helical breakdown. In a later paper by the same authors [100], three-dimensional effects on supersonic vortex breakdown for both external and internal flows were considered. For the internal flow case, the effects of the outer-wall boundary conditions were studied where both viscous and inviscid boundaries were considered. For the external flow case, the effects of the grid shape and number and distribution of the grid points on the vortex breakdown resulting from shock-vortex interaction were studied. The results are presented in Chapter 8 for the internal flow case and in Chapter 9 for the external flow case.

CHAPTER 3
FORMULATION

3.1 Introduction

For decades and because of the limitations on the computational facilities, many restrictions were applied to the formulation of the vortex-breakdown problem. The assumptions of steady, quasi-axisymmetric, inviscid slender vortex cores reduced the Navier-Stokes equations to simpler forms that have been used to predict the possibility of vortex breakdown occurrence and its approximate position. The experimental measurements showed the vortex breakdown to be an unsteady, three-dimensional phenomenon. Therefore, some of the mathematical assumptions should be relaxed. A set of unsteady quasi-axisymmetric viscous equations was recently used to solve for the evolution and behavior of vortex breakdown of the bubble type [96]. However, the full Navier-Stokes equations should be solved to account for the three-dimensional effects and various modes of vortex breakdown.

In vortex flows, viscous effects are of great importance especially downstream of a vortex breakdown region. In high Reynolds number viscous flows, the viscous effects are concentrated near the vortex axis, adjacent to solid walls and in wake regions. More grid points are needed in these regions for good resolution of those effects.

In this study, the unsteady, compressible, full Navier-Stokes equations are used to formulate the problem of supersonic vortex breakdown. The usage of full Navier-Stokes equations is made possible because of the available super-computer capabilities which were not available few years ago.

Assuming the flow to be steady and quasi-axisymmetric and the vortex core to be slender, the Navier-Stokes equations are reduced to a simpler set that is used to predict the possibility of vortex breakdown and its approximate position. Moreover, this set can be used to produce a compatible set of inflow boundary conditions for the Navier-Stokes computations.

3.2 Three-Dimensional Navier-Stokes Equations

The conservative form of the nondimensional, unsteady, compressible, Navier-Stokes equations in terms of Cartesian coordinates (x_1, x_2, x_3) is given by

$$\frac{\partial \vec{q}}{\partial t} + \frac{\partial\left(\vec{E}_j - \vec{E_{v_j}}\right)}{\partial x_j} = 0 \quad ; \; j = 1-3 \tag{3.1}$$

where the flow field vector, $\vec{q}$ is given by

$$\vec{q} = [\rho, \rho u_1, \rho u_2, \rho u_3, \rho e]^t \tag{3.2}$$

and the inviscid flux vectors are given by

$$\vec{E}_j = \left[\rho u_j, \rho u_1 u_j + \delta_{j1} p, \rho u_2 u_j + \delta_{j2} p, \rho u_3 u_j + \delta_{j3} p, \rho u_j\left(e + \frac{p}{\rho}\right)\right]^t \; ; \; j = 1-3 \tag{3.3}$$

where δ_{ij} is the Kronecker delta function, $\delta_{ij} = \begin{cases} 1 & i = j \\ 0 & i \neq j \end{cases}$

and the viscous fluxes are

$$\left(\vec{E_v}\right)_j = [0, \tau_{j1}, \tau_{j2}, \tau_{j3}, u_m \tau_{jm} - q_j]^t \quad ; \quad j = 1-3, \; m = 1-3 \tag{3.4}$$

In the equations above, the variables are nondimensionalized using the corresponding freestream variables. The reference parameters are L, a_∞, L/a_∞, ρ_∞ *and* μ_∞ for the length, velocity, time, density and molecular viscosity, respectively.

The total energy per unit mass, e , is nondimensionalized by a_∞^2 and the pressure, p, is nondimensionalized by $\rho_\infty a_\infty^2$.

The pressure is related to the total energy per unit mass and density by the perfect gas equation

$$p = (\gamma - 1)\rho\left[e - \frac{1}{2}(u_1^2 + u_2^2 + u_3^2)\right] \tag{3.5}$$

where γ is the ratio of specific heats which is assumed to be constant and its value is 1.4 in this study.

In Eq. (3.4), the τ terms represent the Cartesian components of the shear-stress tensor for a Newtonian fluid, where Stokes hypothesis is employed and the fifth term represents the shear-dissipation power, $u_m\tau_{jm}$, and heat flux components.

The Cartesian components of the shear-stress tensor are given by

$$\tau_{ij} = \frac{\mu M_\infty}{R_e}\left(\frac{\partial u_i}{\partial x_j} + \frac{\partial u_j}{\partial x_i} - \frac{2}{3}\delta_{ij}\frac{\partial u_k}{\partial x_k}\right) \;\; ; \;\; i,j,k = 1-3 \tag{3.6}$$

the shear-dissipation power and the heat flux components are given by

$$\begin{aligned} u_m\tau_{jm} &= \frac{\mu M_\infty}{R_e}\, u_m\left(\frac{\partial u_j}{\partial x_m} + \frac{\partial u_m}{\partial x_j} - \frac{2}{3}\delta_{jm}\frac{\partial u_k}{\partial x_k}\right) \;\; ; \;\; j,k,m = 1-3 \\ q_j &= \frac{-\mu M_\infty}{(\gamma-1)P_r R_e}\,\frac{\partial T}{\partial x_j} \;\; ; \;\; j = 1-3 \end{aligned} \tag{3.7}$$

where the dimensionless viscosity, μ, is calculated from Sutherland's law

$$\mu = T^{\frac{3}{2}}\left(\frac{1+c}{T+c}\right) \tag{3.8}$$

where T is the dimensionless temperature and c is Sutherland's constant, $c \approx 0.4317$. The Prandtl number, P_r, is assumed to be constant with a value of 0.72 throughout the calculations.

The freestream Reynolds number, R_e, is defined by $R_e = \frac{\rho_\infty U_\infty L}{\mu_\infty}$ and the characteristic length (L) is the initial radius of the vortex or the duct inlet radius. According to

the characteristic parameters, the freestream flow variables are given by:

$$\rho_\infty = 1.0$$

$$u_{1_\infty} = M_\infty$$

$$u_{2_\infty} = 0.0$$

$$u_{3_\infty} = 0.0$$

$$e_\infty = \frac{1}{\gamma(\gamma-1)} + \frac{M_\infty^2}{2} \tag{3.9}$$

$$p_\infty = \frac{1}{\gamma}$$

$$a_\infty = T_\infty = 1.0$$

$$U_\infty = \sqrt{u_{1_\infty}^2 + u_{2_\infty}^2 + u_{3_\infty}^2} = u_{1_\infty}$$

$$M_\infty = \frac{U_\infty}{a_\infty} = u_{1_\infty}$$

where M_∞ is the freestream Mach number.

The unsteady Navier-Stokes equations in the Cartesian system are transformed into time-independent body-conformed coordinates, ξ^1, ξ^2 and ξ^3; where

$$\xi^m = \xi^m(x_1,\ x_2,\ x_3) \tag{3.10}$$

The conservative form of the equations, in terms of the body-conformed coordinates, is given by:

$$\frac{\partial \vec{Q}}{\partial t} + \frac{\partial}{\partial \xi^m}\left(\widehat{E} - \widehat{E}_v\right)_m = 0 \ ;\ m = 1-3 \tag{3.11}$$

and

$$\vec{Q} = \frac{\vec{q}}{J} = \frac{1}{J}[\rho,\ \rho u_1,\ \rho u_2,\ \rho u_3,\ \rho e]^t \tag{3.12}$$

where $\frac{1}{J} = J^{-1}$ is the Jacobian of the transformation from the Cartesian coordinates to the body-conformed coordinates and is given by

$$J^{-1} = \frac{\partial(x_1, x_2, x_3)}{\partial(\xi^1, \xi^2, \xi^3)} = \begin{vmatrix} x_{1_{\xi^1}} & x_{1_{\xi^2}} & x_{1_{\xi^3}} \\ x_{2_{\xi^1}} & x_{2_{\xi^2}} & x_{2_{\xi^3}} \\ x_{3_{\xi^1}} & x_{3_{\xi^2}} & x_{3_{\xi^3}} \end{vmatrix} \tag{3.13}$$

The inviscid fluxes are given by

$$\begin{aligned}\widehat{E}_m &= \frac{1}{J}\left[\partial_k \xi^m \vec{E}_k\right]^t \\ &= \frac{1}{J}[\rho U_m, \rho u_1 U_m + \partial_1 \xi^m p, \rho u_2 U_m + \partial_2 \xi^m p, \rho u_3 U_m + \partial_3 \xi^m p, U_m(\rho e + p)]^t\end{aligned} \tag{3.14}$$

where the contravariant velocity component in the ξ^m, U_m, is given by

$$U_m = \partial_k \xi^m u_k \qquad ; \; k = 1 - 3 \tag{3.15}$$

and $\partial_k \equiv \frac{\partial}{\partial x_k}$

The viscous and heat flux terms in the ξ^s direction, $\left(\widehat{E}_v\right)_s$, is given by

$$\left(\widehat{E}_v\right)_s = \frac{1}{J}[0, \; \partial_k \xi^s \tau_{k1}, \; \partial_k \xi^s \tau_{k2}, \; \partial_k \xi^s \tau_{k3}, \partial_k \xi^s \left(u_p \tau_{kp} - q_k\right)]^t \; ; k, p = 1 - 3 \tag{3.16}$$

The shear-stress and heat-transfer terms in the above equation are given by

$$\begin{aligned}\tau_{kl} &= \frac{\mu M_\infty}{R_e}\left(\partial_l \xi^m \frac{\partial u_k}{\partial \xi^m} + \partial_k \xi^m \frac{\partial u_l}{\partial \xi^m} - \frac{2}{3}\delta_{kl}\partial_j \xi^m \frac{\partial u_j}{\partial \xi^m}\right) \\ q_k &= -\frac{\mu M_\infty}{(\gamma - 1) P_r R_e}\partial_k \xi^m \frac{\partial a^2}{\partial \xi^m}\end{aligned} \tag{3.17}$$

Expanding the first element of the three momentum elements of equation (3.16), we get

$$\partial_k \xi^s \tau_{k1} \equiv \frac{\mu M_\infty}{R_e}\left[\left(\partial_k \xi^s \partial_1 \xi^n - \frac{2}{3}\partial_1 \xi^s \partial_k \xi^n\right)\frac{\partial u_k}{\partial \xi^n} + \partial_k \xi^s \partial_k \xi^n \frac{\partial u_1}{\partial \xi^s}\right] \tag{3.18}$$

The second and third elements of the momentum elements are obtained by replacing the subscript "1", everywhere in equation (3.18), with 2 and 3, respectively. The last element of equation (3.17) is given by

$$\begin{aligned}\partial_k \xi^s \left(u_p \tau_{kp} - q_k\right) \equiv \frac{\mu M_\infty}{R_e} &\left[\left(\partial_k \xi^s \partial_p \xi^n - \frac{2}{3}\partial_p \xi^s \partial_k \xi^n\right) u_p \frac{\partial u_k}{\partial \xi^n}\right. \\ &\left. + \partial_k \xi^s \partial_k \xi^n u_p \frac{\partial u_p}{\partial \xi^n} + \frac{1}{(\gamma - 1) P_r}\partial_k \xi^s \partial_k \xi^n \frac{\partial a^2}{\partial \xi^n}\right]; \quad k, s, n, p = 1 - 3\end{aligned} \tag{3.19}$$

where a is the dimensionless local speed of sound and $a^2 = T$.

3.3 Slender Quasi-Axisymmetric Formulation

Starting with the steady, compressible Navier-Stokes equations which are expressed in the cylindrical coordinates ($\tilde{x}, \tilde{r}$ *and* ϕ), assuming the isolated vortex core to be slender $\left[\ \frac{\tilde{r}}{L} = O\left(\frac{1}{\sqrt{R_e}}\right),\ \frac{\tilde{v}}{U_\infty} = O\left(\frac{1}{\sqrt{R_e}}\right)\ \right]$, where L is the breakdown length, $\tilde{v}$ the radial velocity component and R_e is the freestream Reynolds number, and assuming the flow is quasi-axisymmetric $\left[\frac{\partial(\ )}{\partial\phi} = 0\right]$, and performing an order-of-magnitude analysis, $\left[\ \frac{\partial}{\partial\tilde{x}} \ll \frac{\partial}{\partial\tilde{r}}\ ,\ \tilde{v} \ll \tilde{u}\right]$, the equations are reduced to a compressible, quasi-axisymmetric, boundary-layer-like set.

The dimensionless form of the equations are given by:

Continuity:

$$\frac{\partial}{\partial x}(\rho u) + \frac{1}{r}\frac{\partial}{\partial r}(\rho r v) = 0 \tag{3.20}$$

Axial momentum:

$$\rho\left(u\frac{\partial u}{\partial x} + v\frac{\partial u}{\partial r}\right) = -\frac{\partial p}{\partial x} + \frac{M_\infty}{r}\frac{\partial}{\partial r}\left(\mu r\frac{\partial u}{\partial r}\right) \tag{3.21}$$

Radial momentum:

$$\rho\frac{w^2}{r} = \frac{\partial p}{\partial r} \tag{3.22}$$

Circumferential momentum:

$$\rho\left(u\frac{\partial w}{\partial x} + v\frac{\partial w}{\partial r} + \frac{vw}{r}\right) = \frac{M_\infty}{r^2}\frac{\partial}{\partial r}\left(\mu r^3\frac{\partial}{\partial r}\left(\frac{w}{r}\right)\right) \tag{3.23}$$

The energy equation:

$$\begin{aligned}\rho\left(u\frac{\partial T}{\partial x} + v\frac{\partial T}{\partial r}\right) =& u\frac{\partial p}{\partial x} + v\frac{\partial p}{\partial r} + \frac{M_\infty}{P_r r}\frac{\partial}{\partial r}\left(r\mu\frac{\partial T}{\partial r}\right) + \\ & \mu M_\infty\left[\left(\frac{\partial u}{\partial r}\right)^2 + \left\{r\frac{\partial}{\partial r}\left(\frac{w}{r}\right)\right\}^2\right]\end{aligned} \tag{3.24}$$

Equation of state:

$$p = \frac{\gamma - 1}{\gamma}\rho T \tag{3.25}$$

In equations (3.20)-(3.25), the nondimensional density, ρ, pressure, p, viscosity, μ, speed of sound, a, the cylindrical velocity components u, v and w along the x, r and ϕ coordinate directions and temperature, T, are defined as the ratio of the corresponding physical quantities to those in the freestream; namely ρ_∞, $\rho_\infty a_\infty^2$, μ_∞, a_∞ and a_∞/c_p, where c_p is the specific heat at constant pressure. Moreover, M_∞ is the freestream Mach number, where $M_\infty = \frac{U_\infty}{a_\infty}$, $P_r = \mu c_p/K$ the Prandtl number where K is the coefficient of thermal conductivity and γ the ratio of specific heats. The Prandtl number value is chosen as 0.72. The radius r and the radial velocity component v have been stretched by a small parameter ϵ; where

$$\epsilon^2 = \frac{1}{R_e} = \frac{\mu_\infty}{\rho_\infty a_\infty r_1} = \frac{M_\infty}{R_e}$$
$$R_e = \frac{\rho_\infty U_\infty r_1}{\mu_\infty} \tag{3.26}$$

where r_1 is the vortex viscous-core radius at the initial axial station. The molecular viscosity is evaluated by Sutherland's law, Eq. (3.8).

Next, a Levey-Lee-type transformation is introduced to transfer the diverging physical domain into a constant-outer-boundary computational domain. The transformation from the physical domain coordinates, (x, r), to the computational domain coordinates, (ξ, η), is given by

$$\xi = \int_0^x \rho_e \mu_e \, dx \quad , \quad \eta = \frac{\rho_e}{\lambda(\xi)} \int_0^r \frac{\rho}{\rho_e} \, dr \tag{3.27}$$

where λ is given by

$$MSF = \frac{\lambda(\xi)}{f(\rho)} = \frac{r_e(\xi)}{r_r(\xi_i)} \tag{3.28}$$

where MSF is the modified shape factor characterizing the growth of the vortex-core boundary and $f(\rho)$ is a function relating the density integral at any axial station to that at the initial station. Its value equals unity for incompressible flows. The subscript "e" refers to external conditions and the subscript "i" refers to conditions at the initial station.

The governing equations take the following form in the computational domain:

Continuity equation:

$$\frac{\partial V}{\partial \eta} + \frac{1}{r\lambda}\frac{\partial}{\partial \xi}(\lambda u r) + \frac{\lambda}{\rho r}V = 0 \tag{3.29}$$

the relation between v and V is given by

$$\begin{aligned} v &= \frac{\rho_e \mu_e \lambda}{\rho} V - \eta_x \frac{\lambda u}{\rho} \quad , \quad \eta_x = \frac{\partial \eta}{\partial x} \\ where \qquad V &= -\frac{1}{\lambda r}\frac{\partial}{\partial \xi}\left(\int_0^{\eta} ru\lambda \quad d\eta\right) \end{aligned} \tag{3.30}$$

Axial momentum:

$$u\frac{\partial u}{\partial \xi} + V\frac{\partial u}{\partial \eta} = -\frac{1}{\rho}\frac{\partial p}{\partial \xi} - \frac{\lambda}{\rho}\theta\frac{w^2}{r} + \frac{M}{\lambda r}\frac{\partial}{\partial \eta}\left(\frac{cr}{\lambda}\frac{\partial u}{\partial \eta}\right) \tag{3.31}$$

where $\theta = \frac{1}{\rho_e \mu_e}\eta_x$ and $c = \frac{\rho \mu}{\rho_e \mu_e}$.

Radial momentum:

$$\frac{\lambda}{r}w^2 = \frac{\partial p}{\partial \eta} \tag{3.32}$$

Circumferential momentum:

$$u\frac{\partial w}{\partial \xi} + V\frac{\partial w}{\partial \eta} + \frac{\lambda}{\rho r}(V - \theta u)w = \frac{M}{\lambda^2 r^2}\frac{\partial}{\partial \eta}\left[cr^3\frac{\partial}{\partial \eta}\left(\frac{w}{r}\right)\right] \tag{3.33}$$

Energy equation:

$$\begin{aligned} u\frac{\partial T}{\partial \xi} + V\frac{\partial T}{\partial \eta} =& \frac{u}{\rho}\frac{\partial p}{\partial \xi} + \frac{\lambda}{\rho}\frac{Vw^2}{r} + \frac{M}{P_r \lambda^2 r}\frac{\partial}{\partial \eta}\left(cr\frac{\partial T}{\partial \eta}\right) \\ &+ \frac{Mc}{\lambda^2}\left\{\left(\frac{\partial u}{\partial \eta}\right)^2 + \left[r\frac{\partial}{\partial \eta}\left(\frac{w}{r}\right)\right]^2\right\} \end{aligned} \tag{3.34}$$

3.3.1 Inflow and Boundary Conditions

At the initial axial station, $x = x_i$, the axial and circumferential velocity components, u and w, respectively, and the temperature, T, are specified as follows:

$$\begin{aligned} u(r, x_i) &= u_i(r) \\ w(r, x_i) = w_i(r) &= \begin{cases} \beta u_i r(2.0 - r^2) & r \le 1 \\ \beta u_i / r & r \ge 1 \end{cases} \\ T(r, x_i) &= T_i(r) \end{aligned} \tag{3.35}$$

The quasi-axisymmetric condition is used to obtain the following boundary conditions at the vortex axis, $r = 0$

$$\frac{\partial u}{\partial r}(0,x) = V(0,x) = w(0,x) = \frac{\partial T}{\partial x}(0,x) = 0 \tag{3.36}$$

The vortex outer boundary, $r = r_o$, is assumed to be a stream surface and the flow is assumed inviscid with negligible diffusion. The kinematic equation of the stream surface is given by:

$$\frac{v_e}{u_e} = r_o \frac{\rho_e \mu_e}{\lambda} \acute{\lambda} \quad ; \quad \acute{\lambda} = \frac{d\lambda}{d\xi} \tag{3.37}$$

The circumferential momentum reduces to

$$\left(\frac{\partial w}{\partial \xi}\right)_{\eta_o} + \frac{\acute{\lambda}}{\lambda} w_e = 0 \tag{3.38}$$

where the viscous term has been neglected and equation (3.30) has been used to cancel the coefficient of the $\left(\frac{\partial w}{\partial \eta}\right)_{\eta_o}$ term and to replace V_e. This equation is integrated to give the corresponding condition on the circumferential velocity at the boundary, w_e:

$$w_e = \frac{1}{\lambda} w_{e_i} \tag{3.39}$$

where $w_{e_i} = w(r_o, x_i)$

Neglecting the viscous term in the axial momentum equation, Eq. (3.31), using the stream surface condition, along with the radial momentum equation, the following equation is obtained

$$\rho_e u_e \frac{\partial u_e}{\partial \xi} = -\frac{\partial p_e}{\partial \xi} + \rho_e \frac{\acute{\lambda}}{\lambda} w_e^2 \tag{3.40}$$

which can be reduced, using equation (3.39) to an equation on u_e which is given by

$$u_e \frac{\partial u_e}{\partial \xi} = -\frac{1}{\rho_e} \frac{\partial p_e}{\partial \xi} + \frac{\acute{\lambda}}{\lambda^3} w_{e_i}^2 \tag{3.41}$$

Neglecting the viscous terms in the energy equation, (3.34), and using the stream-surface condition, the following equation is obtained

$$\rho_e \frac{\partial T_e}{\partial \xi} = \frac{\partial p_e}{\partial \xi} \tag{3.42}$$

From the equation of state, we get the condition on the density

$$\rho_e = \frac{\gamma}{\gamma - 1} \frac{p_e}{T_e} \tag{3.43}$$

The pressure distribution at the outer boundary is specified

$$p(r_o, x) = p_e(x) \tag{3.44}$$

In order to ensure that the vortex is slender, a compatibility condition must be satisfied for the ratio between the radial velocity and axial velocity at any station. The equation and the procedure are given in Appendix A.

CHAPTER 4
COMPUTATIONAL SCHEMES FOR THREE-DIMENSIONAL NAVIER-STOKES EQUATIONS

4.1 Introduction

In this Chapter, an upwind scheme is applied to the inviscid fluxes of the conservative form of the full Navier-Stokes equations in a body-conformed generalized coordinate system. The scheme is a flux-difference splitting, finite-volume scheme. The aim of upwind schemes is to mimic the physical propagation of disturbances of the flow equations into the difference equations. This can be achieved by the recognition of the direction of propagation of information according to the theory of characteristics. Accordingly, type-dependent differencing of the information travelling in opposite directions is introduced in a separate and stable manner. Using upwind schemes, which take into account the essential physical properties of the equations, prevents the creation of unwanted oscillations like those created by central-differencing schemes in the vicinity of discontinuities which have to be damped by the addition of artificial-dissipation terms. In the flux-vector splitting methods, only information from the physical properties is introduced, depending upon the sign of eigenvalues of the inviscid Jacobians. The flux terms are split and discretized directionally according to the sign of the associated propagation speed. The physical properties can be introduced into the differencing equations by considering the conservative variables as piecewise constant over the grid cells at each time step and the time evolution is determined by the exact solution of the one-dimensional Riemann problem at the inter-cell boundaries. This approach has been modified, where the local

Riemann problem is approximately solved using approximate Riemann solvers. These methods are called flux-difference splitting methods.

Upwind schemes can be used with either conservative or non-conservative forms of the governing equations. The advantage of using the conservative form is that shock waves and contact discontinuities evolve as parts of the solution process. The disadvantage is that upwind differencing can be implemented more economically in a non-conservative formulation but must be supplemented with a shock-fitting scheme for accurate results. The available shock-fitting schemes are not able to treat complex shock wave interactions efficiently. In general, upwind schemes require two-to-three times more arithmetic operations than an equivalent central-difference method, if both are used to solve the conservative formulation. The increase in the computational effort per iteration is substituted by an improved rate of convergence and wider applicability to general problems without the need for adjustable parameters.

In this Chapter, the finite-volume implementations of conservative methods are discussed. Then, the application of the upwind flux-difference scheme to the three-dimensional Navier-Stokes equation is presented. The scheme is capable of solving time-dependent problems by using global time-stepping and the steady-flow problems by using pseudo time-stepping to get asymptotic steady solutions. Because of the unsteady nature of the vortex-breakdown flows, global time-integration technique was used in all the presented calculations. At the end of this Chapter, the boundary and initial conditions for the numerical simulations of quasi-axisymmetric and three-dimensional flow problems are also discussed.

4.2 Implicit Upwind Schemes

The presence of viscosity and heat conduction terms in the compressible, unsteady, Navier-Stokes equations transforms the conservative forms of momentum and energy into second-order partial differential equations. These equations are parabolic in time and elliptic in space. The continuity equation is hyperbolic in space and time. The coupled system of the Navier-Stokes equations is parabolic-hyperbolic in time and elliptic-hyperbolic in space. The unsteady Navier-Stokes equations are integrated in time to take advantage of the parabolic-hyperbolic nature of the equations in time. The unsteady problems are solved using global time-stepping to obtain the solution history, while the steady problems are solved using pseudo time-stepping to obtain an asymptotic steady-state solution. Two types of schemes can be used to integrate the equations in time, explicit and implicit schemes. Explicit schemes are simpler and require less computational effort but the time step is restricted by stability considerations. Implicit schemes require more computational effort and more computational time per iteration but they have less restrictive stability bounds in choosing the time step in comparison with explicit schemes. Thus, an implicit scheme was used in the present study.

4.2.1 Semi-Discrete Finite-Volume Formulation

The conservative form of the time-dependent, three-dimensional, full Navier-Stokes equations, Eq. (3.1), is integrated over the computational domain coordinates (ξ^1, ξ^2, ξ^3) as follows

$$\begin{gathered} \frac{\partial \vec{Q}}{\partial t} + \frac{\partial\left(\widehat{E}_m - \widehat{E}_{v_m}\right)}{\partial \xi^m} = 0 \\ \int_V \frac{\partial \vec{Q}}{\partial t}\, d\xi^1 d\xi^2 d\xi^3 + \int_V \frac{\partial\left(\widehat{E}_m - \widehat{E}_{v_m}\right)}{\partial \xi^m}\, d\xi^1 d\xi^2 d\xi^3 = 0 \end{gathered} \tag{4.1}$$

It should be noted here that the product $d\xi^1 d\xi^2 d\xi^3$ does not represent the cell volume. We apply the equation in the integral form to a region $\mathcal{R}$ with closed boundaries $\partial\mathcal{R}$. The boundaries are aligned with the coordinate lines ξ^1, ξ^2 and ξ^3 in the physical domain. The resulting integral equation takes the form

$$\int_R \frac{\partial \vec{Q}}{\partial t}\, d\xi^1 d\xi^2 d\xi^3 + \int_{\partial R} \left(\widehat{E}_1 - \widehat{E}_{v_1}\right) d\xi^2 d\xi^3 + \int_{\partial R} \left(\widehat{E}_2 - \widehat{E}_{v_2}\right) d\xi^1 d\xi^3 + \int_{\partial R} \left(\widehat{E}_3 - \widehat{E}_{v_3}\right) d\xi^1 d\xi^2 = 0 \tag{4.2}$$

The region $\mathcal{R}$ is divided into very small hexahedral cells. The boundaries of each cell are aligned with the coordinate lines ξ^1, ξ^2 and ξ^3 in the physical domain.

The integral equation is applied to each hexahedral cell and then the hexahedral cell in the physical domain is mapped on a unit cube in the computational domain whose centroid is denoted by the subscripts i, j and k as shown in Fig. 4.1. The resulting equation is given by

$$\begin{aligned}\left(\frac{1}{J}\frac{\partial \vec{Q}}{\partial t}\right)_{i,j,k} = &- \left(\widehat{E}_1 - \widehat{E}_{v_1}\right)_{i+\frac{1}{2},j,k} + \left(\widehat{E}_1 - \widehat{E}_{v_1}\right)_{i-\frac{1}{2},j,k} \\ &- \left(\widehat{E}_2 - \widehat{E}_{v_2}\right)_{i,j+\frac{1}{2},k} + \left(\widehat{E}_2 - \widehat{E}_{v_2}\right)_{i,j-\frac{1}{2},k} \\ &- \left(\widehat{E}_3 - \widehat{E}_{v_3}\right)_{i,j,k+\frac{1}{2}} + \left(\widehat{E}_3 - \widehat{E}_{v_3}\right)_{i,j,k-\frac{1}{2}} = \widehat{R}\left(\vec{Q}_{i,j,k}\right)\end{aligned} \tag{4.3}$$

where the conservative variables, $\vec{Q}$, located at the cell-center (i, j, k), are cell-averaged values rather than point-wise values and the fluxes are evaluated at the cell interfaces $i \pm \frac{1}{2}$, $j \pm \frac{1}{2}$ and $k \pm \frac{1}{2}$.

The term $\frac{1}{J}$ represents the cell volume bounded by the coordinates lines ξ^1, ξ^2 and ξ^3. This volume is determined by summing the volumes of the six pentahedra forming the hexagonal cell. Each pentahedron is defined by one of the six cell faces and a point within the cell, which is the average of the eight vertices composing the cell.

4.2.1.1 Time Integration

The Euler implicit-time differencing method is used to integrate numerically the semi-discretized equation, Eq. (4.3), in order to advance the solution in time from some set of initial conditions.

Using a Taylor series expansion, the flow vector $\vec{Q}$ at time level $n+1$ is expressed in terms of the vector value at time level n as follows

$$\vec{Q}^{n+1} = \vec{Q}^n + \Delta t\left(\frac{\partial \vec{Q}}{\partial t}\right)^{n+1} + O(\Delta t)^2, \tag{4.4}$$

where Δt is the time step and the term $\left(\frac{\partial \vec{Q}}{\partial t}\right)$ is evaluated implicitly at time level $n+1$.

The governing equations at time level $n+1$ are given by

$$\frac{1}{J}\left(\frac{\partial \vec{Q}}{\partial t}\right)^{n+1} + \left(\frac{\partial\left(\hat{E}_m - \hat{E}_{v_m}\right)}{\partial \xi^m}\right)^{n+1} = 0 \tag{4.5}$$

Substituting Eq. 4.5 into Eq. 4.4 gives

$$\frac{1}{J}\frac{\Delta \vec{Q}}{\Delta t} + \left(\frac{\partial\left(\hat{E}_m - \hat{E}_{v_m}\right)}{\partial \xi^m}\right)^{n+1} = O(\Delta t) \tag{4.6}$$

where

$$\Delta \vec{Q} = \vec{Q}^{n+1} - \vec{Q}^n \tag{4.7}$$

Using Taylor series expansion, the inviscid and viscous fluxes at time level $n+1$ can be linearized as follows

$$\frac{1}{J}\frac{\Delta \vec{Q}}{\Delta t} + \left[\delta_{\xi^m}\left(\frac{\partial\left(\hat{E}_m - \hat{E}_{v_m}\right)}{\partial \vec{Q}}\right)^n\right]\Delta \vec{Q} + \delta_{\xi^m}\left(\hat{E}_m - \hat{E}_{v_m}\right)^n = 0 \tag{4.8}$$

$$\left[\frac{I}{J\Delta t} + \left\{\delta_{\xi^m}\left(\frac{\partial\left(\hat{E}_m - \hat{E}_{v_m}\right)}{\partial \vec{Q}}\right)^n\right\}\right]\Delta \vec{Q} = -\delta_{\xi^m}\left(\hat{E}_m - \hat{E}_{v_m}\right)^n \; ; m = 1-3 \tag{4.9}$$

where I is the identity matrix and δ_{ξ^m} , $m = 1 - 3$, are spatial difference operators in the ξ^1, ξ^2 and ξ^3 directions, respectively.

The right-hand side of Eq. (4.9) represents the inviscid and viscous steady-state residuals where the inviscid residual is given by

$$\begin{aligned} \widehat{R}^n &= \delta_{\xi^m}\widehat{E}_m \\ &= \delta_{\xi^1}\widehat{E}_1 + \delta_{\xi^2}\widehat{E}_2 + \delta_{\xi^3}\widehat{E}_3 \end{aligned} \tag{4.10}$$

and the viscous residual is given by

$$\begin{aligned} \widehat{R}^n &= \delta_{\xi^m}\widehat{E}_{v_m} \\ &= \delta_{\xi^1}\widehat{E}_{v_1} + \delta_{\xi^2}\widehat{E}_{v_2} + \delta_{\xi^3}\widehat{E}_{v_3} \end{aligned} \tag{4.11}$$

For steady flows, the total residual goes to zero as time goes to infinity.

Solution of Eq. (4.9) requires solving a large banded block matrix at each time step, which is very expensive. Therefore, the approximate factorization method by Beam and Warming [101] is used to split the left-hand side of Eq. (4.9) into a sequence of simpler operators in order to reduce the computational effort. The left-hand side of Eq. (4.9) can be approximately factored as follows

$$\begin{aligned} &\left[I + J\Delta t\delta_{\xi^1}\left(\frac{\partial\widehat{E}_1}{\partial\vec{Q}} - \frac{\partial\widehat{E}_{v_1}}{\partial\vec{Q}}\right)\right]\left[I + J\Delta t\delta_{\xi^2}\left(\frac{\partial\widehat{E}_2}{\partial\vec{Q}} - \frac{\partial\widehat{E}_{v_2}}{\partial\vec{Q}}\right)\right] \\ &\left[I + J\Delta t\delta_{\xi^3}\left(\frac{\partial\widehat{E}_3}{\partial\vec{Q}} - \frac{\partial\widehat{E}_{v_3}}{\partial\vec{Q}}\right)\right]\Delta\vec{Q} = -J\Delta t\left(\widehat{R}^n - \widehat{R}_v^n\right) \end{aligned} \tag{4.12}$$

In this form, the solution is obtained by solving the following three one-dimensional problems

$$\begin{aligned} &\left[I + J\Delta t\delta_{\xi^1}\left(\frac{\partial\widehat{E}_1}{\partial\vec{Q}} - \frac{\partial\widehat{E}_{v_1}}{\partial\vec{Q}}\right)\right]\Delta\vec{Q}^* = -J\Delta t\left(\widehat{R}^n - \widehat{R}_v^n\right) \\ &\left[I + J\Delta t\delta_{\xi^2}\left(\frac{\partial\widehat{E}_2}{\partial\vec{Q}} - \frac{\partial\widehat{E}_{v_2}}{\partial\vec{Q}}\right)\right]\Delta\vec{Q}^{**} = \Delta\vec{Q}^* \\ &\left[I + J\Delta t\delta_{\xi^3}\left(\frac{\partial\widehat{E}_3}{\partial\vec{Q}} - \frac{\partial\widehat{E}_{v_3}}{\partial\vec{Q}}\right)\right]\Delta\vec{Q}^n = \Delta\vec{Q}^{**} \end{aligned} \tag{4.13}$$

where the superscripts * and ** denote intermediate values. Solving each step of Eq. (4.13) only requires the solution of a block tri- or penta-diagonal set of equations depending on the spatial accuracy of the left-hand side operator. The solution of Eq. (4.13) is accomplished through three sweeps in the ξ^1, ξ^2 and ξ^3 directions and $\vec{Q}^{n+1}$ is obtained using the relation

$$\vec{Q}^{n+1} = \vec{Q}^n + \Delta\vec{Q}^n \tag{4.14}$$

If a steady-state solution exists, the solution continues until the residual reaches a specified small value. The convergence of the solution is accelerated using a local time stepping procedure in which each cell is advanced in time by its own time step, according to stability considerations at that point. If a time-accurate solution is required, a global time stepping is used for all the grid cells.

Next, we consider the linearization and discretization of the inviscid flux vectors on the left-hand side of Eq. (4.13) and the treatment of the viscous terms. The upwind scheme used in the present study will be reviewed.

4.2.2 Higher Order Spatial Differencing of the Inviscid Fluxes

In order to difference the inviscid fluxes a Monotone Upstream-Centered Scheme for Conservation Laws (MUSCL) is implemented in the solver used in the present study which is called FTNS3D. This solver is a modified version of the CFL3D code [102, 103, 104, 105].

Consider the spatial operator in the ξ^1 direction, namely δ_{ξ^1}, operating on the flux vector $\widehat{E}_1$. The difference equation can be written as

$$\delta_{\xi^1}\widehat{E}_1 = \widehat{E}_{i+\frac{1}{2}} - \widehat{E}_{i-\frac{1}{2}} \tag{4.15}$$

where the interface flux is constructed as

$$\begin{aligned}\widehat{E}_{1_{i+\frac{1}{2}}} &= \widehat{E}_1\left(\bar{q}^-, \bar{q}^+\right)_{i+\frac{1}{2}} \\ &= \widehat{E}_1\left(\bar{q}_{i-1}, \bar{q}_i, \bar{q}_{i+1}, \bar{q}_{i+2}, \nabla\xi^1/J\right)\end{aligned} \tag{4.16}$$

In the equation above, j, k and n are kept constant and were dropped for convenience, and the term $\left|\nabla\xi^1\right|/J$ represents the directed area of the cell face. The directed areas are calculated as one-half the vector cross-product of the two diagonal vectors connecting opposite vertex points of a cell face, taken such that the directed area is parallel to the direction of increasing ξ^1. The flow field vectors $\bar{q}^{\pm}$ denote state variables on cell interfaces determined from upwind-biased interpolations of the primitive variables which are given by

$$\begin{aligned}\bar{q}^-_{i+\frac{1}{2}} &= \bar{q}_i + \frac{1}{4}[(1-\kappa)\Delta_- + (1+\kappa)\Delta_+]\bar{q}_i \\ \bar{q}^+_{i+\frac{1}{2}} &= \bar{q}_{i+1} - \frac{1}{4}[(1-\kappa)\Delta_+ + (1+\kappa)\Delta_-]\bar{q}_{i+1}\end{aligned} \tag{4.17}$$

where $\Delta_+\bar{q}_i \equiv$ forward differencing $=\bar{q}_{i+1} - \bar{q}_i$.

$\Delta_-\bar{q}_i \equiv$ backward differencing $=\bar{q}_i - \bar{q}_{i-1}$.

$\bar{q} = (\rho, u_1, u_2, u_3, p)^t$

The parameter κ forms a family of difference schemes; κ=-1 corresponds to second-order fully upwind differencing whose second-order truncation-error term in the ξ^1 direction has a value of $\frac{1}{3}\Delta\xi^{1^2}\left(\partial^3\bar{q}/\partial\xi^{1^3}\right)$, $\kappa = 0$ corresponds to Fromm scheme whose truncation-error is $\frac{1}{12}\Delta\xi^{1^2}\left(\partial^3\bar{q}/\partial\xi^{1^3}\right)$, $\kappa = 1/3$ corresponds to third-order upwind biased differencing with third-order truncation error and $\kappa = 1$ corresponds to central differencing with the first term of the truncation error equals to $-\frac{1}{6}\Delta\xi^{1^2}\left(\partial^3\bar{q}/\partial\xi^{1^3}\right)$.

For the upwind-biased schemes, sometimes a flux limiter is needed to eliminate oscillations in shock regions. A min-mod limiter [102] is used in most of the present research applications. Flux-limited interpolations are identical in form to Eq. (4.17), except that the operators Δ_+ and Δ_- are replaced with $\overline{\Delta}_+$ and $\overline{\Delta}_-$, respectively, where:

$$\overline{\Delta}_+ = max[0, min(\Delta_+ sign\Delta_-, \beta\Delta_- sign\Delta_+)]sign\Delta_+$$

$$\overline{\Delta}_- = max[0, min(\Delta_- sign\Delta_+, \beta\Delta_+ sign\Delta_-)]sign\Delta_- \qquad (4.18)$$

$$and \qquad \beta = \frac{3-\kappa}{1-\kappa}$$

The effect of the limiter is negligible in smooth flow regions. In the regions of flow with high gradients, the accuracy reduces to first order. The interface flux values are evaluated according to the flux-splitting method employed. In this study, the flux-difference splitting method was considered.

4.3 Flux-Difference Splitting

The approximate Riemann solver of Roe [106] is based on a characteristic decomposition of the fluid differences while ensuring the conservation properties of the scheme.

Consider a one-dimensional equation in the form

$$\frac{\partial \vec{q}}{\partial t} + \frac{\partial \vec{E}}{\partial x_1} = 0 \qquad (4.19)$$

when $\vec{E}$ is a linear function of $\vec{q}$, Eq. (4.19) can be written as

$$\frac{\partial \vec{q}}{\partial t} + A\frac{\partial \vec{q}}{\partial x_1} = 0 \qquad (4.20)$$

where $A = \frac{\partial \vec{E}}{\partial \vec{q}}$. The exact solution of the Riemann problem in terms of the flux difference is given by

$$\vec{E}_R - \vec{E}_L = \sum_{k=1}^{3} \alpha_k \lambda_k e_k \qquad (4.21)$$

where λ_k and e_k are the eigenvalues and eigenvectors of the Jacobian matrix A, respectively, and α_k represents the projection of the difference in $\vec{q}$ between the initial right and left states onto the eigenvectors of A. From Fig. 4.2, it is clear that the flux at the interface could be determined by either one of the following equations

$$E_{i+\frac{1}{2}}(\vec{q}_L, \vec{q}_R) = \vec{E}_L + \sum^{-} \alpha_k \lambda_k e_k \qquad (4.22)$$

$$E_{i+\frac{1}{2}}(\vec{q}_L, \vec{q}_R) = \vec{E}_R - \sum^{+} \alpha_k \lambda_k e_k \tag{4.23}$$

where the signs on the summation symbols refer to the directions of the wave speeds. Averaging Eq. (4.22) and Eq. (4.23), we get

$$E_{i+\frac{1}{2}}(\vec{q}_L, \vec{q}_R) = \frac{1}{2}\left[\left(\vec{E}_L + \vec{E}_R\right) - \sum_{k=1}^{3} \alpha_k |\lambda|_k e_k\right] \tag{4.24}$$

If $\vec{E}$ is not a linear function of $\vec{q}$, e.g. one-dimensional Euler equations, Roe [106] developed the following solution for the approximate linearized problem

$$\frac{\partial \vec{q}}{\partial t} + \widetilde{A}\frac{\partial \vec{q}}{\partial x_1} = 0 \tag{4.25}$$

where $\widetilde{A}$ is called Roe-average matrix. It is required for the matrix $\widetilde{A}$ to have the following list of properties to ensure uniform validity across flow discontinuities

1. It constitutes a linear mapping from $\vec{q}$ to $\vec{E}$.
2. As $\vec{q}_R \rightarrow \vec{q}_L \rightarrow \vec{q}$, then $\widetilde{A}(\vec{q}_R, \vec{q}_L) \rightarrow A(\vec{q})$.
3. For any $\vec{q}_R$, $\vec{q}_L$, $\quad \widetilde{A}(\vec{q}_R, \vec{q}_L) * (\vec{q}_R - \vec{q}_L) = \vec{E}_R - \vec{E}_L$.
4. The eigenvectors of $\widetilde{A}$ are linearly independent.

Using the third property, the flux difference between the left and right states can be written as

$$\vec{E}_R - \vec{E}_L = \widetilde{A}(\vec{q}_R - \vec{q}_L) \tag{4.26}$$

The interface flux is thus

$$E_{i+\frac{1}{2}}(\vec{q}_R, \vec{q}_L) = \frac{1}{2}\left[\left(\vec{E}_L + \vec{E}_R\right) - \left|\widetilde{A}\right|(\vec{q}_R, -\vec{q}_L)\right]_{i+\frac{1}{2}} \tag{4.27}$$

For three-dimensional generalized flows, Eq. (4.27) can be written as

$$\widehat{E}_{m_{i+\frac{1}{2}}}\left(\vec{Q}_R,\vec{Q}_L\right)=\frac{1}{2}\left[\left(\widehat{E}_{m_R}+\widehat{E}_{m_L}\right)-\left|\widetilde{A}\right|\left(\vec{Q}_R,-\vec{Q}_L\right)\right]_{i+\frac{1}{2}};\ m=1-3 \qquad (4.28)$$

Where j,k and n are kept constants.

The last term in the above equation represents the dissipation contribution to the interface flux and is given by [103]

$$\left|\widetilde{A}\right|\left(\vec{Q}_R-\vec{Q}_L\right)=\left|\widetilde{A}\right|\Delta\vec{Q}$$

$$=\begin{bmatrix}\alpha_4\\ \widetilde{u}_1\alpha_4+\xi^m_{x_1}\alpha_5+\alpha_6\\ \widetilde{u}_2\alpha_4+\xi^m_{x_2}\alpha_5+\alpha_7\\ \widetilde{u}_3\alpha_4+\xi^m_{x_3}\alpha_5+\alpha_8\\ \widetilde{H}\alpha_4+\widetilde{\widetilde{u}}_m\alpha_5+\widetilde{u}_1\alpha_6+\widetilde{u}_2\alpha_7+\widetilde{u}_3\alpha_8-\left(\frac{\widetilde{a}^2}{\gamma-1}\right)\alpha_1\end{bmatrix} \qquad (4.29)$$

where

$$\alpha_1=\left|\frac{grad(\xi^m)}{J}\right|\left|\widetilde{\widetilde{u}}_m\right|\left(\Delta\rho-\frac{\Delta p}{\widetilde{a}^2}\right) \qquad (4.30)$$

$$\begin{aligned}\alpha_2&=\frac{1}{2\widetilde{a}^2}\left|\frac{grad(\xi^m)}{J}\right|\left|\widetilde{\widetilde{u}}_m+\widetilde{c}\right|(\Delta p+\widetilde{\rho}\,\widetilde{a}\,\Delta\widetilde{\widetilde{u}}_m)\\ \alpha_3&=\frac{1}{2\widetilde{a}^2}\left|\frac{grad(\xi^m)}{J}\right|\left|\widetilde{\widetilde{u}}_m-\widetilde{c}\right|(\Delta p-\widetilde{\rho}\,\widetilde{a}\,\Delta\widetilde{\widetilde{u}}_m)\end{aligned} \qquad (4.31)$$

$$\alpha_4=\alpha_1+\alpha_2+\alpha_3 \qquad (4.32)$$

$$\alpha_5=\widetilde{a}(\alpha_2-\alpha_3) \qquad (4.33)$$

$$\alpha_{5+j}=\left|\frac{grad(\xi^m)}{J}\right|\left|\widetilde{\widetilde{u}}_m\right|\left(\widetilde{\rho}\Delta u_j-\xi^m_{x_1}\widetilde{\rho}\Delta\widetilde{\widetilde{u}}_m\right)\ ;\ j=1-3 \qquad (4.34)$$

The ˜ superscript denotes Roe-averaged values where

$$\begin{aligned}
\widetilde{\rho} &= \sqrt{\rho_L \rho_R} \\
\widetilde{u}_j &= (u_{j_L} + u_{j_R}\sqrt{\rho_L \rho_R})/(1+\sqrt{\rho_L \rho_R}) \\
\widetilde{H} &= (H_L + H_R\sqrt{\rho_L \rho_R})/(1+\sqrt{\rho_L \rho_R}) \\
\widetilde{a}^2 &= (\gamma-1)\Big[\widetilde{H} - (\widetilde{u}_1^2 + \widetilde{u}_2^2 + \widetilde{u}_3^2)/2\Big]
\end{aligned} \tag{4.35}$$

where $\widetilde{H}$ is the Roe-average enthalpy.

The contravariant velocity normal to the cell interface is given by

$$\bar{U}_m = \hat{\xi}^m_{x_j} u_j \qquad ; \qquad j = 1-3 \tag{4.36}$$

The state variables, Q_R and Q_L, are obtained from Eq. 4.17 by replacing q^+ and q^- by Q_R and Q_L, respectively.

4.4 Discretization of the Viscous Fluxes

In this section, the discretization of the viscous fluxes on the left-hand and right-hand sides of Eq. (4.13) are considered. The viscous flux contributions on the left-hand side of the difference equations are given by

$$\delta\xi^1 \frac{\partial \widehat{E}_{v_1}}{\partial \vec{Q}} + \delta\xi^2 \frac{\partial \widehat{E}_{v_2}}{\partial \vec{Q}} + \delta\xi^3 \frac{\partial \widehat{E}_{v_3}}{\partial \vec{Q}} \equiv \delta\xi^m \frac{\partial \widehat{E}_{v_m}}{\partial \vec{Q}} \qquad ; \; m = 1-3 \tag{4.37}$$

This can be written as

$$\delta\xi^m \frac{\partial}{\partial \vec{Q}} \Big(\widehat{E}_{v_m}(\xi^1) + \widehat{E}_{v_m}(\xi^2) + \widehat{E}_{v_m}(\xi^3) \Big) \tag{4.38}$$

where $\widehat{E}_{v_m}(\xi^n)$; $n = 1,2$ *or* 3 denotes the portion of the vector $\widehat{E}_{v_m}$ containing only terms that are functions of ξ^n.

Differentiating the portions with terms that are functions of ξ^n (where $n \neq m$) will produce cross-derivative terms. The presence of these terms on the left-hand side of the equation would destroy the efficiency of the upper and lower triangular matrix

solution, by requiring a central differencing of these terms. Also, in some applications, the viscous terms containing derivatives parallel to the solid body surface can be neglected relative to those in the normal direction. This approximation is known as the thin-layer approximation where only the viscous terms containing derivatives normal to the body surface (along the coordinate line), are retained. In this study, the thin-layer approximation was used only to simplify the viscous terms on the left-hand side of the difference equation for better efficiency of the computer code; while the cross derivative terms were retained on the right-hand side of the difference equation where they can be evaluated explicitly. For the vortex-breakdown problem considered in this study, the viscous effects are important in all three directions. The thin-layer-type viscous terms are obtained from Eq. (3.16) by keeping only terms with derivatives in the direction under consideration. For example, consider the first momentum term in the ξ^3 direction. These terms are obtained by setting the dummy and summation indices, s and m, respectively equal to 3.

$$\partial_k \xi^3 \tau_{k1} \equiv \frac{\mu M_\infty}{R_e}\left[\frac{1}{3}\partial_k \xi^3 \partial_1 \xi^3 \frac{\partial u_k}{\partial \xi^3} + \partial_k \xi^3 \partial_k \xi^3 \frac{\partial u_1}{\partial \xi^3}\right] \quad ; \; k = 1-3 \tag{4.39}$$

The second and third momentum terms are obtained by replacing the subscript "1" by "2" and "3" respectively.

In general, the three momentum equations in the ξ^m directions are given by

$$\partial_k \xi^m \tau_{kn} \equiv \frac{\mu M_\infty}{R_e}\left[\frac{1}{3}\partial_k \xi^m \partial_n \xi^m \frac{\partial u_k}{\partial \xi^m} + \partial_k \xi^m \partial_k \xi^m \frac{\partial u_n}{\partial \xi^3}\right] \quad ; \; k,m,n = 1-3 \tag{4.40}$$

The energy equation in the ξ^m direction is given by

$$\begin{aligned}\partial_k \xi^m \left(u_p \tau_{kp} - q_k\right) \equiv \frac{\mu M_\infty}{R_e} & \left[\frac{1}{3}\partial_k \xi^m \partial_p \xi^m u_p \frac{\partial u_k}{\partial \xi^m}\right. \\ & \left. + \partial_k \xi^m \partial_k \xi^m \left(\frac{\partial u_n}{\partial \xi^m} + \frac{1}{(\gamma-1)P_r}\frac{\partial a^2}{\partial \xi^m}\right)\right] ; \; k,m,n,p = 1-3\end{aligned} \tag{4.41}$$

The implicit viscous terms can be written as

$$\delta_{\xi^m}\left(\frac{\partial \widehat{E}_{v_m}(\xi^m)}{\partial \vec{Q}}\right) \equiv \delta_{\xi^m}\hat{A}_{v_m} \tag{4.42}$$

where all the cross-derivative terms were dropped.

On the right-hand side of the difference equation, Eq. (4.3), the viscous terms' contribution in the residual is given by

$$\widehat{R}_v = \delta_{\xi^1}\widehat{E}_{v_1} + \delta_{\xi^2}\widehat{E}_{v_2} + \delta_{\xi^3}\widehat{E}_{v_3} = \delta_{\xi^m}\widehat{E}_{v_m} \;\; ; \;\; m = 1-3 \tag{4.43}$$

The viscous fluxes are linearized in time as follows:

$$\widehat{E}^{n+1}_{v_m} = \widehat{E}^{n}_{v_m} + O(\Delta t) \tag{4.44}$$

The result is that the viscous terms at a time step $n+1$ are evaluated using the information from the previous time step, n.

The fluxes are centrally differenced and a second-order approximation to the cross-derivative terms were used. For example, the term $\frac{\partial^2 u_1}{\partial \xi^1 \partial \xi^2}$ can be written as:

$$\begin{aligned}\frac{\partial^2 u_1}{\partial \xi^1 \partial \xi^2} &\equiv \delta_{\xi^1\xi^2}(u_1)_{i,j} \\ &= \alpha^+\left(\delta_{\xi^1\xi^2}(u_1)_{i+\frac{1}{2},j+\frac{1}{2}} + \delta_{\xi^1\xi^2}(u_1)_{i-\frac{1}{2},j-\frac{1}{2}}\right) \\ &+ \alpha^-\left(\delta_{\xi^1\xi^2}(u_1)_{i-\frac{1}{2},j+\frac{1}{2}} + \delta_{\xi^1\xi^2}(u_1)_{i+\frac{1}{2},j-\frac{1}{2}}\right)\end{aligned} \tag{4.45}$$

where

$$\delta_{\xi^1\xi^2}(u_1)_{i+\frac{1}{2},j+\frac{1}{2}} = (u_1)_{i+1,j+1} - (u_1)_{i,j+1} + (u_1)_{i,j} - (u_1)_{i-1,j} \tag{4.46}$$

and

$$\alpha^+ + \alpha^- = \frac{1}{2} \tag{4.47}$$

If a symmetric difference is chosen, [107], then $\alpha^+ = \alpha^- = \frac{1}{4}$ which gives

$$\delta_{\xi^1\xi^2}(u_1)_{i,j} = \frac{1}{4}\left((u_1)_{i+1,j+1} - (u_1)_{i+1,j-1}\right) - \frac{1}{4}\left((u_1)_{i-1,j+1} - (u_1)_{i-1,j-1}\right) \tag{4.48}$$

4.5 Initial and Boundary Conditions

4.5.1 Initial Conditions

All the numerical calculations for the swirling flows in bounded computational domains were obtained by using stagnation initial conditions for the interior domain. Prescribed inflow conditions were used at the first axial station. These initial conditions simulated the case of impulsively placing the duct in a supersonic swirling flow.

The numerical calculations of the swirling jet interacting with a shock wave in an unbounded domain were obtained using freestream conditions for the entire computational domain. This was done by assuming that the flow conditions in the entire computational domain were equal to those of the wind-tunnel measurements. Hence, the present flow case simulates a sudden discharge of a swirling supersonic jet from a nozzle into a uniform supersonic flow.

4.5.2 Wall Boundary Conditions

The boundary conditions for the present work are implemented explicitly. On the solid duct wall, two boundary conditions are used. The first boundary conditions are those of a viscous surface where the no-slip and no-penetration conditions are enforced. The velocity components are set equal to zero and the normal pressure gradient is assumed to be zero. The adiabatic condition is maintained on the solid surface. The second type of boundary condition is the inviscid surface boundary condition where the no-slip condition is relaxed.

4.5.3 Exit Boundary Conditions

Several types of boundary conditions were investigated in this study. Some examples are: extrapolation, Riemann-type boundary conditions, placing a solid disc at the exit section and extrapolating the pressure gradient from the interior cell centers. Different

types of exit boundary conditions are described in detail in the corresponding Chapters of results, later in this study.

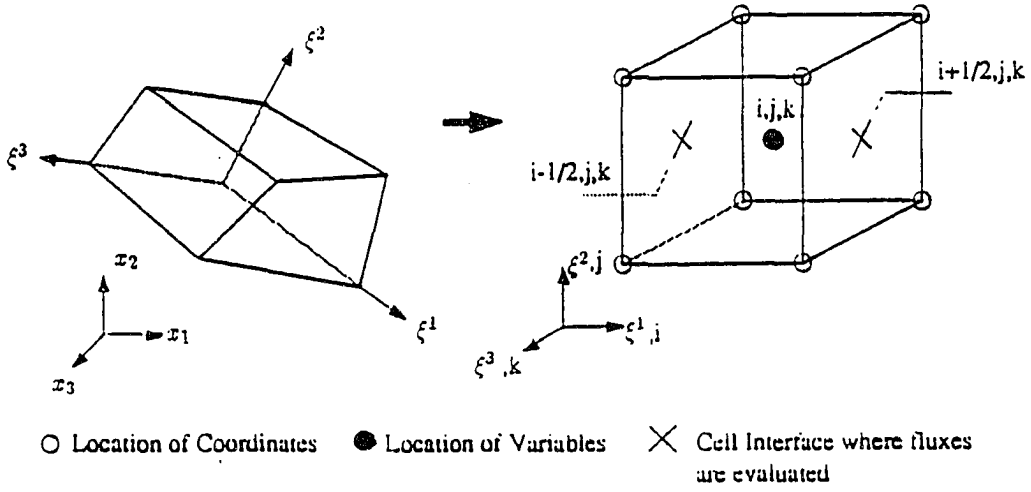

Figure 4.1 Finite-volume discretization

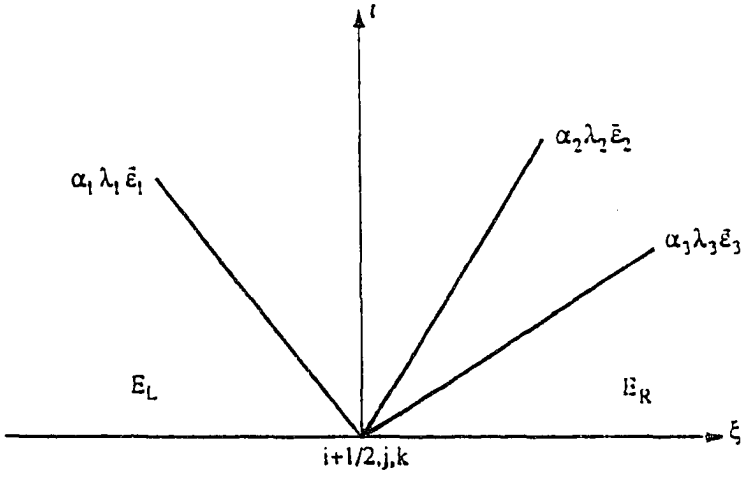

Figure 4.2 Schematic representation of the waves at a cell interface

CHAPTER 5
COMPRESSIBLE QUASI-AXISYMMETRIC SLENDER-VORTEX FLOW AND BREAKDOWN

5.1 Introduction

In this Chapter, results obtained using the slender-vortex formulation described in Chapter 3 are presented. The objective of the slender-vortex computations was to obtain compatible inflow profiles that can be used for computations with the full Navier-Stokes equations. Moreover, this method can be used to test the potential of some inflow profiles to produce vortex breakdown under certain flow conditions. However, it cannot be used to study the vortex-breakdown region or to study the effects of downstream boundary conditions. A parametric study is presented which includes the effects of the Mach number, the external axial pressure gradient and the swirl ratio on the vortex-breakdown length. The vortex-breakdown length is the axial distance at which the computations stop because of the failure of the iterative scheme to converge. Then, the radial distributions of the flow variables for two of the cases under consideration are presented at different axial stations. Finally, the results obtained using the slender-vortex equations and those of a full Navier-Stokes solver, for a case of a stable vortex, are compared.

In the present numerical results, the outer edge of the computational domain, η_e, is taken as 10.0 which equals the stretched outer radius of the vortex at the initial station. A grid of 1000 grid points in the radial direction, with a constant step size of 0.01, is used in the analysis. The results are shown for two initial Mach numbers; M = 0.5 and M = 0.75. The step size in the axial direction is 0.02 for M = 0.5 and 0.04 for M =

0.75. The inflow profiles for the axial velocity, u_i, the tangential velocity, w_i, and the temperature, T_i, are given by

$$\begin{aligned} u_i &= constant = M_i \\ w_i &= \begin{cases} \beta u_i r(2.0 - r * r) & for \ r \leq 1 \\ \beta u_i / r & for \ r \geq 1 \end{cases} \\ T_i &= constant = 2.5 \end{aligned} \tag{5.1}$$

where β = swirl ratio = w/u at r = 1.

5.2 Effects of Initial Mach Number on the Vortex-Breakdown Length

Fig. 5.1 shows the axial variations of the modified shape factor, MSF, the axial velocity, u_a, the static pressure, p_a, and the temperature, T_a, which are referred to by curves A, B, C and D, respectively, and the subscript, a, denotes the properties at the vortex axis (r = 0.0). In Fig. 5.1-a and Fig. 5.1-b, the initial swirl ratio, β, and the external axial pressure gradient, $dp/dx)_e$, are kept constant at 0.4 and 0.125, respectively. In Figures 5.1-c and 5.1-d, the values of β and $dp/dx)_e$ are kept constant at 0.4 and 0.25, respectively. The vortex-breakdown location is detected by the failure of the computer code to converge because of the violation of the slender-vortex assumption near the vortex-breakdown position. The vortex-breakdown position detected by the present method may be slightly different than the experimentally observed value because no upstream influence of the breakdown zone is included in this analysis since the equations are parabolic. From Fig. 5.1, it is noted that the breakdown length is more than doubled when the Mach number increases from 0.5 to 0.75. This shows that increasing the Mach number has a favorable effect on stabilizing the vortex core in subsonic flows. Similar results are obtained in Fig. 5.2 where the swirl ratio, β, is kept constant at 0.2 and the

external axial pressure gradient is varied from 0.125 to 0.25 for Mach numbers of 0.5 and 0.75.

5.3 Effects of the External Axial Pressure Gradient on the Vortex Breakdown Length

In Fig. 5.3, the Mach number is kept constant at 0.5, the initial swirl ratio is kept at 0.4 and the external pressure gradient is varied from 0.125 to 0.25. Fig. 5.3-a shows the breakdown length to be 1.6 for $dp/dx)_e$ = 0.125 and from Fig. 5.3-b, the detected breakdown length is 0.57 for a pressure gradient of 0.25. This means that the breakdown length is decreased significantly by increasing the external axial pressure gradient. The same result can be obtained from Fig. 5.4 where the initial Mach number is 0.75 and the initial swirl ratio is 0.4 with the same pressure gradients as in the previous case. It is noted that the breakdown length decreased from 2.55, for $dp/dx)_e$ = 0.125, to 1.62 , for $dp/dx)_e$ = 0.25. It is concluded that the external pressure gradient is a dominant parameter in controlling vortex breakdown. The influence of axial pressure gradient decreases as the Mach number increases.

5.4 Effects of the Initial Swirl Ratio on the Vortex Breakdown Length

Fig. 5.5 shows the axial distributions of MSF, u_a, p_a, and T_a for M = 0.5 and $dp/dx)_e$ = 0.25. The initial swirl ratio, β , is varied from 0.2 to 0.4. It is noted that the breakdown length decreases from 0.6 for β = 0.2 to 0.565 for β = 0.4. This means that doubling the swirl ratio slightly decreases the breakdown length. Similar result is obtained in Fig. 5.6, where M = 0.75 and $dp/dx)_e$= 0.25 and the breakdown length decreases from 1.75 for β = 0.2 to 1.62 for β = 0.4.

5.5 Radial Profiles for M = 0.5 and M = 0.75

The radial profiles of the velocity components, the static pressure and the density for M = 0.5 are shown in Fig. 5.7. In this set of results, the initial swirl ratio is 0.4 and the external axial pressure gradient is 0.25. The step size in the axial direction is 0.02 and the results are shown at every other station. The profiles at the first station are denoted by number 1 and the next displayed station, at ξ = 0.04, is indicated by the number 3. Figure 5.7-a shows the radial distributions of the axial velocity, u. It is noted that, the axial velocity is continuously decreasing with increasing axial distance, x. The computations started with a uniform distribution at the first station and a wake-type radial distribution was developed such that a minimum value existed at the axis, which increased to reach a constant maximum value at the viscous core edge. It is shown that the viscous core radius increased from 1.0 at the first station to a value of about 4.0 at last shown station. It is noted that the outer edge of the physical domain is increased accordingly from 10.0 at the initial station to 14.0 at the last shown station. Figure 5.7-b shows the radial distributions of the tangential velocity, w. It can be seen that, with increasing axial distance, x, the flow tends to the no swirl condition where the value of w tends to be zero along the radial direction. Fig. 5.7-c shows the pressure distribution along the distance, r. As the computations march downstream, the pressure increases and the difference between its value at the axis and that at the outer edge decreases until they become the same at the last shown station. Fig. 5.7-d shows the radial profiles of the density at different axial stations. It is shown that the density follows the same trends as the pressure. The difference between the density at the axis and that at the outer edge becomes minimum at the last axial station.

Figure 5.8 shows the radial profiles for M = 0.75. The initial swirl ratio is 0.4 and the external axial pressure gradient is 0.25. The axial step size is 0.04 and the results

are shown for alternating stations. It is noticed that the pressure and density gradients in the axial direction decrease faster than those at M = 0.5. The profiles show that the viscous diffusion at M = 0.75 is larger than that at M = 0.5. They also show that, while the outer boundary continuously increases for M = 0.5, it initially decreases and then increases for M = 0.75.

5.6 Comparison of the Slender-Vortex-Equation Results and Navier-Stokes Results

Figures 5.9 show the profiles of the velocity components, u, w, and v, and the static pressure, p, which have been computed by the present method, while Figs. 5.10 show the results obtained by an upwind flux-difference splitting finite-volume Navier-Stokes solver for a case of a stable vortex at $M = 0.5$, β = 0.6 and no axial pressure gradient on the outer edge. For the Navier-Stokes solver, a rectangular grid of 100x51x51 grid points in the axial and cross-flow directions, respectively, is used. The curves are labeled by the letters A, B, ... etc for the successive axial stations. Comparing the curves of the two sets, a remarkable agreement is seen. It is noted that the curves of the slender vortex are much smoother than those of Navier-Stokes equations because of using a very large number of grid points in the radial direction, 1000, for the slender-vortex solution compared to 26 points for the Navier-Stokes solution. It is also noted that viscous effects in the present method affect a narrow region near the vortex axis because of the slenderness restrictions on the governing equations.

5.7 Conclusion

It is concluded that the method used in this Chapter is an excellent fast method to study the effects of flow parameters on the occurrence of vortex breakdown. Because the method requires only the solution of a very simplified set of equations, it does not require

a large computer memory or time. The solution of this set of equations on a CONVEX machine requires less than ten seconds for any of the presented cases. It can be used to examine the potential of a set of inflow profiles to produce vortex breakdown under certain flow conditions. For stable vortex flows, the results are in excellent agreement with those of the Navier-Stokes equations. But, for flows with vortex breakdown some differences are expected because of the restrictions and assumptions applied to the method as described below. In the region of vortex breakdown, the flow is unsteady and the vortex core is not slender. The governing equations are parabolic in space and a marching-in-space scheme is used to solve the equations by marching in the axial direction. That is why, the method is not capable of taking into account the effects of downstream boundary conditions and also computing for the reversed flow region.

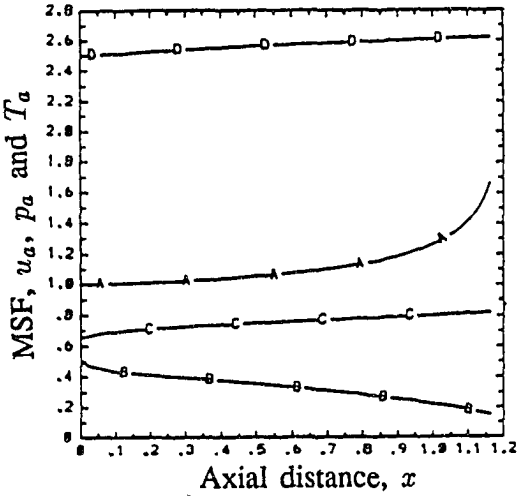

a- $M = 0.5$ $dp/dx = 0.125$ $\beta = 0.4$

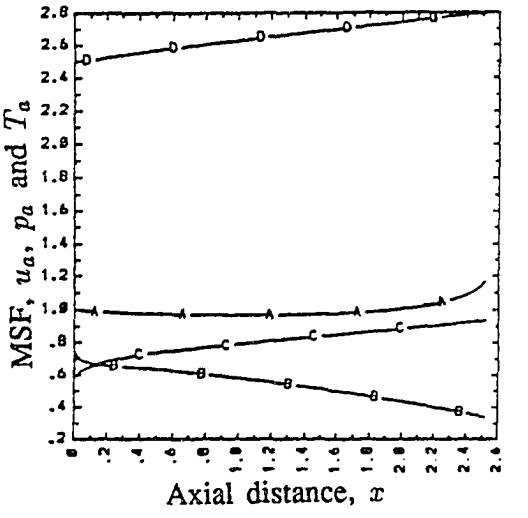

b- $M = 0.75$ $dp/dx = 0.125$ $\beta = 0.4$

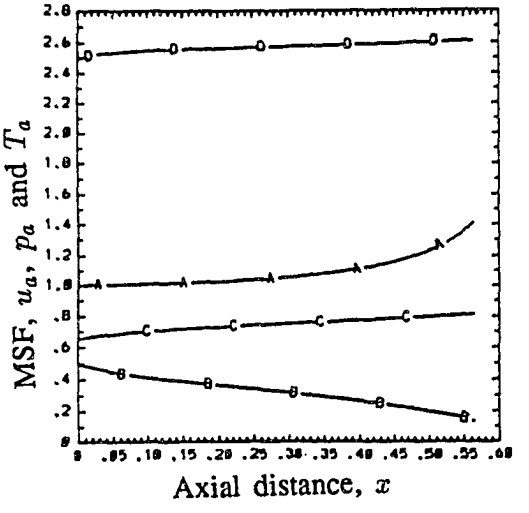

c- $M = 0.5$ $dp/dx = 0.25$ $\beta = 0.4$

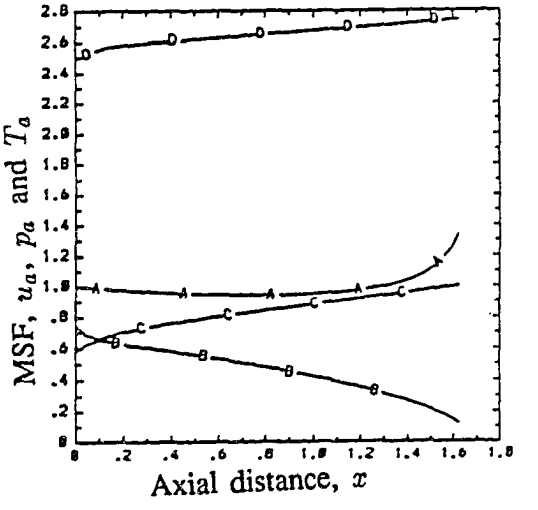

d- $M = 0.75$ $dp/dx = 0.25$ $\beta = 0.4$

A = MSF, B = u_a, C = p_a, D = T_a

Figure 5.1 Slender quasi-axisymmetric flow solutions for the effect of the initial Mach number on the vortex-breakdown length.

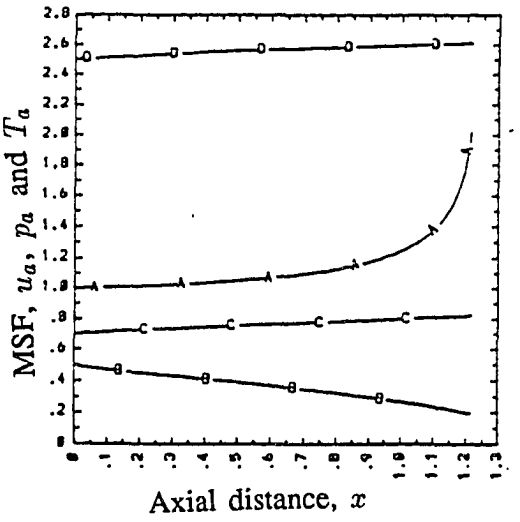

a- $M = 0.5$, $dp/dx = 0.125$ $\beta = 0.2$

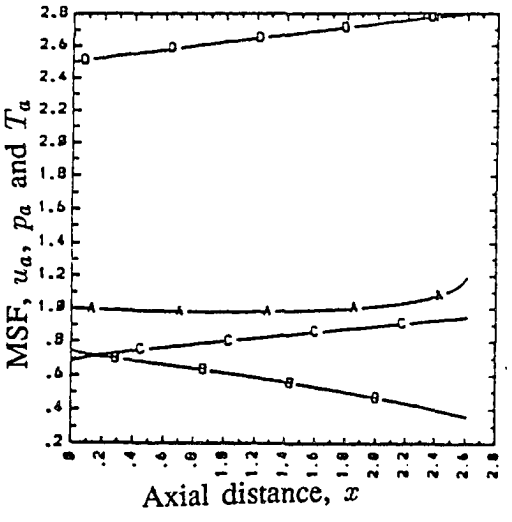

b- $M = 0.75$ $dp/dx = 0.125$ $\beta = 0.2$

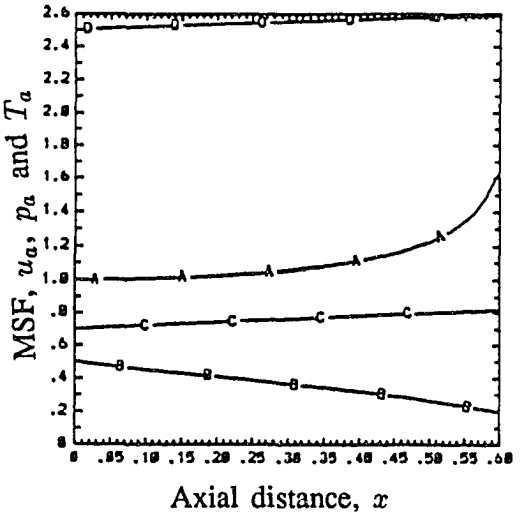

c- $M = 0.5$ $dp/dx = 0.25$ $\beta = 0.2$

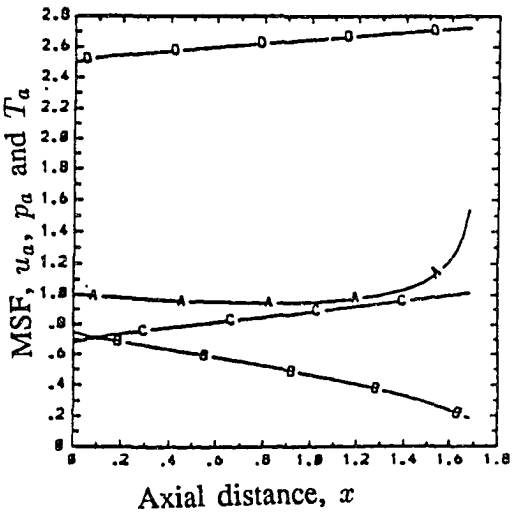

d- $M = 0.75$ $dp/dx = 0.25$ $\beta = 0.2$

Figure 5.2 Slender quasi-axisymmetric flow solutions for the effect of the initial Mach number on the vortex-breakdown length.

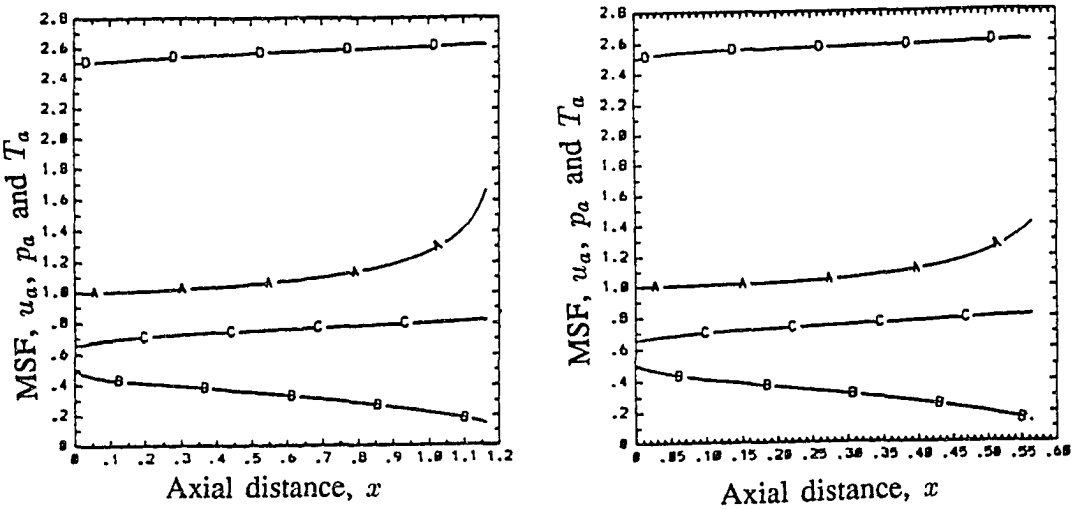

$M = 0.5$ $dp/dx = 0.125$ $\beta = 0.4$ $M = 0.5$ $dp/dx = 0.25$ $\beta = 0.4$

Figure 5.3 Slender quasi-axisymmetric flow solutions for the effect of the external axial pressure gradient on the vortex-breakdown length, $M = 0.5$.

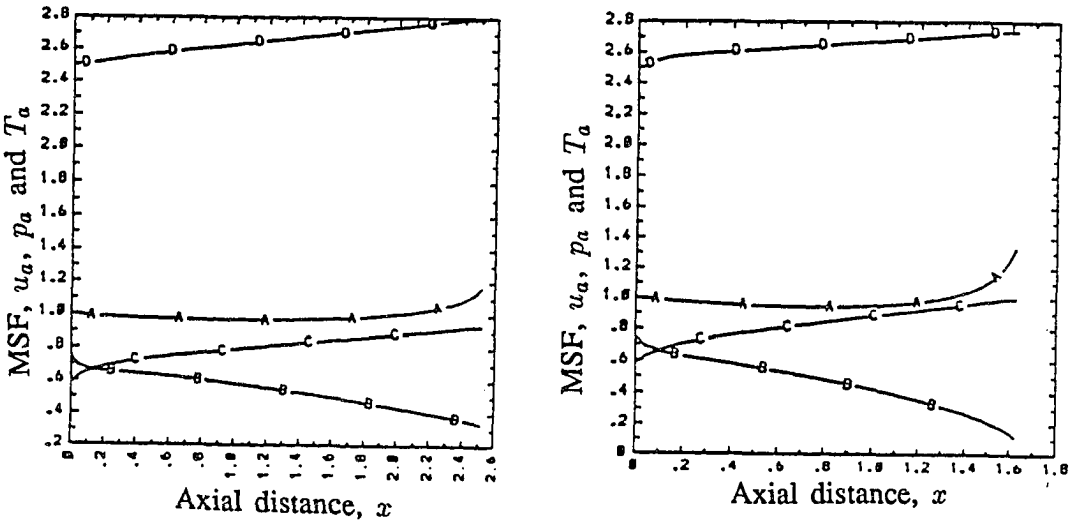

$M = 0.75$ $dp/dx = 0.125$ $\beta = 0.4$ $M = 0.75$ $dp/dx = 0.25$ $\beta = 0.4$

A = MSF, B = u_a, C = p_a, D = T_a

Figure 5.4 Slender quasi-axisymmetric flow solutions for the effect of the external axial pressure gradient on the vortex-breakdown length, $M = 0.75$.

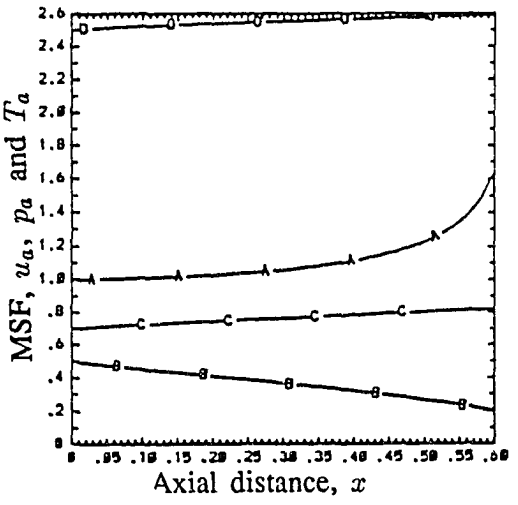

$M = 0.5 \quad dp/dx = 0.25 \quad \beta = 0.2$

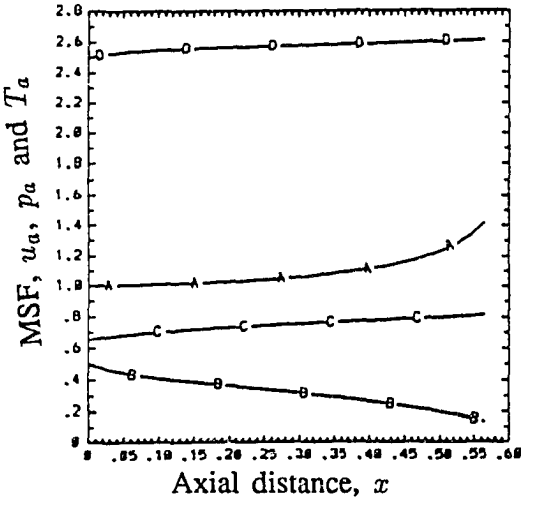

$M = 0.5 \quad dp/dx = 0.25 \quad \beta = 0.4$

Figure 5.5 Slender quasi-axisymmetric flow solutions for the effect of the initial swirl ratio β on the vortex-breakdown length, $M = 0.5$.

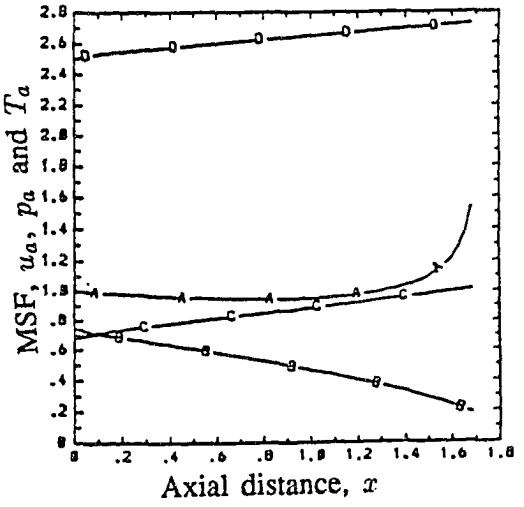

$M = 0.75 \quad dp/dx = 0.25 \quad \beta = 0.2$

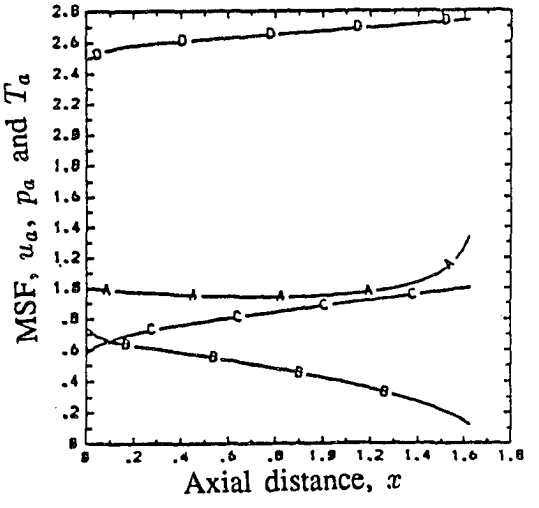

$M = 0.75 \quad dp/dx = 0.25 \quad \beta = 0.4$

A = MSF, B = u_a, C = p_a, D = T_a

Figure 5.6 Slender quasi-axisymmetric flow solutions for the effect of the initial swirl ratio β on the vortex-breakdown length, $M = 0.75$.

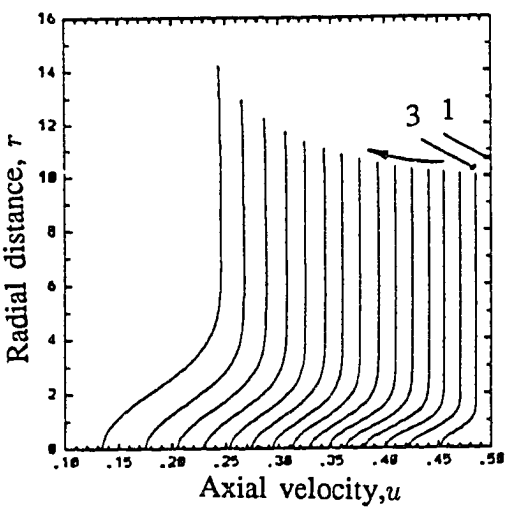

a- $M = 0.5 \quad dp/dx = 0.25 \; \beta = 0.4$

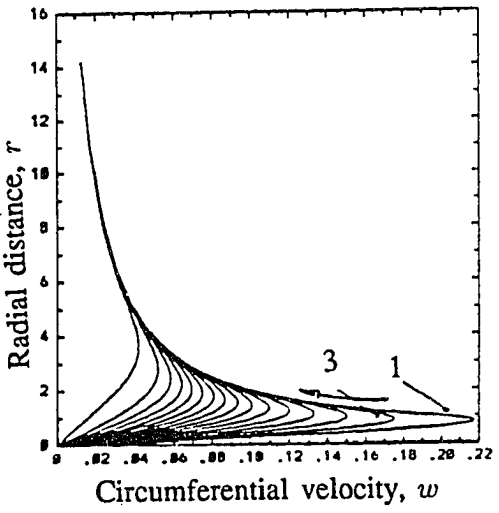

b- $M = 0.5 \quad dp/dx = 0.25 \; \beta = 0.4$

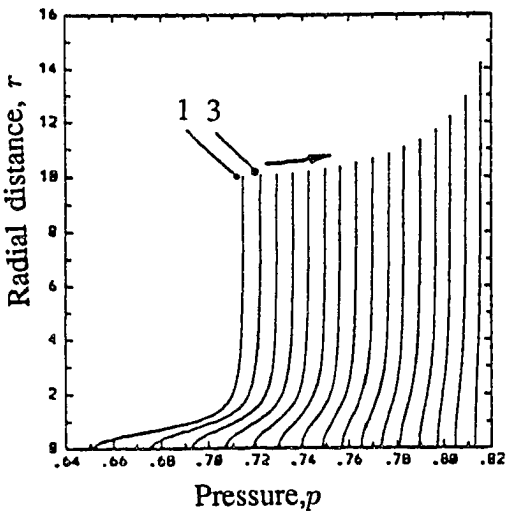

c- $M = 0.5 \quad dp/dx = 0.25 \; \beta = 0.4$

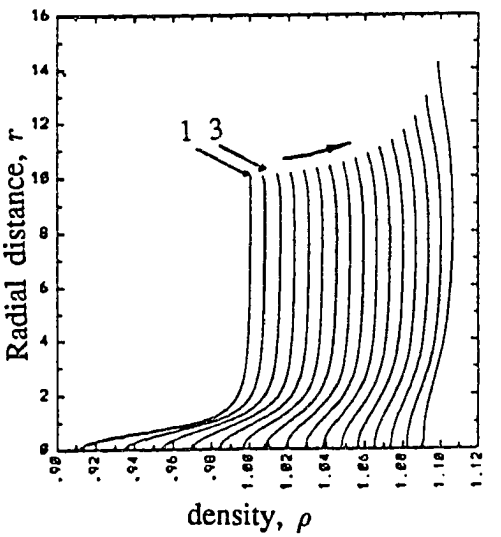

d- $M = 0.5 \quad dp/dx = 0.25 \; \beta = 0.4$

Figure 5.7 Flow profiles for slender quasi-axisymmetric flow solutions at $M = 0.5$, $\beta = 0.4$ and $dp/dx)_e = 0.25$.

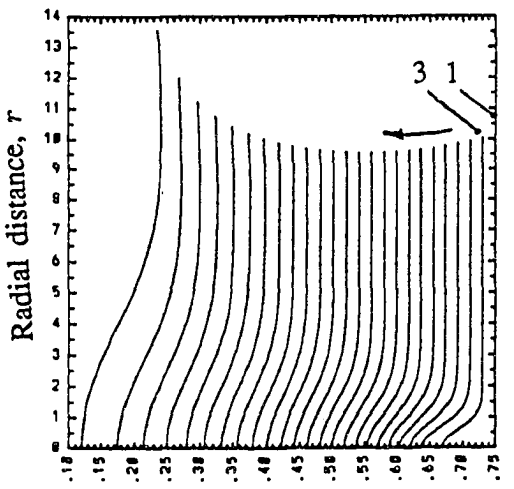

$M = 0.75 \quad dp/dx = 0.25 \; \beta = 0.4$

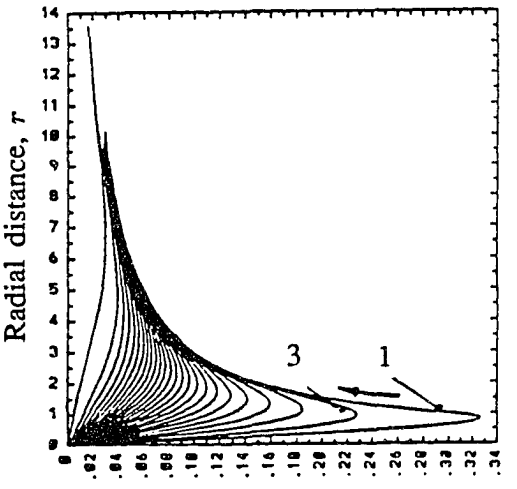

$M = 0.75 \quad dp/dx = 0.25 \; \beta = 0.4$

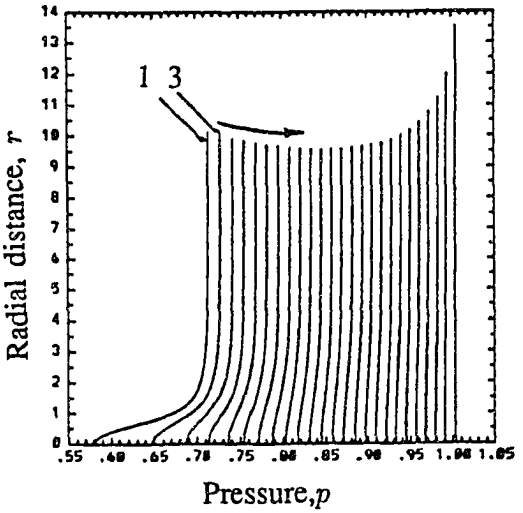

$M = 0.75 \quad dp/dx = 0.25 \; \beta = 0.4$

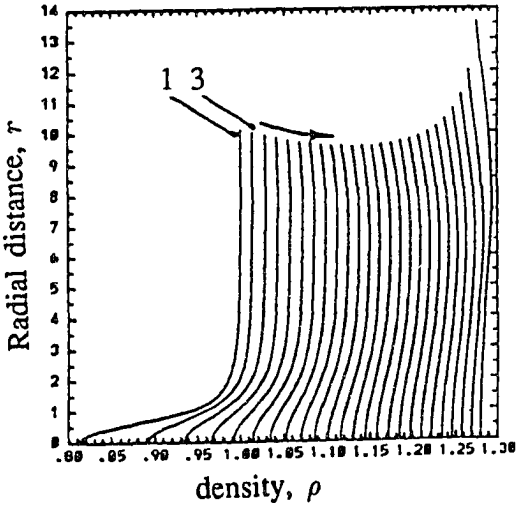

$M = 0.75 \quad dp/dx = 0.25 \; \beta = 0.4$

Figure 5.8 Flow profiles for slender quasi-axisymmetric flow solutions at $M = 0.75$, $\beta = 0.4$ and $dp/dx)_e = 0.25$.

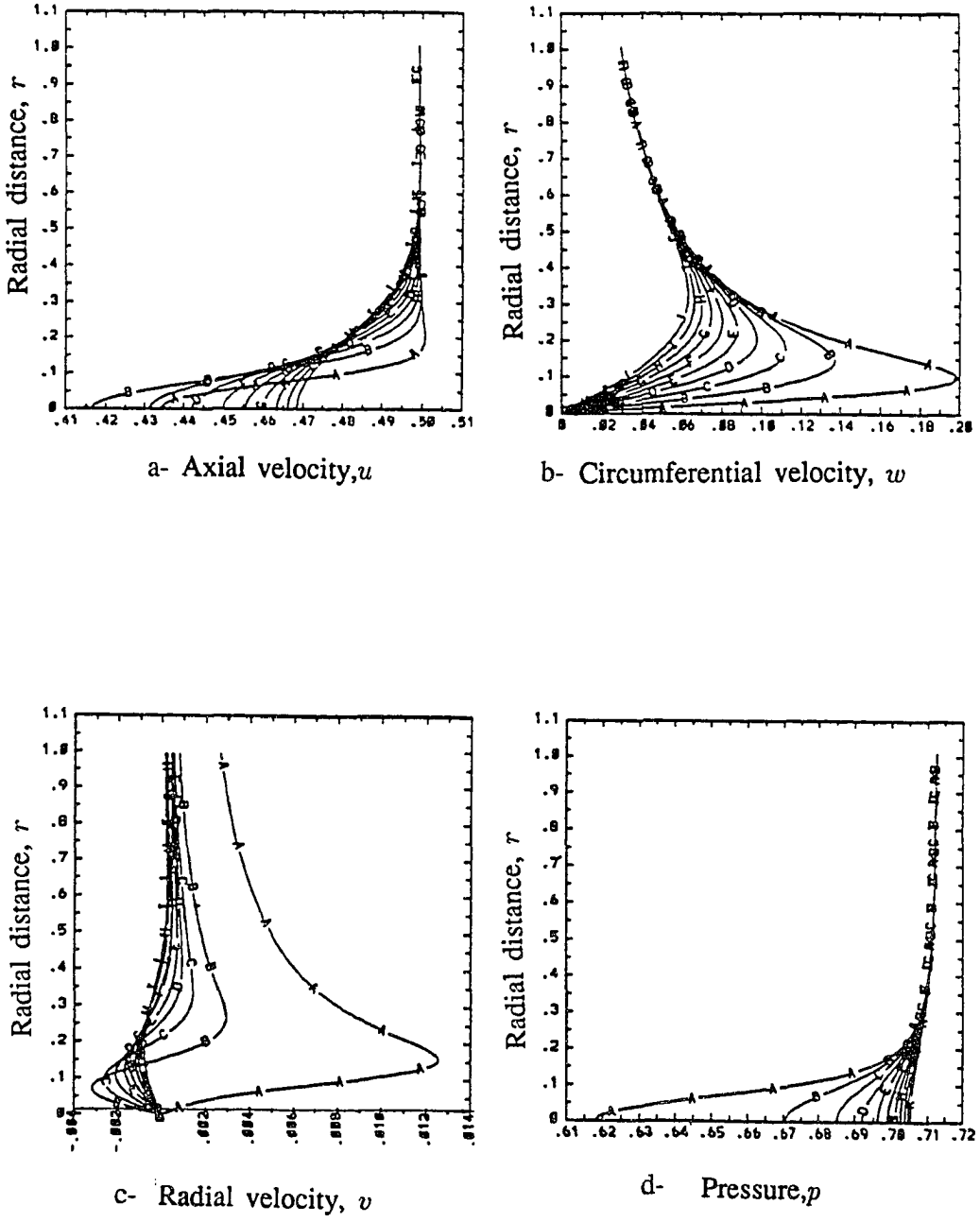

Figure 5.9 Flow profiles for slender quasi-axisymmetric stable vortex flow using the present method, $M = 0.5$, $\beta = 0.6$ and $dp/dx)_e = 0.0$.

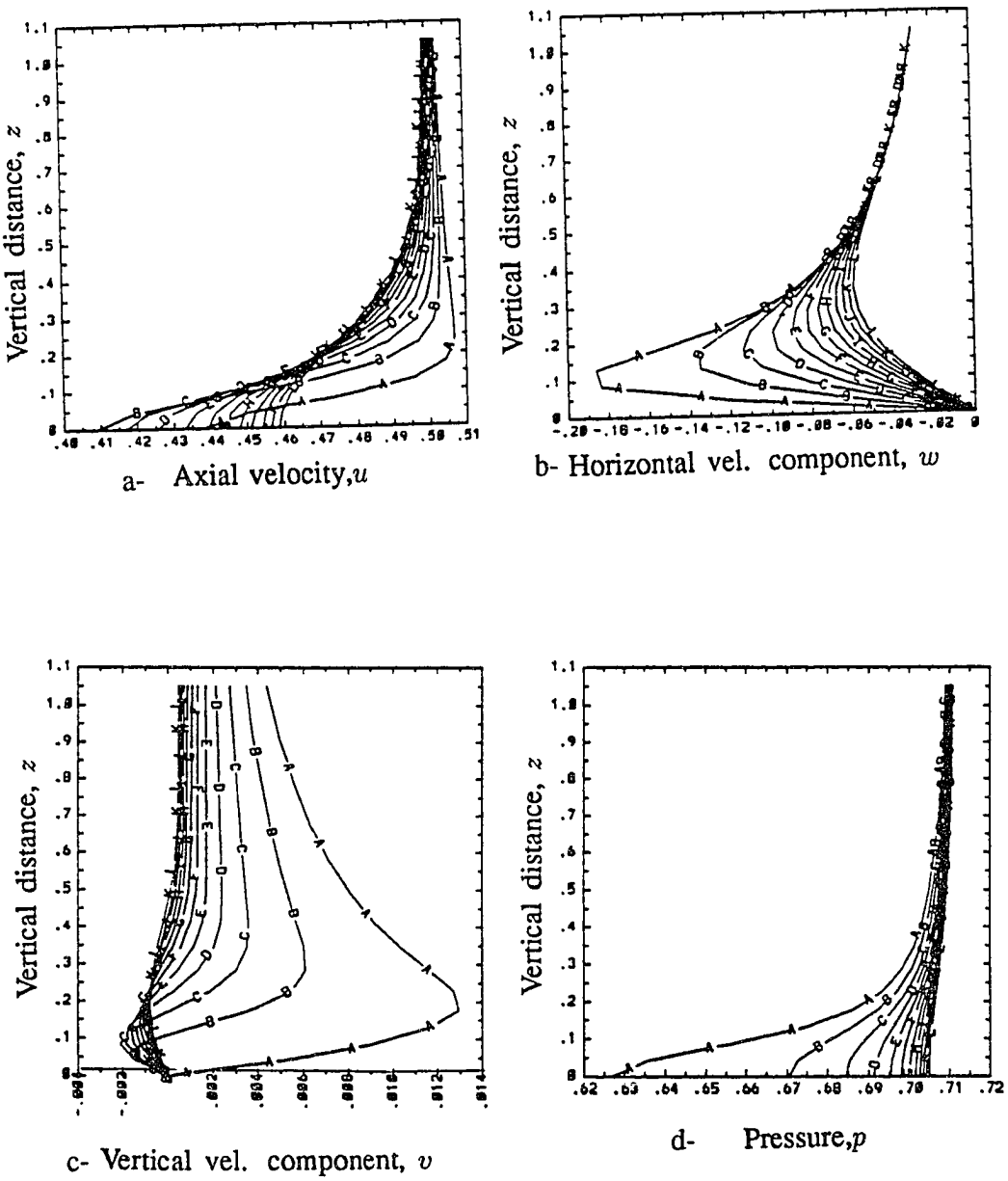

Figure 5.10 Flow profiles for slender quasi-axisymmetric stable vortex flow using a full Navier-Stokes solver, $M = 0.5$, $\beta = 0.6$ and $dp/dx)_e = 0.0$.

CHAPTER 6
QUASI-AXISYMMETRIC SUPERSONIC VORTEX BREAKDOWN IN A CIRCULAR DUCT

6.1 Introduction

In this Chapter, we consider the supersonic vortex flow in a configured circular duct. The flow is assumed to be quasi-axisymmetric. By quasi-axisymmetric flow it is meant that the flow variables are not functions of the angle ϕ of the cylindrical coordinates while the tangential velocity component is of a nonzero value. The experimental observations showed that this assumption is acceptable for axisymmetric geometries such as gas-turbine combustors. To study this flow, the time-accurate solution of the unsteady, compressible Navier-Stokes equations is obtained using the implicit, upwind, flux-difference splitting scheme which was presented in Chapter 4. Because of the unsteady nature of the vortex-breakdown flows, global time stepping was used to advance the solutions in time. A global time step of 0.0025 was used in all the present results.

A shock wave is generated near the duct inlet and vortex breakdown occurs behind the shock as a result of the vortex/shock interaction. Several issues are addressed in this Chapter. First, the duct geometrical design, computational domain and computational grid are described. Second, the initial and boundary conditions are presented. Then, the computational results are presented. The computational results include the effects of Reynolds number on the temporal evolution and persistence of vortex-breakdown bubbles behind the shock wave, the effects of the duct–wall and exit boundary conditions on the vortex flow and breakdown in the duct and finally the effects of the swirl ratio and

Mach number at the inlet section on vortex-breakdown behavior. In studying the effects of the Reynolds number, the other flow conditions are kept fixed and the downstream boundary conditions are obtained by extrapolating all the flow variables from the interior cell centers. Although the flow is supersonic over most of the duct exit, subsonic flow exists over a small portion of the exit section around the duct centerline. Therefore, four types of downstream boundary conditions were selected and tested and the results are compared and discussed.

6.2 Duct Geometry and Computational Domain

The computational domain consists of a configured circular duct as shown in Fig. 6.1. The duct is designed such that a strong shock wave is formed in the entrance portion and intersects the longitudinal vortex core. This design was also intended to have a supersonic flow at the exit section, but as the results show, a small portion of the exit section became subsonic which made it difficult to specify reasonable boundary conditions at the exit section. The duct consists of a straight cylindrical part of radius 1.0 followed by a small divergent part in order to stabilize the resulting shock in the entrance section. The divergence angle is 6°. A straight cylinder is followed which ends with a convergent-divergent nozzle, with a throat radius of 0.95, intended for accelerating the flow downstream of the vortex breakdown to become supersonic at the exit section. The duct exit radius is 0.98 and its total length is 2.9. The computational grid consists of 51x221x2 grid points in the radial, axial and tangential directions, respectively. The two axial planes are spaced circumferentially at a certain angle such that the aspect ratio of the minimum grid size will be less than 2.0. The grid points are clustered around the duct axis for good resolution of the vortex core, near the entrance section for good resolution

of the shock wave and the interaction region and on the duct solid wall for good resolution of the boundary layer. The minimum radial grid size at the center line is 0.002.

6.3 Boundary and Initial Conditions

At the inlet section, flow variables corresponding to an inviscid vortex flow are prescribed. The upstream Mach number is kept at 1.75 for most of the computed cases and the Reynolds number is varied from 2,000 up to 100,000. The tangential velocity component at the inlet section is given by:

$$\frac{w}{U_\infty} = \frac{k_e}{r}\left[1 - exp\left(-\frac{r^2}{r_m^2}\right)\right], \tag{6.1}$$

where U_∞ is the freestream velocity (= 1.74 for $M = 1.75$), w is the tangential velocity at the radial distance, r. Choosing the constants k_e and r_m controls the swirl ratio, β, which is the ratio between the maximum tangential velocity and the axial velocity at the inlet section, and its radial position. For example, for $k_e = 0.1$ and $r_m = 0.2$ the swirl ratio is 0.32 at $r = 0.224$. The axial velocity is assumed to have a constant value of 1.74 for $M = 1.75$ at the inlet section. The radial velocity, v, at the inlet section is set equal to zero. The inviscid radial momentum equation is integrated to obtain the inflow pressure profile. Finally, the density, ρ, is obtained from the definition of the speed of sound for the inlet flow. The inflow profiles for $M = 1.75$ and $\beta = 0.32$ are shown in Fig. 6.2.

At the duct centerline, quasi-axisymmetric boundary conditions are used. The flow is assumed to have a rigid-body rotation which requires the tangential velocity at the axis to be zero. No-penetration (no sink or source) condition requires the radial velocity to vanish at the axis. The normal derivatives of the axial velocity, pressure and density are

set equal to zero. These conditions enforce the symmetry of the axial velocity, pressure and density profiles.

On the duct walls, viscous boundary conditions are used. The no-slip and no-penetration conditions require all the velocity components to be zero.

On the meridian planes, quasi-axisymmetric conditions are used, where components of the flow field vector are forced to be equal on the two axial planes under consideration.

At the exit section, several boundary conditions are used because of the subsonic portion that occurs at certain time steps in some flow cases. For the supersonic portion of the exit section, the extrapolation boundary conditions are used where all the flow variables are extrapolated from the interior cell centers. Another boundary conditions such as Riemann-Invariant type are used for the subsonic portion of the exit section. The different types of boundary conditions will be discussed when we consider the effects of the exit boundary condition in this Chapter.

6.4 Computational Results

The computational results include the effects of Reynolds number, the inlet swirl ratio and Mach number and the duct-wall and exit boundary conditions on the development and behavior of the vortex breakdown under specified flow conditions. The effect of decreasing the global-time step on the accuracy of computational results is investigated in the case of R_e = 10,000.

6.4.1 Effects of Reynolds Number

For the present flow cases, the chosen Reynolds number values are 2,000, 4,000, 10,000, 20,000 and 100,000. The swirl ratio, β, is kept fixed at 0.32. The inlet Mach number is kept constant at 1.75. The exit boundary conditions are obtained by extrapolating all the flowfield vector components from the interior cell centers.

6.4.1.1 Case 1: R_e = 2,000

Figure 6.3 shows the streamlines and Mach-number contours for this flow case at a dimensionless time level of 11.0, which is equivalent to 4,400 time steps. The results show that no vortex breakdown develops. The Mach-number contours show the formation of a shock wave at the duct inlet which is a normal shock over most of the duct inlet. The shock-wave strength is not enough to decelerate the axial velocity to stagnation. The Mach contours also show the flow to be supersonic at the duct exit section.

6.4.1.2 Case 2: R_e = 4,000

Figure 6.4 shows snapshots of the streamlines and Mach-number contours for this flow case. It should be noted here that the streamlines are shown only for a radial distance of 0.49. The streamlines show the formation of a single breakdown bubble at t = 5.0. The bubble was convected downstream as the computations advanced in time. The breakdown bubble was formed during the downstream motion of the shock wave, which reached its maximum downstream displacement at t = 5.0. Later on, as the Mach contours show, the shock moved upstream to reach the inlet section at t = 8.0. The breakdown bubble was convected in the downstream direction as can be seen at t = 8.0. Thereafter, the shock stayed stationary at the inlet section. This swirling flow case shows a transient single-bubble vortex-breakdown flow. It was noticed that at t = 5.0, a small portion of the duct exit near the center line was subsonic. At t = 8.0, the subsonic region expanded radially to about 25% of the exit radius.

6.4.1.3 Case 3: R_e = 10,000

Figure 6.5 shows snapshots of the streamlines and Mach-number contours for the flow case of $R_e = 10,000$. The streamlines are shown for only a radial distance of 0.49. At t = 3.0, a single breakdown bubble was formed behind the downstream moving

shock. In the time range from t = 3 to t = 5.0, the bubble grew in all directions while the shock moved downstream. At t = 8.0, two bubbles could be recognized where the old bubble was shedding and a new bubble was formed behind the shock wave. The new bubble pushed the shock wave towards the inlet section. The Mach contours at t = 8.0 show the position of the inlet shock and the new bubble behind it. The shedding bubble can be seen accompanied by a separated boundary-layer bubble from the duct wall. The separation of the wall boundary layer was caused by the interaction of the boundary layer with the inlet shock and the pressure field caused by the breakdown bubble formation. It is noted that the boundary-layer-separation-bubble formation, shape and motion are affected by the shape and motion of the vortex-breakdown bubble. The space between the separation bubble and the breakdown bubble is acting like a nozzle which accelerates the flow in between and creates a pressure field which increases the disturbances inside the duct. At t = 10.0, no bubbles could be seen in the duct as a result of the bubble-system shedding. At t = 12, a new cycle started by the formation of a small bubble behind the inlet shock which was moving in the downstream direction. The Mach contours showed no boundary-layer separation because the breakdown bubble was very small. At t = 15, the bubble grew in all directions as was the case at earlier time levels, t = 3-5. At t = 17, a multi-bubble breakdown could be recognized behind the shock wave. The Mach contours show the effects of the breakdown bubbles on the boundary-layer separation where a long separation zone is seen starting at the duct inlet. The shape of the inlet shock wave was also affected by the shape of the bubbles behind it. The flow at the exit section was supersonic except for a very small portion at the axis. The breakdown bubbles were then convected downstream at t = 19 while the inlet shock moved upstream. A new cycle started at t = 26.0 and a single bubble could be seen at t = 27. The bubble-system was shed while the oscillation of the inlet shock became

very slow as can be seen at the time range from t = 25 to t = 36. The shedding of the breakdown bubbles continued from t = 28 to t = 32. At later time levels, no new breakdown bubbles were formed and the shock wave stayed fixed in its location without any oscillations. It was noted that the boundary layer separated at most of the duct wall and about 25% of the duct exit section was subsonic. This swirling flow case shows a transient multi-bubble breakdown flow.

This flow case was recomputed using a time step of 0.00125 to investigate the effect of the time step on the accuracy of the computational results. The results at selected time levels are shown in Fig. 6.6. The comparison with corresponding results of a time step of 0.0025 shows negligible differences. Therefore, it was decided to use the higher time step for all the presented results in order to increase the efficiency of the computations without degrading the accuracy of the results.

6.4.1.4 Case 4: R_e = 20,000

Figure 6.7 shows snapshots of the streamlines and Mach-number contours for the flow case of $R_e = 20,000$. The streamlines are shown for a radial distance of 0.5. The mechanism of evolution, convection and shedding of the vortex-breakdown bubbles with the oscillation of the inlet shock wave was very similar to the previous case of $R_e = 10,000$. However, there were some differences as a result of increasing the Reynolds number. First, the size, number and strength of the breakdown bubbles were larger than those of $R_e = 10,000$. Second, the oscillation amplitudes of the inlet shock wave were larger than those of the case of $R_e = 10,000$. Third, the transient time of the multi-bubble breakdown was longer than that of the case of $R_e = 10,000$. Again this swirling flow case shows a transient multi-bubble breakdown flow.

6.4.1.5 Case 5: R_e = 100,000

Figures 6.8 and 6.9 show snapshots of the streamlines and Mach-number contours for the flow case of $R_e = 100,000$. The streamlines are shown for a radial distance of 0.6, which is larger than those of $R_e = 2,000 - 20,000$ cases because the bubbles are larger. Again, the mechanism of evolution, convection and shedding of the vortex-breakdown bubbles up to t = 30.0 was very similar to the previous flow cases of smaller Reynolds numbers. It was noticed that the size, number and strength of the breakdown bubbles were larger than those of smaller Reynolds numbers. Moreover, it was noticed in the present case that short periodic evolution, merging, convection and shedding cycles of the breakdown bubbles occurred, e.g.; the time periods of 16-21, 22-27 and 28-32.

At t = 33 and beyond, a new mode of evolution, convection and shedding of the breakdown bubbles occurs. It should be noticed that the inlet shock wave keeps on moving slowly in the downstream direction. The space between the breakdown structure and the wall acts as a convergent-divergent nozzle that accelerates the subsonic flow behind the inlet shock to supersonic speeds which are terminated by another shock wave, as can be seen at t = 30 and t = 35. The terminating shock does not extend to the duct axis. That shock keeps moving in the downstream direction as a result of the inlet shock motion and the change in the space between the convecting bubbles and the duct-wall boundary layer. The Mach-number contours show the separation of the duct-wall boundary layer in the time period from t = 30 to t = 66. During that period, the breakdown bubble behind the inlet shock grows while another bubble is located near the exit section. The upstream breakdown bubble becomes larger and stronger than the downstream bubble. The downstream bubble is convected through the exit section at t = 78. Next, the upstream breakdown bubble is convected downstream and new breakdown

bubbles appear behind the inlet shock. In the time range of t = 84-95, the mechanism of evolution, merging, convection and shedding which is similar to that in the time range of t = 24-35 is repeated. In the time range of t = 96-120, the flow is similar to that of the time range of t = 37-78. At t = 123 and beyond, the whole process of vortex-breakdown-bubble evolution, merging, convection and shedding is repeated. It is seen that the snapshots of streamlines at t = 124 and 130 are similar to those at t = 3 and 17. Therefore, it is concluded that the vortex-breakdown mechanism for this flow case is quasi-periodic with a long period of time. Within this long cycle, short periodic cycles of vortex breakdown develop. In summary, this flow case shows that several periodic modes of vortex breakdown develop, which correspond to different frequencies.

6.4.1.6 Case 6: Inviscid Flow

As a limiting flow case to investigate the effects of Reynolds number on the vortex breakdown, a test case is considered where the viscous effects were neglected and the solution was obtained using the Euler equations. Figure 6.10 shows snapshots of the streamlines and Mach contours for this flow case at selected time levels up to t = 69. At early time levels up to t = 10, the vortex breakdown structure was similar to that of $R_e = 100,000$ with larger bubbles. As the solution was advanced in time, new modes of vortex breakdown, different than those of viscous flows, occurred. The streamlines at t = 22 show the formation of a large stable bubble while in the flow case of $R_e = 100,000$, the streamlines show the merging of two bubbles at the same time level. At time levels beyond t = 22, a stable mode of breakdown was developed. That mode is characterized by no reversed flow regions along the duct axis. Two stable recirculation regions could be recognized off the duct axis. The inlet shock wave had a stable location at the end of the divergent portion of the duct wall. It should be noted here that the upper end of the

inlet shock could slip freely on the duct wall since no viscous effects were considered. The stable mode of vortex breakdown was similar to an axisymmetric bubble structure reported experimentally, which will be discussed at the end of this Chapter. It is noted that the whole picture of the flow structure in the duct did not change as time increased. However the internal structure of the breakdown region has experienced minor changes as can be seen from the streamlines.

6.4.2 Effects of the Exit-Boundary Conditions

In this section, the problem of specifying the downstream boundary conditions and their critical effects on the supersonic vortex breakdown for internal flows are addressed. For this purpose, the unsteady, compressible, full Navier-Stokes equations are used along with the implicit, upwind, flux-difference splitting, finite-volume scheme of Chapter 4 for the time-accurate solutions. Four types of exit-boundary conditions are considered. Keeping the duct geometry and upstream flow conditions fixed, the exit-boundary conditions were varied. The four exit-boundary conditions included: extrapolation of all the five flow variables from the interior cell centers, specifying the downstream pressure and extrapolating the other four flow variables from the interior cell centers, specifying the downstream pressure gradient and extrapolating the other four variables from the interior cell centers and placing a disk of specified radius at the exit section along with specifying solid-surface boundary conditions. For all the exit-boundary conditions used, the flow conditions at the inlet section are $R_e = 100,000$, $M = 1.75$ and the swirl ratio, $\beta = 0.32$.

6.4.2.1 Extrapolation from Interior Cell Centers

Snapshots of the streamlines and Mach contours for this case were presented in Fig. 6.8 and 6.9 of section 6.4.1. The exit-boundary conditions are obtained by extrapolating

all the flow variables from the interior cell centers at the exit. The streamline snapshots show multi-bubble vortex breakdown evolution, convection, merging and shedding. The time-accurate integration was carried out up to t = 200 and the solution showed periodic multi-frequency cycles of vortex breakdown bubbles. According to the theory of characteristics, extrapolating all the flow variables from the interior cell centers is mathematically correct only for the case of supersonic flow at the exit section. Form Fig. 6.9, it was noticed that the flow was subsonic at a small portion of the exit section near the duct axis at certain time levels. The use of extrapolation boundary conditions for this portion is mathematically improper. However, the extrapolation boundary conditions were used for incompressible flows by most of the researchers. The use of these boundary conditions in such applications was physically justified as the flow variables did not change across the downstream boundary.

6.4.2.2 Riemann-Invariant Type Boundary Conditions with $p_b = p_\infty$

In this case, the back pressure at the subsonic points of the duct exit, p_b, was specified to be equal to p_∞ and the other four variables were extrapolated from the interior cell centers. The computations have been repeated on the same grid and for the same flow conditions as that of the previous case. Figure 6.11 shows snapshots of the streamlines and Mach contours of the solution. Comparing the present solution with the previous case (see Fig. 6.8&9), it is seen that the two solutions are the same until t = 35. Thereafter, for t > 35, the inlet shock wave moved continuously in the downstream direction with the vortex-breakdown bubbles ahead of it. The shock and the vortex-breakdown bubbles were shed and disappeared from the duct at a later time. The reason behind the disappearance of the shock-vortex-breakdown-bubble system is that the back pressure was so low that it could not support the inlet shock and keep it in the inlet region. Moreover, the Riemann-

invariant type conditions at the subsonic portion let the downstream effects propagate upstream as the computations advanced in time. The breakdown mode may be termed as a "transient multi-bubble vortex breakdown".

6.4.2.3 Riemann-Invariant Type Boundary Conditions with $p_b = 2p_\infty$

In this case, the back pressure at the subsonic points of the duct exit was increased to be $p_b = 2p_\infty$ and the other four variables were extrapolated from the interior cell centers. Figure 6.12 shows snapshots of the streamlines and Mach contours of the solution. Comparing the present solution with the solution of the first case (Fig. 6.8,9), it is seen that the two solutions are similar with the exception that the present solution lags that of the first case in time. The reason behind this behavior is that the back pressure p_b in this case is larger than that of the first case. It should be noted here that the back pressure in the first case was extrapolated from the interior and its value never exceeded $2p_\infty$. Moreover, the Riemann-invariant type conditions at subsonic points let the downstream effects propagate upstream as time increases. The existence of the large back pressure which was felt upstream supported the inlet shock and kept it in the inlet region with the vortex-breakdown bubbles behind it.

6.4.2.4 Extrapolating the Pressure Gradient, $\frac{\partial p}{\partial x} = constant$

In this case, the back pressure was obtained from the condition $\frac{\partial p}{\partial x} = constant$ at the subsonic points of the duct exit. The other four flow variables were extrapolated from the interior cell centers. This is equivalent to solving the axial momentum equation at the exit boundary for the pressure. Similar boundary conditions were used by Breuer, et al. [78]. Figure 6.13 shows snapshots of the streamlines and Mach contours of the solution. Comparing the present solution with the solution of the first case (Fig. 6.8,9), it is seen that the two solutions are similar until t = 22. Thereafter, for t > 22, the

inlet shock continuously moves in the downstream direction with the vortex-breakdown bubbles moving ahead of the shock. The shock and vortex-breakdown-bubbles are shed and disappear from the duct at advanced time levels. The reason behind disappearance of the shock-vortex-breakdown-bubble system is that the back pressure obtained from $\frac{\partial p}{\partial x} = constant$ condition is so low it is unable to support the inlet shock and keep it in the inlet region. Moreover, extrapolating the pressure gradient from the interior cell centers increases the possibility of reaching very small values of the pressure at the exit section. The breakdown is termed as a "transient multi-bubble vortex breakdown".

6.4.2.5 Placing a Disk of r = 0.33 at the Exit Section

In the experimental study by Altgeld, et al. [108], isothermal measurements showed an unexpected inflow in the center region of the tube at the exit section of a model combustor. It is an undesirable feature since the measurements showed that this did not exist under burning conditions. Some of the unsuccessful attempts to eliminate the inflow were increasing the length of the combustor, adding a convergent nozzle to the combustor exit and inserting honeycomb section just upstream from the exit to remove the swirl. It was found that the inflow region at the exit section could be eliminated by placing a round baffle at the combustor exit. Downstream contraction was also used by Chao, et al. [109] to simulate the downstream boundary effects on the characteristics of the combustor swirling flow field.

In the present study, it was noticed that at some time levels, reversed flow exists in a narrow portion of the exit section around the duct axis. This makes it difficult to specify the boundary conditions since at least four of the flow variables should be specified. An attempt was made to eliminate the inflow at the exit section by placing a disk of radius r = 0.333 at the center region of the exit section. No–slip boundary conditions are

applied on the disk surface. For the remaining portion of the exit section, the boundary conditions were obtained by extrapolation from the interior cell centers. Figure 6.14 shows snapshots of the streamlines and Mach contours of the solution. In this case, the computations started with supersonic conditions in the duct. A shock wave was formed upstream of the disk and a vortex breakdown bubble was located behind the shock as a result of the vortex-shock interaction. The shock then moved towards the duct inlet with the vortex-breakdown bubble behind it. The vortex breakdown bubbles were then located between the inlet shock and the circular disk at the exit section. It was noticed from the Mach contours that most of the exit points were subsonic.

6.4.3 Effects of the Inlet Swirl Ratio

In this section, we study the effects of the swirl ratio at the initial station on the formation and behavior of the vortex-breakdown bubbles. Two values of Reynolds numbers were selected for this study. The first Reynolds number is 10,000 which gives a transient multi-bubble vortex breakdown with a swirl ratio of 0.32 as shown in Fig. 6.5. This value was chosen to test the effect of the swirl ratio on the duration of the vortex breakdown bubbles. The second Reynolds number is 100,000 which gives unsteady multi-bubble vortex breakdown at a swirl ratio of 0.32, as shown in Fig. 6.8,9. For all the cases presented in this section, the Mach number is fixed at 1.75 for the same grid and time step. The exit boundary conditions are obtained by extrapolating all the flowfield vector components from the interior cell centers.

6.4.3.1 Swirling Flow with R_e = 10,000 and β = 0.26

Figure 6.15 shows the streamlines and Mach contours for this flow case at different dimensionless time levels. Figure 6.16 shows the velocity vectors and axial distributions of flow properties along the duct axis at selected time levels. The snapshots at t =

2.0 show the formation of a normal shock wave with no vortex breakdown behind it. Although the axial velocity distribution at the first axial station is uniform, the velocity vectors at t = 4.0 show a wake-like distribution of the velocity behind the shock wave. The axial velocity along the duct axis drops to a very small positive value as shown in Fig. 6.16 at t = 4.0. At this level of swirl ratio no stagnation point exists and no vortex-breakdown bubbles are formed. As a result of the drop in the momentum behind the shock wave, a pressure field was created which caused the boundary layer on the duct wall to separate as can be seen from the Mach contours at t = 7.0. The high pressure region moved downstream causing the area of separated boundary layer to move accordingly downstream. As the high pressure region left the duct, the Mach contours show the attachment of the boundary layer on the duct wall. The shock wave became stable and no vortex breakdown was formed. This flow case shows a stable vortex flow with no breakdown bubbles.

6.4.3.2 Swirling Flow with R_e = 10,000 and β = 0.28

In this flow case, the swirl ratio was increased to 0.28 while keeping all other parameters fixed as in the previous case. Figure 6.17 shows snapshots of the streamlines and Mach contours at certain time levels. The streamlines at t = 4.0 show a vortex breakdown bubble behind the normal part of the shock wave at x = 1.0. The Mach contours show the separation of the boundary layer at the duct wall because of the high pressure gradient caused by the vortex breakdown bubble and the shock wave. The bubble moved downstream, as can be seen at t = 6.0, with the separated boundary layer moving accordingly. The shock wave was oscillating around an axial position in the inlet portion of the duct as can be seen by comparing its location at t = 6, 7 and 10. The bubble was then shed outside the duct and no more bubbles were formed as shown in

Fig. 6.17 at t = 10 where the flow reached a stable condition. This flow case shows a transient single-bubble vortex breakdown.

6.4.3.3 Swirling Flow with R_e = 10,000 and β = 0.3

In this flow case, the swirl ratio was increased to 0.3 with the other flow parameters kept fixed at the same values as in the previous two cases. Figure 6.18 shows snapshots of the streamlines and Mach contours of the solution of this flow case at selected time levels. The streamlines at t = 4.0 show a vortex-breakdown bubble behind the shock wave at x = 0.75. This bubble is larger than that of the previous flow case at β = 0.28. As the solution was advanced in time, the bubble moved downstream towards the duct exit. The separation of the boundary layer on the duct wall can be noticed at time levels greater than 4.0. At t = 8.0, no bubbles could be noticed behind the shock wave while the old bubble was shed as can be noticed from the deformation of the streamlines at x = 2.0. A new bubble was formed at t = 9.0 behind the shock wave. The new bubble became larger at t = 13 and reached its maximum size at t = 15 where the pressure gradient caused by the growing bubble was enough to separate the boundary layer as can be seen from the Mach contours. The bubble was shed outside the duct. The snapshots at t = 20 show a vortex flow with no vortex-breakdown bubbles. This flow case shows a transient multi-bubble vortex-breakdown flow.

In summary, increasing the swirl ratio from 0.26 to 0.3 changes the flow from a stable vortex flow with no vortex-breakdown bubbles at β = 0.26 to a flow with a single-bubble vortex breakdown at β = 0.28 to a flow with multi-bubble vortex breakdown at β = 0.3. Comparing the present results with those at β = 0.32, that are shown in Fig. 6.5, shows the effect of the swirl ratio on the transient period of the vortex-breakdown

bubble, where in the case of β = 0.32 the vortex-breakdown bubble lasted for a longer time than that with β = 0.3.

One concludes that the effects of increasing the swirl ratio is similar to increasing the Reynolds number as discussed in section 6.4.1.

6.4.3.4 Swirling Flow with R_e = 100,000 and β = 0.15

Figure 6.19 shows snapshots of the streamlines and Mach contours for this flow case. The snapshots show the formation of a very small bubble behind the shock wave at t = 3.0. The bubble enlarged in all directions and it reached its maximum size at t = 5.0 where two bubbles could be recognized behind the shock wave. At t = 7.0, the bubbles convected downstream while the boundary layer on the duct wall was separated because of the pressure gradient caused by the vortex-breakdown bubbles. As the solution was advanced in time, new vortex-breakdown bubbles were formed behind the shock wave while the old ones were shed, as can be seen at t = 9. This flow case shows the dependence of the bubble size on the swirl ratio where the bubbles' sizes in this flow case are much smaller than those of the flow case with β = 0.32 (see Fig. 6.8). This flow case shows a multi-bubble vortex breakdown.

6.4.3.5 Swirling Flow with R_e = 100,000 and β = 0.20

Figure 6.20 shows the streamlines and Mach contours for this flow case at selected time levels. As in the previous case at β = 0.15, a very small bubble was formed at t = 3.0. The bubble enlarged in all directions and the shock wave was deformed accordingly as can be seen at t = 5.0. As the solution was advanced in time, new bubbles were formed behind the shock wave while old bubbles were shed outside the duct. Comparing this flow case with the previous case for β = 0.15, one concludes that the sizes of the

bubbles in this case are larger than those with the smaller swirl ratio case. This flow case shows multi-bubble vortex breakdown flow.

It was then decided to increase the swirl ratio beyond 0.32. Values of 0.38 and 0.44 were used to study the effects of increasing the swirl ratio on the persistence of the vortex breakdown bubbles.

6.4.3.6 Swirling Flow with R_e = 100,000 and β = 0.38

Figure 6.21 shows snapshots of the streamlines and Mach-number contours for this flow case up to t = 30. The streamlines are shown for a radial distance of 0.6. It is noticed that the breakdown bubbles in this flow case are larger than those of smaller swirl ratios. The process of vortex-breakdown evolution, merging and shedding took place in the time levels up to t = 19. At t = 22 and beyond, a stable mode of vortex breakdown was established which is characterized by an almost stationary inlet shock wave with a very large vortex breakdown behind it. During the same period of time, no reversed flow regions occurred along the duct axis and the internal structure of the vortex breakdown bubble was nearly steady. The Mach contours show a strong shear layer between the breakdown region and the rest of the flow. It is seen that the shear layer did not change in the time period from t = 25 to t = 30.

It is thought that the flow reached a stable limit in the flow case under consideration. This idea was further investigated by solving for the flow case of a swirl ratio of 0.44.

6.4.3.7 Swirling Flow with R_e = 100,000 and β = 0.44

Figure 6.22 shows snapshots of the streamlines and Mach contours for this flow case at β = 0.44. The results are similar to those of β = 0.38. However, the development of the stable mode of vortex breakdown started earlier in this flow case. Comparing the streamlines of this flow case with those of the previous flow case of β = 0.38, we notice

that the downstream bubble appearing from t = 12 through t = 19 was smaller in size in this flow case than that of the previous case. This resulted in the early development of the stable structure as the upstream structure could move faster, pushing the small bubble further downstream. The downstream bubble disappeared at t = 27. From the results of this flow case and those of the flow case of β = 0.38, it was concluded that the flow reaches a stable phase beyond a certain swirl ratio. During the stable phase, only small internal changes occur. No reversed flow regions occur along the duct axis and no vortex-breakdown bubble shedding takes place. This streamline pattern is similar to some experimental observations that will be discussed at the end of this Chapter.

6.4.4 Effects of the Inlet Mach Number

In this section, the effects of the inlet Mach number on the formation and behavior of vortex breakdown are studied. For the presented cases, the Reynolds number was kept constant at 10,000 and the swirl ratio was fixed at 0.26. Three Mach numbers, M = 1.75, 2.0 and 2.25, are used in this study. The grid and the time step are the same for all three cases. The extrapolation boundary conditions were used at the duct exit section.

6.4.4.1 Swirling Flow with M_∞ = 1.75, R_e = 10,000 and β = 0.32.

The results of this case are shown in Fig. 6.15. Those results were presented and discussed in the previous section. This flow case gave no vortex breakdown.

6.4.4.2 Swirling Flow with M_∞ = 2.00, R_e = 10,000 and β = 0.32.

The results of this flow case are shown in Fig. 6.23 in terms of streamlines and Mach contours. The streamlines at t = 4.0 show the formation of a single vortex-breakdown bubble. It should be noticed here that the same swirl ratio did not give any vortex-breakdown bubbles with M = 1.75. The bubble moved downstream as can be seen at t = 5 and it was convected off the duct axis. The streamlines at t = 7 show no bubbles

in the duct. As the solution was advanced in time, no more bubbles were formed. This flow case shows a transient single-bubble vortex-breakdown flow.

6.4.4.3 Swirling Flow with M_∞ = 2.25, R_e = 10,000 and β = 0.32.

Figure 6.24 shows the results of this flow case in terms of streamlines and Mach contours. At t = 2.0, a small bubble was formed behind the shock wave. The streamlines at t = 3.0 show two bubbles moving downstream. The convection of the bubbles continued where new bubbles were formed behind the shock wave as can be seen at t = 5.0. As the solution was advanced in time, the cycle of formation and shedding of the bubbles continued. This flow case shows multi-bubble vortex breakdown flow.

In summary, increasing the Mach number changes the flow from no breakdown to single bubble vortex-breakdown to transient multi-bubble vortex breakdown. The effects of increasing the Mach number are similar to those of increasing the swirl ratio or increasing the Reynolds number.

6.4.5 Swirling Flow in a Duct with an Inviscid Wall

It is noticed that the duct-wall boundary layer may separate as a result of its interaction with the inlet shock wave and/or because of the pressure field created by the vortex-breakdown bubbles behind the inlet shock. The effect of the duct-wall boundary-layer flow on the behavior of the vortex-breakdown bubble is investigated by assuming that the duct wall is inviscid and hence no boundary layer exists on the wall. Two flow cases are considered. In the first flow case, the Reynolds number is kept constant at 10,000 and in the second case the Reynolds number is kept constant at 100,000. For both cases the Mach number is 1.75 and the swirl ratio is 0.32.

6.4.5.1 Flow Case with R_e = 10,000

The results of this flow case are shown in Fig. 6.25 at selected time levels up to t = 60. These results are compared with those of viscous duct-wall at the same flow conditions in Fig. 6.5. It is noted that the development of vortex-breakdown bubbles in this flow case is faster than that of the viscous duct-wall as can be seen by comparing the streamlines at t = 5 and t = 12. While the inlet shock wave in the viscous wall case was oscillating with its upper end fixed at the duct entrance, the inlet shock of the inviscid-wall case is always moving downstream until it reaches a stable location at t = 39 and beyond. This is because it can slip freely on the duct-wall surface. In the viscous-wall case, no vortex breakdown was formed beyond t = 32. It is noticed that the formation of new vortex-breakdown bubbles continued in a periodic sequence for the inviscid-wall case which is similar to the flow at higher Reynolds numbers. It is concluded that the effect of using the inviscid wall assumption is similar to solving for a higher value of Reynolds number.

6.4.5.2 Flow Case with R_e = 100,000

The results of this flow case are shown in Fig. 6.26. The streamlines show the evolution, merging and shedding of vortex-breakdown bubbles for time levels up to t = 50. The Mach contours show the motion of the upper end of the inlet shock wave to reach a stable location at the end of the divergent portion of the duct wall. At early time levels, the solution was similar to that of the viscous wall with the same flow conditions. As the solution was advanced in time, the flow became similar to that of the Euler equations. The formation of a stable vortex-breakdown mode was recognized at t = 59 and beyond. It started at t = 36 in the case of the Euler equations, as can be seen from Fig. 6.10. In the flow case under consideration, the size of the breakdown region was smaller than

that of the Euler equations. It should be noticed here that the flow case with the viscous wall was characterized by an unsteady, multi-bubble, multi-frequency vortex breakdown and no stable mode of breakdown was recognized as was the case of the Euler equations. As in the case of R_e = 10,000, it is concluded that using the assumption of an inviscid duct-wall has a similar effect as simulating flows at higher Reynolds numbers.

6.4.6 Interaction of a Supersonic Vortex Flow with an Oblique Shock Wave.

The interaction of a supersonic vortex flow and an oblique shock wave is a very important application for internal and external flows. This type of flow was studied experimentally in References [92, 93] and computationally in References [95, 110]. In both cases, no vortex breakdown was detected and no physical explanation was given for the critical conditions required for the vortex breakdown to take place. In the present study, the problem of vortex/oblique shock interaction is solved using the upwind scheme presented in Chapter 4 and the oblique shock was created by placing a straight wedge on the duct wall in the supersonic flow stream. The computational domain is similar to that used in the other duct cases in this Chapter but the divergent part was replaced by a convergent part which forms a wedge at the duct wall. Two values of the wedge angles, 6° and 10°, are used. The inflow conditions are kept constant and their values are as follows: R_e = 100,000, M = 1.75 and β = 0.32. It should be noted here that these flow conditions gave multi-bubble vortex breakdown with normal shock wave cases (see Figures 6.8&9).

6.4.6.1 Supersonic Vortex Flow in a Duct with a 6°Wedge.

Figure 6.27 shows the results of this flow case in terms of streamlines and Mach contours. The Mach contours show the formation of an oblique shock wave at the wedge. The streamlines show no recirculation zones behind the shock wave. The Mach

number contours show the formation of another oblique shock wave at the convergent-divergent-nozzle entrance because the flow downstream of the first oblique shock wave was supersonic. As the snapshots show, both shock waves are deforming according to the pressure fields behind them. For instance, the central part of the entrance shock wave is almost normal. As the solution was advanced in time, a pressure field built up behind the shock wave which in return caused the normal part of the oblique shock to expand. For example, at t = 20, a long segment of the shock wave became normal but no vortex breakdown was formed behind it because the critical conditions were not reached. At t = 30, the entrance shock wave became almost normal causing the flow behind it to be subsonic and the second shock wave to disappear. The shock wave at the duct entrance moved upstream towards the duct inlet section to reach the cylindrical part at t = 35. The flow fields at t = 30 and t = 35 are similar to those of the duct without the wedge. An interesting snapshot is shown at t = 35 where the shock wave became normal and a vortex-breakdown bubble was formed behind the normal shock. As the solution was advanced in time, the vortex-breakdown bubble was dissipated and the shock wave was stationed at the duct entrance with no new vortex-breakdown bubbles formed behind it. The results show that certain critical swirl ratio should be satisfied for the vortex breakdown to exist. Since the tangential velocity is not affected by transverse shock waves, increasing the swirl ratio is only caused by decreasing the axial velocity component. In the case of oblique shock waves, the drop of the axial velocity is not enough to obtain the required critical swirl ratio. Also, the pressure rise across oblique shock waves is not enough to cause vortex breakdown.

6.4.6.2 Supersonic Vortex Flow in a Duct with a 10°Wedge.

Figure 6.28 shows the streamlines and Mach contours for the supersonic swirling flow in a circular duct with a wedge at an angle of 10°. As in the case of α = 6°, no breakdown was formed as a result of the vortex/shock interaction. Comparing the results of the present case with those of the smaller wedge angle, it was noticed that the shock in this case became stronger faster than that of the smaller wedge angle. The vortex-breakdown bubble is detected at t = 30 where the normal shock wave is located at the duct entrance. It should be noticed here that the bubble was formed at t = 35 with α = 6°. As in the case with the smaller wedge angle, the shock wave left the duct and it became stationed at the entrance.

6.5 Summary and Discussion

In this Chapter, the quasi-axisymmetric assumption was used for the solution of a supersonic swirling flow in a configured circular duct. The applications included the effects of the Reynolds number, the type of exit-boundary conditions, swirl ratio, Mach number and duct-wall boundary-layer flow on the development and behavior of vortex-breakdown structures. To investigate the effects of Reynolds numbers, values from 2,000 to 100,000 were used along with a limiting case of the Euler equations. It was shown that, increasing the Reynolds number from 2,000 to 100,000, the vortex-breakdown mode changed from no-breakdown to a transient single-bubble breakdown to a transient multi-bubble breakdown to an unsteady multi-bubble, multi-frequency breakdown. The flow solution using the Euler equations showed a stable mode of vortex breakdown with no reversed flow regions along the duct axis.

Swirl ratios ranging from 0.26 to 0.32 were used with the flow case of Reynolds number of 10,000, and swirl ratios from 0.15 to 0.44 were used with the flow case of

Reynolds number of 100,000. It was shown that increasing the swirl ratio has a similar effect as increasing the Reynolds number. As the swirl ratio was increased, the flow changed from no breakdown to transient multi-bubble breakdown for the flow case of Reynolds number of 10,000 and from multi-bubble breakdown with very small bubbles to a stable breakdown for the flow case of Reynolds number of 100,000.

Mach numbers of 1.75, 2.0 and 2.25 were used with the flow case of R_e = 10,000 and swirl ratio of 0.26. The flow changed from a no-breakdown flow to a transient multi-bubble breakdown flow as a result of increasing the Mach number.

It was shown that assuming the flow at the duct wall to be inviscid has a similar effect as simulating flows at higher Reynolds numbers. The flow case of R_e = 100,000 with inviscid duct wall produced a stable vortex-breakdown mode similar to that obtained using the Euler equations. The breakdown in the flow case of R_e = 10,000 lasted for a longer time in comparison with that of viscous duct wall.

Five types of exit-boundary conditions were used to investigate the effect of the type of exit-boundary conditions on the breakdown mode. It was shown that, by controlling the exit-boundary conditions it was possible to control the breakdown mode. For example, quasi-steady modes could be obtained by placing a circular disc at the duct exit section.

Two flow cases were presented for the interaction of supersonic swirling flows with oblique shock waves. It was shown that certain strengths of the inlet shock should be reached in order for the breakdown to take place. This suggested that certain reductions in the axial velocity should be obtained to satisfy the required critical swirl ratio for the vortex breakdown to occur.

6.5.1 Internal Structure of Vortex-Breakdown Bubbles in View of the Available Experimental Results.

Figure 6.29 shows the mean streamline pattern inside the breakdown region of an incompressible swirling flow in a duct which was published by Faler and Leibovich in reference [39]. For a long time, since the publication of that result, it has been a goal for many researchers to obtain similar vortex-breakdown-bubble internal structure in order to validate their results. Some researchers who solved the unsteady Navier-Stokes equations; e. g. [62, 67], obtained several modes of breakdowns including a two-cell mode similar to Faler & Leibovich (FL) mode. They compared their results with this experimental result without relating this mode to the other modes they obtained. In this study, several modes of breakdowns were obtained including the two-cell mode of Faler and Leibovich. For example, Fig. 6.30 shows the streamlines at t = 125 for the flow case of R_e = 100,000, M_∞ = 1.75 and β = 0.32. The streamlines show the internal structure the vortex-breakdown bubble that consists of two recirculation cells. The rotational directions of the two cells are the same as those of the experimental results. It is clear that the computational result is in a good qualitative agreement with the experimental result.

Another experimental streamline pattern for the internal structure of an incompressible vortex breakdown in a duct is shown in Fig. 6.31, which was published by Escudier in Reference [12]. It appears confusing to notice that Escudier's pattern is different from the FL pattern. For instance, Fig. 6.31 shows no reversed flow regions along the duct axis while Fig. 6.29 shows two regions of reversed flow along the duct axis. Escudier [12] stated that it is impossible to know which streamline pattern is accurate and he could not give any reason for the differences between the two modes. The computational results of this study show that the two modes are different, and they may occur at different

time levels for the same flow case. Figure 6.32-a shows the streamline pattern inside the breakdown region for the flow case of R_e = 100,000, M_∞ = 1.75 and β = 0.44 at t = 30. The streamlines show two regions of reversed flow off the duct axis. This breakdown mode is similar to the experimental mode in Fig. 6.31. The computational result shows some details inside the breakdown region that were not reported experimentally. For example, two small bubbles could be recognized in the recirculation region near the duct wall. At some other time levels, these two bubbles merged into one stronger bubble, see Fig. 6.22. Some streamlines are terminated inside the breakdown region forming very small bubbles. It is very interesting to notice the expansion of the vortex core underneath of the recirculation regions that was noticed also in the experimental pattern of Fig. 6.31. The computational streamlines show that this expansion was caused by two small bubbles near the duct axis. It was noticed that this breakdown mode is a stable mode that does not convert to any other mode. Figure 6.22 shows the two-cell pattern of FL at t = 12. The present results show that the FL mode is a transient mode and as time passes, it transformed into another breakdown mode.

Figure 6.32-b shows the streamlines of the flow case of the Euler equations at t = 69 with M_∞ = 1.75 and β = 0.32. The snapshot shows two recirculation regions off the duct axis with no reversed flow regions along the duct axis. This breakdown mode is similar to Escudier's mode. As the results in Fig. 6.10 show, this mode is stable and it does not change to any other mode. The present results show that the FL mode occurred at t = 12 and it was transformed later on to the Escudier mode.

Figure 6.32-c shows the streamlines of the flow case of R_e = 100,000, M_∞ = 1.75 and β = 0.32 using the inviscid duct-wall at t = 69. The snapshot shows two recirculation regions off the duct axis with no reversed flow region along the duct axis. This breakdown mode is similar to Escudier's mode. As the results in Fig. 6.26 show, this mode is stable

and it does not change to any other mode. The results show that, the FL mode occurred at t = 12 then it was transformed to another mode. In summary, the two experimental patterns are different where the FL mode is a transient mode that may convert to anther mode as time goes by, while Escudier's mode is a stable mode that may stay for a long time. The FL mode may exist in any flow case while Escudier's mode exists only for flow cases with very high potential to vortex breakdown, e. g., flows with high swirl ratios, inviscid flows or flows at high Reynolds numbers with inviscid duct walls. These conclusions might not be generalized for incompressible flows, since they were based on the supersonic flow cases under consideration.

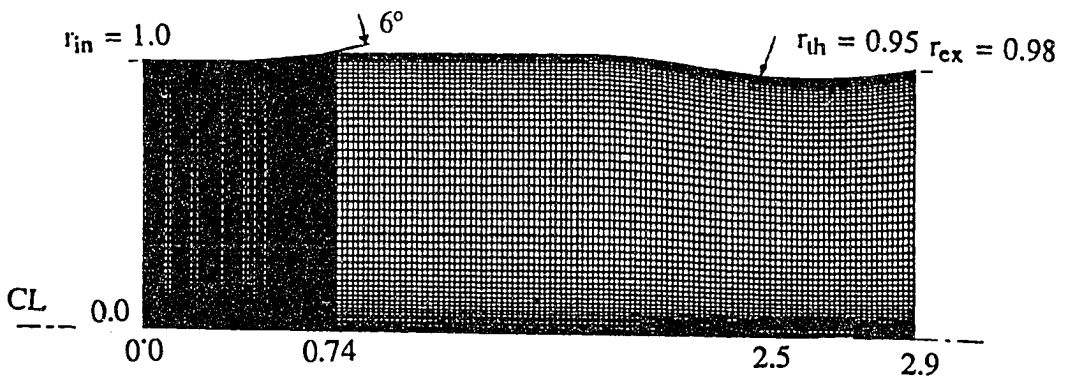

Figure 6.1 Typical grid for the configured circular duct, 221x51x2 grid points.

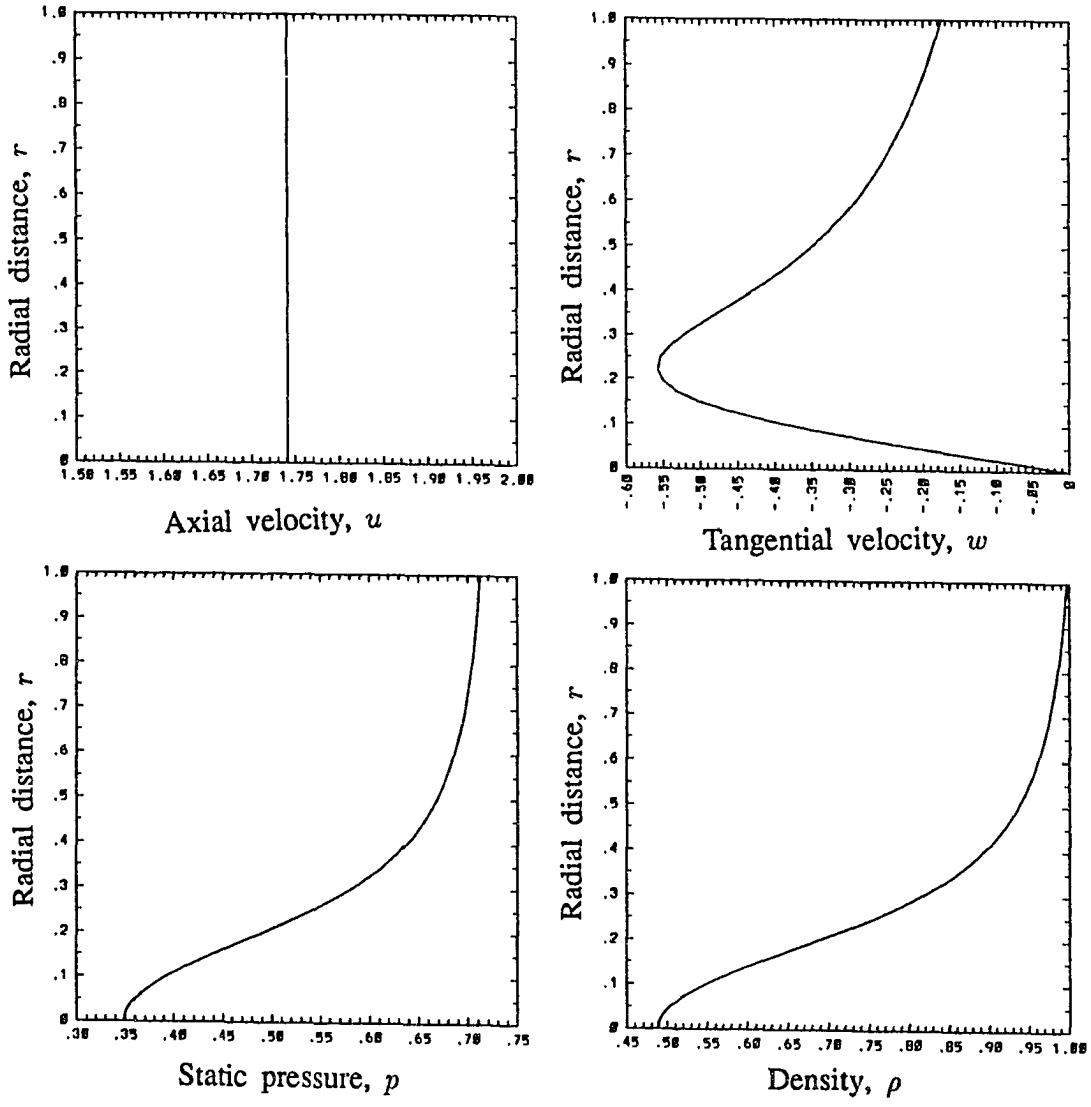

Figure 6.2 Initial profiles for a supersonic swirling flow with $M_\infty = 1.75$, $\beta = 0.32$.

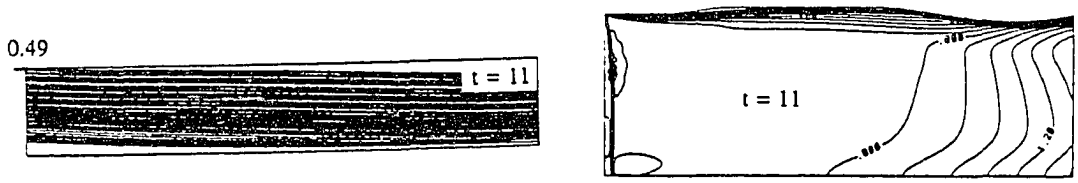

Figure 6. 3 Streamlines and Mach contours for a swirling flow without breakdown, $M_\infty = 1.75$, $\beta = 0.32$ and $R_e = 2,000$.

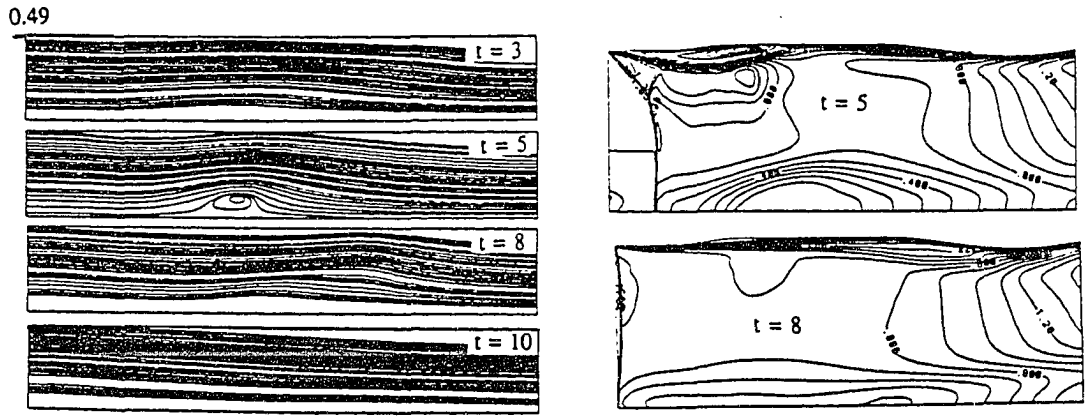

Figure 6.4 Streamlines and Mach contours for a swirling flow with a transient single-bubble breakdown, $M_\infty = 1.75$, $\beta = 0.32$ and $R_e = 4,000$.

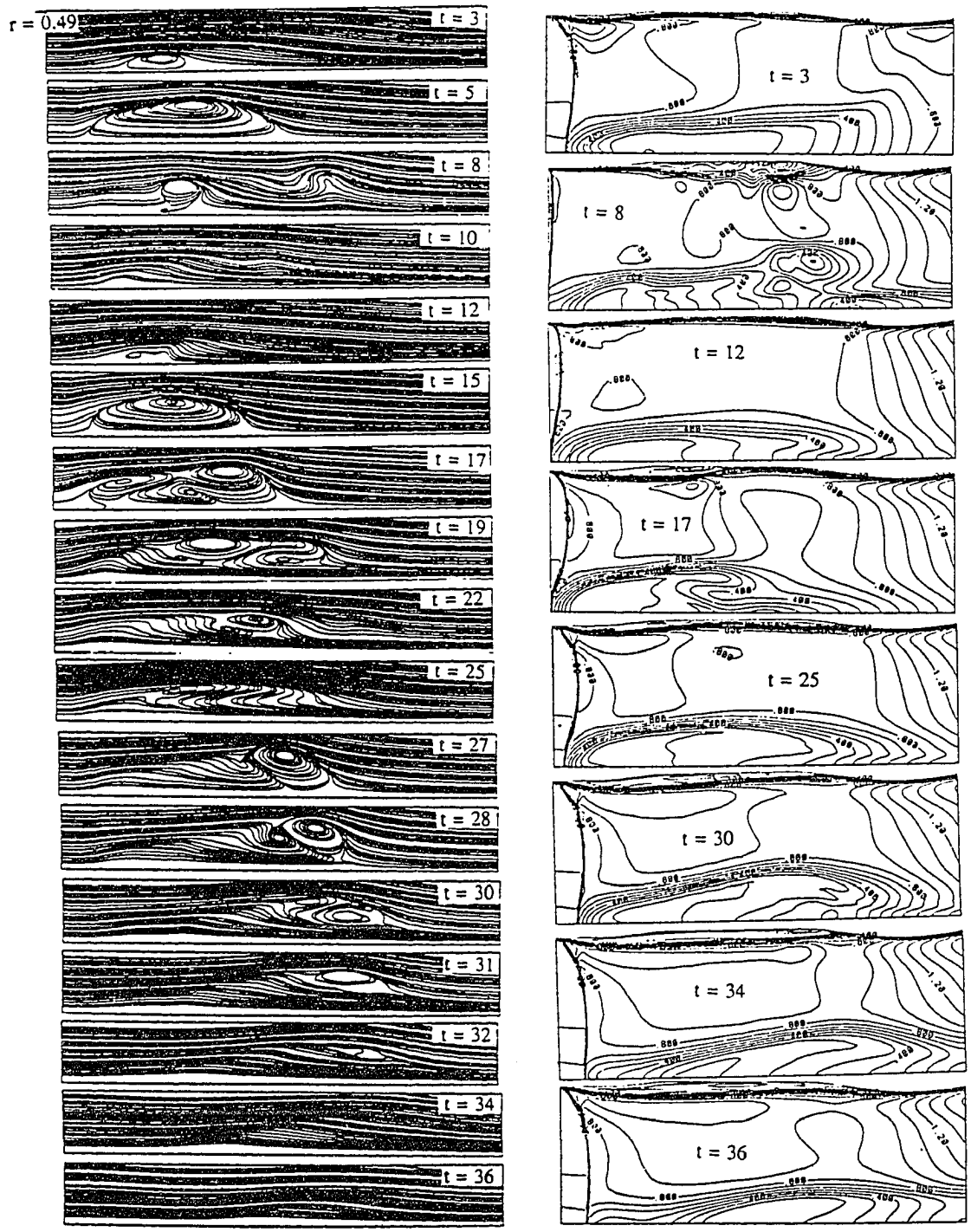

Figure 6.5 Streamlines and Mach contours for a swirling flow with a transient multi-bubble breakdown, $M_\infty = 1.75$, $\beta = 0.32$ and $R_e = 10,000$.

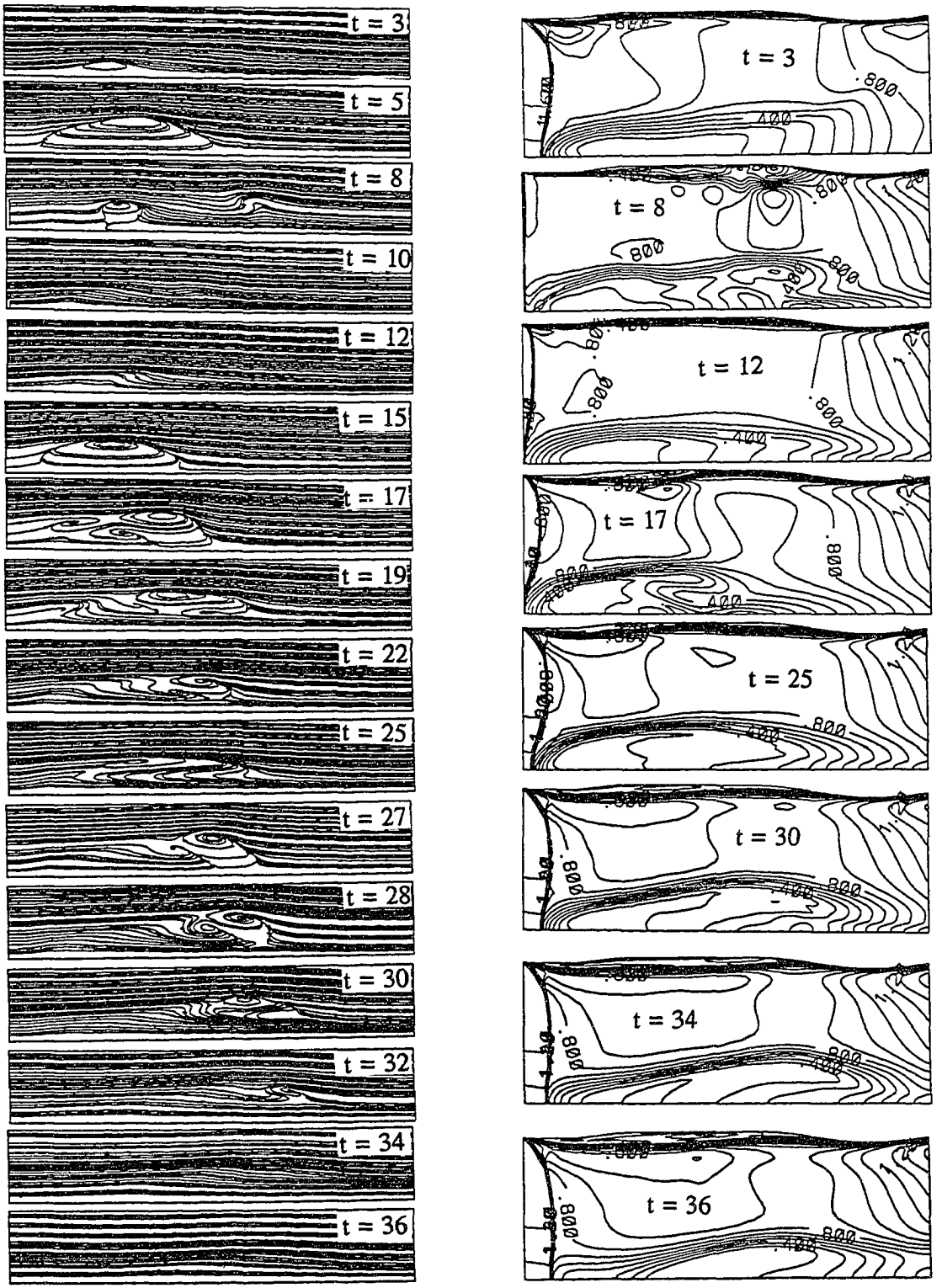

Figure 6.6 Streamlines and Mach contours for a swirling flow with a transient multi-bubble breakdown, $M_\infty = 1.75$, $\beta = 0.32$, $R_e = 10,000$ and $\Delta t = 0.00125$.

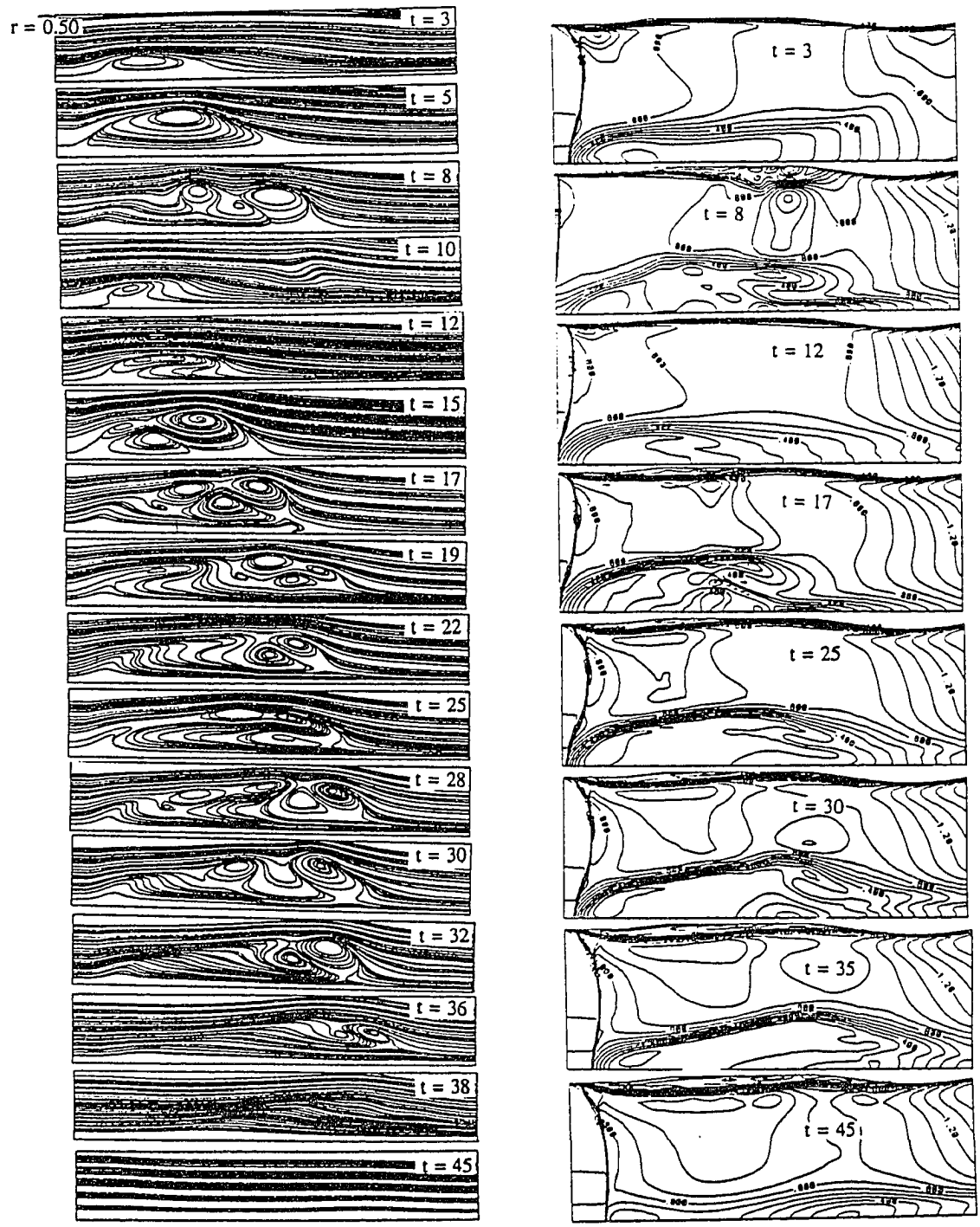

Figure 6.7 Streamlines and Mach contours for a swirling flow with a transient multi-bubble breakdown, $M_\infty = 1.75$, $\beta = 0.32$ and $R_e = 20,000$.

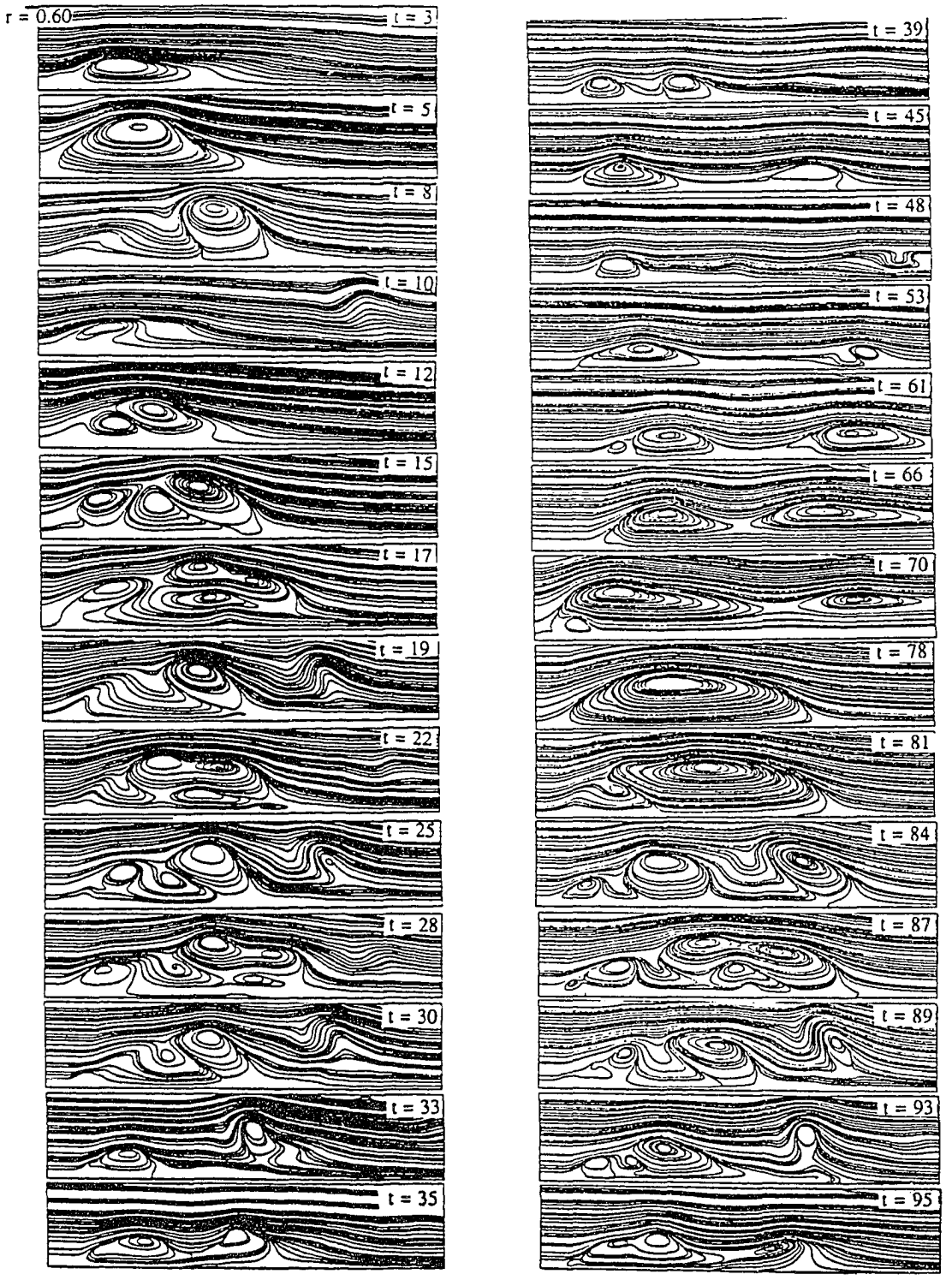

Figure 6.8 Streamlines for a swirling flow with unsteady multi-frequency multi-bubble breakdown, $M_\infty = 1.75$, $\beta = 0.32$ and $R_e = 100,000$.

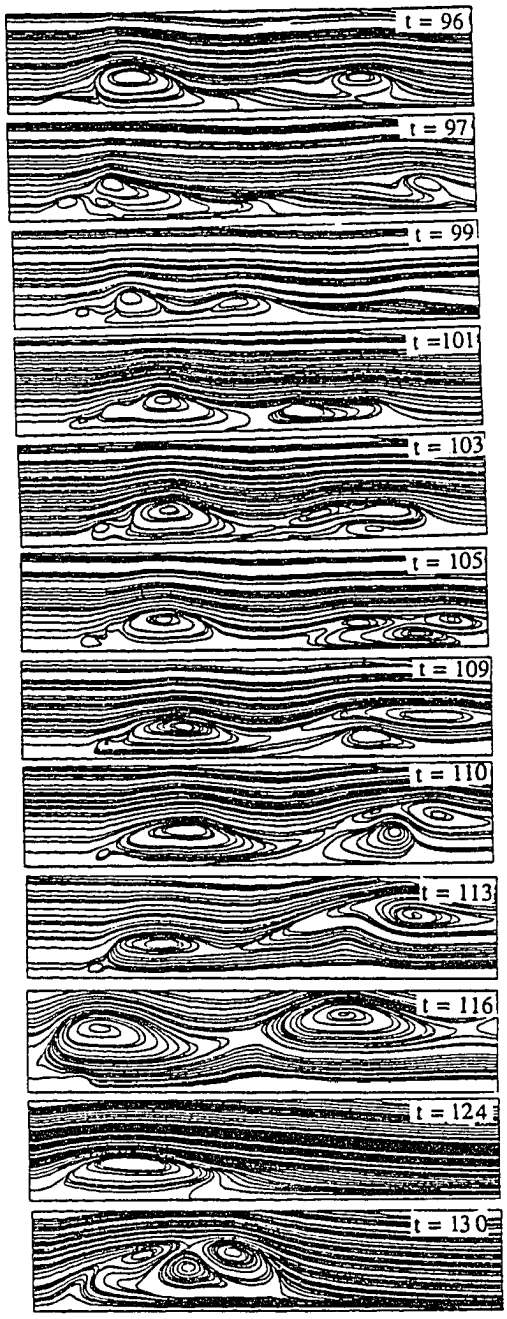

Figure 6.8: Cont'd

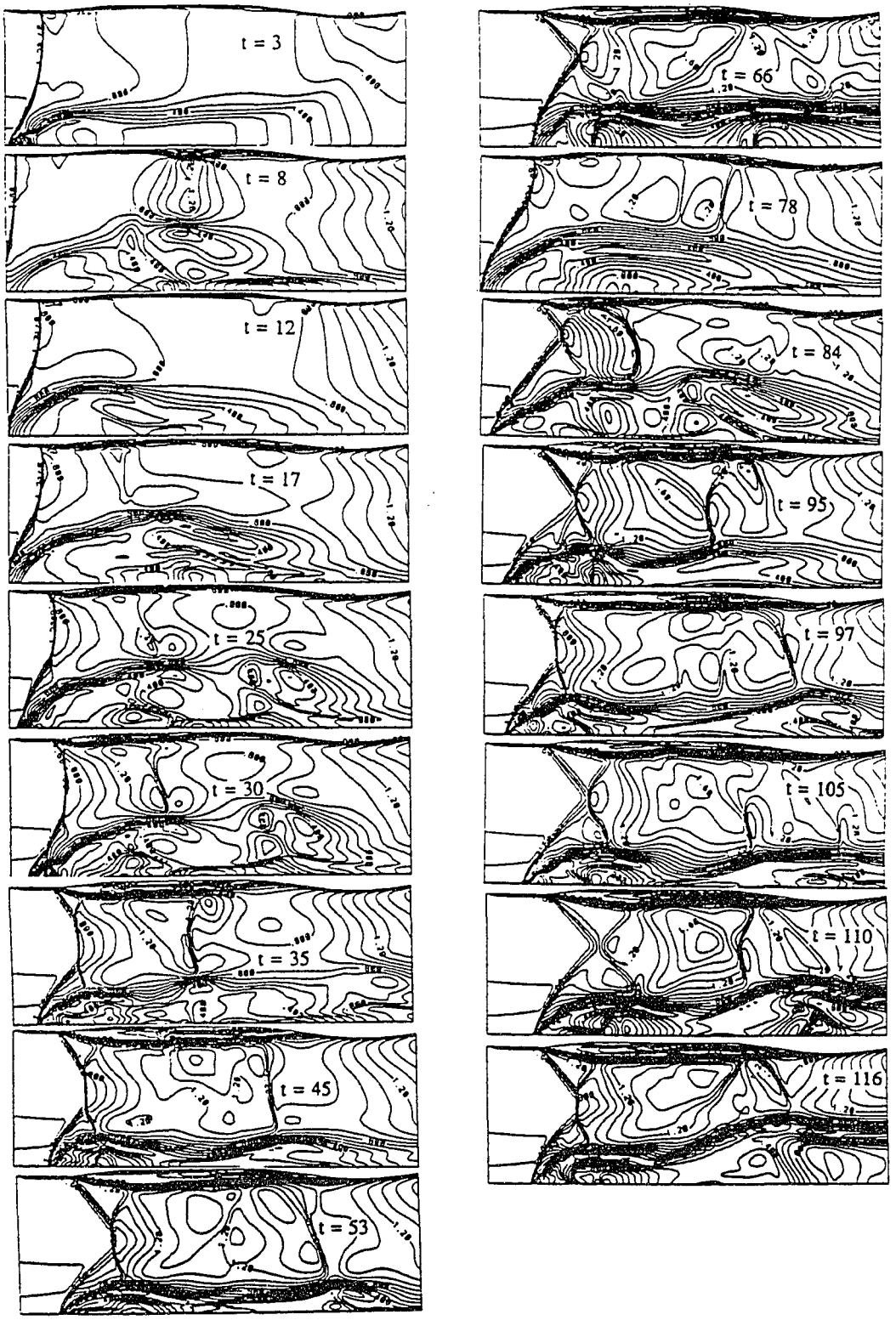

Figure 6.9 Mach contours for a swirling flow with unsteady multi-frequency multi-bubble breakdown, $M_\infty = 1.75$, $\beta = 0.32$ and $R_e = 100,000$.

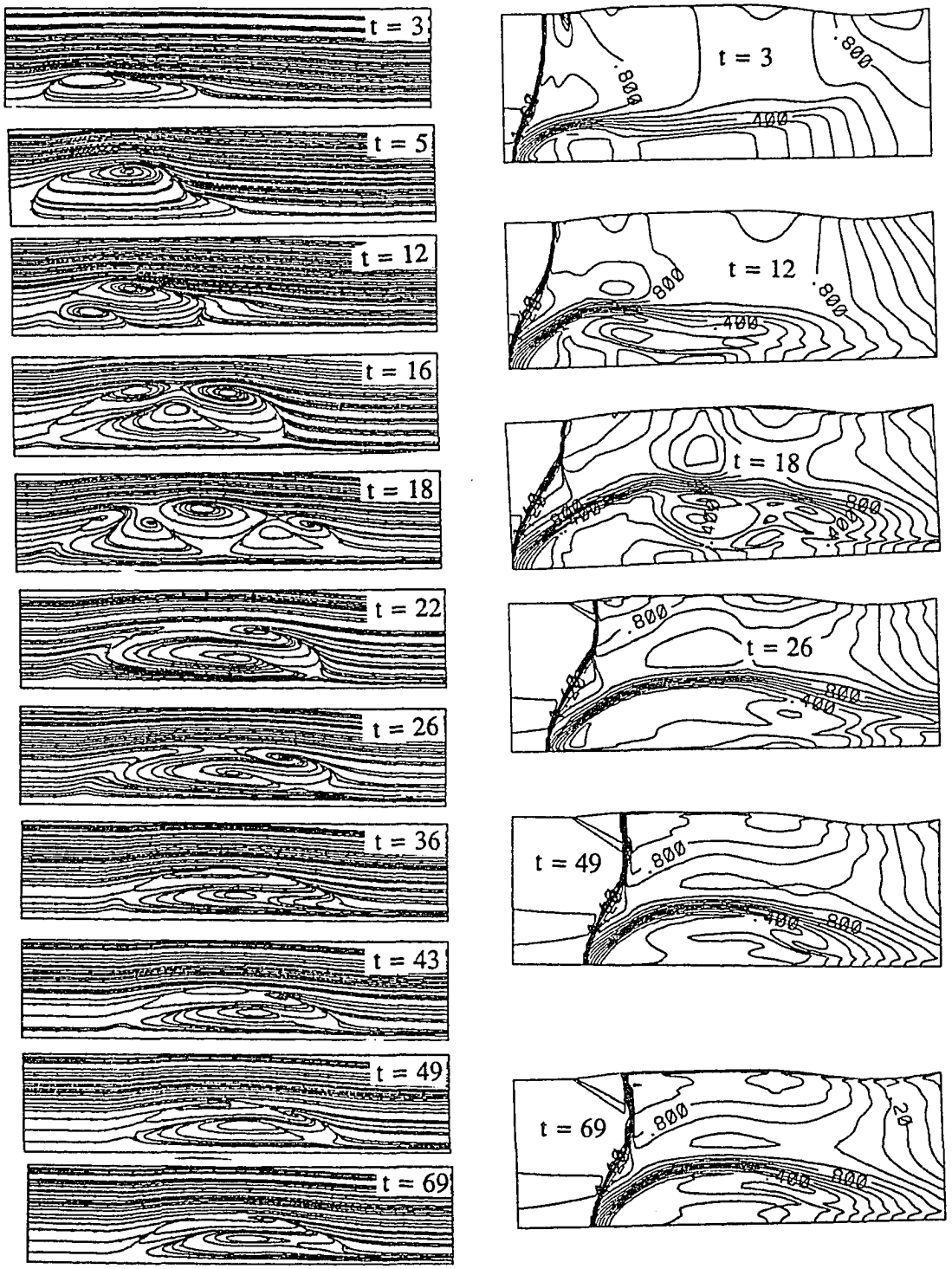

Figure 6.10 Streamlines and Mach contours for a swirling flow using Euler equations, $M_\infty = 1.75$ and $\beta = 0.32$.

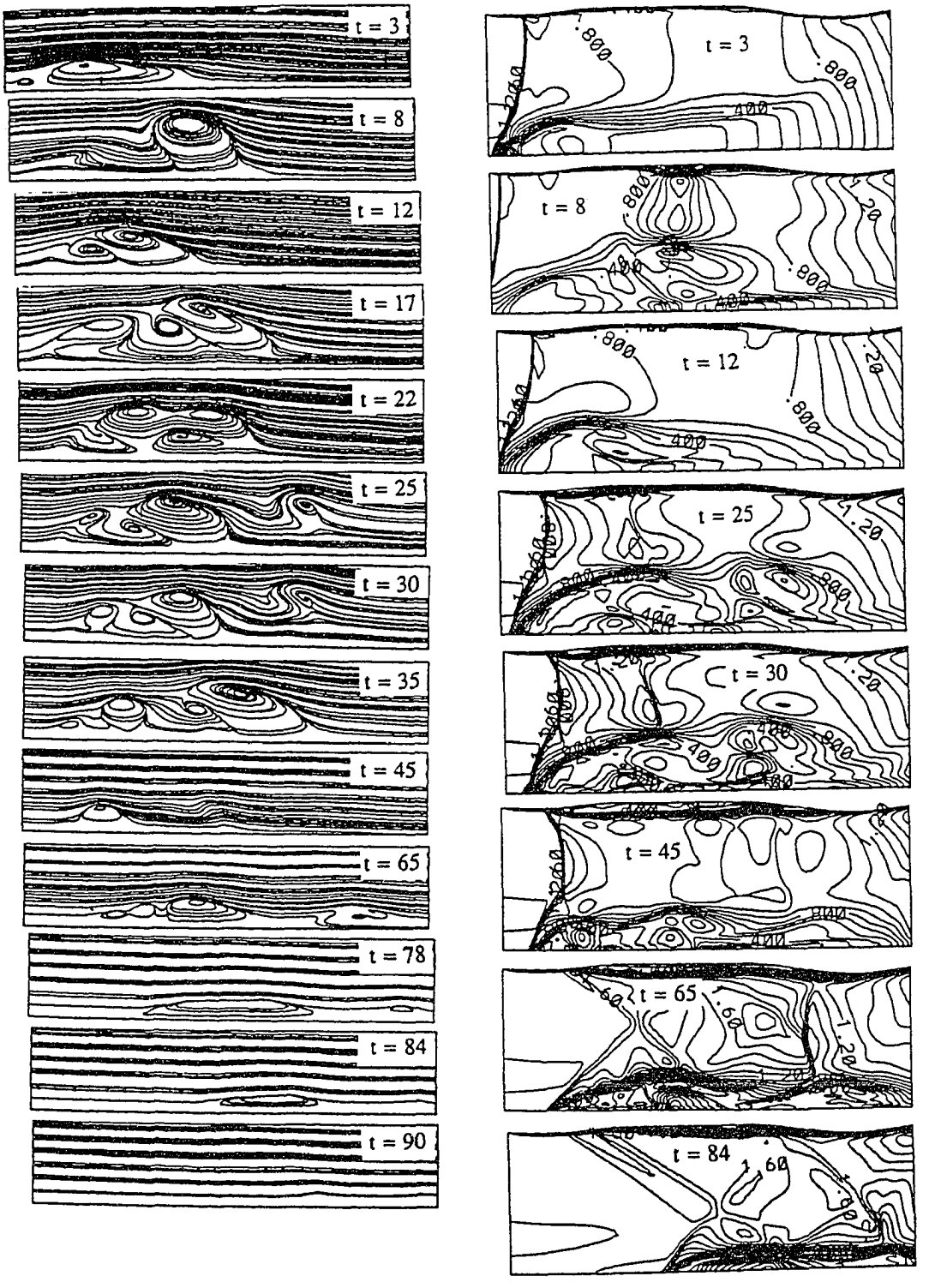

Figure 6.11 Streamlines and Mach contours for a swirling flow with transient multi-bubble breakdown, $p_b = p_\infty$, Riemann invariant exit-boundary conditions.

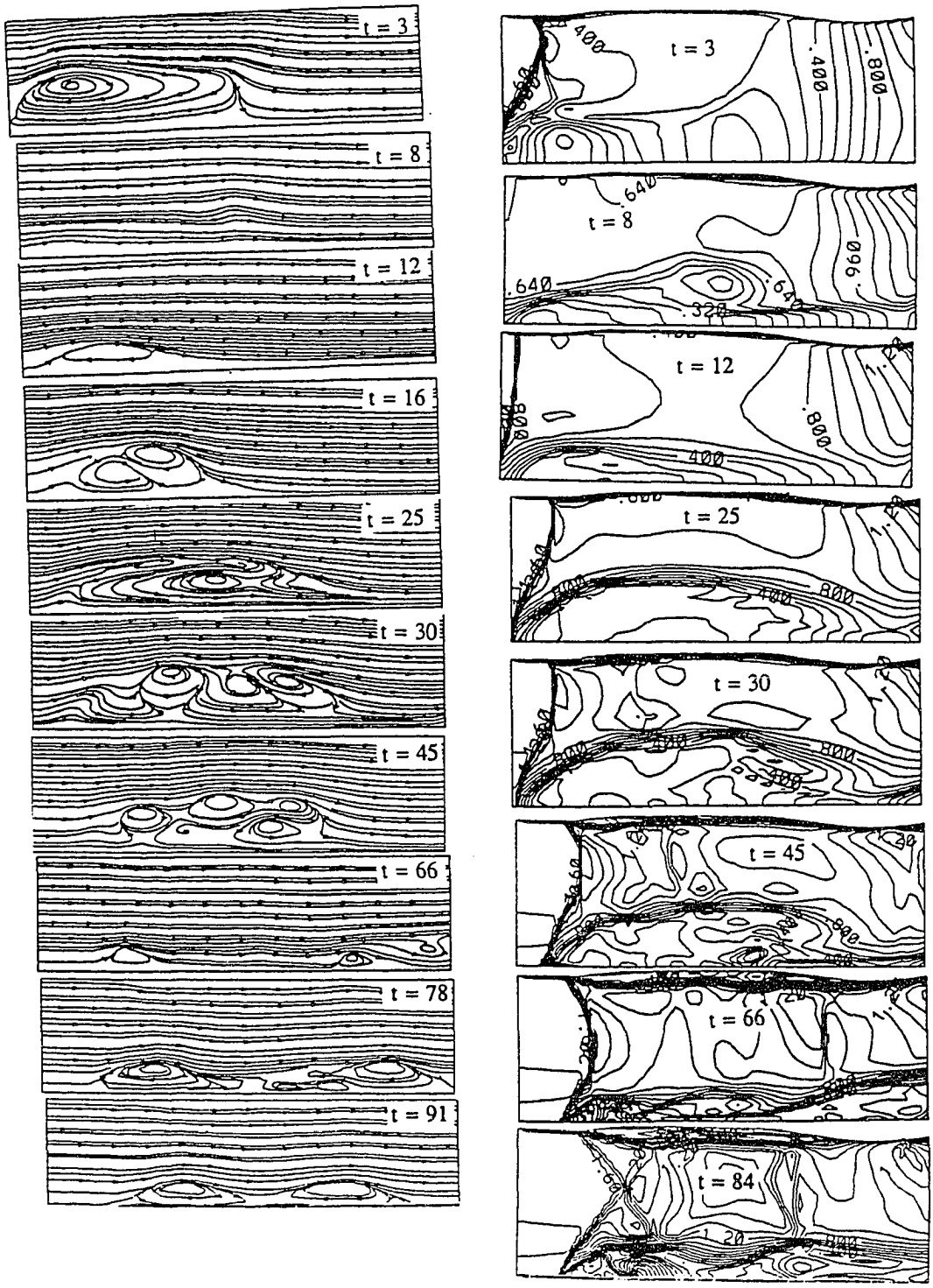

Figure 6.12 Streamlines and Mach contours for a swirling flow with transient multi-bubble breakdown, $p_b = 2p_\infty$, Riemann invariant downstream boundary conditions.

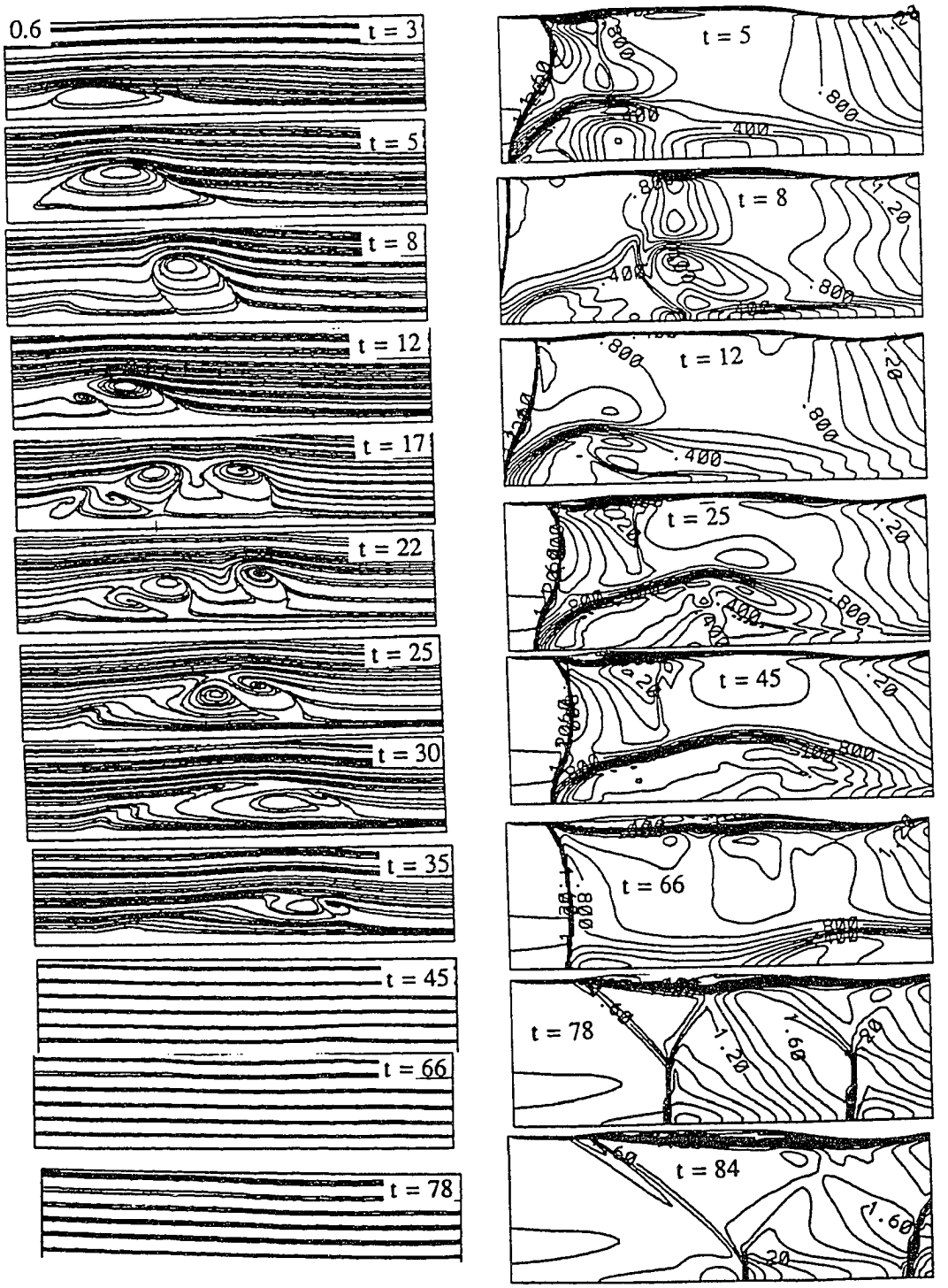

Figure 6.13 Streamlines and Mach contours for a swirling flow with transient multi-bubble breakdown, $\frac{\partial p}{\partial x} = constant$, downstream boundary conditions.

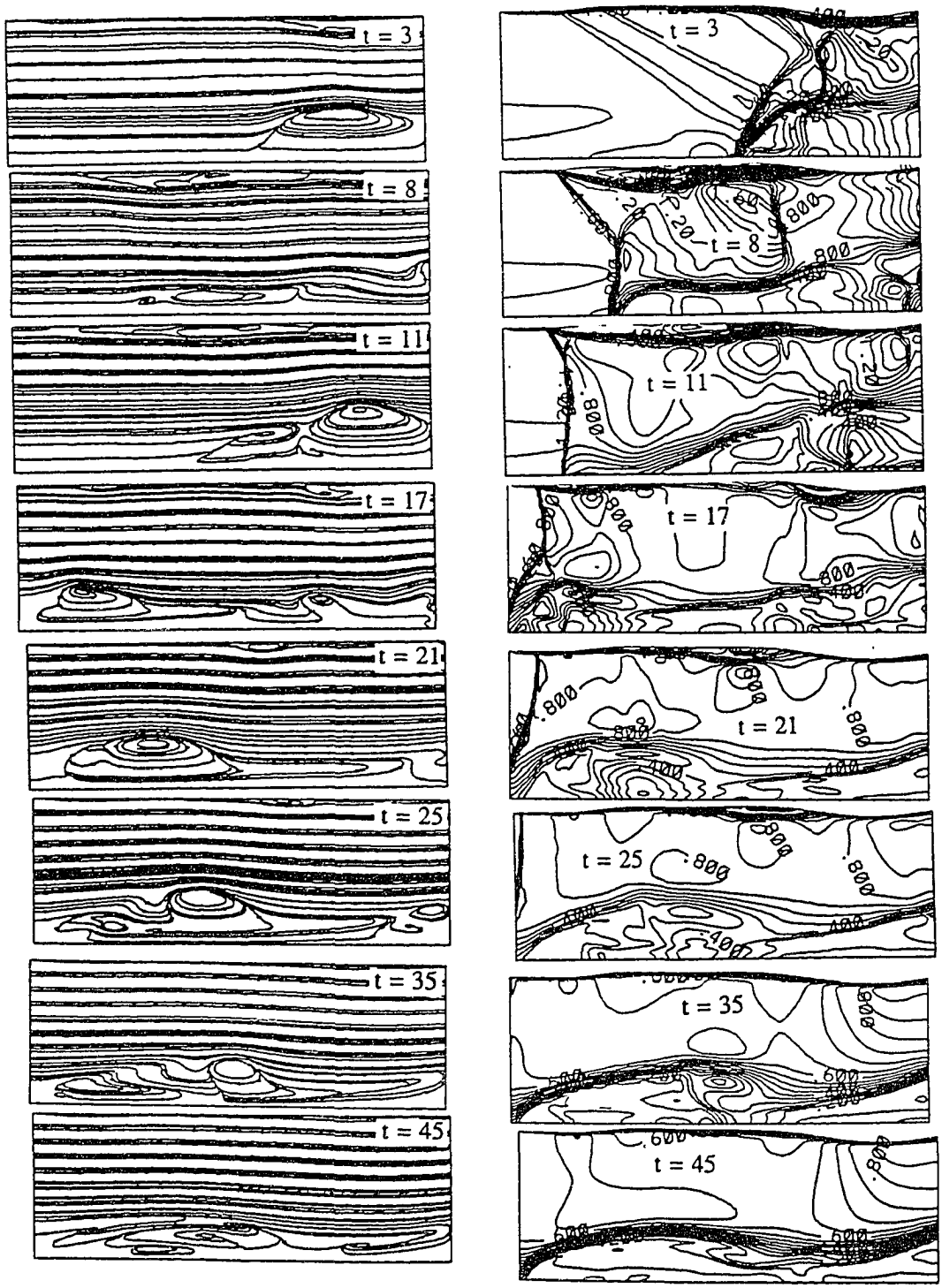

Figure 6.14 Streamlines and Mach contours for a swirling flow with quasi—steady multi-bubble breakdown, downstream disk of $r = 0.333$.

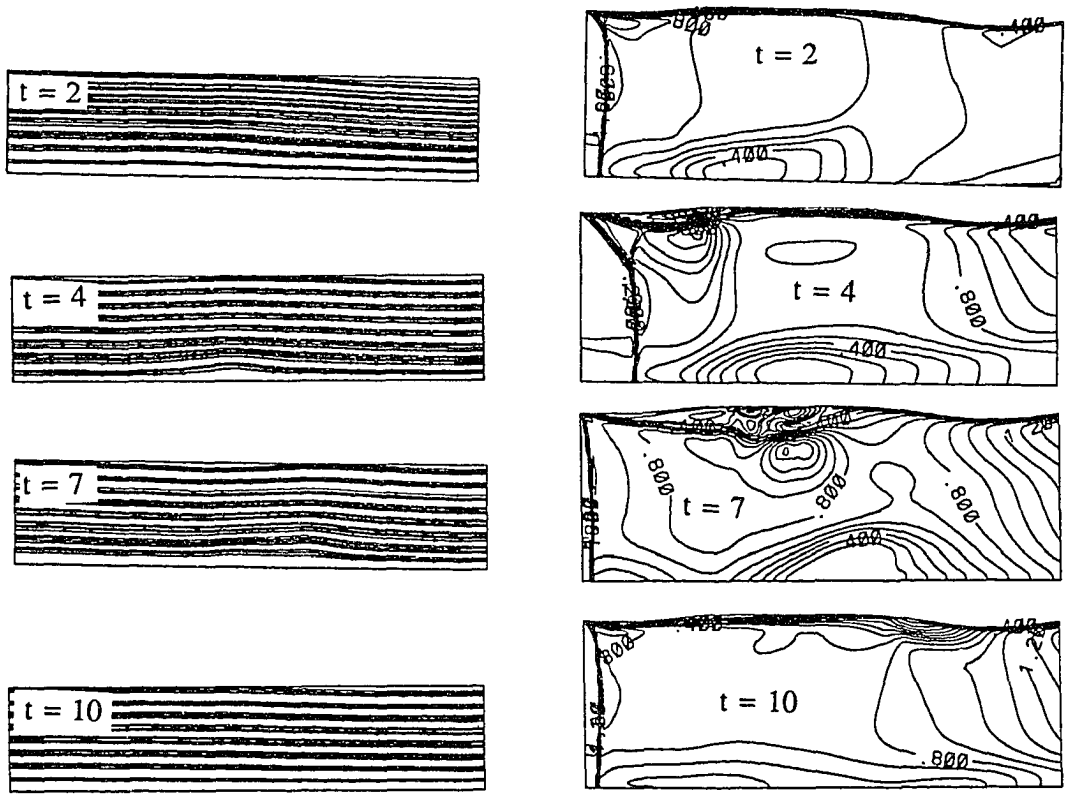

Figure 6.15 Streamlines and Mach contours for a swirling flow without breakdown, $M_\infty = 1.75$, $\beta = 0.26$ and $R_e = 10,000$.

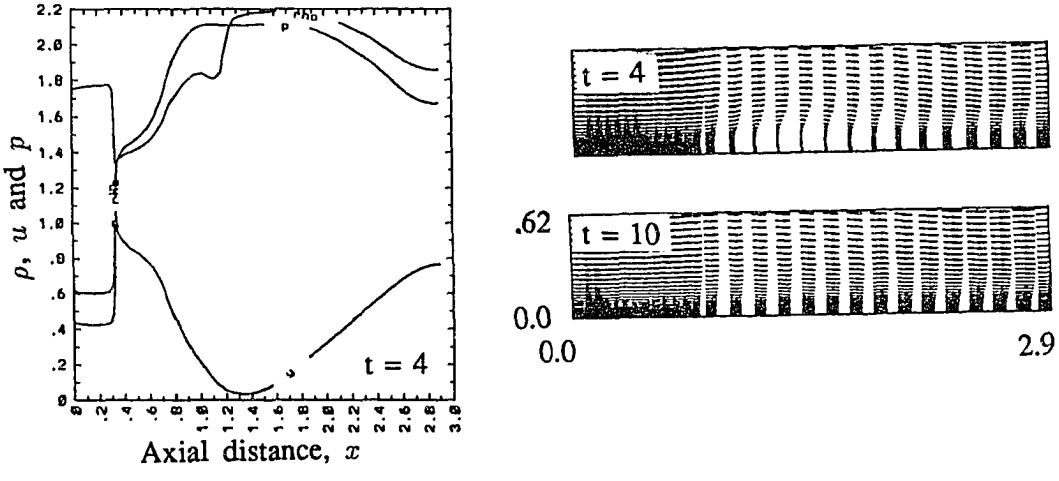

Figure 6.16 Velocity vectors and axial distributions for a swirling flow without breakdown, $M_\infty = 1.75$, $\beta = 0.26$ and $R_e = 10,000$.

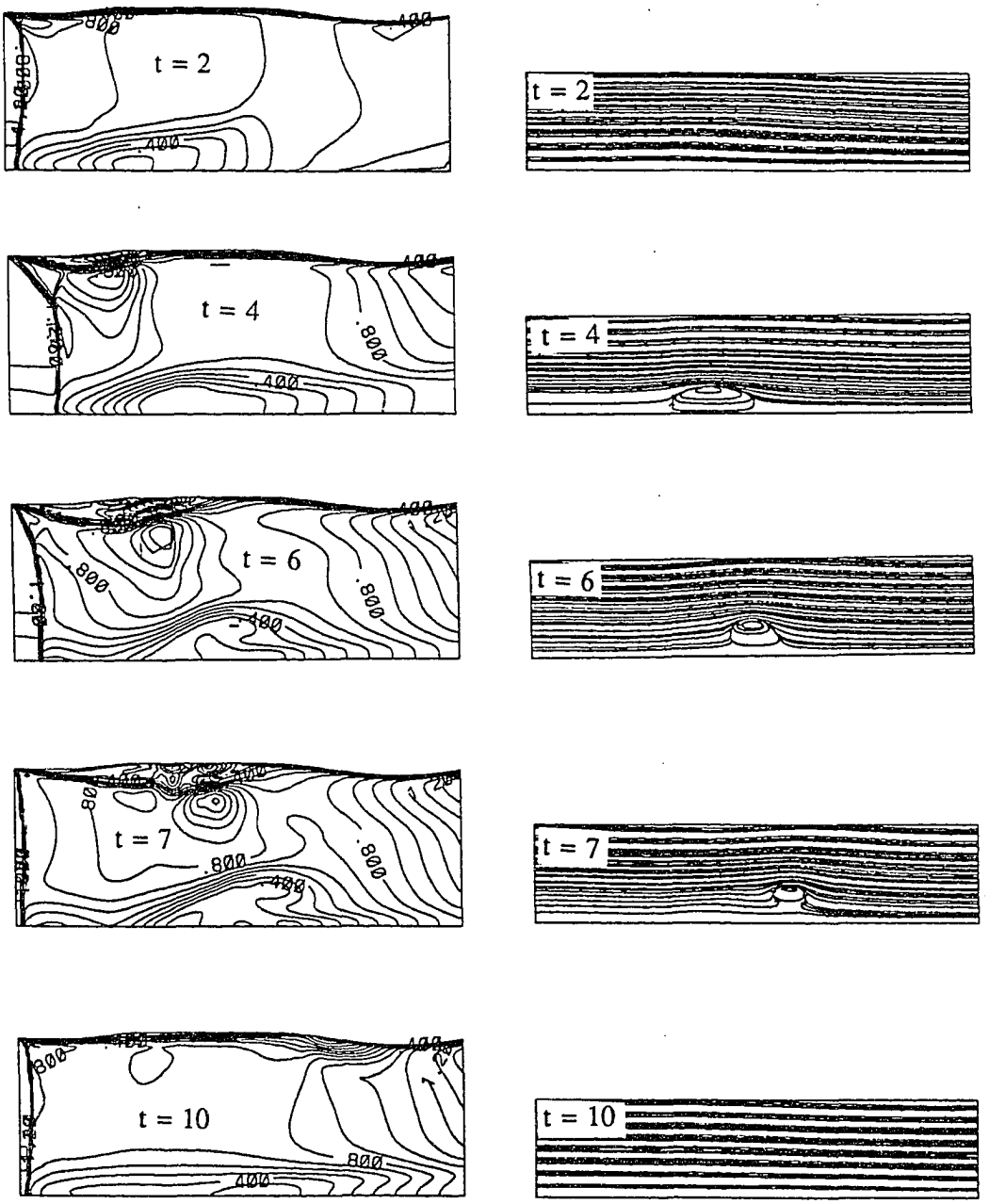

Figure 6.17 Streamlines and Mach contours for a swirling flow with a transient single-bubble breakdown, $M_\infty = 1.75$, $\beta = 0.28$ and $R_e = 10,000$.

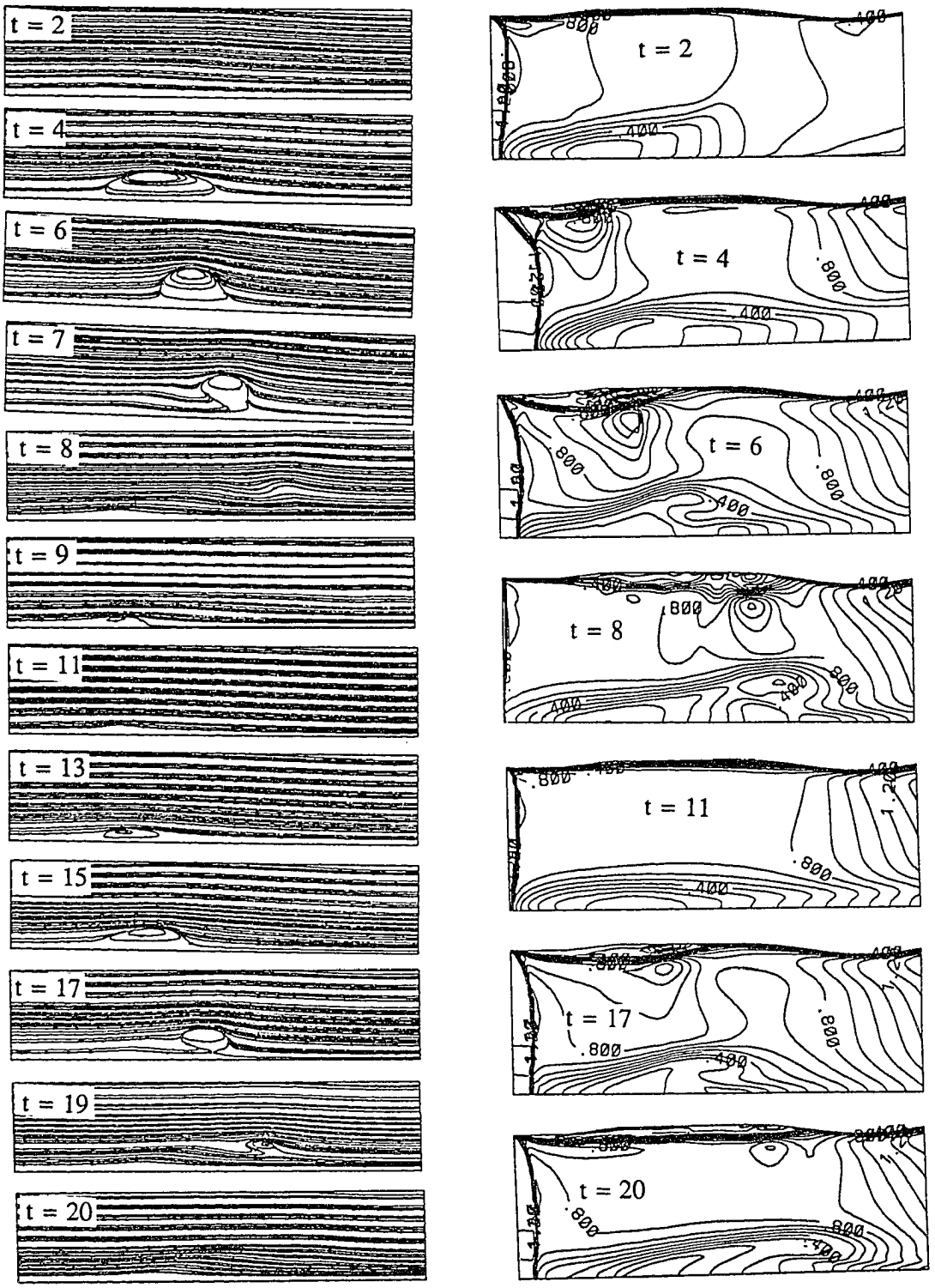

Figure 6.18 Streamlines and Mach contours for a swirling flow with a transient multi-bubble breakdown, $M_\infty = 1.75$, $\beta = 0.30$ and $R_e = 10,000$.

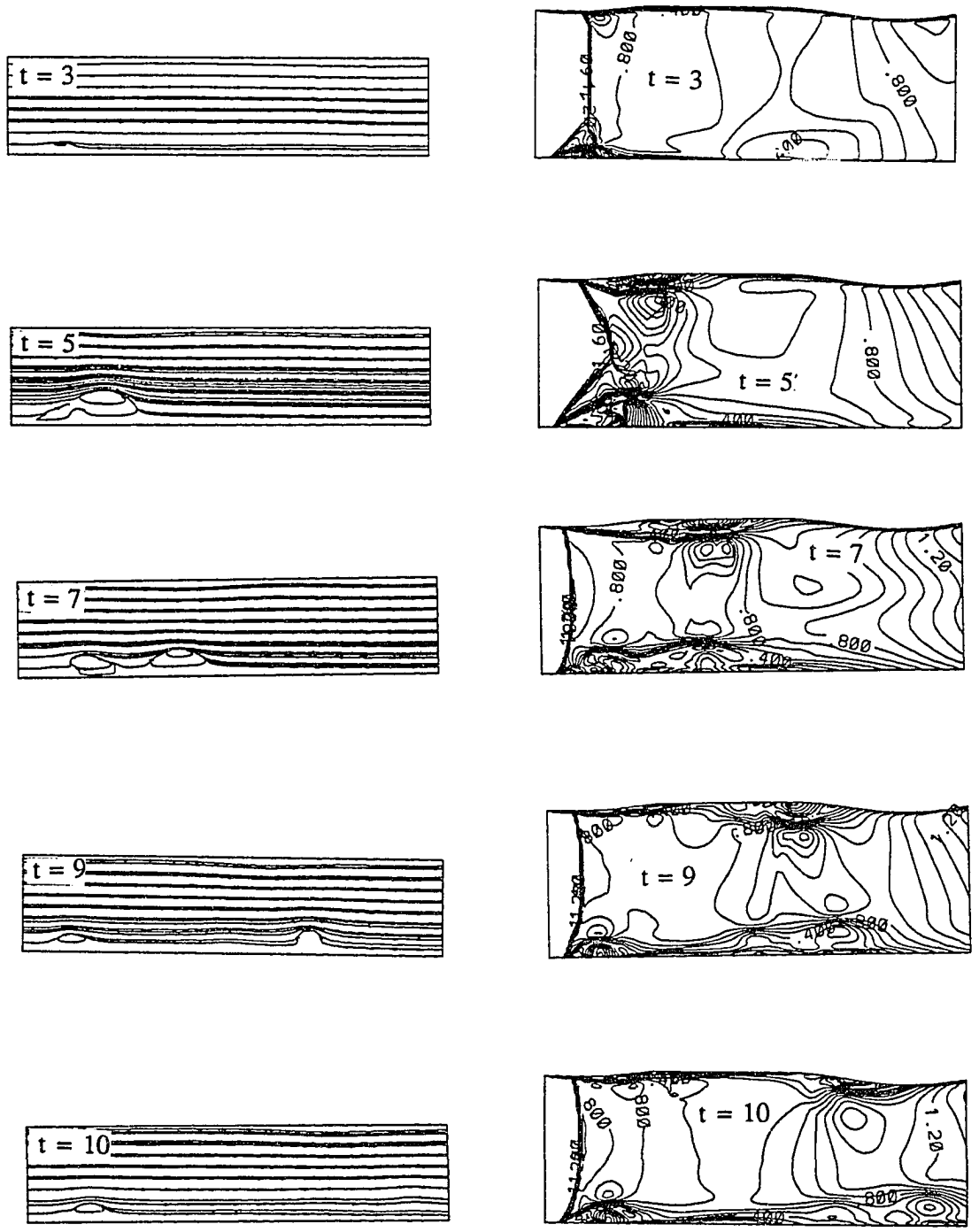

Figure 6.19 Streamlines and Mach contours for a swirling flow with unsteady multi-bubble breakdowns, $M_\infty = 1.75$, $\beta = 0.15$ and $R_e = 100,000$.

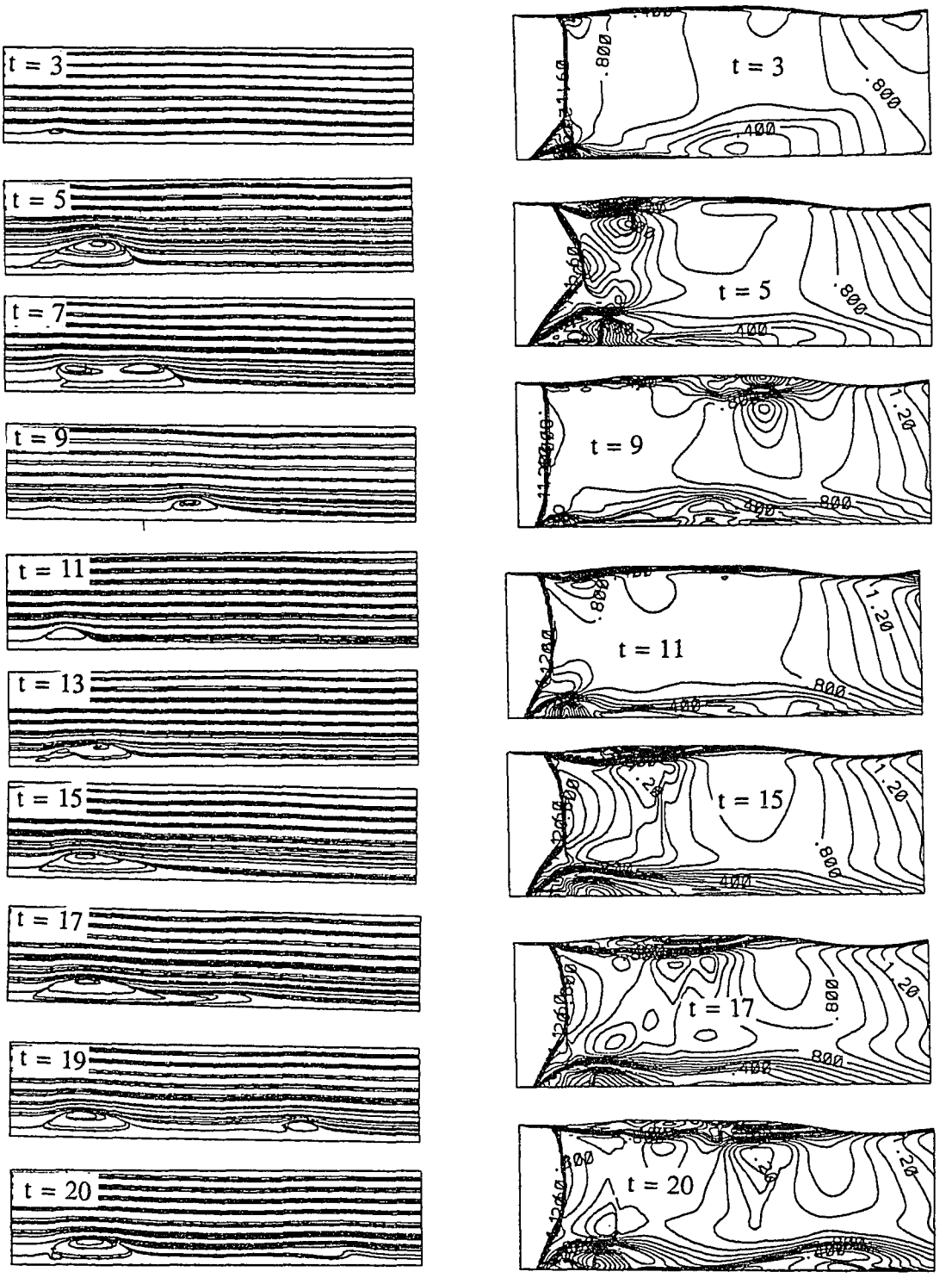

Figure 6.20 Streamlines and Mach contours for a swirling flow with unsteady multi-bubble breakdowns, $M_\infty = 1.75$, $\beta = 0.2$ and $R_e = 100,000$.

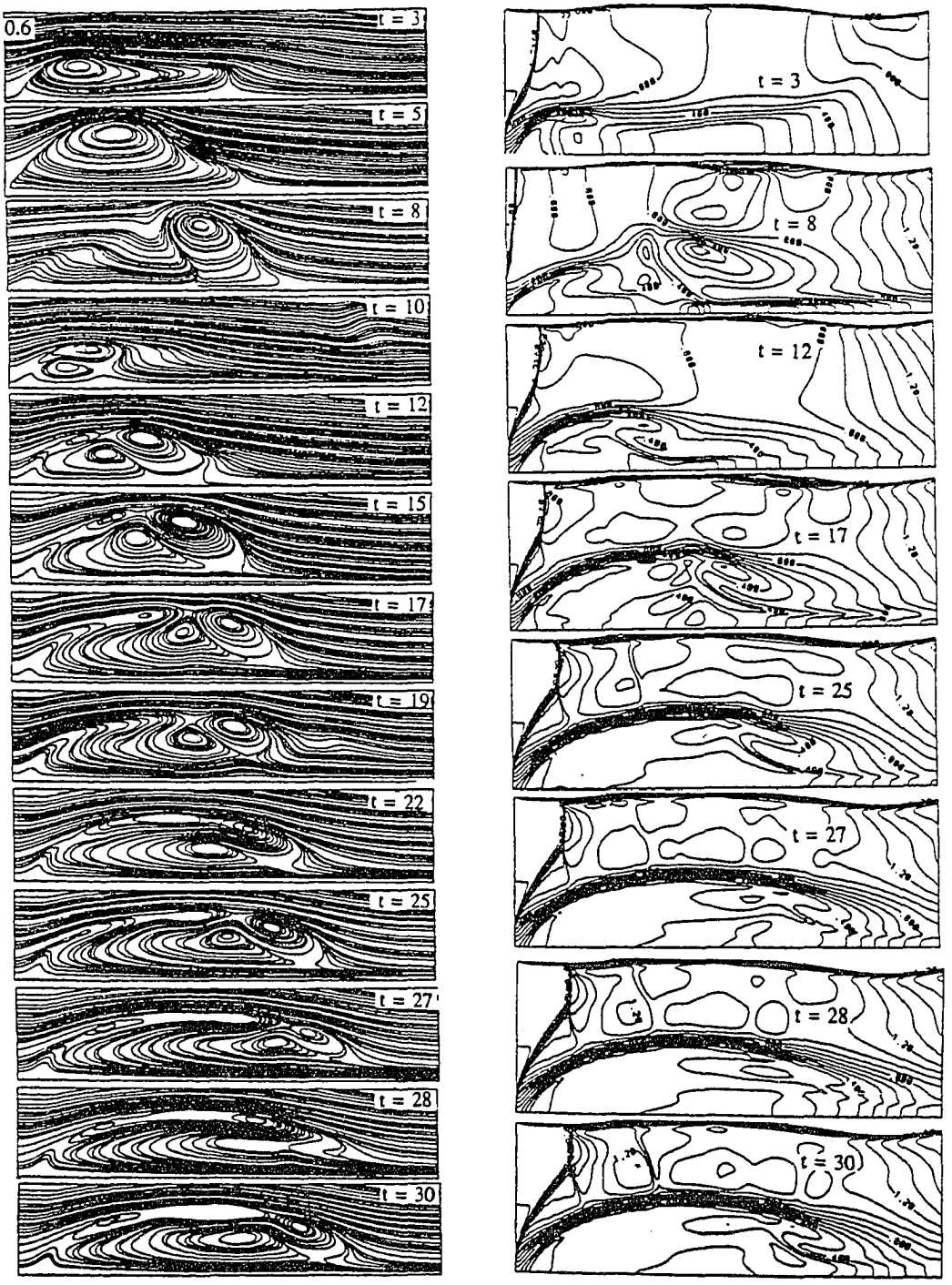

Figure 6.21 Streamlines and Mach contours for a swirling flow with unsteady multi-bubble breakdowns, $M_\infty = 1.75$, $\beta = 0.38$ and $R_e = 100,000$.

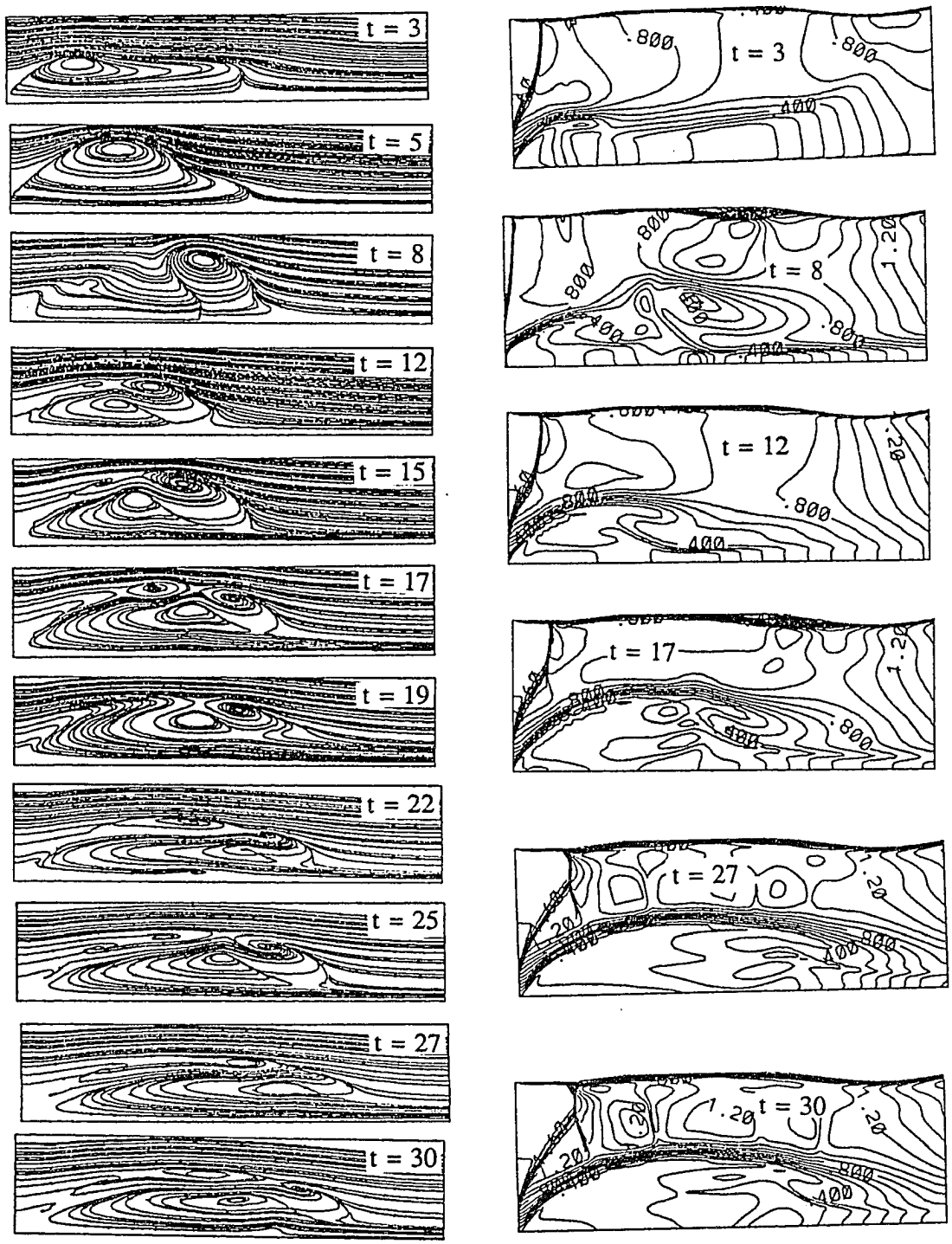

Figure 6.22 Streamlines and Mach contours for a swirling flow with multi-bubble breakdowns, $M_\infty = 1.75$, $\beta = 0.44$ and $R_e = 100,000$.

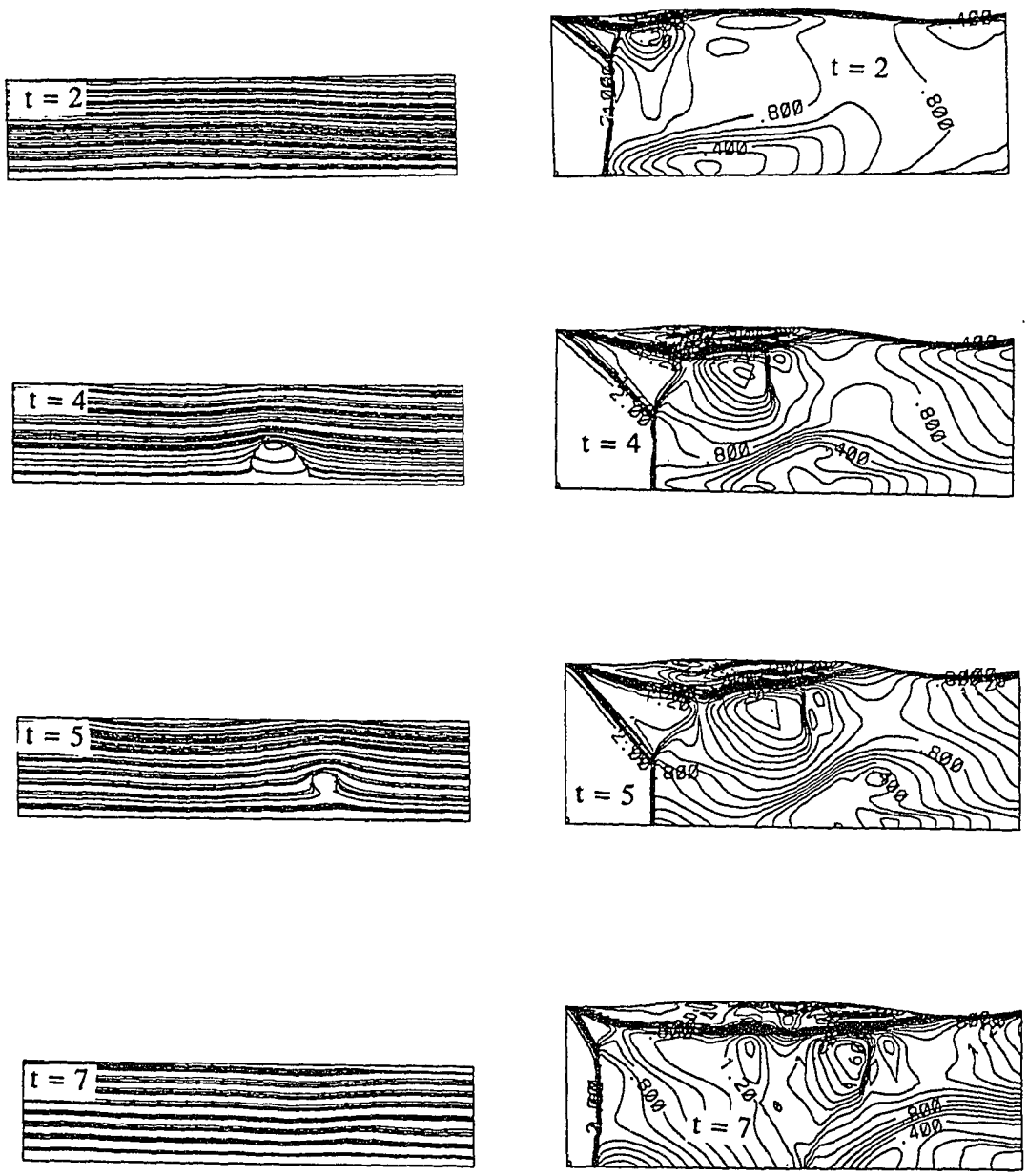

Figure 6.23 Streamlines and Mach contours for a swirling flow with a transient single-bubble breakdown, $M_\infty = 2.0$, $\beta = 0.26$ and $R_e = 10,000$.

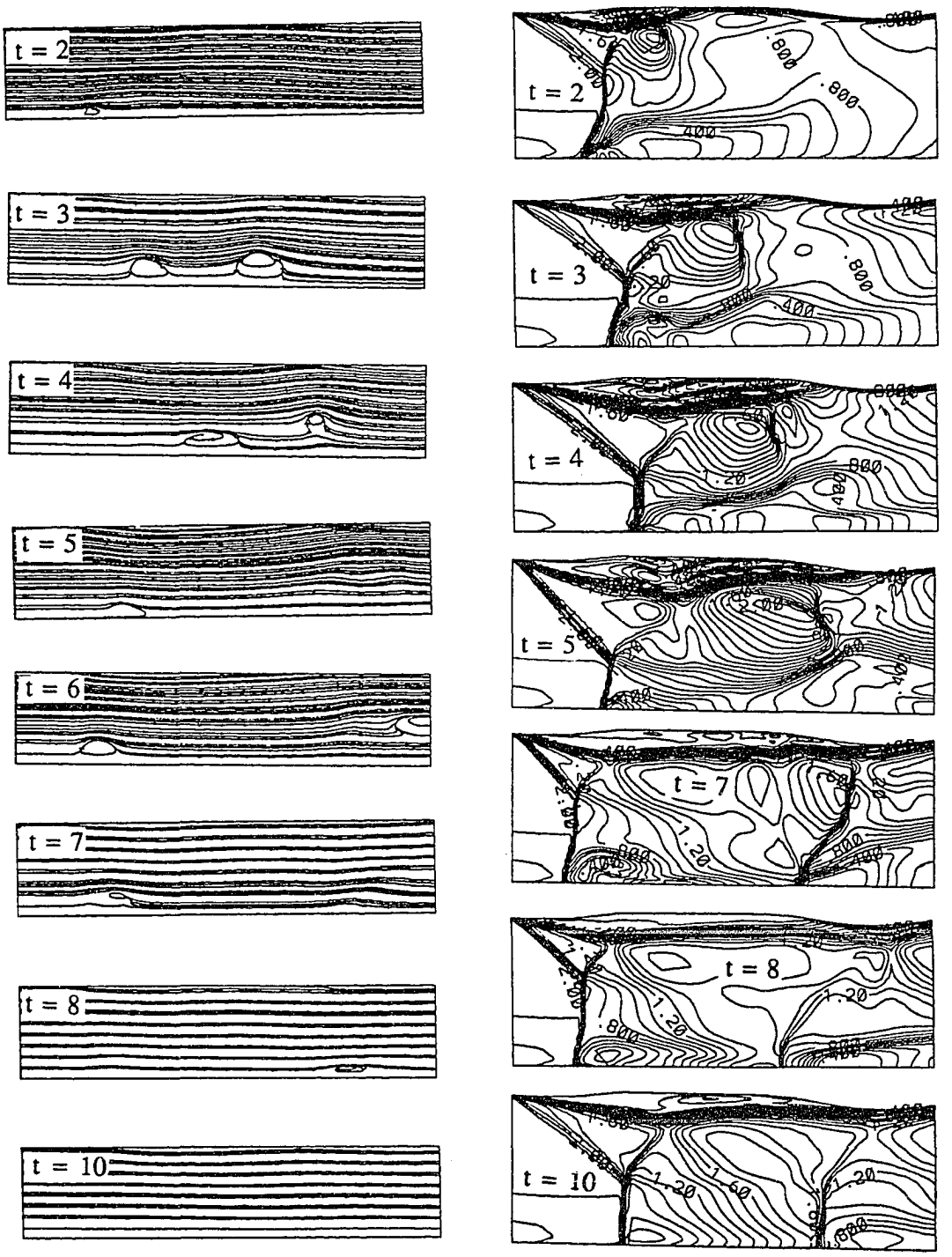

Figure 6.24 Streamlines and Mach contours for a swirling flow with a transient multi-bubble breakdown, $M_\infty = 2.25$, $\beta = 0.26$ and $R_e = 10,000$.

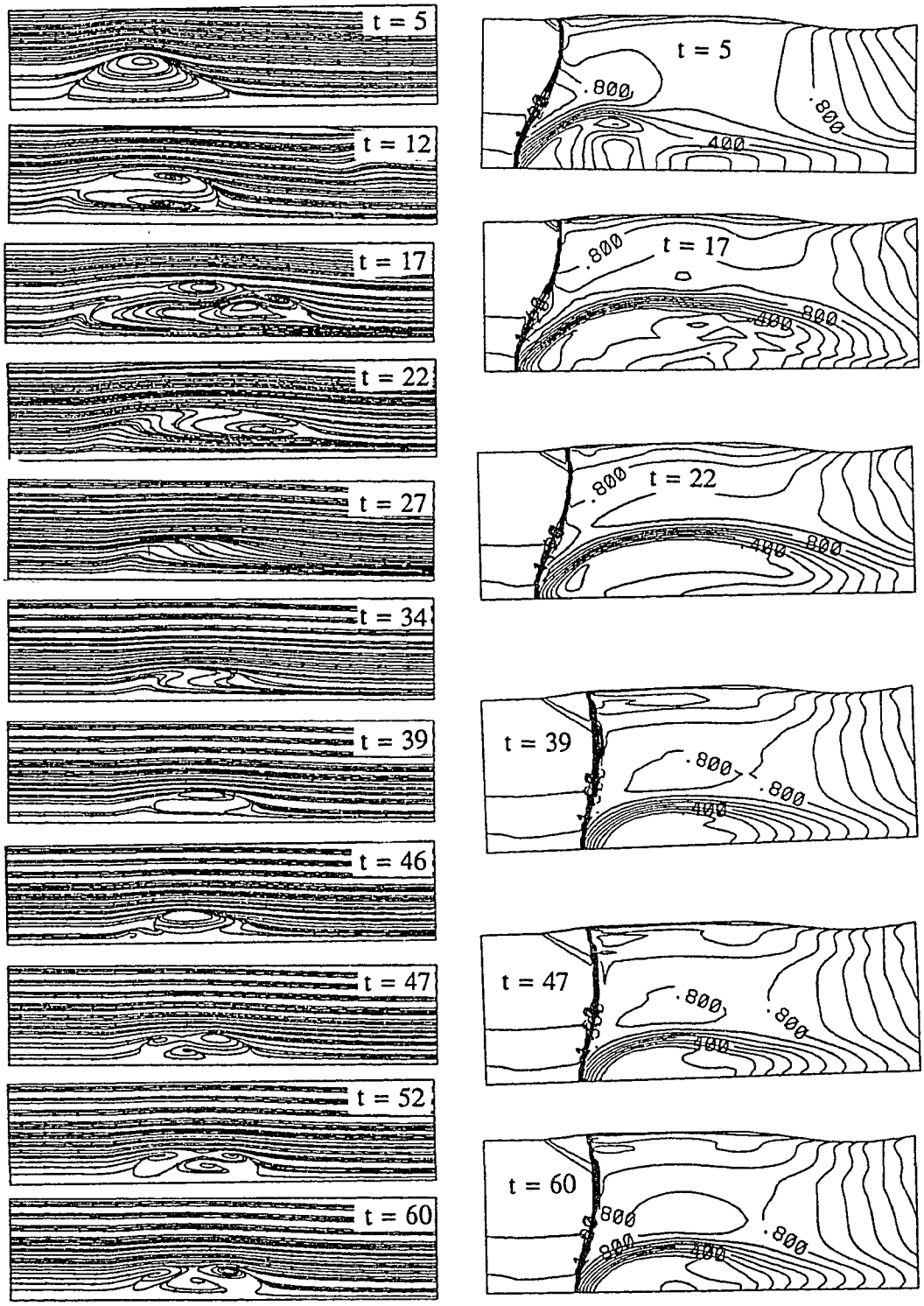

Figure 6.25 Streamlines and Mach contours for a swirling flow in a duct with an inviscid-wall, $M_\infty = 1.75$, $\beta = 0.32$ and $R_e = 10,000$.

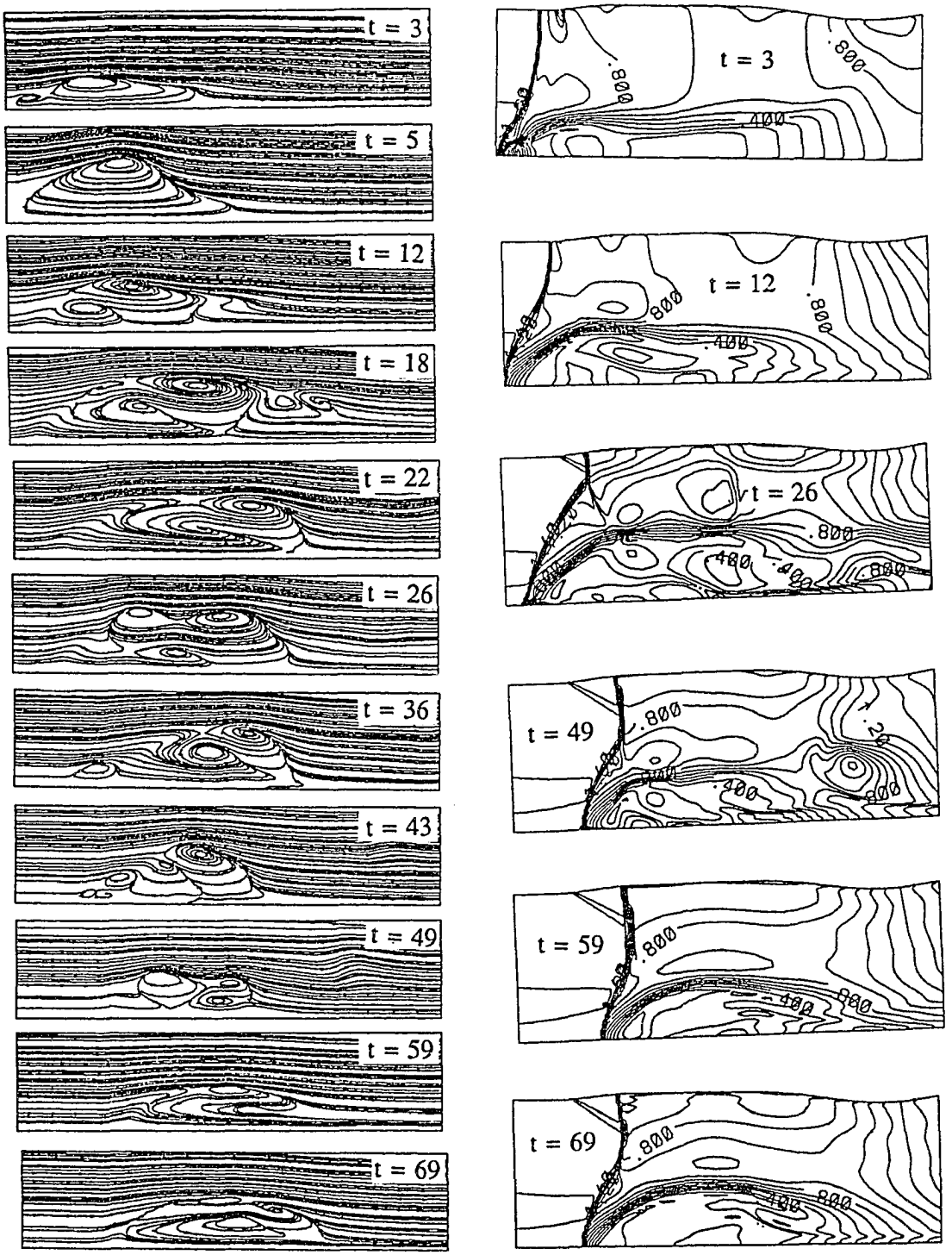

Figure 6.26 Streamlines and Mach contours for a swirling flow in a duct with an inviscid-wall, $M_\infty = 1.75$, $\beta = 0.32$ and $R_e = 100,000$.

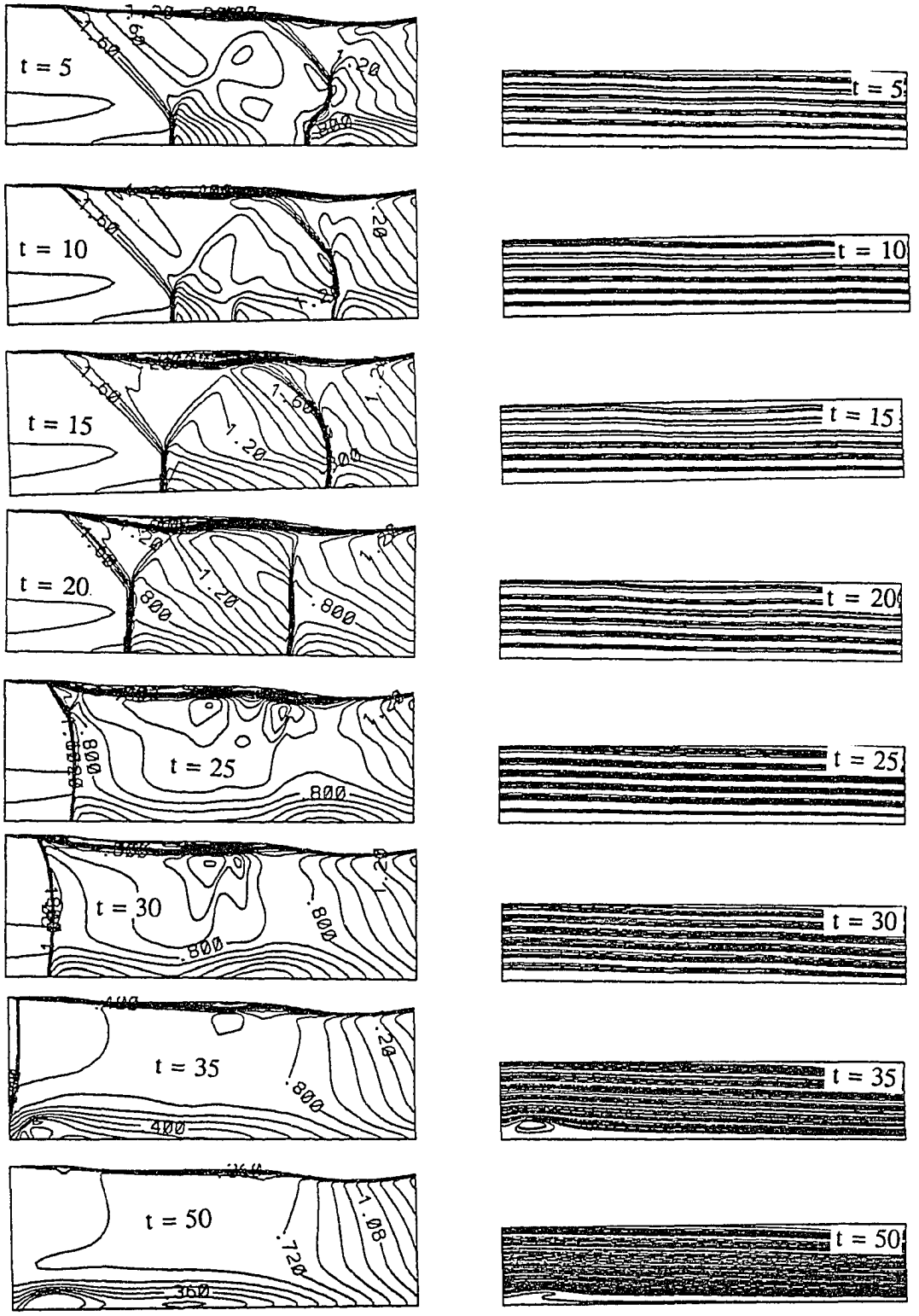

Figure 6.27 Streamlines and Mach contours for a swirling flow with a transient single-bubble breakdown, $M_\infty = 1.75$, $\beta = 0.32$ and $R_e = 100,000$ with a wedge angle of 6°.

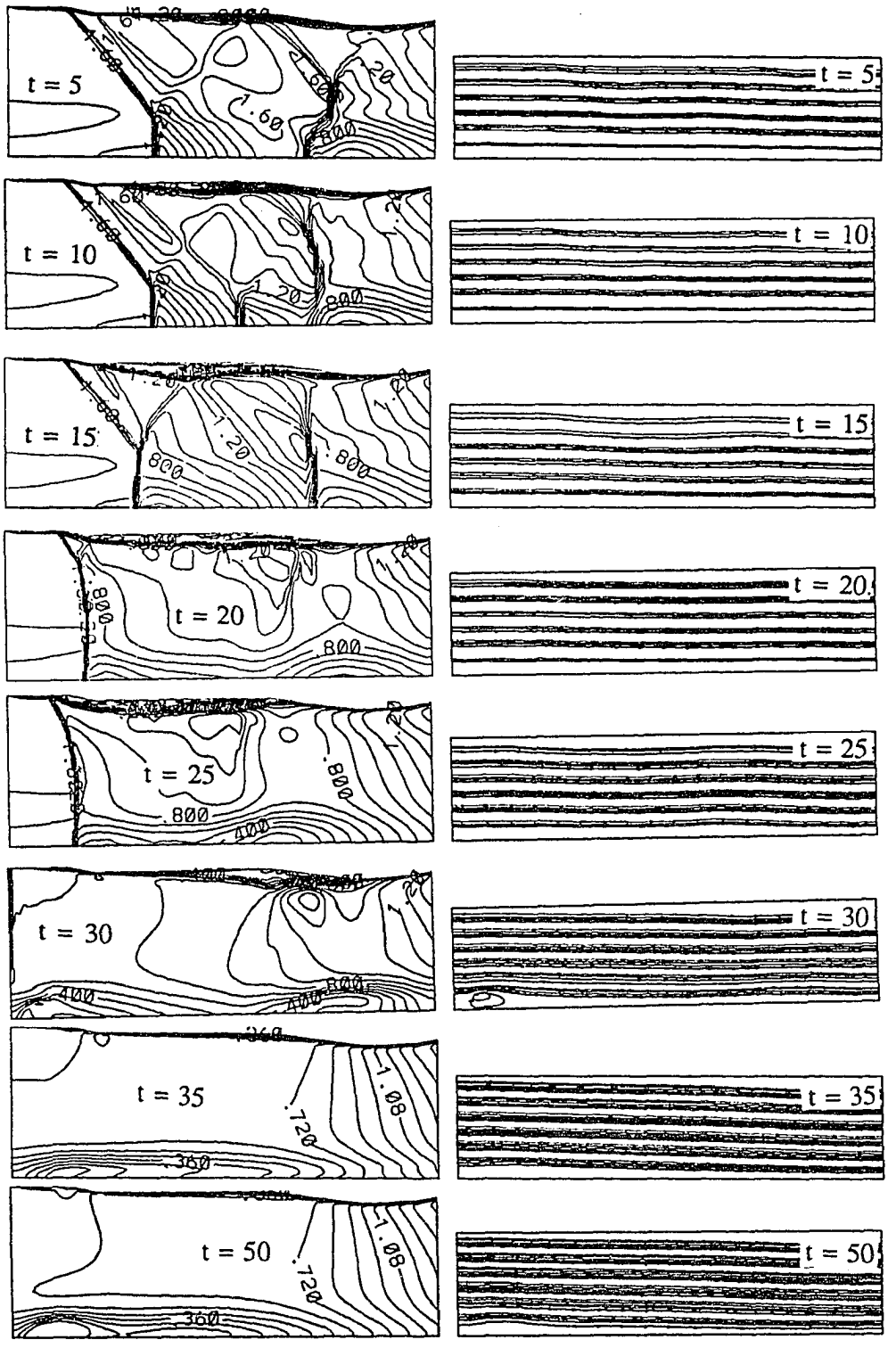

Figure 6.28 Streamlines and Mach contours for a swirling flow with a transient single-bubble breakdown, $M_\infty = 1.75$, $\beta = 0.32$ and $R_e = 100,000$ with a wedge angle of 10°.

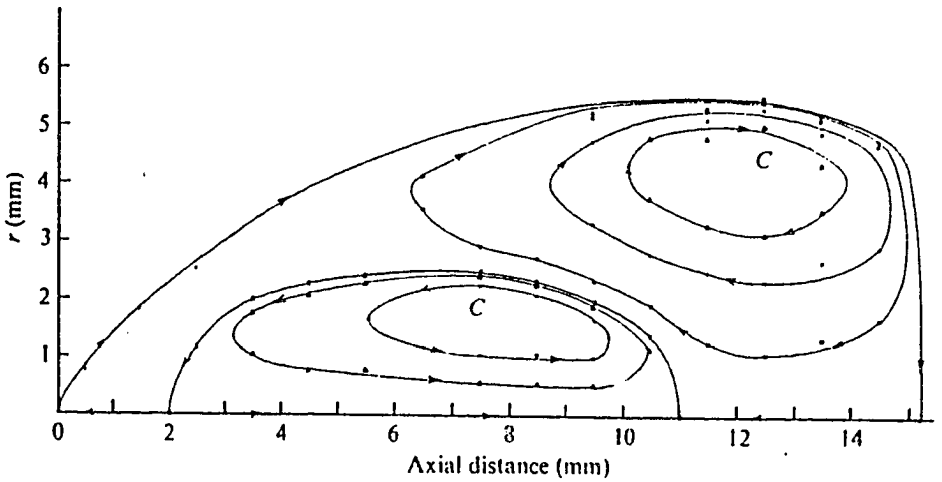

Figure 6.29 The mean experimental streamline pattern inside the breakdown. The C's denote the centers of the recirculation cells, [39].

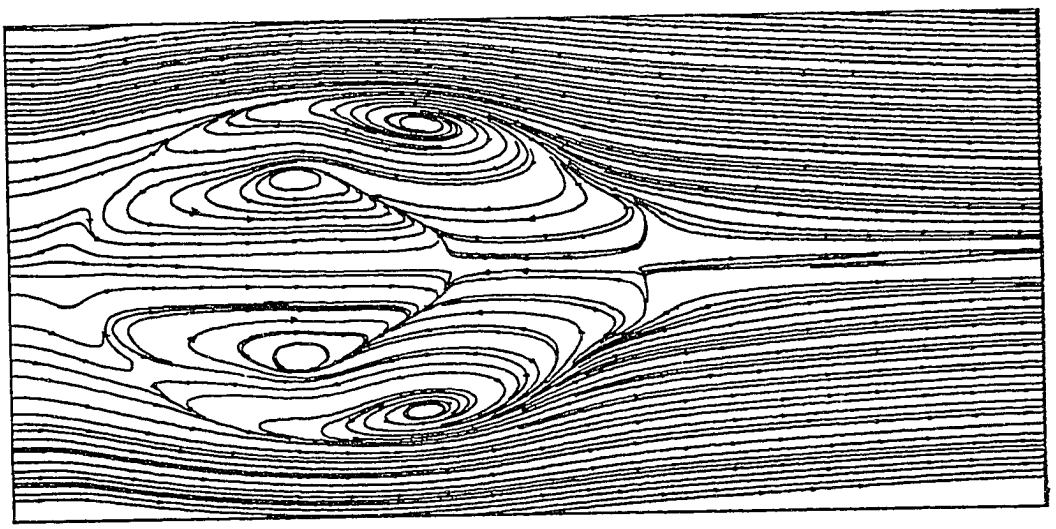

Figure 6.30 The computational streamline pattern inside the breakdown for the flow case of R_e = 100,000, M = 1.75 and β = 0.32 at t = 125.

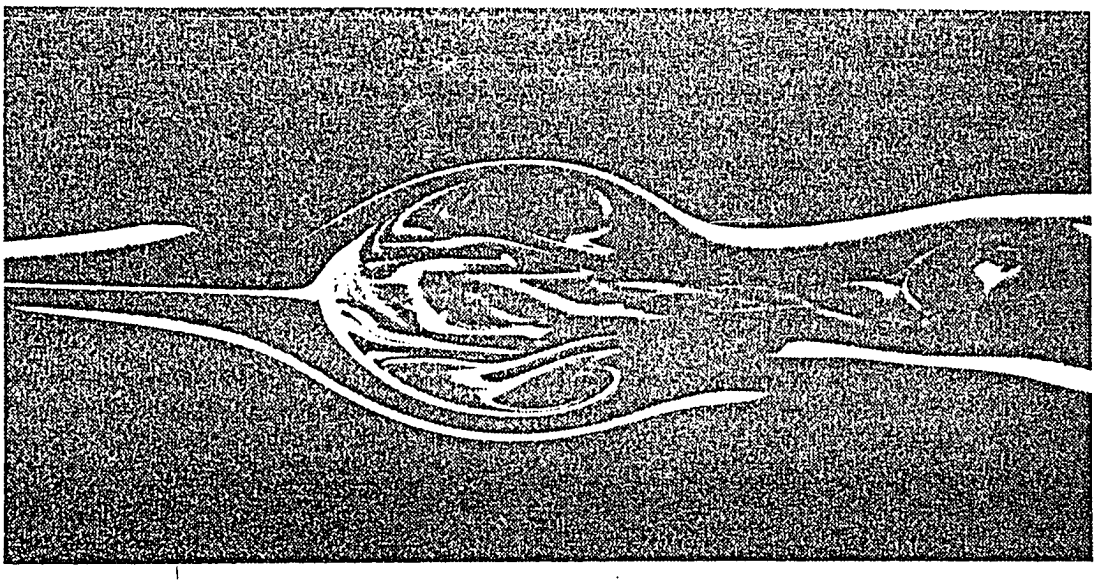

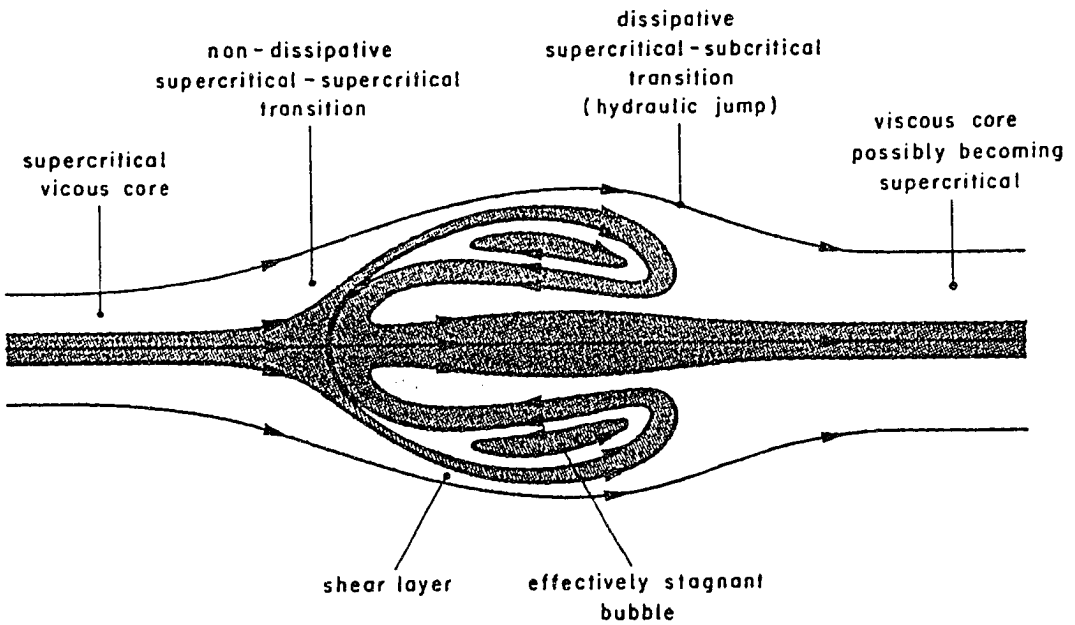

Figure 6.31 Photograph and Schematic representation of axisymmetric (bubble) vortex breakdown, [12]

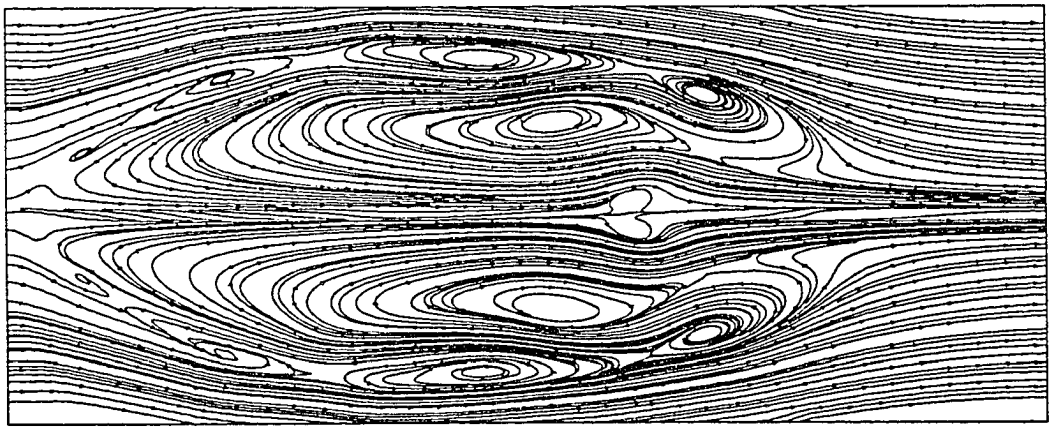

a: flow case of R_e = 100,000, M = 1.75 and β = 0.44 at t = 30

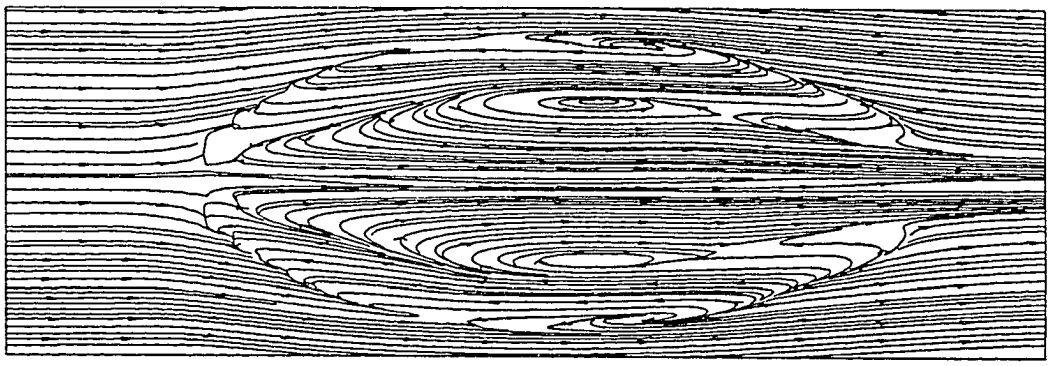

b: flow case of the Euler solution with M = 1.75 and β = 0.32 at t = 69

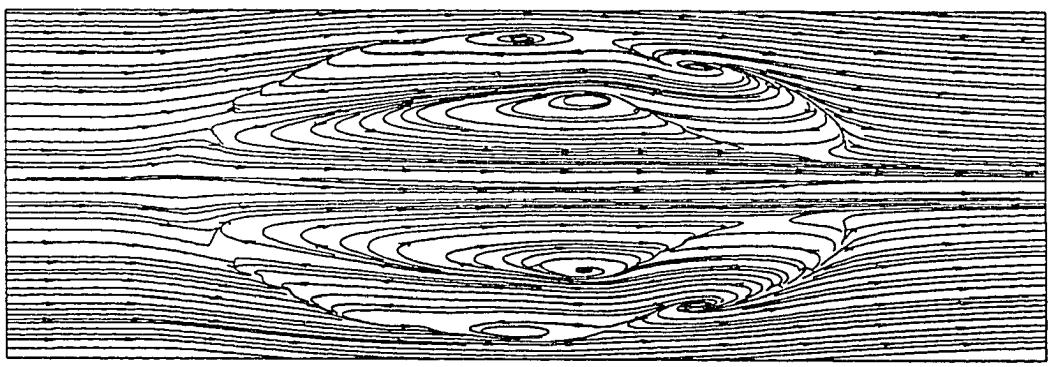

c: flow case of R_e = 100,000, M = 1.75 and β = 0.32 using inviscid wall boundary contions at t = 30

Figure 6.32 Computational streamline patterns for quasi-axisymmetric flow cases with stable vortex-breakdown structures.

CHAPTER 7
INTERACTION OF A SUPERSONIC SWIRLING JET AND A SHOCK WAVE

7.1 Introduction

In this Chapter, the interaction of a supersonic swirling jet, issued from a convergent-divergent nozzle in a supersonic uniform nonswirling flow with lower Mach number, and a normal shock wave is studied. First, the computational domain and the grid used are presented. Then, the boundary and initial conditions, with the simplifying assumptions used, are presented. Finally, some numerical results, in forms of Mach number contours and streamlines at different time levels, are shown. The study of this problem was motivated by the importance of the vortex breakdown phenomenon resulting from the vortex-shock interaction in enhancing the mixing in combustion chambers and the availability of some experimental measurements that can be used as inflow profiles, (see Metwally, et al. [88]). The literature lacks this kind of computational study as described in Chapter 2.

7.1.1 The Computational Domain

The flow is assumed quasi-axisymmetric and hence the computational domain consists of two meridian planes. The angle between the two planes was chosen so that a certain aspect ratio could be satisfied for all the grid cells, for stability purposes. The nozzle exit radius is chosen to be the characteristic length and the domain extends radially to r = 3.5 and axially to x = 7.0 to ensure freestream conditions at the outer boundaries. The grid consists of 51x221x2 points in the radial, axial and cross-flow planes, respectively. The

grid points are clustered around the vortex axis for good resolution of the vortex core and near the nozzle exit, in the axial direction, for good resolution of the vortex/shock interaction region. In both cases an algebraic function was used to cluster the grid points, see Reference [111]. The minimum grid cell side length in the radial direction is taken to be 0.013 and the minimum grid cell side length in the axial direction is 0.014. The computational domain is shown in Fig. 7.1.

7.2 Initial and Boundary Conditions

7.2.1 Initial Conditions

The supersonic swirling jet is issued from a supersonic nozzle in a uniform flow. So that the computations started with freestream initial conditions everywhere in the computational domain. The freestream conditions are isentropic conditions corresponding to a Mach number of 2.0 with experimentally measured wind-tunnel values for the stagnation pressure and temperature. At the first axial station, outside of the nozzle exit, the axial velocity is set equal to the freestream velocity while the radial and tangential velocities are set equal to zero. The freestream density is calculated from the equation of state using the freestream values of the pressure and temperature.

7.2.2 Boundary Conditions

For the inlet-boundary conditions, experimental profiles reported in References [88] and [112] are used at the first axial station. The experimental results are used from the vortex axis, r = 0, to the nozzle exit radius, r = 1.0. For the radial distance from r = 1.0 to the outer radius, r = 3.5, the wind-tunnel freestream conditions are used. The profiles are shown in Fig. 7.2

At the axis of symmetry, r = 0.0, quasi-axisymmetric boundary conditions are used as follows; rigid-body rotation assumption is used and hence the tangential velocity

component is set equal to zero, no source or sink at the axis leads to zero radial velocity component and the other flow variables; axial velocity, density and static pressure, are assumed to be symmetric around the axis and hence their centerline partial derivatives in the radial direction are zero.

At the outer boundary, r = 3.5, wind-tunnel freestream profiles are used. No boundary conditions are needed at the vortex core outer radius, r = 1.0, because it is included in the computational domain and the conditions are obtained as a part of the solution.

At the outflow boundary, two types of boundary conditions are used and the results are compared in section 7.4. The first type of boundary condition is the extrapolation of all the flow variables from interior. It was intended that the flow at the exit section would be supersonic and in this case the extrapolation boundary conditions are exact. But it was found that sometimes the flow at a small portion of the exit boundary was subsonic. In this case, using the extrapolation boundary conditions is not proper according to the theory of characteristics. The use of them can be interpreted physically as the flow properties do not change in the axial direction beyond the exit boundary. This assumption can safely be used if the exit boundary is far away from the recirculation zone. The second type of boundary conditions used at the exit boundary was the standard Riemann-invariant-type boundary conditions. Four variables are extrapolated from inside the computational domain and the fifth variable is taken from the downstream conditions for the subsonic portion of the exit boundary.

For the cross-flow boundaries, quasi-axisymmetric flow conditions are used. The flow variables are assumed to be constant at any two meridian planes.

7.3 Computational Results

Figure 7.3 shows the time evolution of the vortex-breakdown-bubble system formed behind the shock wave. The results are shown in forms of streamlines, Mach number contours and axial variations of flow variables at the axis. The Mach-number contours, shown in Fig 7.3, are for a portion of the computational domain that extends axially from x = 0.0 to x = 1.99 and in the radial direction from r = 0.0 to r = 1.1 which is enough to show the important features of the flow field especially in the vortex-shock interaction and breakdown regions. The increment of the Mach-number contours is 0.1. The projections of the streamlines on the x-r plane are shown in Fig. 7.3 for an axial distance from x = 0.0 to x = 1.69 and a radial distance from r = 0.0 to r = 0.49.

Figure 7.4 shows the distributions of flow variables along the axis, r = 0.0. Shown are the distributions of the axial velocity, u, the density, ρ, and the static pressure, p. The axial distance covers the whole length of the computational domain.

At t = 1.0, the supersonic jet issued at the inlet boundary did not reach the end of the computational domain. The formation of a normal shock wave is noticed at x = 0.4 where the axial velocity at the axis dropped from a supersonic value of 2.3 to a negative value of -1.9 just behind the shock. The shock system is very complicated as shown in Fig. 7.3. The streamlines show the formation of a small bubble behind the central part of the shock wave. This bubble is responsible for the deformation of the shock near the axis.

At t = 2.0, the jet front reached an axial distance of 4.0 and the vortex breakdown region enlarged in the axial and radial directions, where multiple bubbles could be recognized. Figure 7.4 shows two regions of negative axial velocity at the axis. It is noticed that the shock wave was shaped accordingly with the change in the bubble shape.

At t = 3.0, the multiple-bubble system combined in one long bubble. The distribution of the axial velocity shows the reversed flow region covers the axial distance from x = 0.0 to x = 1.0. The small bubble formed at t = 2.0, just behind the shock wave, pushed the lower part of the shock upstream. The breakdown region can be seen from the streamlines and Mach-number contours in Fig. 7.3. The formation of a shock wave inside the bubble can be seen from the variation of the axial velocity at r = 0.0 in Fig. 7.4 and the total Mach-number contours in Fig. 7.3.

At t = 4.0, Fig. 7.3 shows that the narrow reversed flow region behind the shock wave expanded in the radial direction and the shock wave was shaped accordingly. Two regions of negative axial velocity can be recognized because of the shock wave formation inside the bubble. The Mach-number contours show the formation of a large bubble starting at x = 0.0 and show the effects of the shock system inside the bubble at the vortex axis. The shock system was not strong enough to cause a flow separation analogous to that on a delta wing.

At t = 5.0, the shock system inside the vortex breakdown bubble became stronger. The axial velocity variation shows two regions of negative axial velocities separated by a positive velocity region. The streamlines show the formation of three recirculation regions, two with a clockwise rotational direction separated by a counter-clockwise circulating bubble. The Mach-number contours show the counter-clockwise bubble to occur just upstream of a strong shock wave at the vortex axis. It may be looked at as a separation caused by the shock wave. In that sense, the reversed flow of the bubble to the right interacted with the shock wave which caused the flow to separate forming a recirculation region behind the shock wave.

The formation of a three-bubble region behind the shock wave can also be seen at t = 7.0. The Mach contours show the movement of the shock wave downstream as a

result of the reduction in the size of the bubble system .

At t = 9.0, the streamlines show the first and third bubbles to be combined in one long bubble while the second bubble became very weak. The axial velocity distribution shows that the region of positive velocity corresponding to the second bubble became very small.

At a later time level, t = 10.0, the second bubble disappeared and the shock wave inside the bubble system became weak. Only one vortex breakdown bubble could be seen.

At t = 12.0, the shock system inside the bubble gained some strength and a region of separation could be recognized from Fig. 7.4. Figure 7.5 shows a region of positive axial velocity separating two negative axial velocity regions.

The combination of the first and third bubbles and the disappearance of the second bubble, noticed at t = 9.0 and t = 10.0, respectively, can also be seen at t = 13.0 and t = 14.0.

The process of the formation of three bubbles, combination of the fist and third bubbles in one bubble and then disappearance of the second bubble with the weakening of the shock system was repeated in a periodic manner and some cycles can be recognized at t = 18, 19 and 20, t = 24, 25 and 26 and t = 38, 39 and 40.

It was noticed that the position of the shock wave is slightly oscillating around a mean position of x = 0.25. The formation of the three-bubble system was repeated until t = 60.0.

At t = 62.0, the shock system and the bubble behind it moved upstream towards the inlet boundary. It is noted that the axial velocity was negative along the whole vortex axis (not shown). From the Mach contours, it is noted that the negative velocity extends for a very narrow region in the radial direction. At the outflow section, the flow was

supersonic from r = 0.1 to the outer radius of the computational domain, r = 3.5. The bubble size became very large compared to those at earlier time levels. The streamlines show the formation of one large bubble while the Mach contours show a weak shock wave inside the bubble. The shock-bubble system moved downstream away from the inlet boundary at t = 64. The oscillation of the shock-bubble system and the formation of the three-bubble system continued to occur periodically. The computations continued until t = 100. Snapshots are shown at t = 98 and t = 100.

7.4 Effects of the Downstream Boundary Conditions

In the first example, the outflow boundary conditions were obtained by extrapolating all the flow variables from interior cell centers. According to the theory of characteristics, extrapolating all the variables is exact only for supersonic outflow. It was noticed that the flow in a small portion of the exit section was subsonic. It was also noticed that, at higher dimensionless time levels, a very narrow area of negative axial velocity existed at the exit section. In the cases of subsonic or reversed flows, the extrapolation of all variables from interior is not proper. In the subsonic flow regions, one of the variables should be extrapolated from outside the computational domain. Riemann-invariant-type boundary conditions were used and the results are compared with those of the extrapolation boundary conditions.

Snapshots of the results are shown in Fig. 7.5 and Figure 7.6. Fig. 7.5 shows the streamlines and Mach number contours and Fig. 7.6 shows the axial variation of the axial velocity, the static pressure and the density along the axis, r = 0.0.

The snapshots at time levels from t = 1.0 to t = 5.0 show no difference between the present solution and that of the extrapolation boundary conditions. Snapshots at t = 18, 19 and 20 show the same structure of the vortex breakdown bubbles and the shock

system as in the previous case. The only difference was in the axial velocity distribution where we noticed that the axial velocity at the exit section was always positive and it was tending to match the velocity outside the computational domain. This affected only a very small portion of the computational domain and did not affect the interaction region.

As time goes by, the effect of the exit boundary conditions extended upstream in the computational domain. To make a proper comparison, the results of the two types of exit boundary conditions are shown in Fig. 7.7 and 7.8 side by side where the results of the extrapolation are shown on the right and the Riemann-type are shown on the left. At time levels from t = 53 to t = 59, a slight difference could be noticed. The axial velocity is almost constant downstream of the vortex breakdown bubble in the case of extrapolation boundary conditions but in the case of Riemann-type boundary conditions it was increasing to match a higher value outside the computational domain. A slight difference can be noticed in the size of the three-bubble system behind the shock wave.

Starting at t = 61.0, more significant differences could be seen where the shock wave and vortex breakdown system moved upstream towards the inlet section in the case of the extrapolation boundary conditions while the shock wave was fixed in the present case. The bubble size was enlarged in the extrapolation case and the size was constant in the present case. This can be explained by the aid of the axial velocity variation where no inflow occurred at the exit section in the case of Riemann-type boundary conditions as was the case with the extrapolation boundary conditions. The motion of the bubble system, in the case of the extrapolation boundary conditions, pushed the shock wave front outside the computational domain, which was not the case with the Riemann-type boundary conditions. The formation of the three-bubble system at t = 63 is shown in Fig. 7.7. The difference in the bubble sizes was clear and also the level of the negative axial velocity along the axis. As the computations advanced in time, a shift in the

period of occurrence of the three-bubble vortex breakdown was noticed. At t = 73, one bubble is shown for the extrapolation boundary conditions while a small bubble with counter-clockwise rotational direction was located at the axis in the case of Riemann-type boundary conditions. The same result was noticed at t = 75 where three bubbles were formed in one case and only one bubble was formed in the other case.

The observations can be summarized in the following points: 1. At early time levels where the flow at the exit section was supersonic, no differences were noticed between the results of the two cases. 2. When a small portion of the exit section became subsonic, slight differences could be noticed in the variation of the axial velocity but this did not affect the shock-vortex zone structure. 3. When a very narrow portion of the of reversed flow existed near the axis in the case of extrapolation boundary conditions, large differences were noticed because the axial velocity was always positive at the exit section in the case of Riemann-type boundary conditions. These differences include differences in the size and location of the vortex breakdown bubbles, and 4. As the computations were advanced in time, some differences in the period and timing of bubble formation were noticed.

It is concluded that the Riemann-type boundary conditions represent the physical and mathematical boundary conditions better than the extrapolation boundary conditions for subsonic flows.

7.5 Effects of Reynolds Numbers

Figure 7.9 shows snapshots of a quasi-axisymmetric vortex breakdown of a supersonic jet issued from a supersonic nozzle at Mach number of 3.0 in a uniform wind-tunnel supersonic flow at Mach number of 2.0. The inflow profiles are the same as in the previous cases except for the Reynolds number. The Reynolds number in the present

case was 100,000. In Fig. 7.9, the streamlines and Mach-number contours are shown for time levels from t = 2.0 to t = 30.0. The axial distributions of the axial velocity, static pressure and density along the axis are shown in Fig. 7.10. Extrapolation boundary conditions were used for the outflow boundary. The effects of the Reynolds numbers are shown by comparing the present results with the corresponding results at R_e = 296,000 shown in Fig. 7.3 and can be summarized in the following points: 1. In the initial time steps, it was noticed that the oscillations of the shock system were smaller in the present case. At t = 4.0, the shock wave reached the inlet section in the case of higher Reynolds number while in this case it stayed at x = 0.15 from the inlet section. For time levels from t = 6 to t = 30, the shock wave location was fixed for both cases of Reynolds numbers, 2. The development of the three-bubble system repeated periodically in time. It was noted that the streamlines at t = 10, 14, 18 and 22 were similar in the sense of the formation of a small separation bubble behind the shock wave inside the large bubble, and 3. From t = 16 to t = 22, the solutions of both cases show the cycle of the internal shock strengthening and the formation of a reversed supersonic flow with a small bubble in the opposite direction. It can be noticed that the size of the bubble system in the present case was smaller than that of the higher Reynolds number. Because of the higher dissipation level in the present case, the rate of the axial velocity decrease downstream of the bubble system was smaller. This can be seen from the variation along the axis. In the case of higher Reynolds number, the axial velocity at the exit section reached minimum values of 0.1 and 0.03 at time levels of t = 20 and t = 30, respectively, while in the present case a value of axial velocity of 0.5 was kept at the exit section which reduced the effects of the downstream disturbances.

7.6 Summary and Discussion

In this Chapter, the problem of a shock/vortex interaction in an unbounded domain was considered. A supersonic swirling jet was issued from a nozzle into a uniform supersonic flow of a lower Mach number. The mismatch between the pressure fields of the nozzle flow and the external flow generated a conical shock outside the nozzle. The flow was assumed to be quasi-axisymmetric. The results showed the effects of downstream boundary conditions on the vortex breakdown behind the shock wave. Extrapolation and Riemann-type boundary conditions were used and the results were compared. In the case of Riemann-type boundary conditions, the flow reached a nearly steady-state condition, while in the case of extrapolation boundary conditions, the vortex-breakdown bubbles were continuously oscillating while their sizes were changing. The effect of the Reynolds number was also investigated. It was shown that using small Reynolds numbers resulted in the production of vortex-breakdown bubbles of smaller sizes.

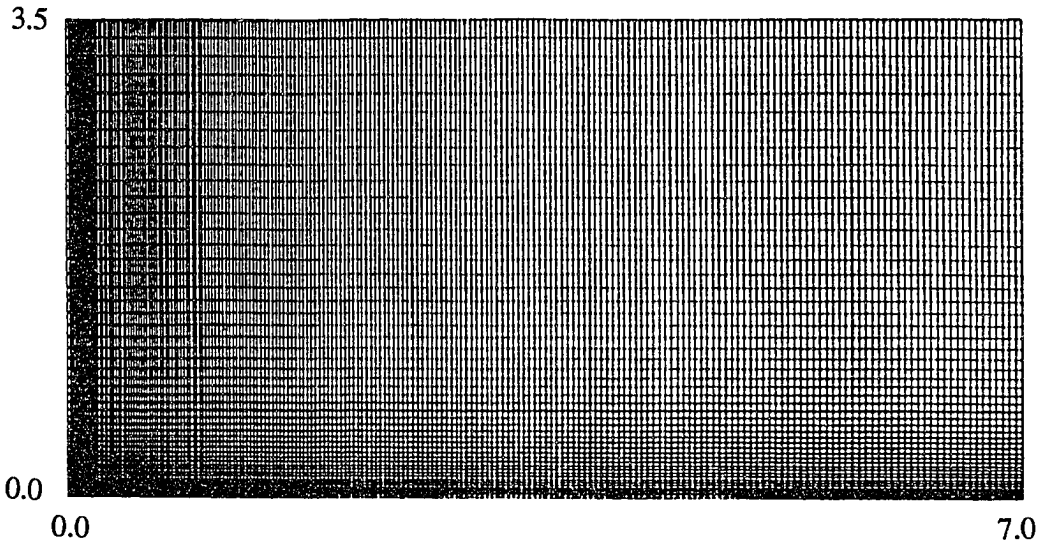

Figure 7.1 Typical grid for supersonic swirling jet from a nozzle, 221x51x2 grid points.

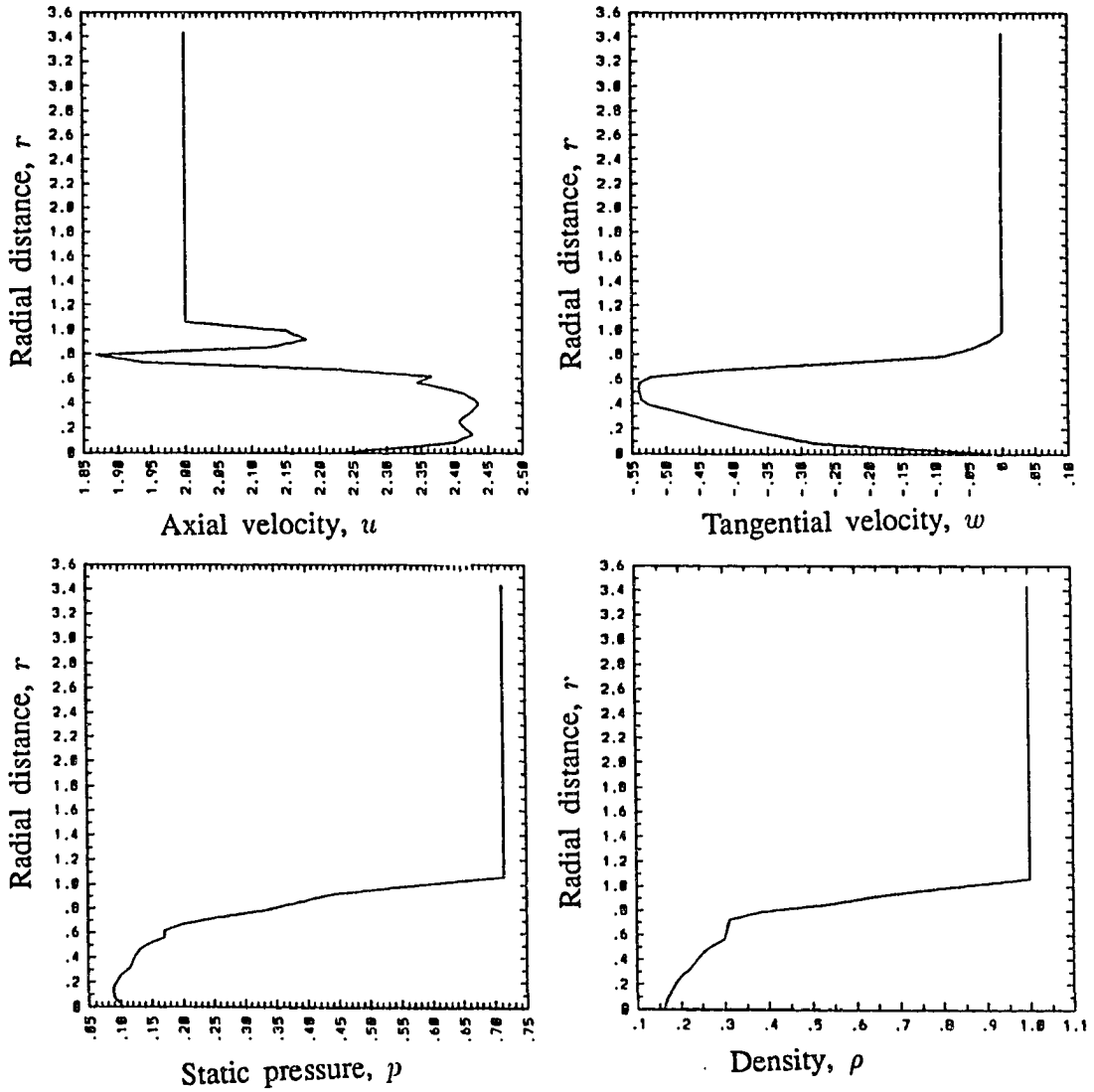

Figure 7.2 Quasi-axisymmetric flow profiles at x = 0.0 for supersonic swirling jet from a nozzle $M_j = 3.0$, $\beta = 0.22$.

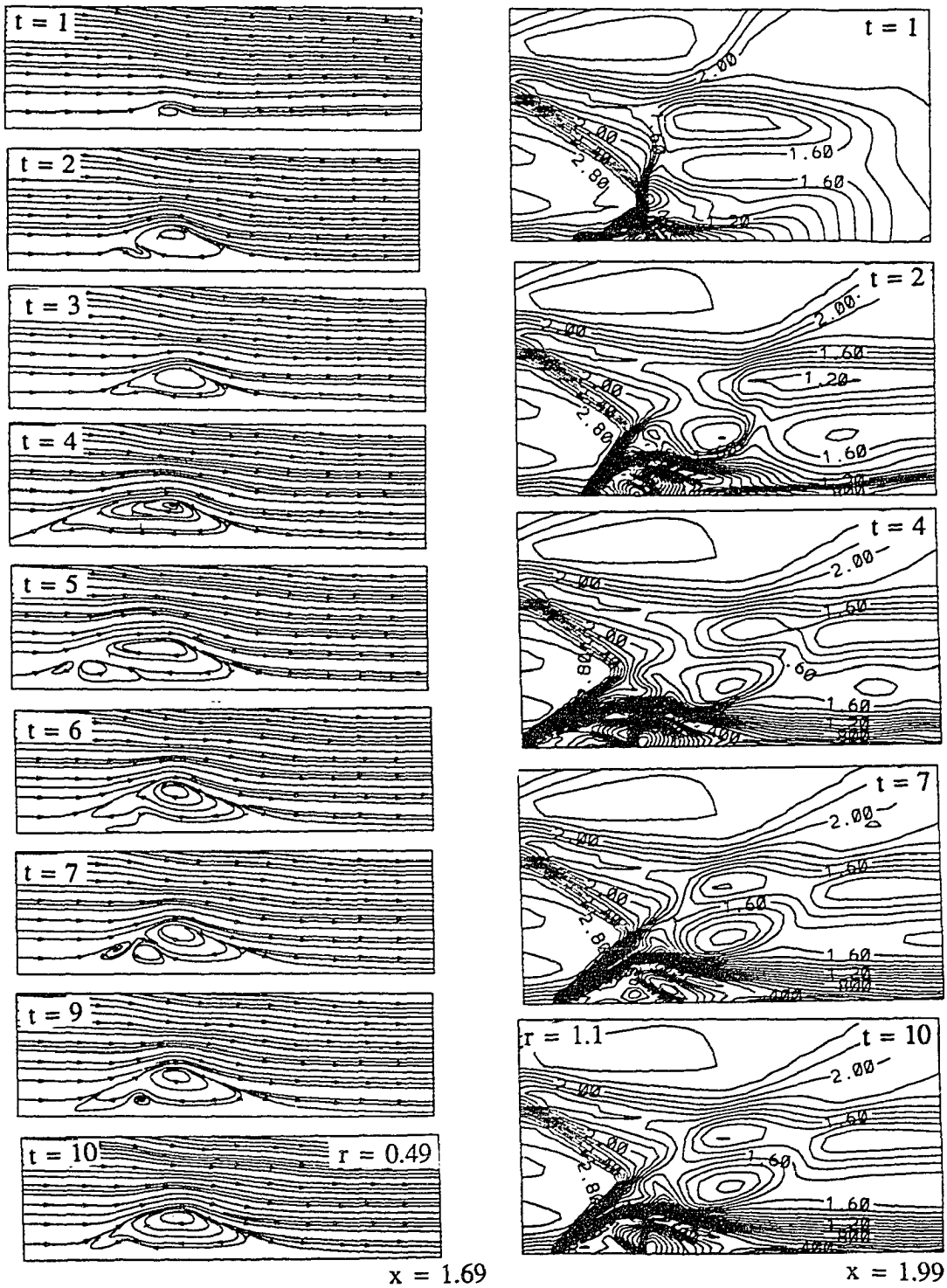

Figure 7.3 Streamlines and Mach contours for supersonic swirling jet from a nozzle with almost single-bubble vortex breakdown, extrapolation downstream boundary conditions.

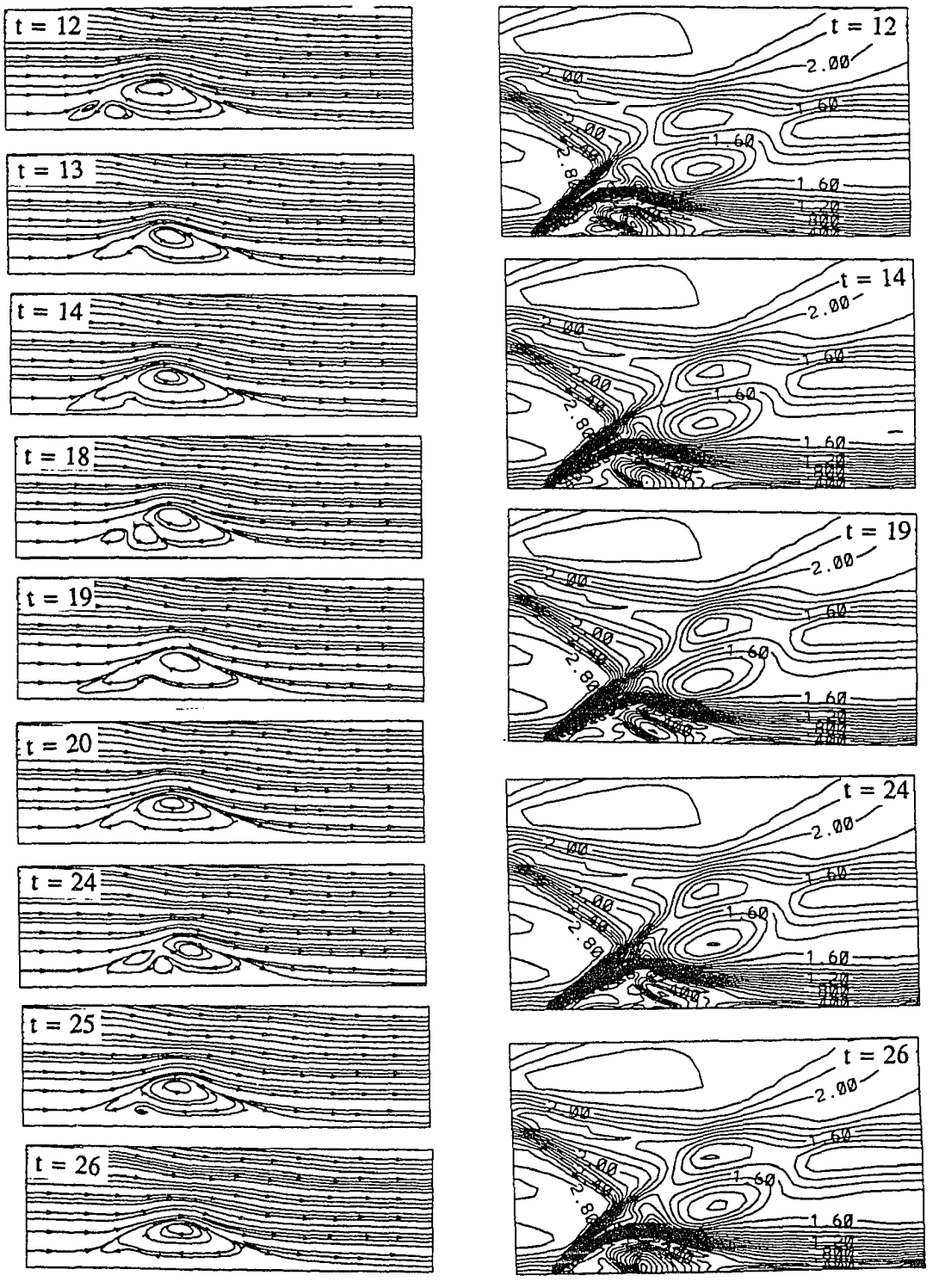

Figure 7.3: Cont'd

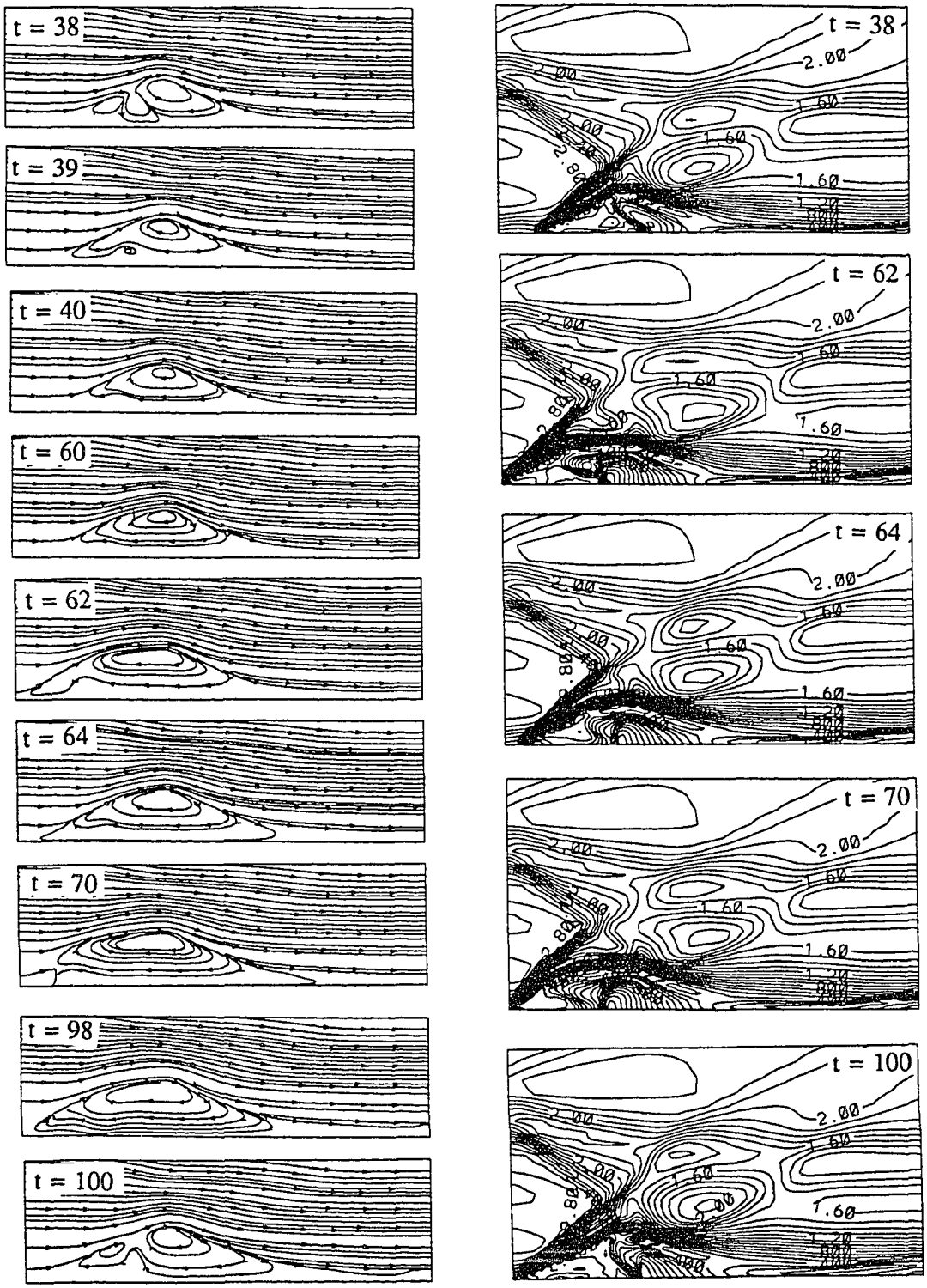

Figure 7.3: Cont'd

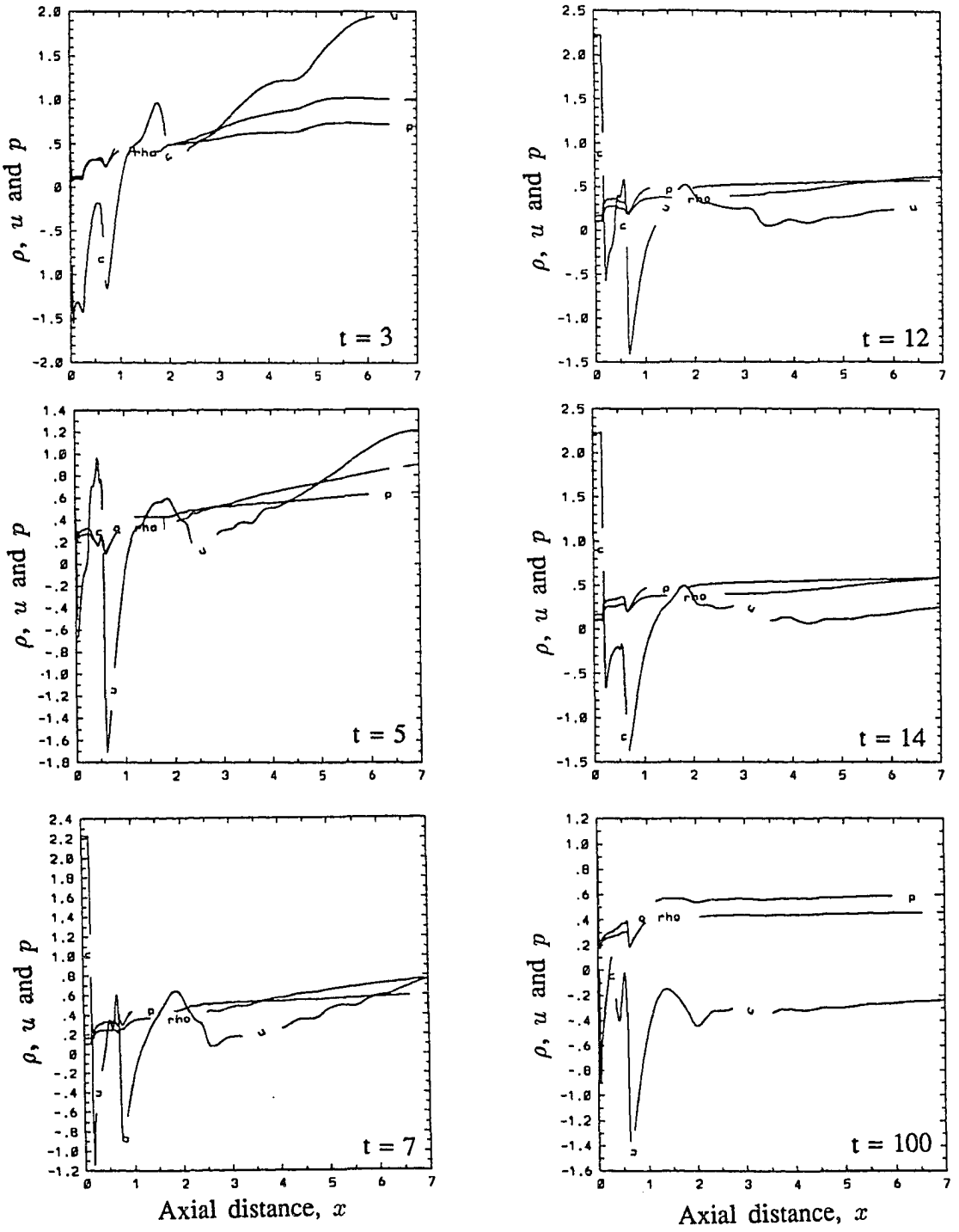

Figure 7.4 Axial distributions of the flow variables, ρ, u and p, along the vortex axis, $r = 0$, for supersonic swirling jet from a nozzle, extrapolation downstream boundary conditions.

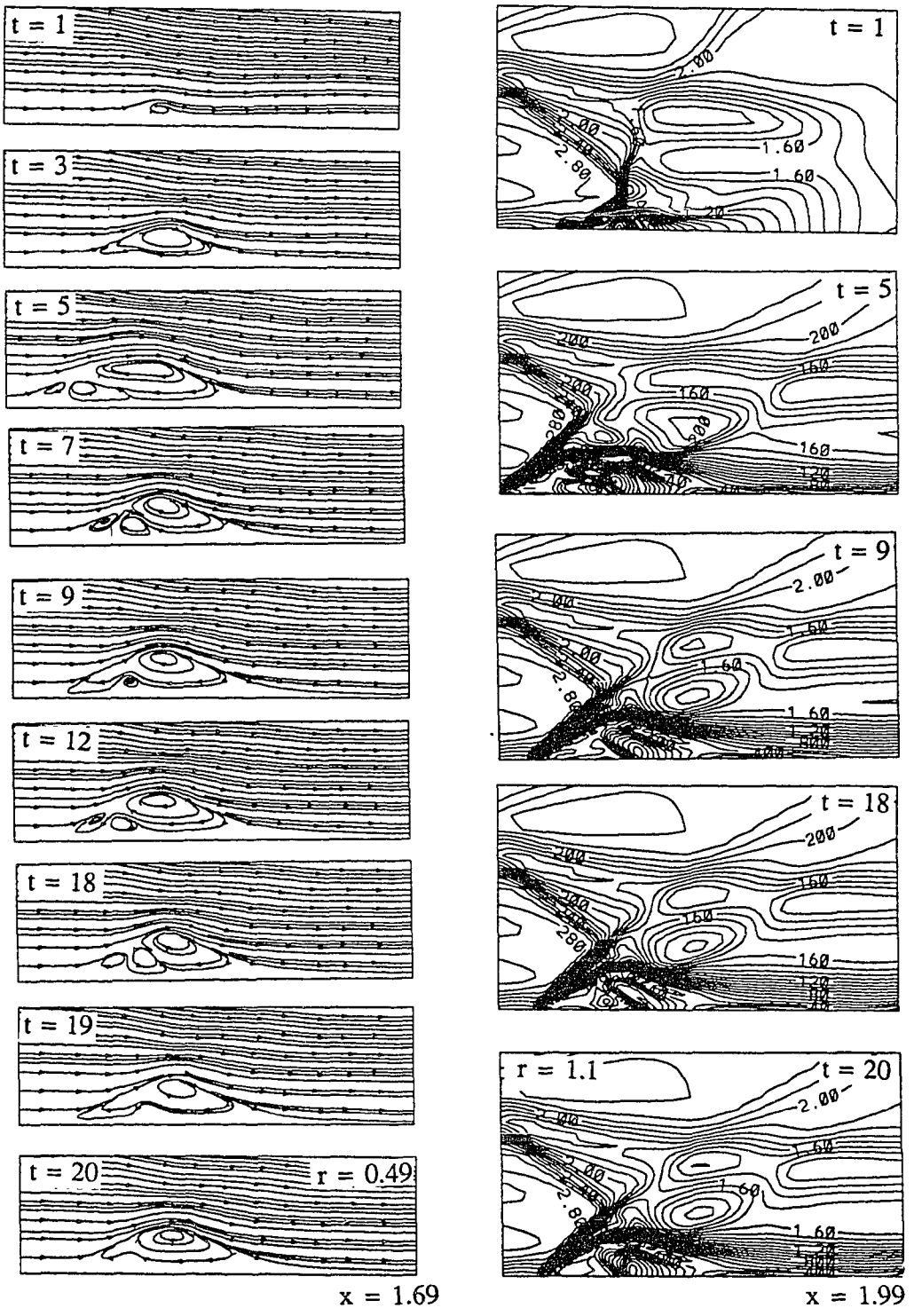

Figure 7.5 Streamlines and Mach contours for supersonic swirling jet from a nozzle with almost single-bubble vortex breakdown, Riemann–invariant downstream boundary conditions.

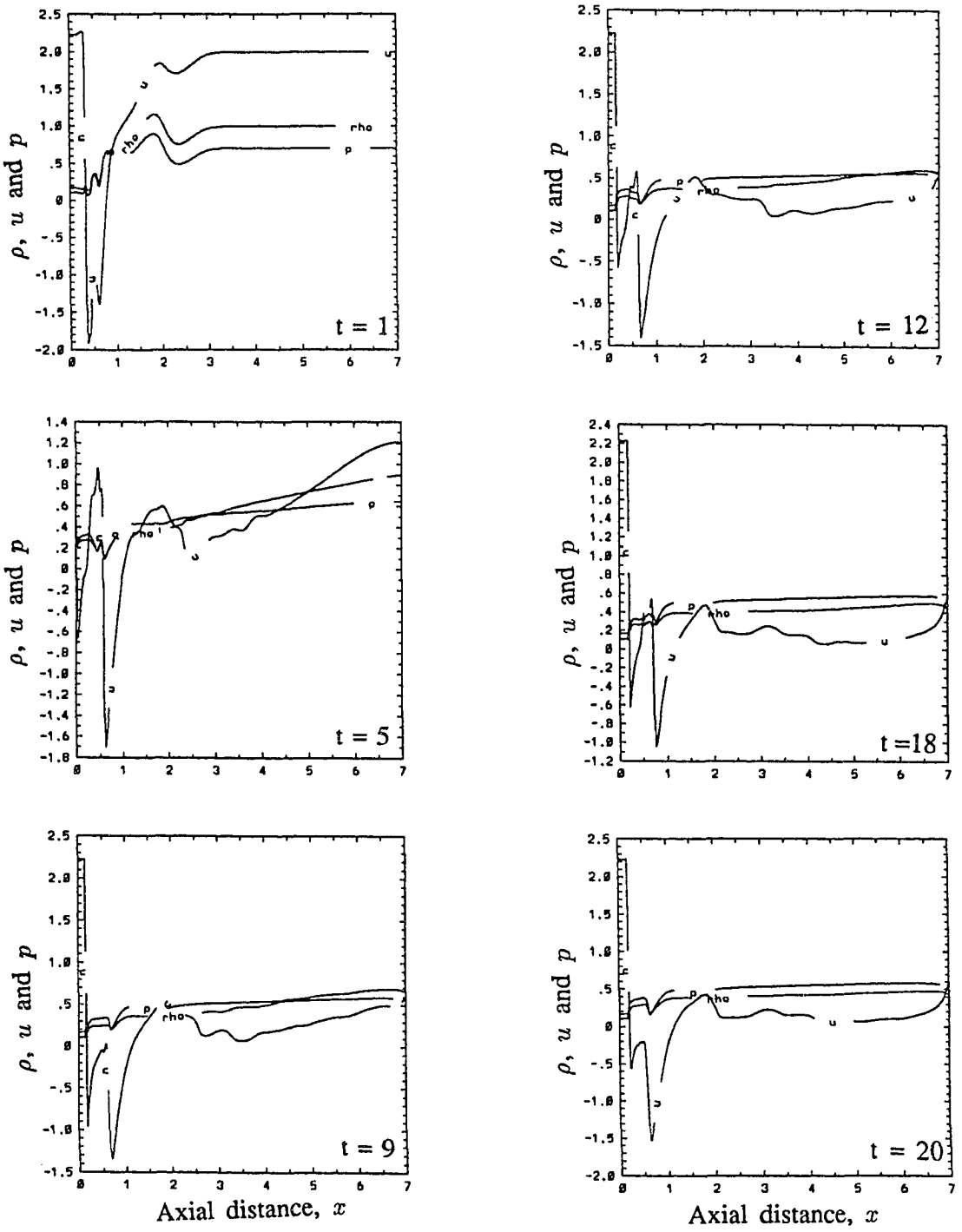

Figure 7.6 Axial distributions of the flow variables, ρ, u and p, along the vortex axis, $r = 0$, for supersonic swirling jet from a nozzle, Riemann-invariant downstream boundary conditions.

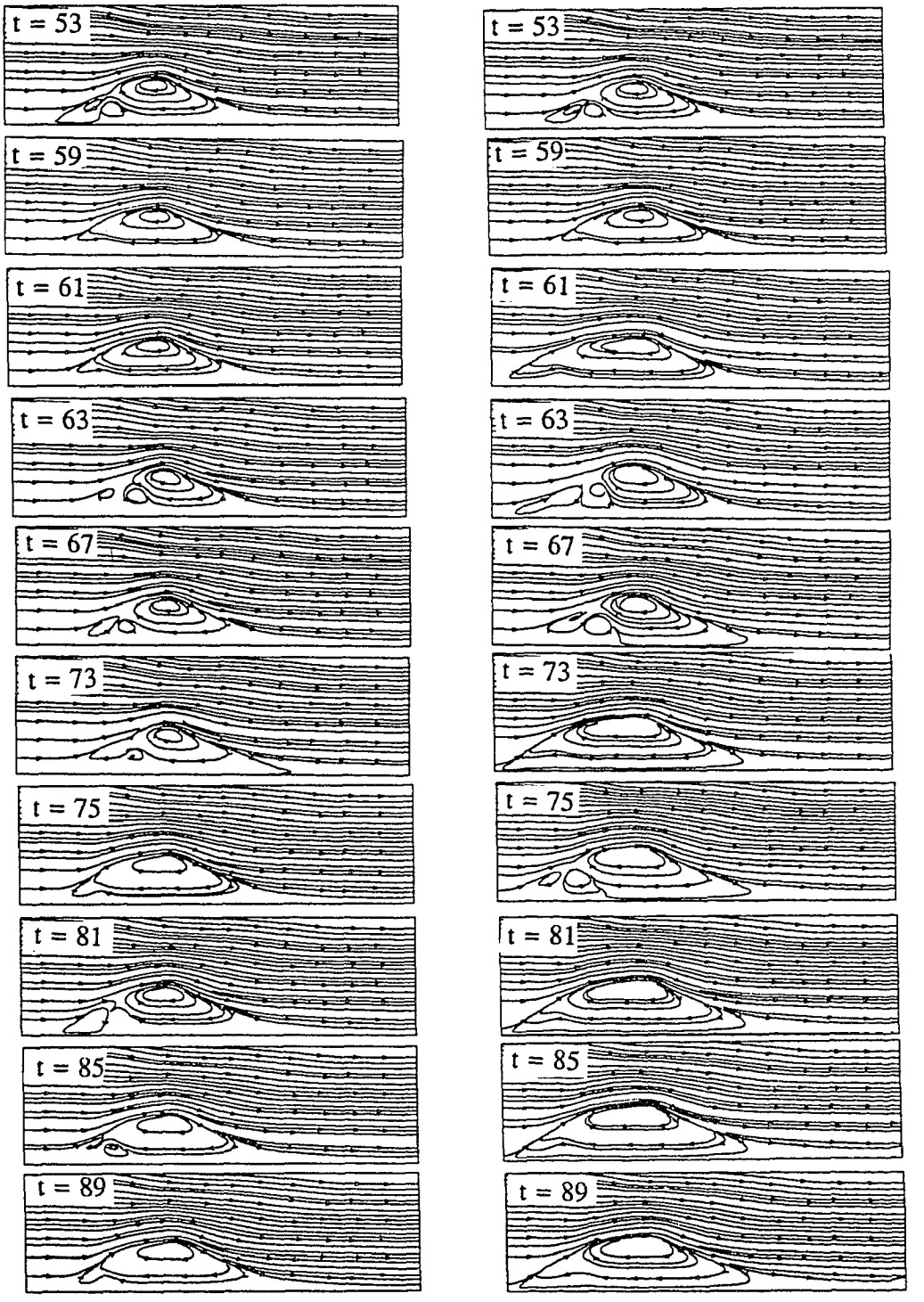

Figure 7.7 Streamlines for supersonic swirling jet from a nozzle with almost single-bubble vortex breakdown using Riemann-invariant and extrapolation downstream boundary conditions.

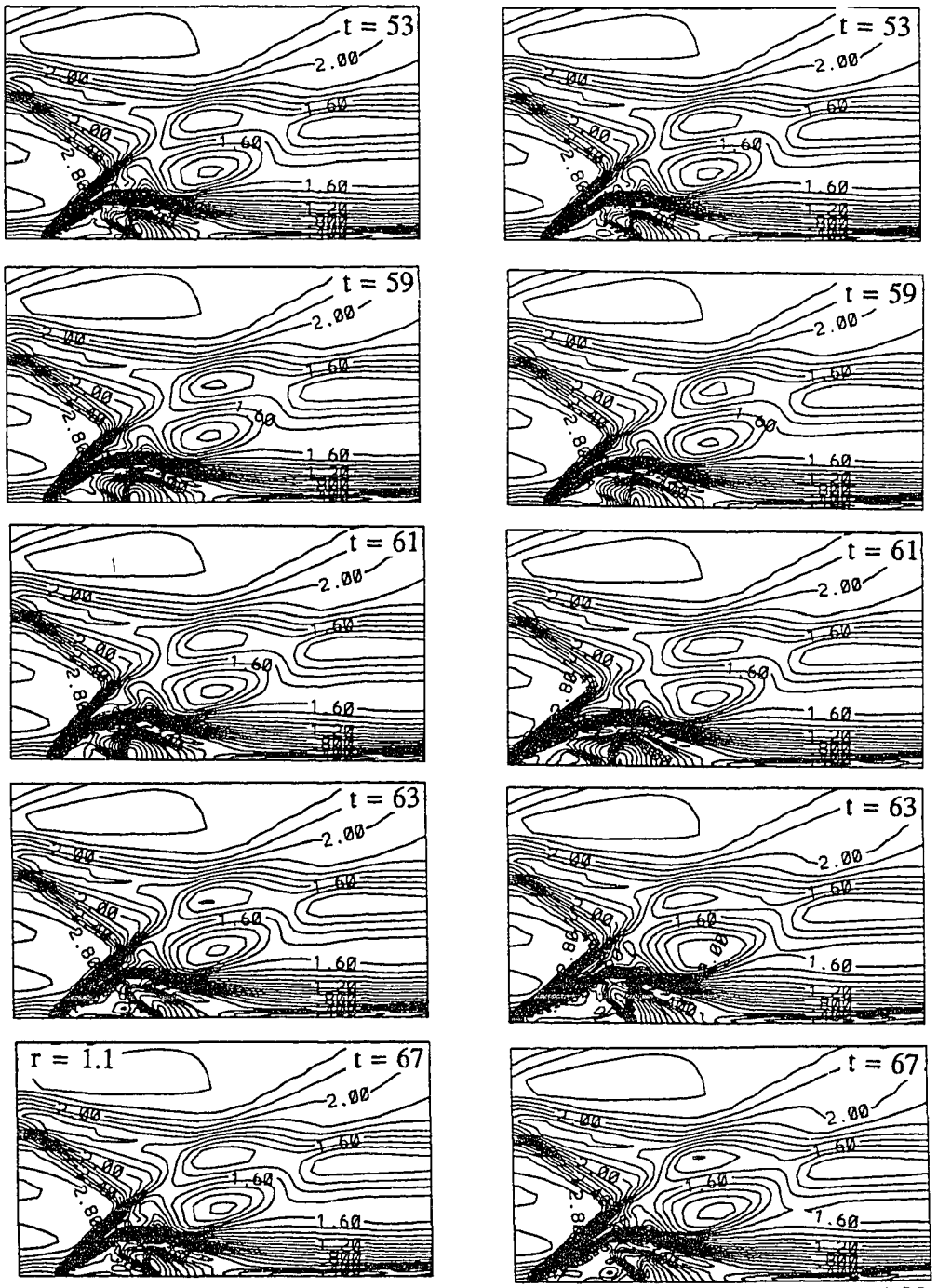

Figure 7.8 Mach contours for supersonic swirling jet from a nozzle with almost single-bubble vortex breakdown using Riemann–invariant and extrapolation downstream boundary conditions.

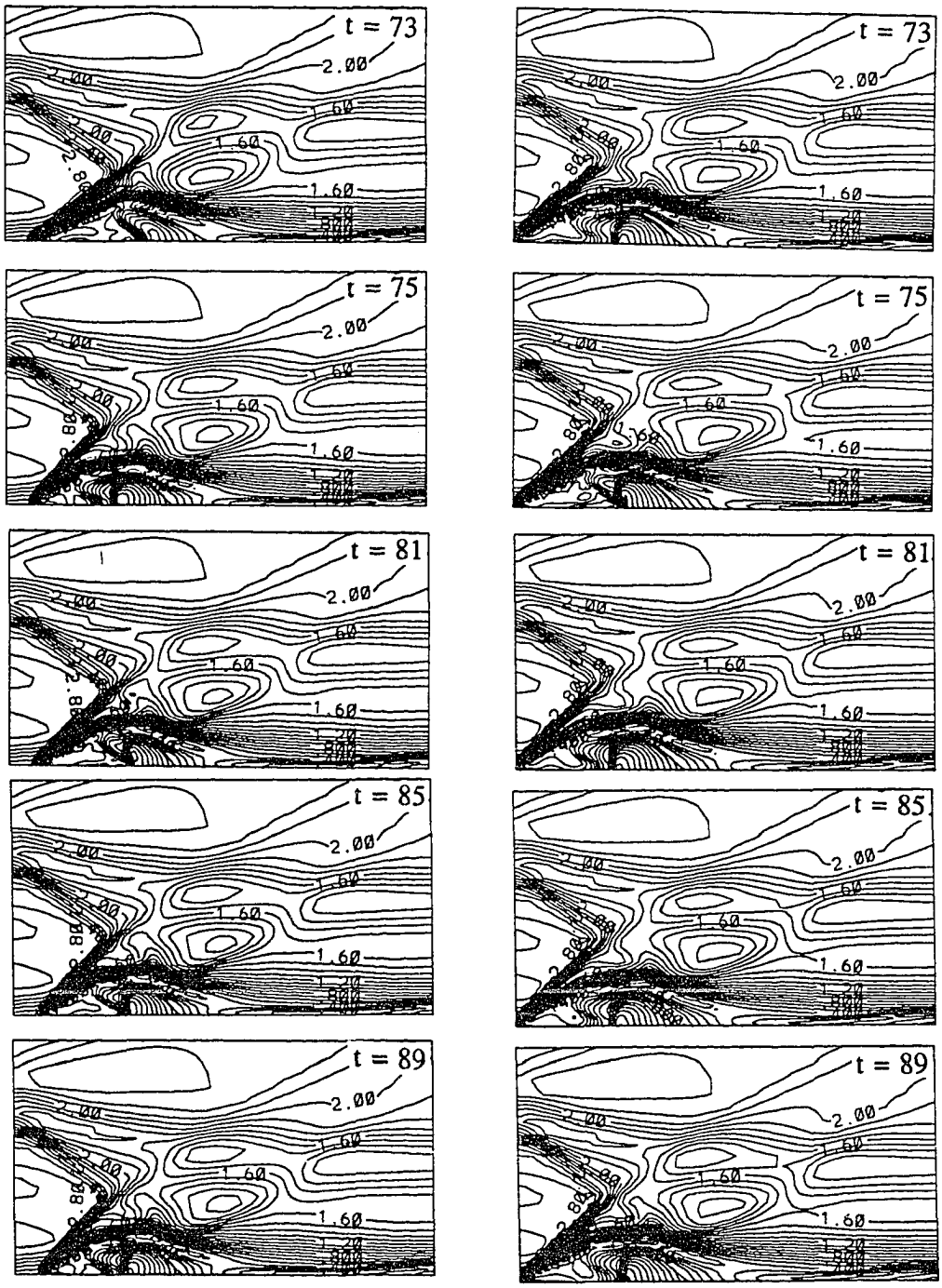

Figure 7.8: Cont'd

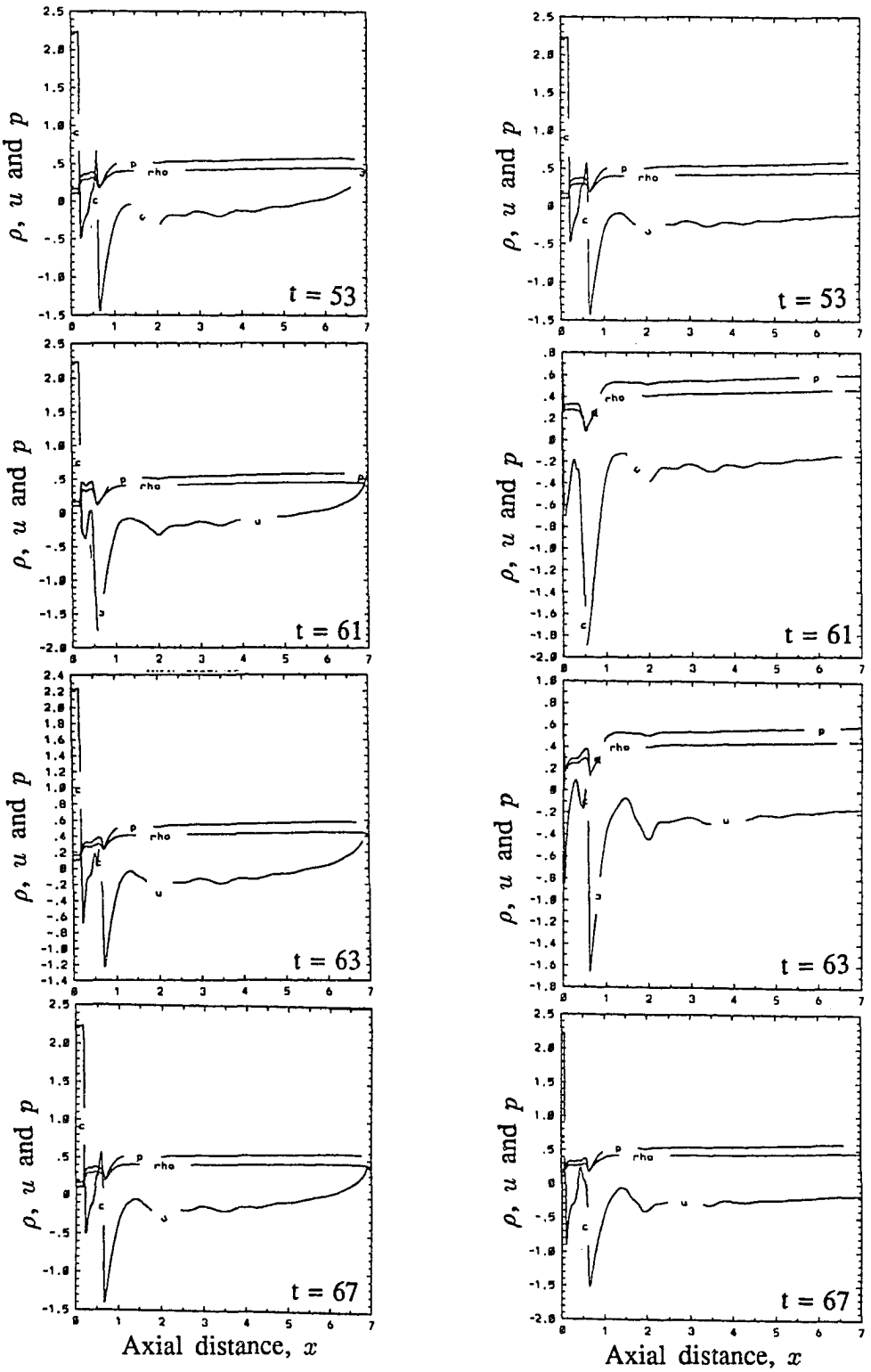

Figure 7.9 Axial variations of the flow variables, ρ, u and p, along the vortex axis, $r = 0$, for supersonic swirling jet from a nozzle using Riemann–invariant and extrapolation downstream boundary conditions.

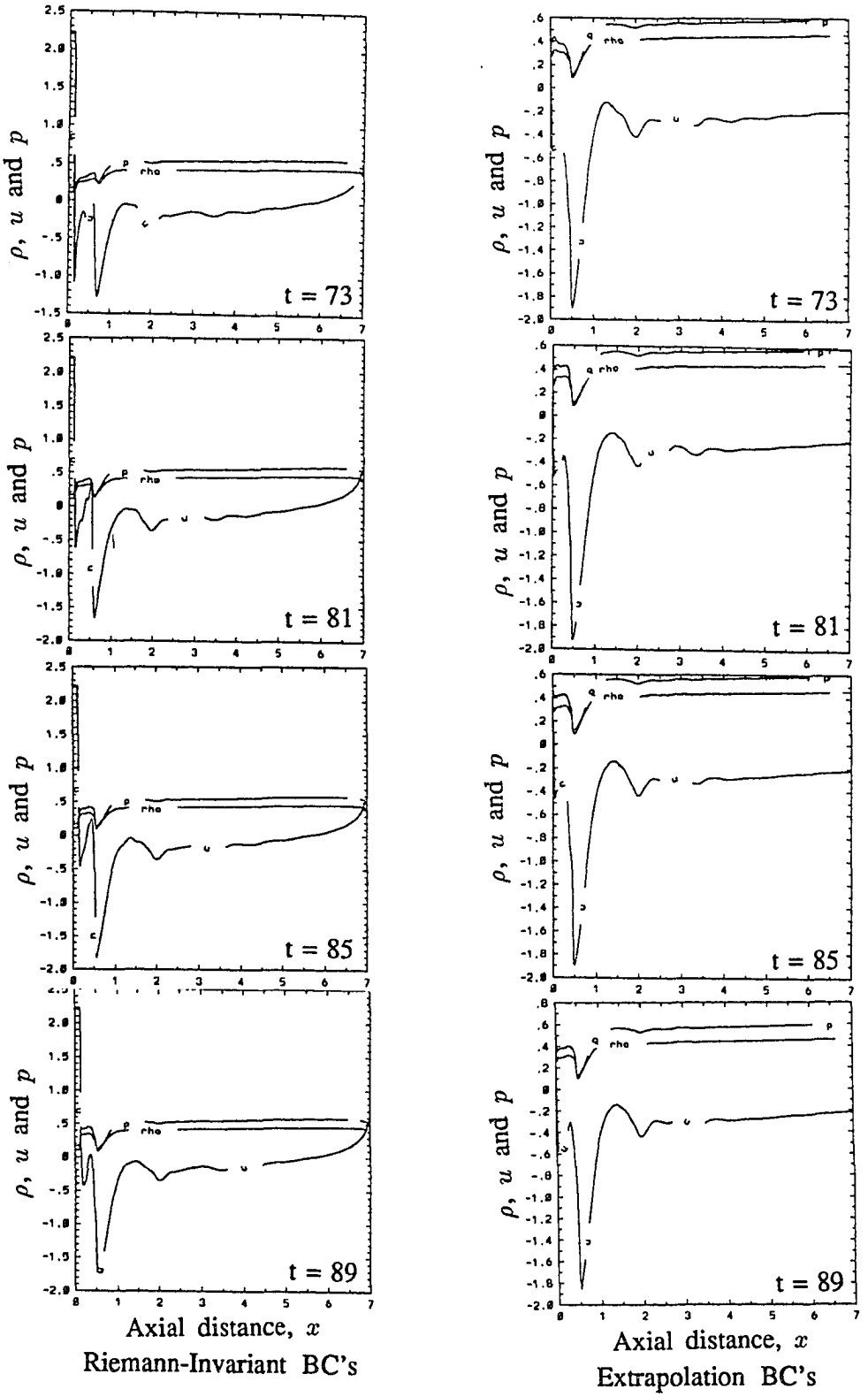

Figure 7.9: Cont'd

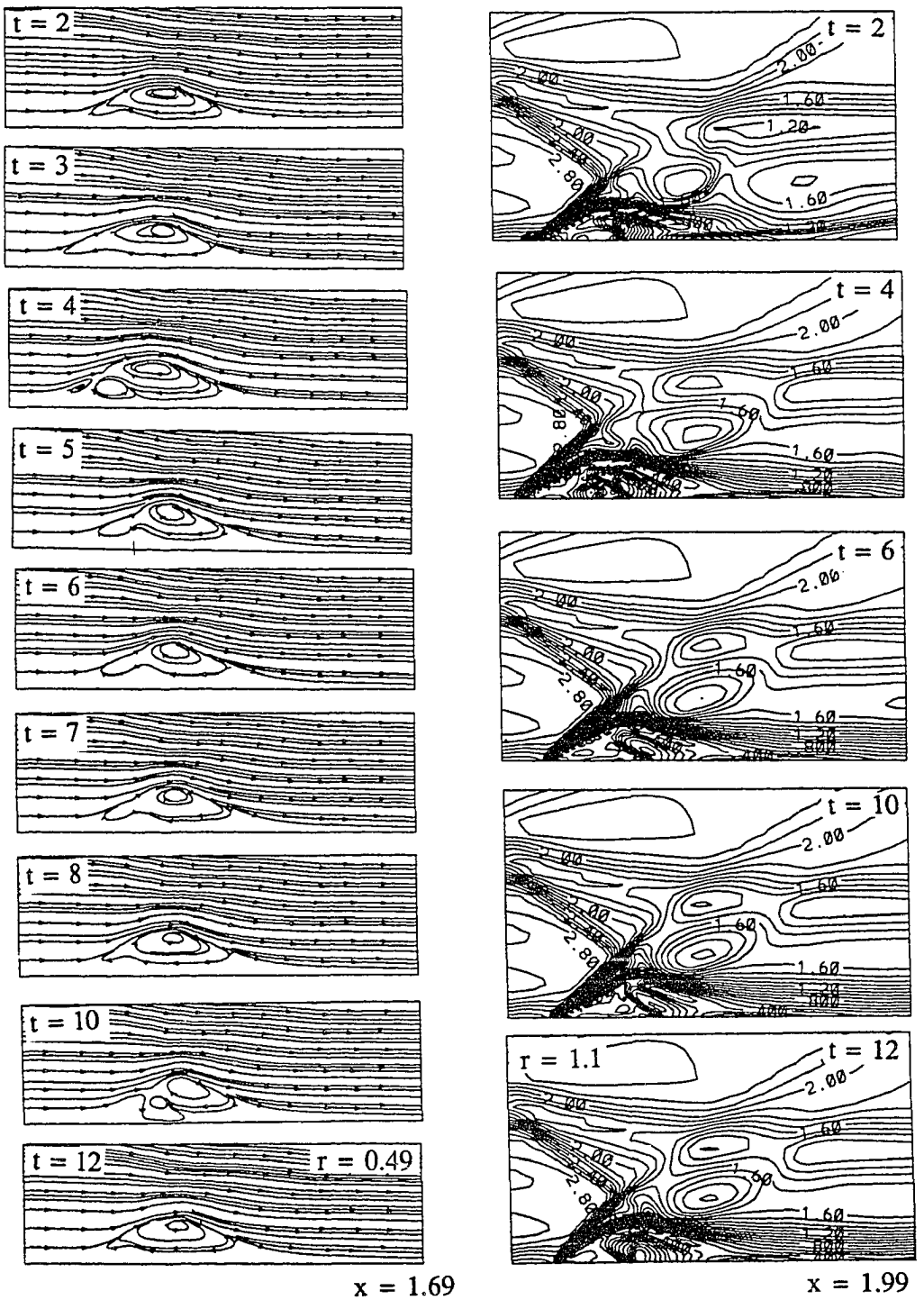

Figure 7.10 Streamlines and Mach contours for supersonic swirling jet from a nozzle with almost single-bubble vortex breakdown, $R_e = 100,000$.

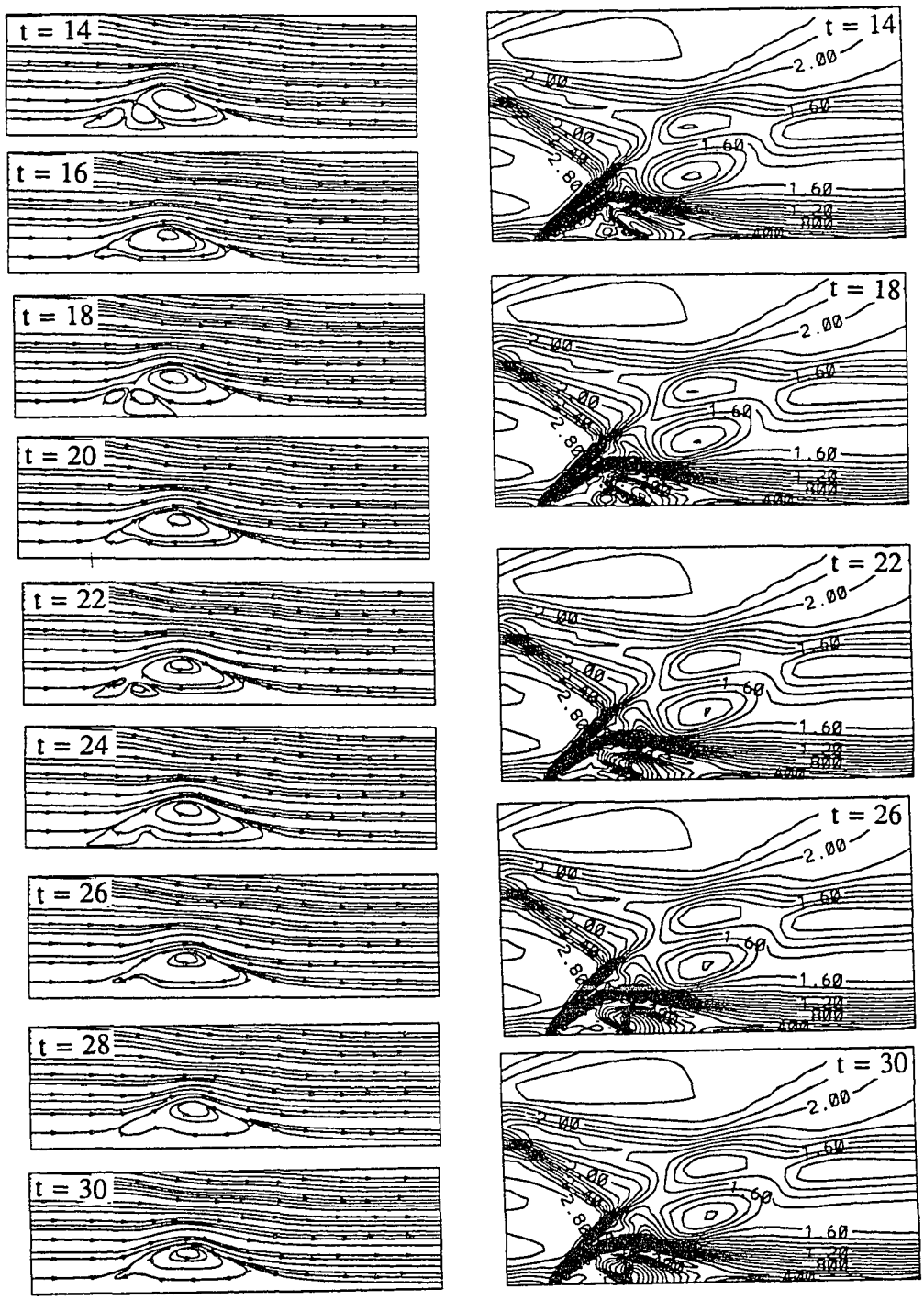

Figure 7.10: Cont'd

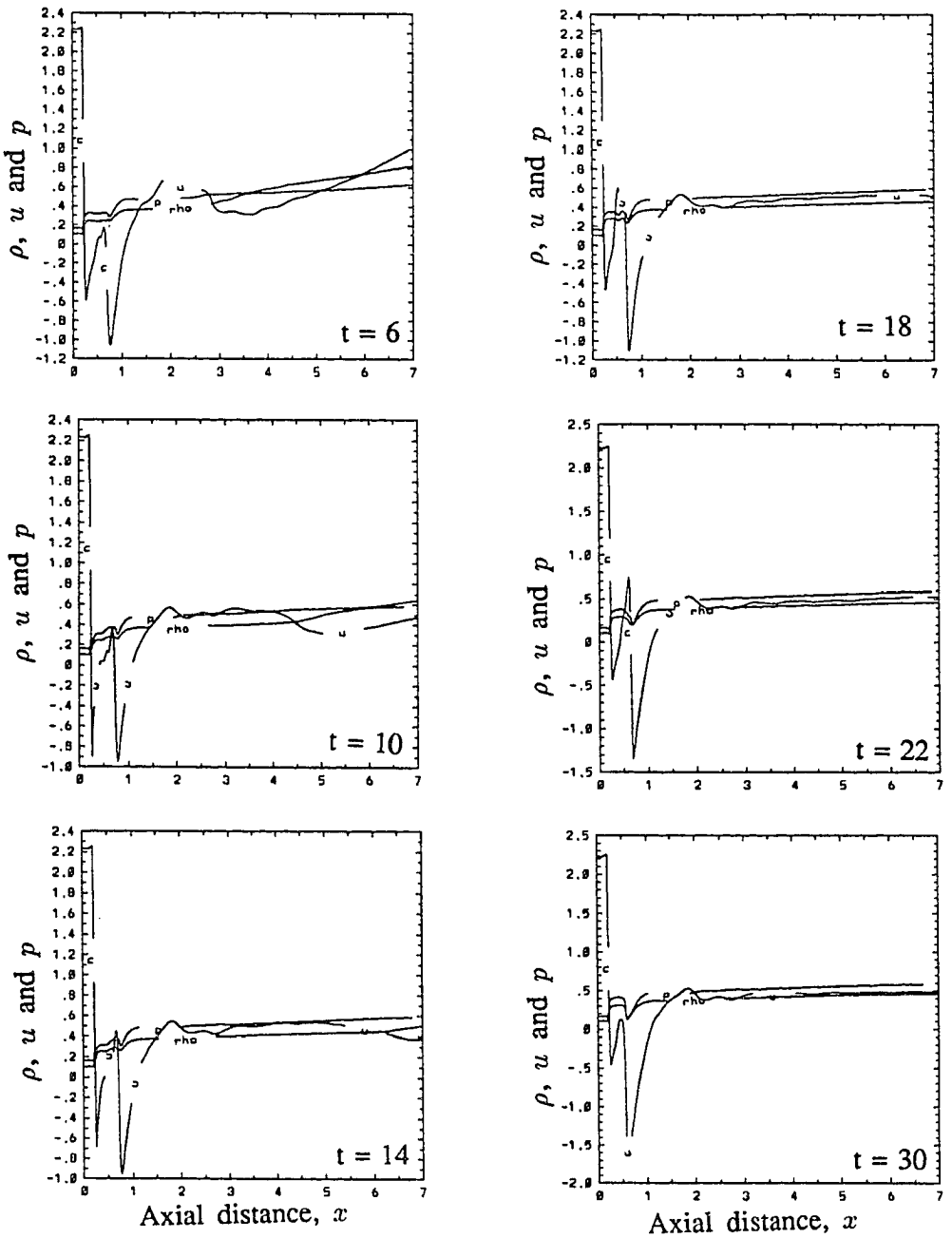

Figure 7.11 Axial distributions of the flow variables, ρ, u and p, along the vortex axis, $r = 0$, for supersonic swirling jet from a nozzle, $R_e = 100,000$.

CHAPTER 8
THREE-DIMENSIONAL SUPERSONIC VORTEX BREAKDOWN IN A CIRCULAR DUCT

8.1 Introduction

The assumption of quasi-axisymmetric flow was used in Chapter 6 in studying the vortex flow and breakdown in a configured circular duct in order to reduce the required computational time and memory. This made it possible to perform a parametric study covering most of the important factors affecting such flows. However, the experimental studies showed the flow to be three-dimensional and hence one should consider the solution of the three-dimensional full Navier-Stokes equations to accurately simulate the physical problem. In this Chapter, the three-dimensional, unsteady, full Navier-Stokes equations are solved using the implicit finite-volume flux-difference scheme of Chapter 4. The solution was advanced in time using globally time stepping because of the unsteady nature of the problem. A time step of 0.0025 was used throughout the computations. The compatible inflow profiles at the inflow boundary were calculated using the same method as in Chapter 6. The calculated conditions were interpolated on the first axial computational plane, assuming the flow to be quasi-axisymmetric only on that plane. All the flow variables were extrapolated from outside because the flow was supersonic at the inlet section. Viscous-wall boundary conditions were used on the duct walls. The quasi-axisymmetric assumption at the vortex axis, used in Chapter 6, was relaxed to study the three-dimensional effects. At the outflow boundary, the flow variables were extrapolated from the interior. The freestream conditions correspond to a Mach number of 1.75 and a

Reynolds number of 100,000 (same flow conditions as those of the quasi-axisymmetric case of Chapter 6). The swirl ratio at the inlet section, which is the ratio between the maximum tangential velocity and the axial velocity, is 0.32 and the radial location of the maximum tangential velocity is r = 0.244.

8.2 Computational Domain and Grid Description

The computational domain consists of a configured circular duct with a total dimensionless length of 2.9, where the duct radius was used as the characteristic length. The duct consisted of a constant diameter cylindrical portion of unit radius, followed by a divergent portion intended to stabilize the formed shock wave, a constant cylindrical part and finally a convergent-divergent nozzle intended to accelerate the exhaust flow to supersonic speeds (same duct geometry as that of Chapter 6). The grid consisted of 200x51x49 grid points in the axial, radial and wrap around directions, respectively. The grid points were clustered near the inlet section in the axial direction for good resolution of the shock system and the shock/vortex interaction region, and in the cross-flow plane around the duct axis for good resolution of the vortex core. The grid points were also clustered near the duct walls for resolution of the boundary-layer flow. Figure 8.1 shows the computational grid where a meridian plane is shown in Fig. 8.1-a and a cross-flow plane is shown in Fig. 8.1-b.

8.3 Computational Results

8.3.1 Vortex-Breakdown Evolution

In this section, snapshots presenting the evolution of the vortex breakdown and bubble formation during the early time levels are presented. Figure 8.2 shows the streamlines and total Mach-number contours on a horizontal plane at time levels from t = 2.0 to t = 7.0. The results are qualitatively compared with the experimental incompressible results

of Escudier [12] which are shown in Fig. 8.3. At t = 2.0, a small recirculation region was formed behind the strong normal part of the shock wave. Two stagnation points could be recognized along the axis, r = 0.0. The total Mach number contours show the position of the shock front near the inlet section and the position of the recirculation zone behind the shock wave. As the computations advanced in time, the bubble size enlarged in the axial and radial directions and the shock-bubble system moved downstream. At t = 3.5, it was noticed that the bubble size was increased and the shock wave was deformed accordingly. The solution was quasi-axisymmetric as shown by the streamlines and Mach-number contours. Starting at t = 4.0, the bubble enlarged in the lateral direction, moved upstream towards the inlet boundary pushing the shock wave in the same direction. Some asymmetric effects could be noticed where the lower and upper halves of the displayed streamlines and Mach-number contours were not mirror images of each other. Comparing the above results with the experimental results in Fig. 8.3 shows that the phenomenon of the bubble evolution in both cases are similar. The increase in the bubble size, then the change in its aspect ratio with the movement towards the inlet boundary, are in fair qualitative agreement. Figure 8.4 shows another phase of the solution history where a reversed shock was formed inside the vortex breakdown bubble. The reversed axial velocity reached a supersonic value of 1.2 at x = 0.6 at t = 5.0. A normal shock wave turned the reversed flow to subsonic. The shock wave can be noticed in Fig. 8.5, where the axial variation of the axial velocity, density and static pressure at r = 0.0 are shown. At t = 5.0, we notice two sources of disturbances that might cause the flow asymmetry, the first was the presence of the shock wave inside the bubble and the second resulted from the interaction of the normal shock with the boundary layer at the duct wall. This interaction resulted in a separation of a bubble at the wall. As the computations advanced in time, the bubble system started to move downstream toward the duct exit with a new

recirculation region behind the shock wave. The flow became quite asymmetric with the separation bubble at the duct wall moving downstream along with the shedding vortex-breakdown bubble system. The space between the moving bubbles acted like a convergent-divergent nozzle which allowed the subsonic flow behind the shock wave to recover supersonic speeds. This resulted in a formation of a shock wave that moved downstream with the shedding bubbles.

As the computations advanced in time, some of the features noticed experimentally for incompressible vortex flows in pipes could be recognized, e.g., an asymmetric vortex breakdown is shown in Fig. 8.5 at t = 11.5. The streamlines clearly show the spiral-type of vortex breakdown and the asymmetric shedding of the vortex breakdown bubbles. It should be noticed here that such phenomenon could not be captured in the computations of Chapter 6, where the quasi-axisymmetric assumption was used. This justified the use of three-dimensional solution for such flows.

At t = 12.0, an almost quasi-axisymmetric vortex breakdown was captured in the reversed flow region, just behind the shock wave, which was followed by an asymmetric flow region, as can be seen from the streamlines and Mach number-contours in Fig. 8.6.

The shedding of the vortex breakdown bubbles continued as new bubble systems were formed behind the shock wave. At t = 16.5 and t = 31, the shedding of two asymmetric bubbles can be seen where a two-bubble system was formed upstream and a very small recirculation region can be recognized just downstream of the central part of the shock wave.

At t = 18.0, the flow downstream from the bubble system was similar to the high-Reynolds number flow behind a sphere with the vortex shedding taking place. The existence of asymmetric vortex breakdown is clearly shown. It is of interest to notice that the fluid inside the vortex-breakdown region moves in the radial direction with a nonzero

radial velocity component which contradicts the quasi-axisymmetric assumption. The flow inside the vortex-breakdown region is very complicated which can be characterized by the existence of multiple asymmetric bubbles that rotate around an axis perpendicular to the main vortex axis. Sometimes two of these bubbles merge forming one bubble as can be seen in Fig. 8.6 at t = 19.0, where two vortex rings were merged to form a single inclined ring. The merging in the upper half of the shown domain was lagging that in the lower half. Two bubbles rotating in the clockwise direction can be recognized in the upper half while a large bubble rotating in the counter-clockwise direction can be seen in the lower half.

An important parameter affecting the flow in the duct is the interaction of the shock wave system with boundary-layer flow on the duct wall which may result in the separation of the boundary layer as can be seen in Fig. 8.7 at t = 33. The Mach number contours show the separation of the boundary as a result of the interaction with the shock wave and the streamlines show the reduction in the vortex-breakdown bubble size as a result of the boundary layer thickening. The asymmetry of the flow is clear where the formation of a weak shock wave is noticed only in the upper half of the duct. The shedding of the inclined vortex rings shown in Fig. 8.7 at t = 33 is similar to the spiral type of vortex breakdown where the upper parts of the vortex rings were rotating in the clockwise direction and the lower parts were rotating in the opposite direction and a new vortex ring was formed behind the shock while the spiral-like system was moving downstream.

As the solution advanced in time, the size of the breakdown region reduced in the radial direction as a result of the boundary layer thickening. An interesting picture is shown in Fig. 8.7 at t = 38.5 where a bubble-type vortex breakdown is followed by a spiral-type vortex breakdown which was formed downstream of the shock wave. This phenomenon was observed experimentally for incompressible vortex flows in pipes and

was never captured computationally.

The reduction of the breakdown-region size continued with the advance in the time as can seen at t = 41, 42, 43 and 44. The formation of multi-bubble systems downstream of the shock wave and the vortex- breakdown-bubble shedding phenomenon were observed but with smaller bubble sizes. At t = 46, no recirculation zone can be observed because the vortex breakdown system was dissipated totally. A small bubble appeared at t = 49.5 behind the shock wave . The new bubble was also dissipated after a short period leaving the duct with no vortex-breakdown regions and a stationary inlet shock.

8.3.2 Effect of the Duct-Wall Boundary-Layer Flow

The effects of the shock/boundary-layer interaction were further investigated by treating the duct walls as inviscid walls. This experiment was started at t = 43.0 where inviscid-wall boundary conditions were applied on the duct walls with all the other boundary conditions remaining the same. Samples of the results are shown in Fig. 8.8. At t = 43.5, the bubble size was noticed to be smaller than that at earlier time steps and the shock wave to be normal at the duct wall. The shedding of the vortex rings continued as the solution advanced in time, as can be seen at t = 45.5, where the vortex rings could be recognized. It was noticed also that the vortex-breakdown-bubble size started to increase in the radial direction. Further increase in the breakdown region size was noticed at t = 47. As time goes by, the size of the bubble was changing according to the number and size of the vortex rings. It was noticed that the position of the shock wave with respect to the duct inlet was fixed while the shape of the central part was changing continuously according to the shape of the bubbles behind the shock. The shedding of the vortex-breakdown bubbles continued in an asymmetric form as can be seen at t = 63 , 69 and 72.5. It is interesting to notice that the vortex-breakdown system

could survive and was not dissipated as in the case of viscous walls. The computations continued to t = 75 without any sign of the vortex-breakdown-bubbles dissipation. It is concluded that the disturbances caused by the wall boundary-layer separation were the reason behind the disappearance of the vortex-breakdown system. This might be caused by the pressure gradients resulting from the change in the vortex-core outer boundaries.

Sarpkaya [37] observed that the boundary layer separated and reversed flow occurred on the tube wall in the case of a swirling incompressible flow in a divergent tube. He suggested that the bubble pressure gradient was caused by the tube divergence and that caused by the vortex breakdown were the reasons behind the separation. He concluded that the wall viscous effects on vortex breakdown in tubes are very significant.

In the case of supersonic vortex breakdown, the problem is much more involved because of the shock/boundary-layer interaction and the assumption of inviscid walls seemed to isolate the wall viscous effects.

8.4 Summary and Discussion

In this Chapter, the three-dimensional interaction of a supersonic swirling flow with a shock wave in a configured circular duct was studied. The duct geometry is the same as that used for the quasi-axisymmetric flow of Chapter 6. Only one set of inlet flow conditions was used. These inlet flow conditions are; R_e = 100,000, M_∞ = 1.75 and β = 0.32. It was very difficult to perform a parametric study similar to that of Chapter 6 because of the large computational requirements for three-dimensional solutions. As in Chapter 6, the effect of the duct-wall boundary-layer flow on the breakdown mode was investigated since the vortex-breakdown bubble was dissipated. The results show several modes of three-dimensional vortex breakdown. A surprising result was that the unsteady multi-bubble multi-frequency breakdown obtained using

the quasi-axisymmetric assumption for the same flow conditions in Chapter 6 was not obtained in the three-dimensional flow case. The three-dimensional case shows transient multi-bubble breakdown where the breakdown disappeared at time levels higher than t = 51. This may be caused by the relieving effect of the three-dimensional duct. By the relieving effect, it is meant that the flow can freely travel around the duct axis. This resulted in several modes different from those obtained using the quasi-axisymmetric assumption. Among the three-dimensional modes that could be recognized are the asymmetric bubble type, the spiral type and the bubble-spiral type. The last type was observed experimentally for incompressible vortex flows in pipes and was never obtained computationally. Figure 8.10 shows a photograph of this type of breakdown from reference [38] for incompressible swirling flows in a pipe. The streamlines at t = 38.5 are shown in Fig. 8.11. It is clear that the two results are in a good qualitative agreement. As in the case of quasi-axisymmetric flow, the use of an inviscid duct wall is similar to simulating flows at higher Reynolds numbers. In the present flow computations, using the inviscid duct-wall boundary conditions caused the breakdown to last for a longer time. It is concluded that the vortex breakdown is a three-dimensional phenomenon and hence, one needs to solve the three-dimensional full Navier-Stokes equations in order to capture the three-dimensional features and simulate the physical problem. However, the quasi-axisymmetric assumption is computationally economic in performing parametric studies and providing physical understanding of the vortex-breakdown modes, which could qualitatively be useful for understanding three-dimensional vortex-breakdown flows.

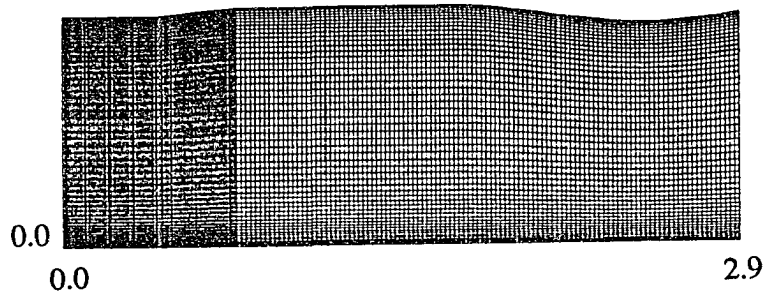

a- Axial plane

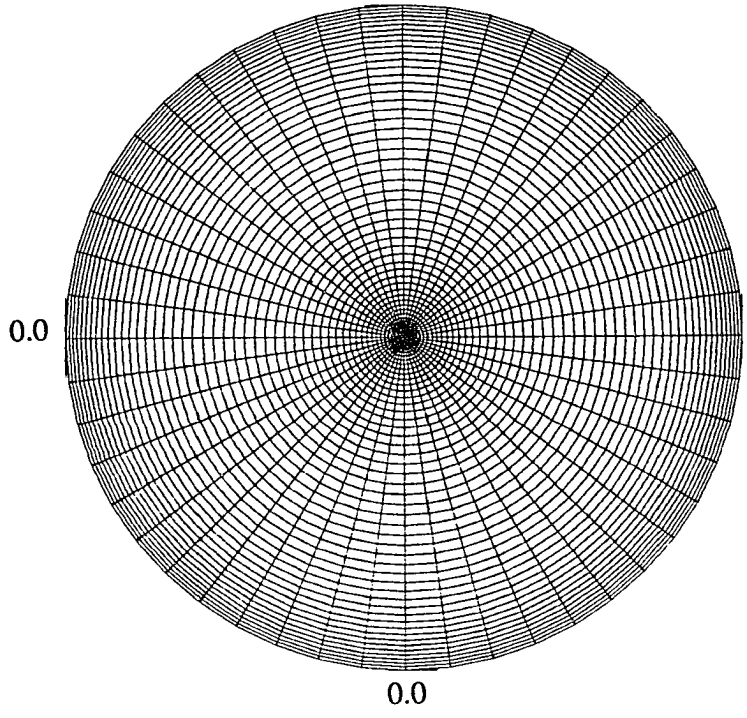

b- Cross-flow plane

Figure 8.1 Configured-circular-duct computational domain and grid, 200x51x49 grid points in the axial, radial and wrap-around directions, respectively.

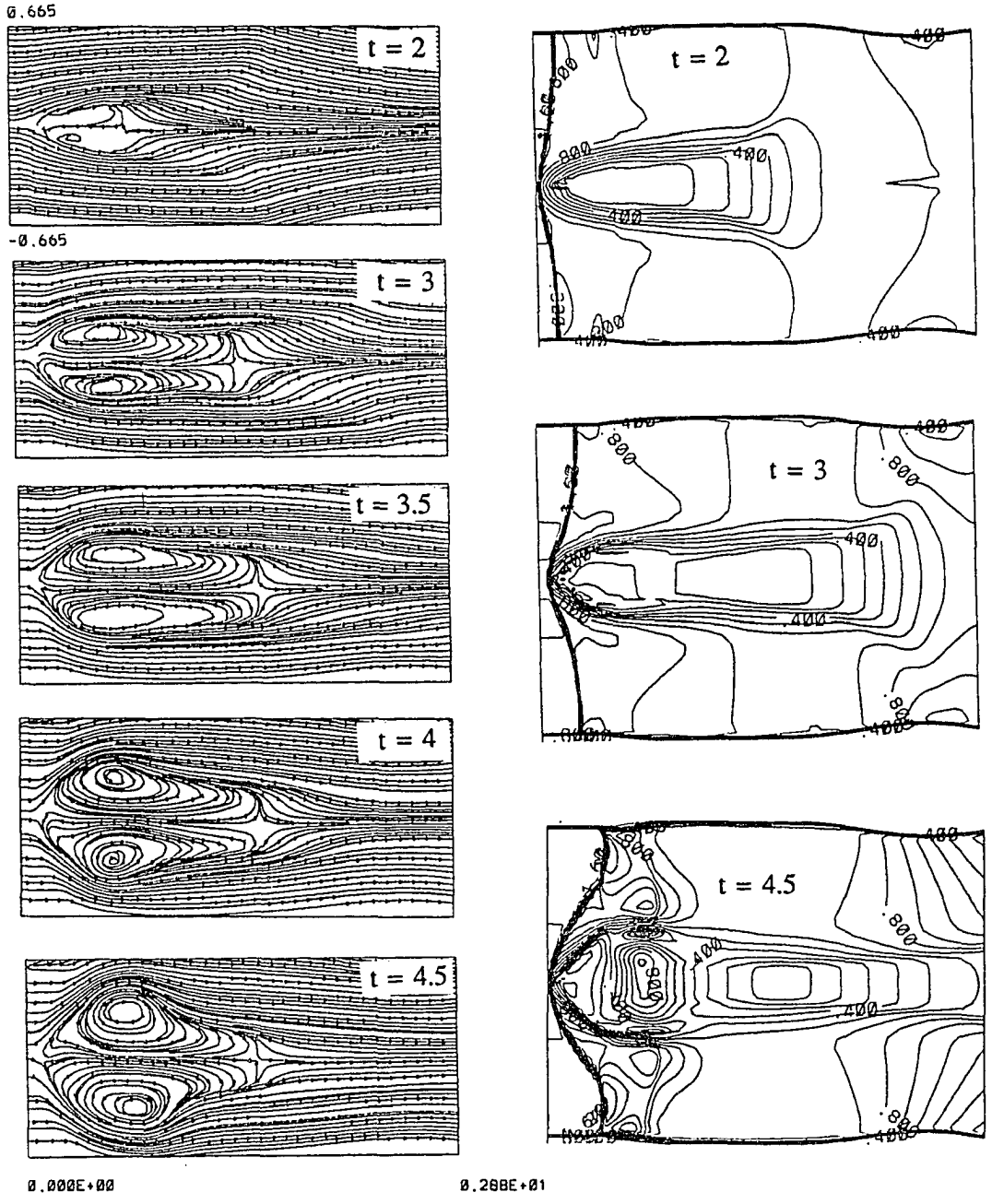

Figure 8.2 Streamlines and Mach contours in a horizontal plane for a supersonic swirling flow in a circular duct, $M_\infty = 1.75$, $\beta = 0.32$ and $R_e = 100,000$.

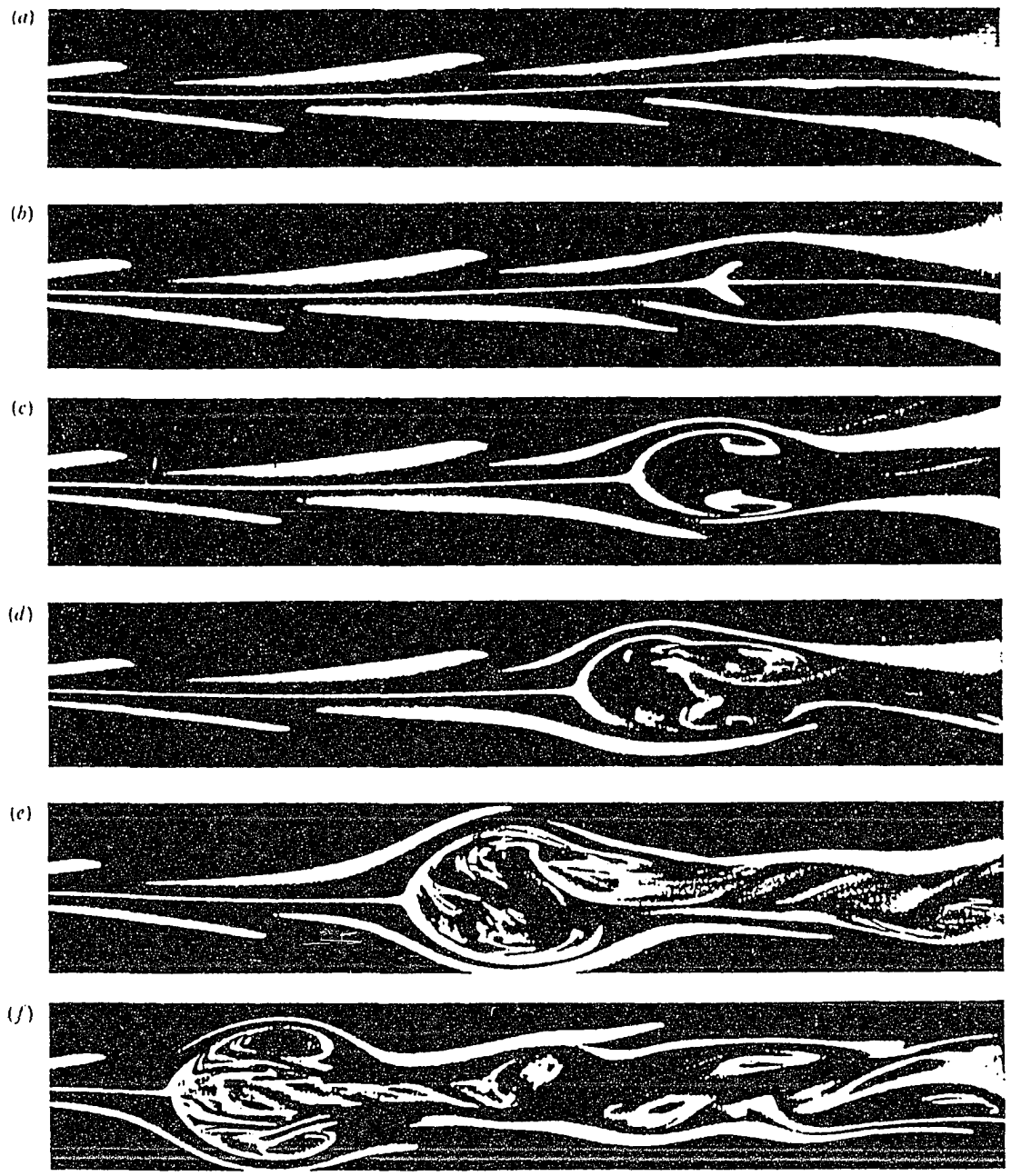

Figure 8.3 Experimental results of an incompressible swirling flow in a circular duct, from reference [12].

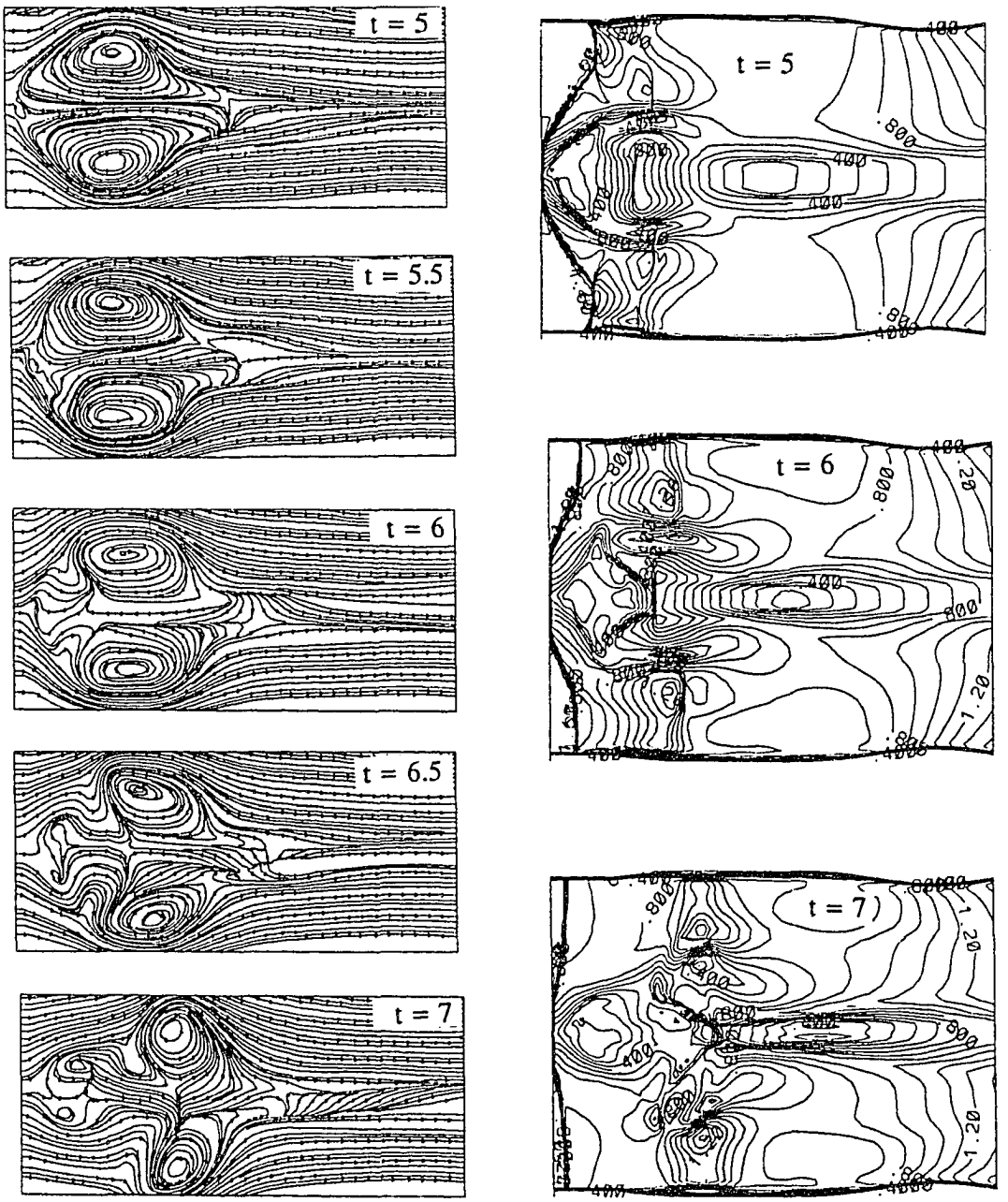

Figure 8.4 Streamlines and Mach contours in a horizontal plane for a supersonic swirling flow in a circular duct, $M_\infty = 1.75$, $\beta = 0.32$ and $R_e = 100,000$.

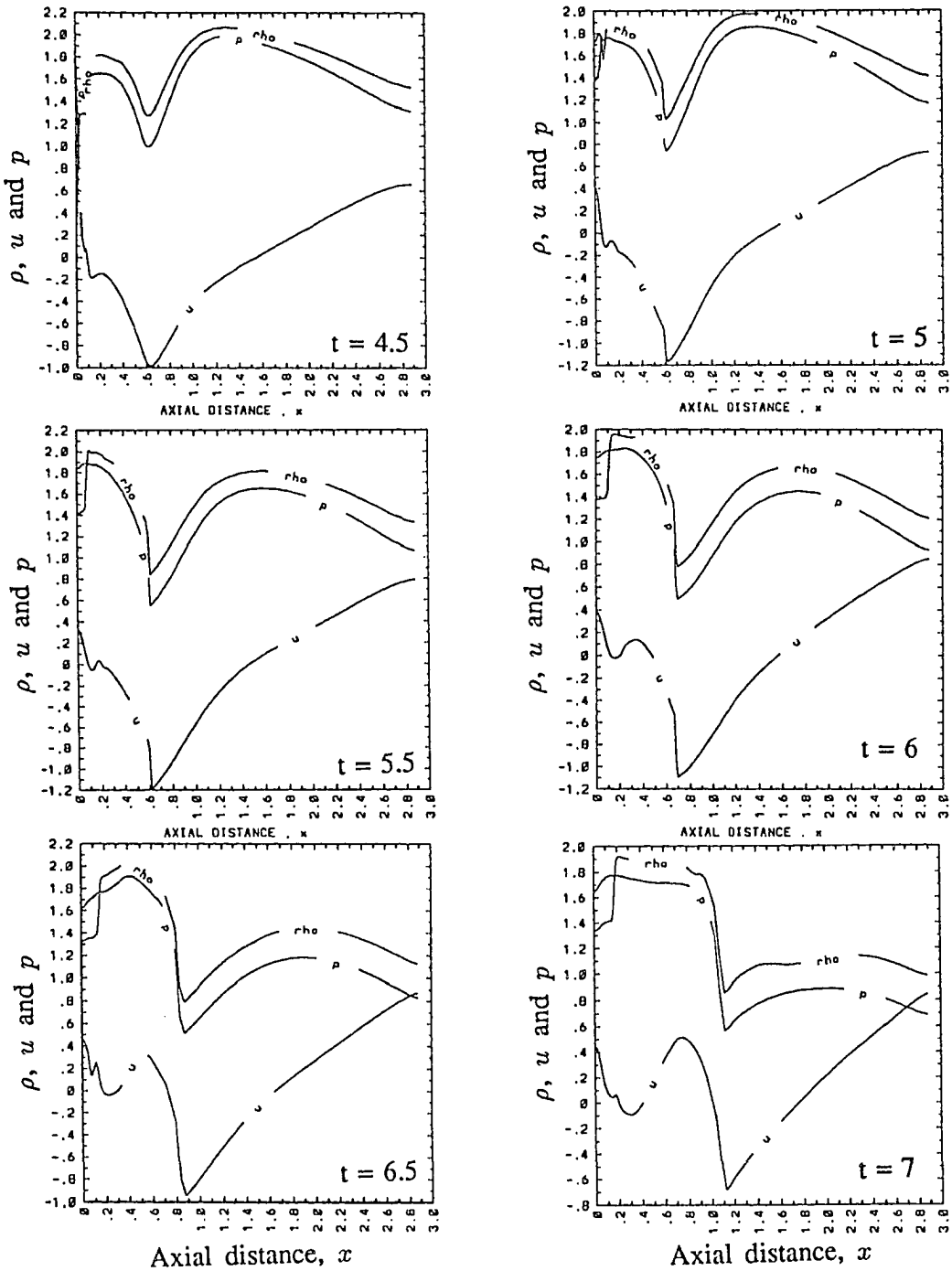

Figure 8.5 Axial distributions of the axial velocity, u, density, ρ and pressure, p, for a supersonic swirling flow in a circular duct, $M_\infty = 1.75$, $\beta = 0.32$ and $R_e = 100,000$.

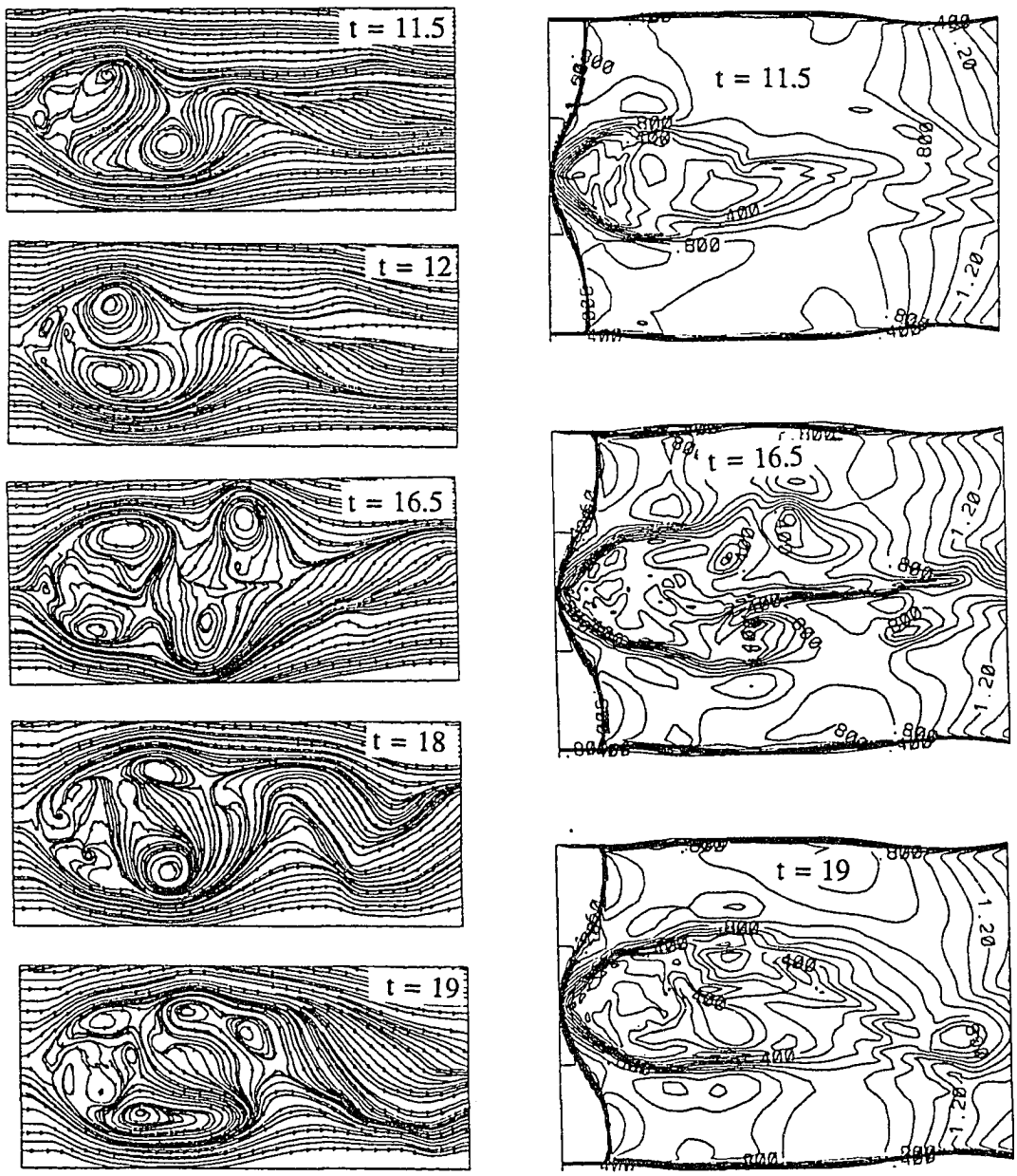

Figure 8.6 Streamlines and Mach contours in a horizontal plane for a supersonic swirling flow in a circular duct, $M_\infty = 1.75$, $\beta = 0.32$ and $R_e = 100,000$.

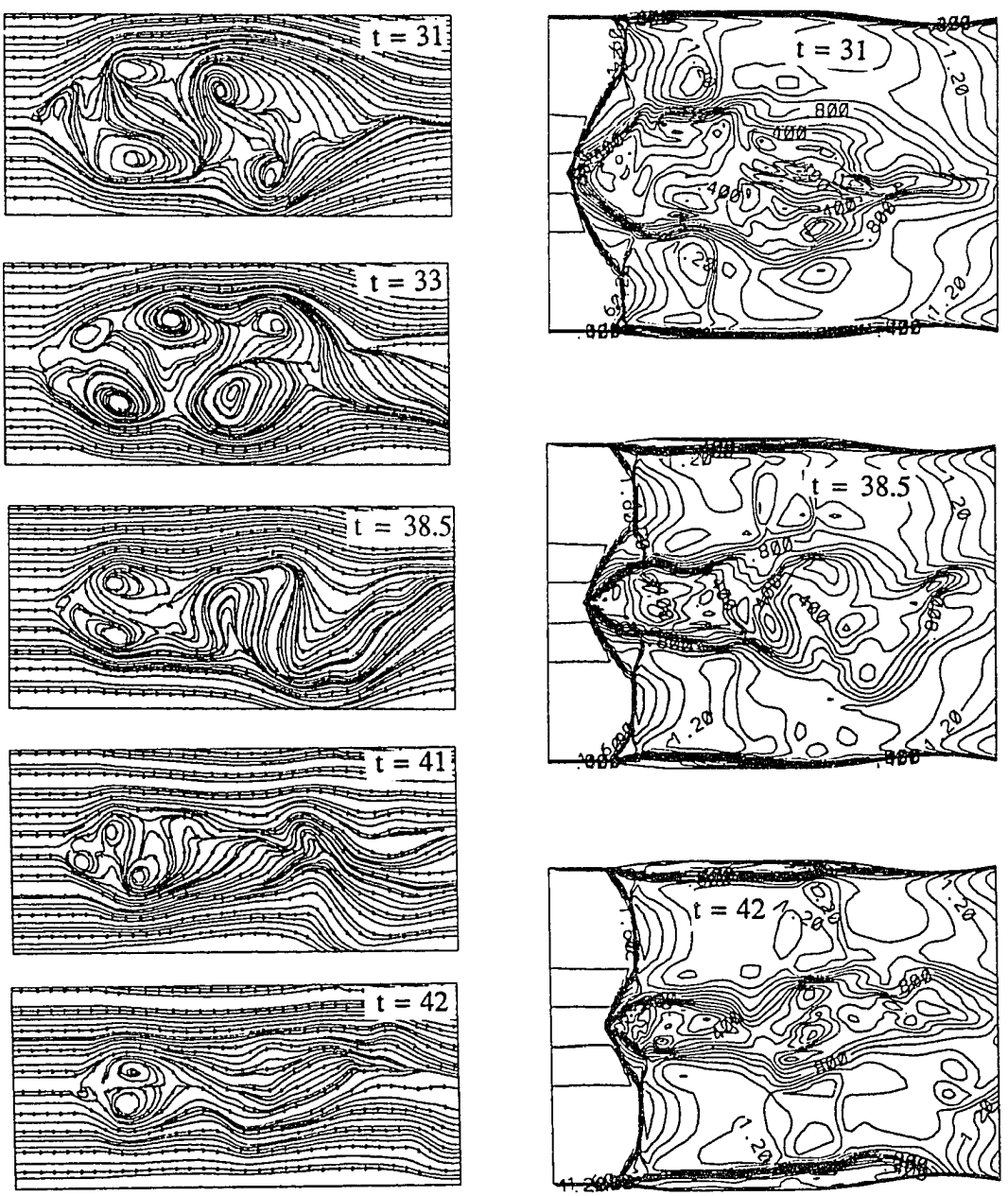

Figure 8.7 Streamlines and Mach contours in a horizontal plane for a supersonic swirling flow in a circular duct, $M_\infty = 1.75$, $\beta = 0.32$ and $R_e = 100,000$.

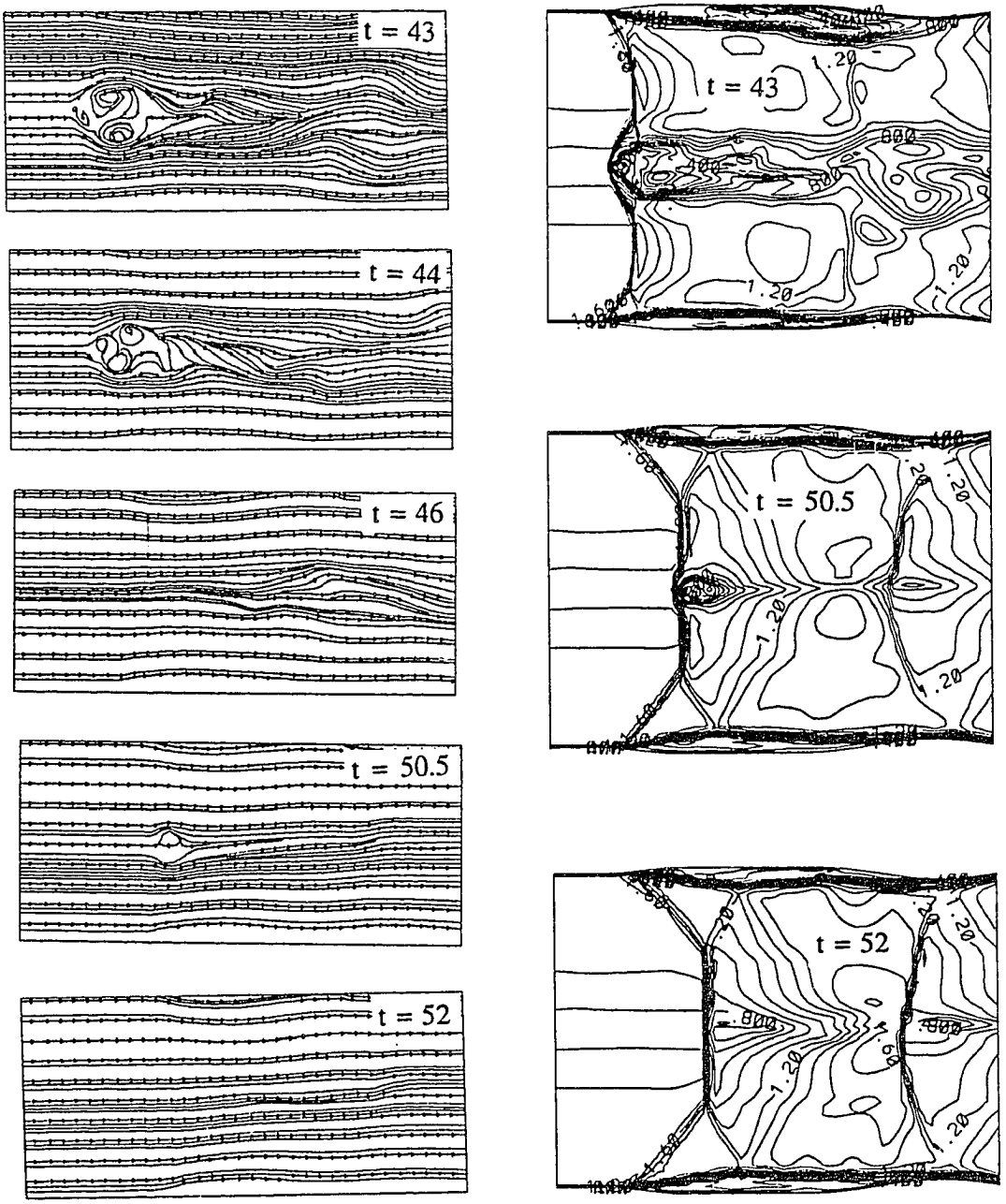

Figure 8.7: Cont'd

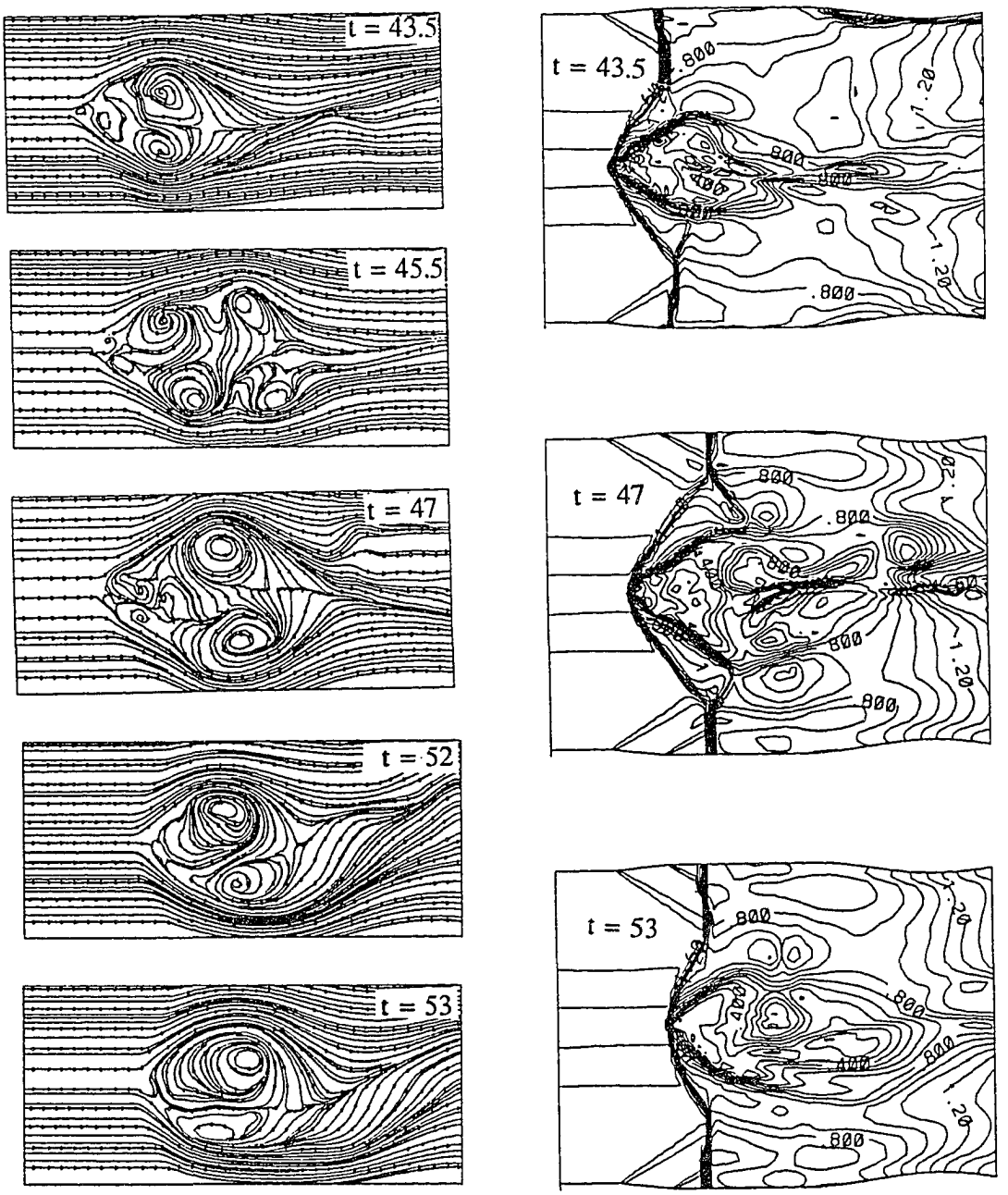

Figure 8.8 Streamlines and Mach contours in a horizontal plane for a supersonic swirling flow in a circular duct, $M_\infty = 1.75$, $\beta = 0.32$ and $R_e = 100,000$ using inviscid-wall boundary conditions.

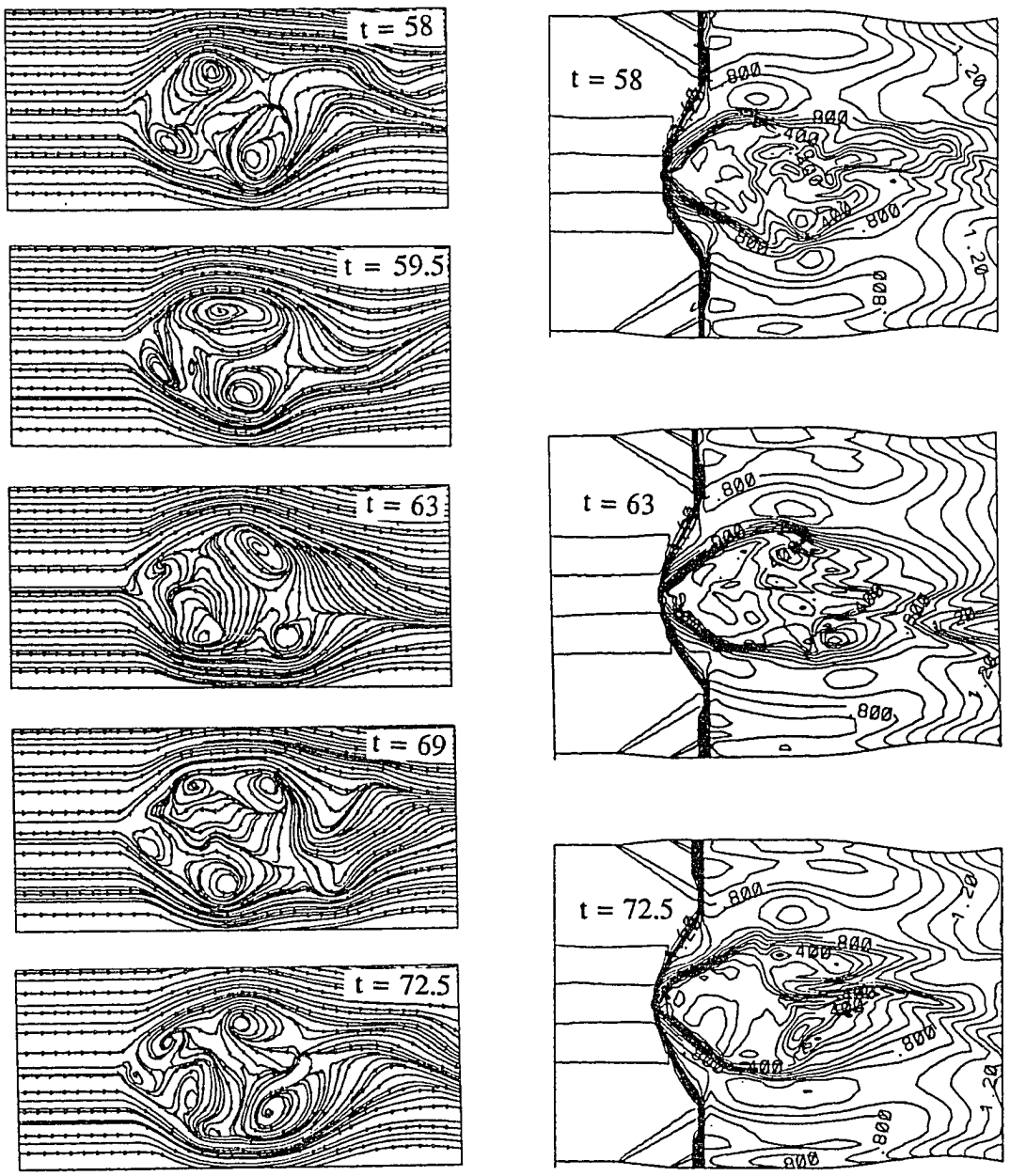

Figure 8.9 Streamlines and Mach contours in a horizontal plane for a supersonic swirling flow in a circular duct, $M_\infty = 1.75$, $\beta = 0.32$ and $R_e = 100,000$ using inviscid-wall boundary conditions.

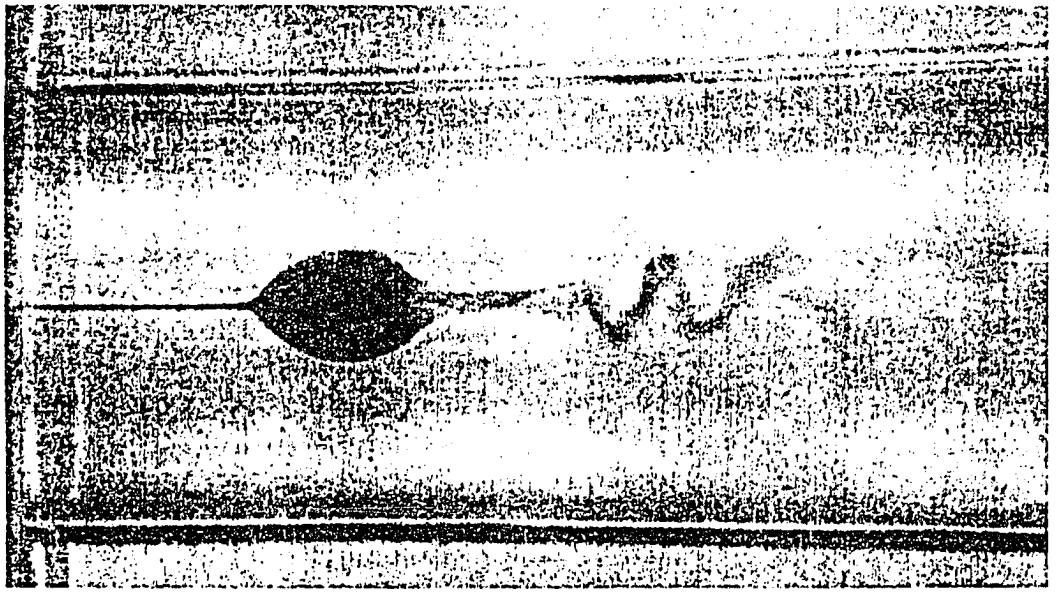

Figure 8.10 Experimental results of an incompressible swirling flow in a circular duct, from reference [38].

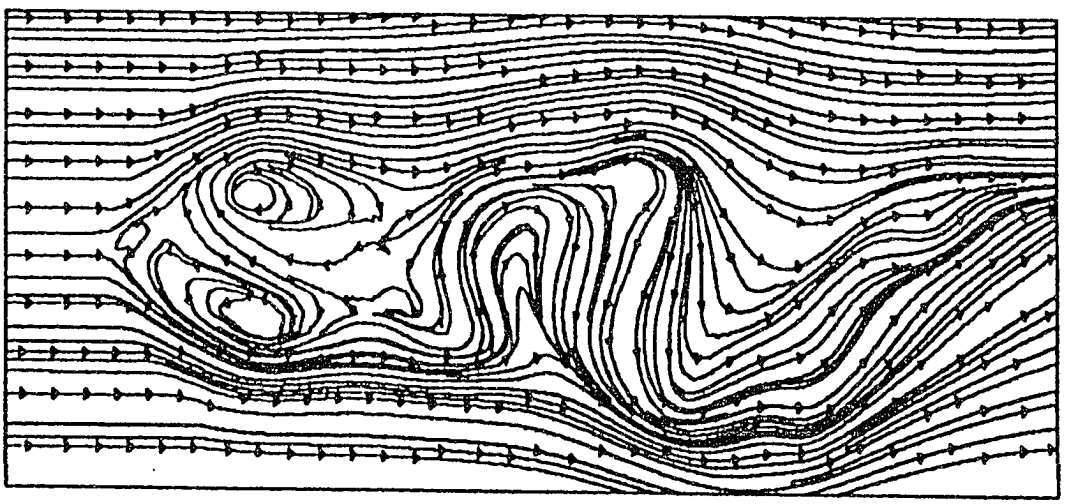

Figure 8.11 Streamlines on a horizontal plane for the flow case of $M_\infty = 1.75$, $\beta = 0.32$ and $R_e = 100,000$ at t = 38.5.

CHAPTER 9
THREE-DIMENSIONAL VORTEX BREAKDOWN OF A SUPERSONIC SWIRLING JET

9.1 Introduction

The problem of quasi-axisymmetric vortex flow and breakdown of a supersonic swirling jet, issued in a uniform supersonic freestream conditions, was considered in Chapter 7. For such problems the assumption of quasi-axisymmetric flow was used to reduce the computational time and memory by solving for only two meridian planes. Most of the available experimental results showed this type of flow to be three-dimensional and unsteady especially when a vortex breakdown occurred. Therefore, one has to consider the solution of the three-dimensional problem using the Navier-Stokes equations. In this Chapter, three-dimensional, unsteady full Navier-Stokes equations are solved using the implicit flux-difference, finite-volume scheme of Chapter 4 to computationally simulate the flow patterns and vortex breakdown due to the interaction of a supersonic swirling jet and a normal shock wave. The numerical examples include transient and quasi-steady supersonic vortex breakdowns. The effects of the grid points number and distribution and the grid type are presented. Finally, the results are compared with the available experimental results, and the three-dimensional effects are discussed as the quasi-axisymmetric results are compared with the present results. For the present numerical examples, the flow conditions at the inlet boundary are given by: $R_e = 296,000$, $M_j = 3.0$ and $M_\infty = 2.0$.

9.2 Boundary and Initial Conditions

9.2.1 Inflow Boundary Conditions

The inflow profiles used in this study are adapted from experimental measurements documented in References [88, 112]. Unfortunately, only one set of measurements was available along a radial line in these references. The experimental results were not symmetric about the vortex axis, as shown in Fig. 9.1. To obtain three-dimensional profiles at the inlet plane, two methods were used. In the first method, the asymmetry of the experimental profiles was kept by assuming the conditions along the upper half of the radial line to be constant on the meridian planes of the right-hand side of the inlet plane and the conditions along the lower half of the radial line were assumed to be constant in the left-hand side of the inlet plane, which means rotating the radial line by an angle of 180 degrees to cover the inflow plane. In the second method, only the upper half was considered and the conditions are assumed quasi-axisymmetric on the inlet plane. The main difference, beside the asymmetry of the flow conditions, is the swirl ratio, where the average swirl ratio in the asymmetric distribution is 0.2 and that of the quasi-axisymmetric is 0.22. Because of the lack of experimental data, this technique was used to study the effects of swirl ratio on the flow. The asymmetric and quasi-axisymmetric distributions of the inlet profiles are shown in Fig. 9.2 and Fig. 9.3, respectively. It should be noted here that the experimental data are used for $r < 1$ and then uniform wind-tunnel conditions corresponding to a Mach number of 2.0 are used to the end of the computational domain, $r = 3.5$. The quasi-axisymmetric assumption was used only at the inlet plane and was relaxed in the rest of the computational domain.

9.2.2 Outflow Boundary Conditions

The computational domain extended for a distance of 7.0 in the axial direction and the conditions at the outflow boundary were expected to be supersonic. Experimental measurements in References [88, 112] showed the flow to be supersonic a few radii downstream of the shock-vortex-interaction region. For such supersonic flows, the directions of the characteristics, according to the characteristic theory, are from inside to outside the computational domain. This was implemented by extrapolating all the flux vector components from the interior cell centers of the last axial plane of the computational domain outside.

The boundary conditions on the outer boundaries of the computational domain were assumed to be uniform conditions corresponding to irrotational wind-tunnel conditions at a Mach number of 2.0

9.2.3 Initial Conditions

The computations started with freestream conditions corresponding to a Mach number of 2.0 in the entire computational domain. This simulates the case of sudden discharge of a jet from a convergent-divergent nozzle in wind-tunnel uniform flow conditions.

9.3 Computational Domain and Types of Computational Grids

The computational domain is 7.0 nondimensional lengths in the axial direction, where the nozzle exit radius is taken to be the characteristic length. Both rectangular and circular grids were used to study the effects of the grid type on the flow patterns and vortex-breakdown modes. In cases of rectangular grids, the cross-flow plane is a square of a side length of 7.0 and in the case of circular grid, the cross-flow plane is a circle with a diameter of 7.0. The computational domain size was chosen such that the freestream conditions can be assumed on the outer boundaries. Four grids, with different grid point

numbers and distributions, were tested with the same initial and boundary conditions to study the grid effects on the vortex-breakdown modes. Three of these grids were rectangular grids ranging from a coarse grid in both the axial and cross-flow directions to a fine grid in all directions. In the following sections, each grid is presented along with snapshots of the solution obtained using this grid.

9.4 Effects of Grid-Point Distributions

9.4.1 Grid Number 1; Coarse Rectangular Grid

In this case, a coarse grid with a minimum grid-cell side length of 0.057 in the y and z directions and 0.0147 in the axial direction was used. The number of grid points was 210x51x51 in the axial and cross-flow directions, respectively. The grid points were clustered in the axial direction, near the inflow boundary, for good resolution of the vortex-shock interaction, and around the vortex-core axis, for good resolution of the vortex core and the recirculation zone. Figure 9.4 shows a cross-flow plane and a side view of grid number 1. The grid has no singularities and it was possible to use large time steps to advance the solution in time. Time-accurate solutions were obtained using a global time stepping with a dimensionless time step of 0.02.

Snapshots of the results are presented in Fig. 9.5 and Fig. 9.6. Figure 9.5 shows the streamline projections on a horizontal plane passing through the domain centerline and the total Mach-number contours on the same plane. Figure 9.6 shows the axial variation of the axial velocity component, density and static pressure along the domain center line.

At t = 2.0, the streamlines show the formation of a small recirculation zone. The deformation of the streamlines in the region from x = 0.75 to x = 1.0 indicates the existence of such a reversed flow zone. The total Mach-number contours, at the same time level, show the existence of a strong shock wave at the centerline. This shock was

formed because of the static pressure mismatch between the supersonic swirling jet and the surrounding wind tunnel conditions. The shock axial position is from x = 0.6 to x = 0.7 which was just ahead of the recirculation zone. The axial velocity distribution along the axis in Fig. 9.6 shows a small negative value at x = 0.75.

At t = 3.0, we notice that the bubble is enlarged and moved upstream to a position of x = 0.55. The formation of a two-bubble cell is clear. The Mach-number contours show the deformation of the shock wave according to the new bubble shape and the movement of the shock upstream. The axial velocity on the axis reached a high negative value of 0.96, as shown in Fig. 9.6.

At t = 4.0, the bubble was enlarged and the bubble diameter reached a maximum value of 0.6. The bubble moved further upstream and the shock system was pushed upstream to reach an axial station of x = 0.2. The axial velocity on the vortex axis had a negative value of 1.2. The enlargement of the bubble and its motion towards the inflow boundary continued as the solution advanced in time, as can be seen at t = 5.0, where the bubble diameter became 0.65 and the shock–front axial position was 0.15. At this time level the axial velocity at the axis was -1.18. Furthermore, the bubble and shock system started to oscillate in the axial direction, where the shock was being deformed and pushed due to the continuous dynamic motion of the bubble system.

Snapshots of the solutions at time levels higher than 10.0 suggested that the solution was quasi-steady where the bubble-shock system was oscillating around a fixed axial location. The snapshots show the maximum change in the bubble size to be less than 10% and hence the computations stopped at t = 20.0. It was noticed also that the axial velocity recovered supersonic values at the outflow boundary and hence the use of extrapolation boundary conditions was justified.

9.4.2 Grid Number 2, Fine Grid in the Cross-Flow Plane and Coarse in the Axial Plane

In this numerical example, the grid points were redistributed in order to have better resolution of the vortex core and the vortex-shock interaction region. The grid consisted of 145x61x61 grid points in the axial and cross-flow directions, respectively. The minimum grid-cell-side length in the cross-flow plane was 0.024 and in the axial direction was 0.014. Cross-flow plane and a side view of the grid are shown in Fig. 9.7.

Exact initial and boundary conditions as those used with grid number 1 were used in this case. Snapshots of the solutions are presented in Fig. 9.8 and Fig. 9.9, where the streamlines and Mach-number contours are shown in Fig. 9.8 and the axial variations of axial velocity, density and static pressure at the vortex axis are shown in Fig. 9.9.

The solution at t = 2.0 shows the formation of a small two-cell bubble-type vortex breakdown behind the shock wave system. the bubble size is larger than that of grid no. 1 at the same time level.

At t = 3.0, The snapshots show the enlargement of the bubble and its movement towards the inlet boundary. The bubble became very large compared to that of grid no. 1 and the bubble-shock-system axial location was nearer to the inlet boundary. It is interesting to notice here the difference in the bubble aspect ratio where the length, in the axial direction, is very large compared to the width, in the radial direction, compared to that of grid no. 1. It should be noted here that the number of grid points in the lateral direction was increased while the number of grid points in the axial direction was decreased, in comparison with grid no. 1. This result will be emphasized more by comparing the solution in further time levels.

At t = 4.0, the snapshots show the motion of the bubble downstream with a reduction in its size. The streamlines in Fig. 9.8 show the formation of a small bubble just behind

the shock wave. It is noticed that this bubble appeared only on one side of the horizontal plane. The formation of a multi-bubble system behind the shock changed its shape, as can be seen in Fig. 9.8.

At t = 5.0, a two-bubble system could be recognized behind the shock. It was noticed that the shock shape changed because of the disappearance of the third asymmetric bubble that was formed at t = 4.0. As mentioned earlier, the bubble aspect ratio reflects the grid aspect ratio.

As the solution advanced in time, it was noticed that continuous change in the bubble size, shape and location took place at larger amplitudes than those in the case of grid no. 1.

Snapshots at t = 10.0 show the size of the bubble to be smaller than that of grid no. 1, with a smaller negative value of the axial velocity at the vortex axis. The shock-bubble system moved downstream where the shock front was located at x = 0.4 compared to 0.1 in case of grid no. 1.

The bubble system at t = 12 was distorted with the vortex ring changing its shape. The change was reflected on the shock shape where a larger normal part can be noticed. The changes continued and the solution was not expected to reach a steady or quasi-steady state as in the case of grid no. 1, as can be seen at t = 16.

A surprising result is shown at t = 20.0 where the bubble system disappeared leaving only some deformations of the streamlines. No reversed flow zones were present behind the shock. At t = 21.0, a small bubble was formed behind the shock wave similar to what happened at t = 2.0.

At t = 22.0, the snapshots show a single bubble with a negative axial velocity of 0.4 at the vortex axis. A two-bubble system was formed at t = 24 where an asymmetric

bubble can be seen from the streamlines in Fig. 9.8. Solutions at t = 26 and t = 28 show the formation of asymmetric recirculation zones with moderate to small values of negative axial velocities. It is clear that the solution is highly unsteady in comparison with that of grid no. 1. Also, the three-dimensional effects are more significant.

9.4.3 Grid Number 3, Fine Grid in All Directions

In this case the number of grid points was kept the same as in grid no. 2, but the grid points in the axial direction were redistributed to have better resolution near the inflow boundary. It was noticed, from the previous cases, that the important variations in the flow variables were in the region upstream of x = 2.0, therefore the grid points in the axial direction were redistributed such that 90 axial stations were located from x = 0 to x = 2.0, compared to 71 stations in grid no. 2. The minimum grid-cell-side length in the axial direction was 0.0084. In the cross-flow plane, the grid points were redistributed such that almost uniform-spacing grid cells were achieved at the computational domain outer edges. The grid is shown in Fig. 9.10 and the results are shown in Fig. 9.11

The results show no recirculation zone at the initial time step level as was the case with previous grids. A small bubble was captured at t = 2.0 off the vortex axis. The small bubble disappeared, as shown at t = 4.0. Another small bubble was formed at t = 6.0 which disappeared after that. No more bubbles were captured which means that the disturbances caused by the shock/vortex interaction were dissipated by the fine grid cells.

It was thought that the quasi-axisymmetric inflow profiles that have higher swirl ratio may be used with this grid to study the effects of the swirl ratio along with the effects of the grid distributions. The results are shown in Fig. 9.12 and Fig. 9.13. The results show the formation of a small two-bubble cell at an axial position of x = 0.75. The shock wave is almost axisymmetric because of the iniflow profile symmetries and the

normal part of the shock was small compared to those of the coarse grids. The bubble shape was changing and some asymmetric variations can be seen at t = 3.0, 5.0 and 16.0. The axial velocity variation at the vortex axis shows small negative values where the maximum negative value was 0.3 at t = 4.0. These values are much smaller than those of the coarser grids.

9.4.4 Grid Number 4, Circular Grid

In this case a circular grid consisting of 145x61x49 grid points in the axial, radial and wrap-around directions, respectively, was used. The grid points were clustered around the axis for resolution of the vortex core and around r = 1 for resolution of the shear layer between the swirling jet and the irrotational freestream flow. In the axial direction, the grid points were distributed as in the case of grid no. 3. The circular grid has the advantage of offering better resolution near the axis, where it is needed. The number of grid points in the radial direction are added up along the vortex diameter to provide better resolution with the same number of grid points used in previous grids. In this case double the number of grid points were employed along the vortex diameter. Figure 9.14 shows the circular grid used in this study.

As in the case of grid no. 3, two sets of inflow profiles, namely quasi-axisymmetric and asymmetric, were used with this grid. The results are shown in Fig. 9.15 for the asymmetric inflow profiles. As with grid no. 3, a small bubble was formed behind the shock system which disappeared after a few time steps.

Figure 9.16 shows the streamlines and Mach number contours for the quasi-axisymmetric inflow profiles. Selected snapshots of the axial distributions of the axial velocity, density and static pressure along the centerline are shown in Fig. 9.17. The results show the formation of a multi-bubble vortex breakdown behind the central strong

part of the shock system. A two-bubble cell was then established and persisted for the rest of the computational time. the relative size of the two bubbles was always changing but the global picture can be looked at as a quasi-steady one. The change in the bubble location with respect to the inflow boundary was negligible. Downstream of the bubble system, asymmetric effects were observed which were also the case with previous grids. The negative axial velocity along the axis reached a maximum value of 0.9 at t = 4.0 and then a constant value of 0.7 was kept for larger time levels.

9.4.5 Topological Study of the Sectional Streamlines on a Horizontal Plane.

Figure 9.17 shows the streamlines on a horizontal plane passing though the vortex-breakdown bubble for the flow case of M_j = 3.0, M_∞ = 2.0 and R_e = 296,000. Those results were obtained using Grid number 1. The topology of the computed bubble is qualitatively compared with the experimental results of Lin and Rockwell [113] in Fig. 9.18. The experimental results were obtained for an incompressible vortex breakdown on a delta wing at high angle of attack. Both computed and experimental streamline patterns display the same number and type of critical points [114, 115, 116] in the breakdown region. Four critical points were recognized; two saddle points (S_1 and S_2), a stable (attracting) focus (F^+) and an unstable (repelling) focus (F^-). The comparison shows that the results are in good qualitative agreement although the supersonic vortex breakdown is developed as a result of the vortex/shock interaction while the incompressible vortex breakdown is caused by the adverse axial pressure gradient on the delta wing. The present computational and experimental bubble structures differ from the mean axisymmetric patterns of Faler and Leibovich [38] and Escudier [12] presented in Chapter 6 since the present flow case is three dimensional. Moreover, it is observed that the internal structure of the breakdown bubble is not symmetric around the vortex axis.

9.5 Summary and Discussion

Four grids were used in the study of three-dimensional vortex breakdown of a supersonic swirling jet issued in a uniform supersonic freestream. Different distributions of the grid points were used to study the effects of the grid on the formation and modes of vortex-breakdown bubbles. It was found that large bubbles were formed with coarse grids while smaller bubbles were formed with finer grids. Using the same inflow profiles, quasi-steady bubbles were formed with coarse grids while transient smaller bubbles were formed with finer grids.

It is interesting to compare the effects of the grid point distributions with those of the Reynolds numbers. In Chapter 6, it was shown that decreasing the Reynolds number has resulted in producing smaller transient bubbles which is similar to using finer grids. This means that using coarse grids has the same effect as simulating flows at higher values of Reynolds numbers. This hypothesis will be discussed further when we discuss some of the previous work of other investigators.

It should be noted here that the coarsest grid used in this study, grid no. 1, is much finer than most of the grids used by previous investigators (e. g. [56], [72] and [78]). In those studies, only small Reynolds numbers could be used while the results were comparable to experimental results at higher Reynolds numbers by at least one order of magnitude. It is understood now that using coarse grids has made it possible to simulate experimental results at higher Reynolds numbers. For a long time it was thought that a Reynolds number of 200 was the upper limit for the numerical methods. Further studies are needed to decide on the grid size needed to simulate experimental measurements with the same Reynolds numbers.

In the experimental study carried out by Metwally, et al. [88], it was reported that

it was very difficult to capture any vortex-breakdown bubble. It is understood now that the size of the bubble was very small for the following reasons: a) in comparing the present results with experimental results, only the results of fine grids are considered. This means that only small transient bubbles are expected for these flow conditions, b) even with larger bubbles, with coarse grids, the size will be very small if the sizes are transformed to actual dimensions. As an example, the largest bubble diameter was 0.6 of the characteristic length which equals 2.4 mm. for a nozzle exit radius of 4.0 mm. Smaller values are expected with finer grids.

Comparing the results with the quasi-axisymmetric results in Chapter 7, it was noticed that the three-dimensional effects are clear especially inside and downstream of the bubble system. The three-dimensional relieving effects downstream of the vortex-breakdown region helped the flow to recover supersonic conditions at the outflow boundary, which justified the use of the extrapolation boundary conditions at the outflow boundary. Similar effects were observed for three-dimensional vortex flows in ducts, Chapter 8.

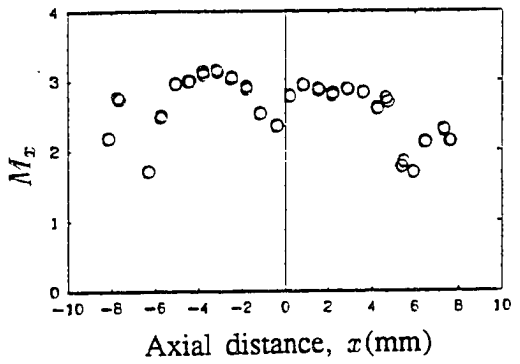

a- Axial Mach number distribution

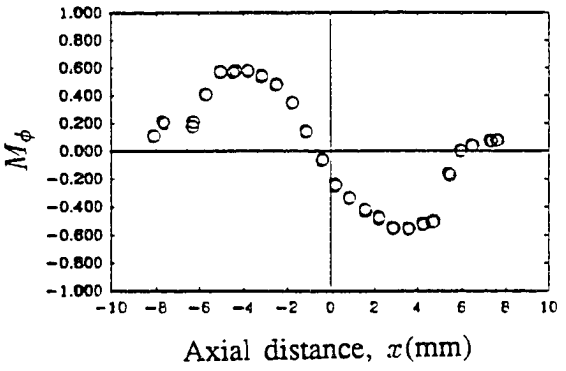

b- Tangential Mach number distribution

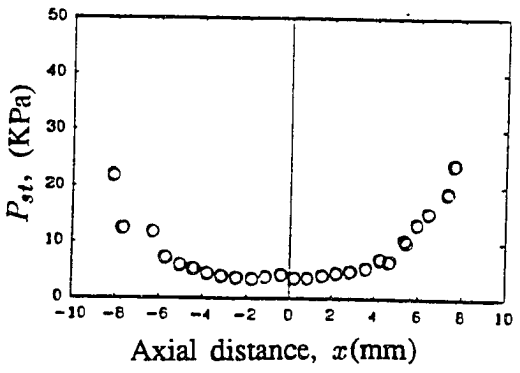

c- Static pressure distribution

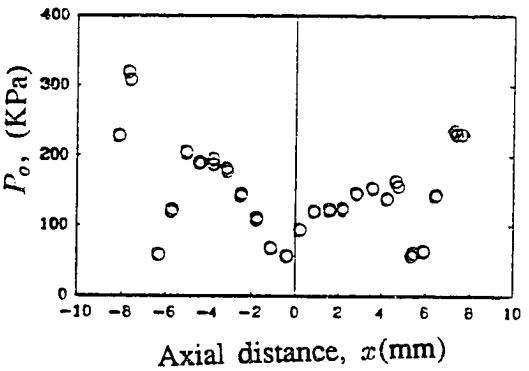

d- Total pressure distribution

Figure 9.1 Experimental measurements at the nozzle exit for a supersonic swirling jet in uniform wind-tunnel conditions, $M_j = 3.0$, $M_\infty = 2.0$ and $R_e = 296,000$.

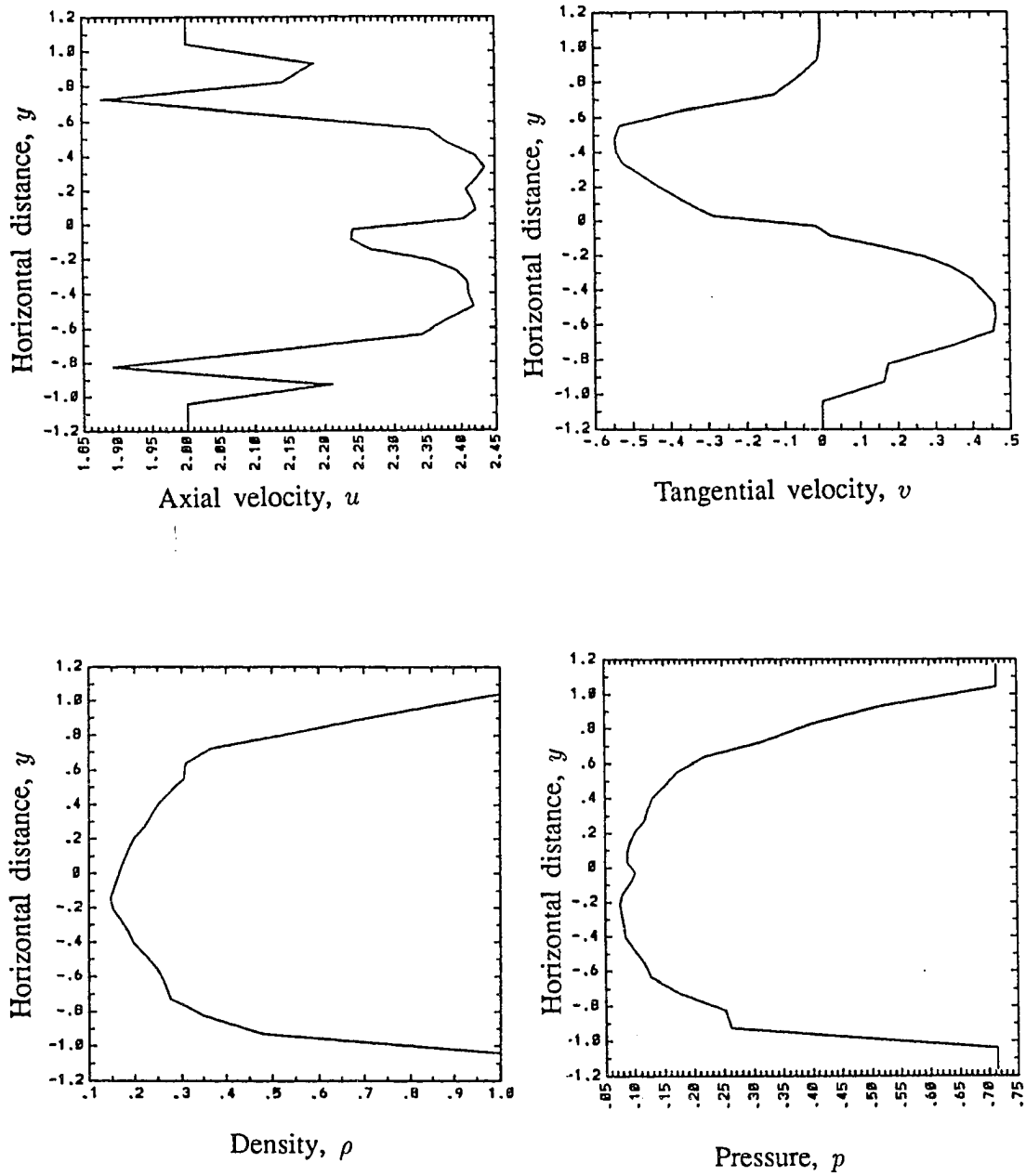

Figure 9.2 Three-dimensional asymmetric initial flow profiles at $x = 0.0$ for supersonic swirling jet from a nozzle, $M_j = 3.0$, $M_\infty = 2.0$ and $R_e = 296,000$.

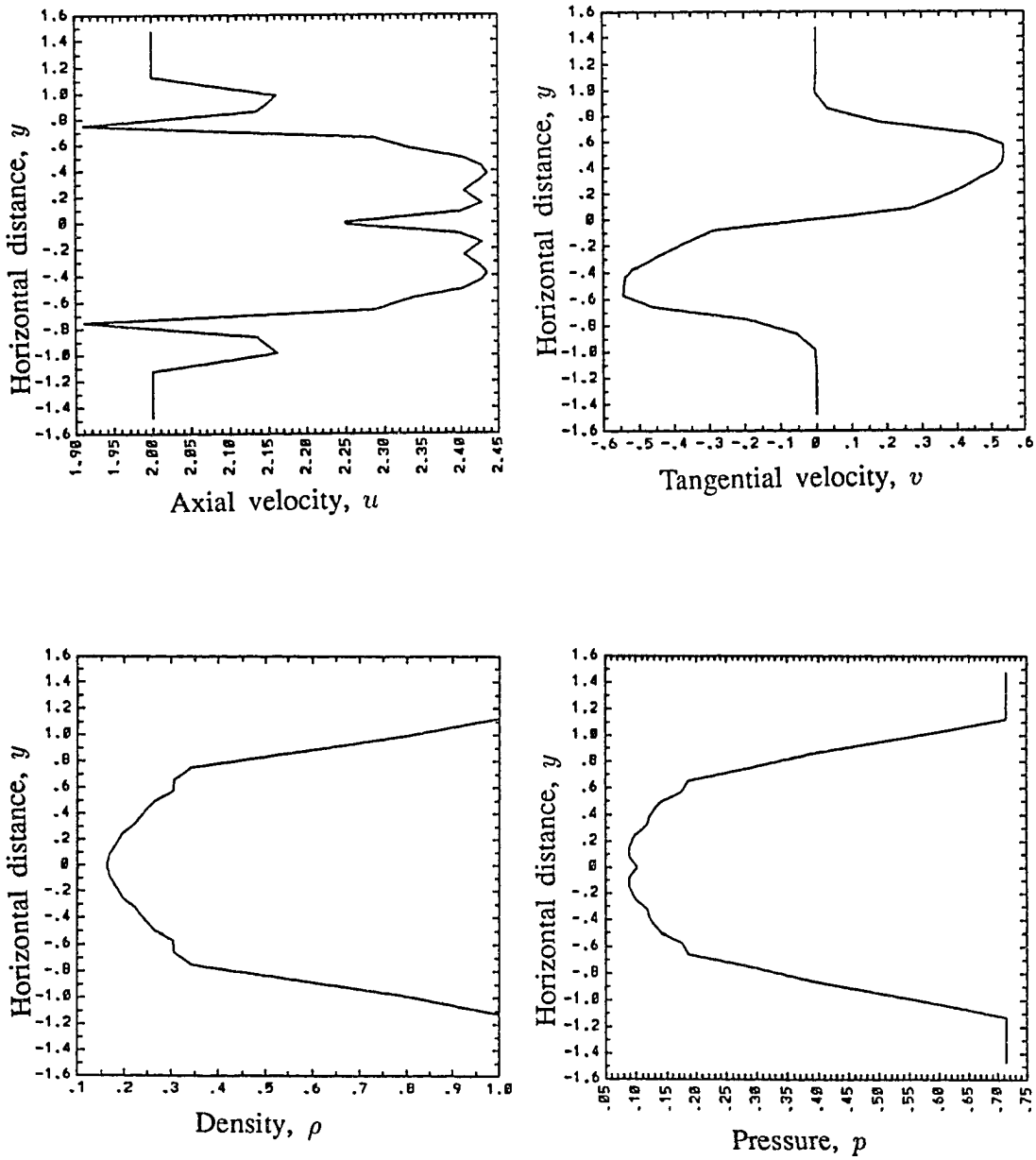

Figure 9.3 Three-dimensional quasi-axisymmetric initial flow profiles at $x = 0.0$ for supersonic swirling jet from a nozzle, $M_j = 3.0, M_\infty = 2.0$ and $R_e = 296,000$.

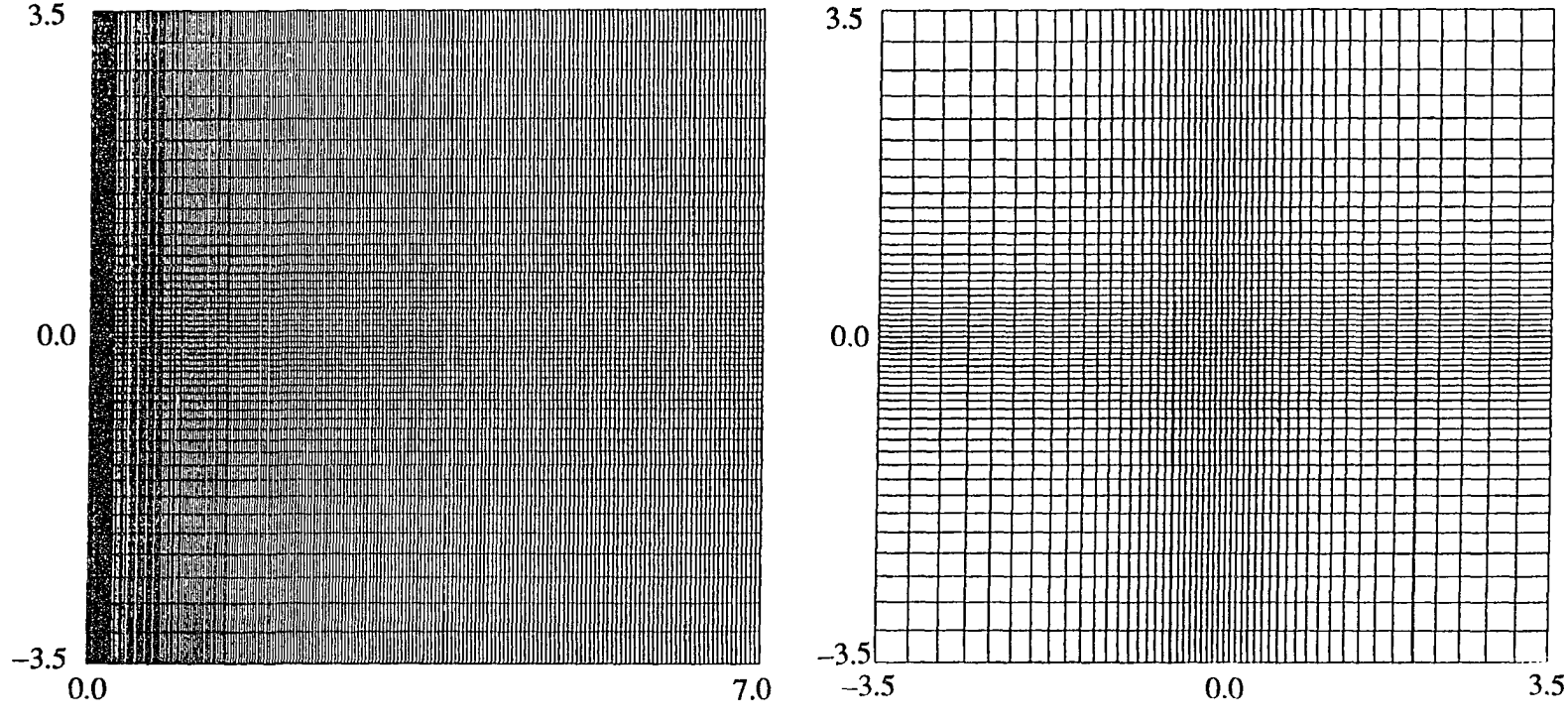

a- Axial plane

b- Cross-flow plane

Figure 9.4 Grid number 1 (rectangular coarse grid in the cross-flow plane), 210x51x51 grid points in the axial and cross-flow plane, respectively.

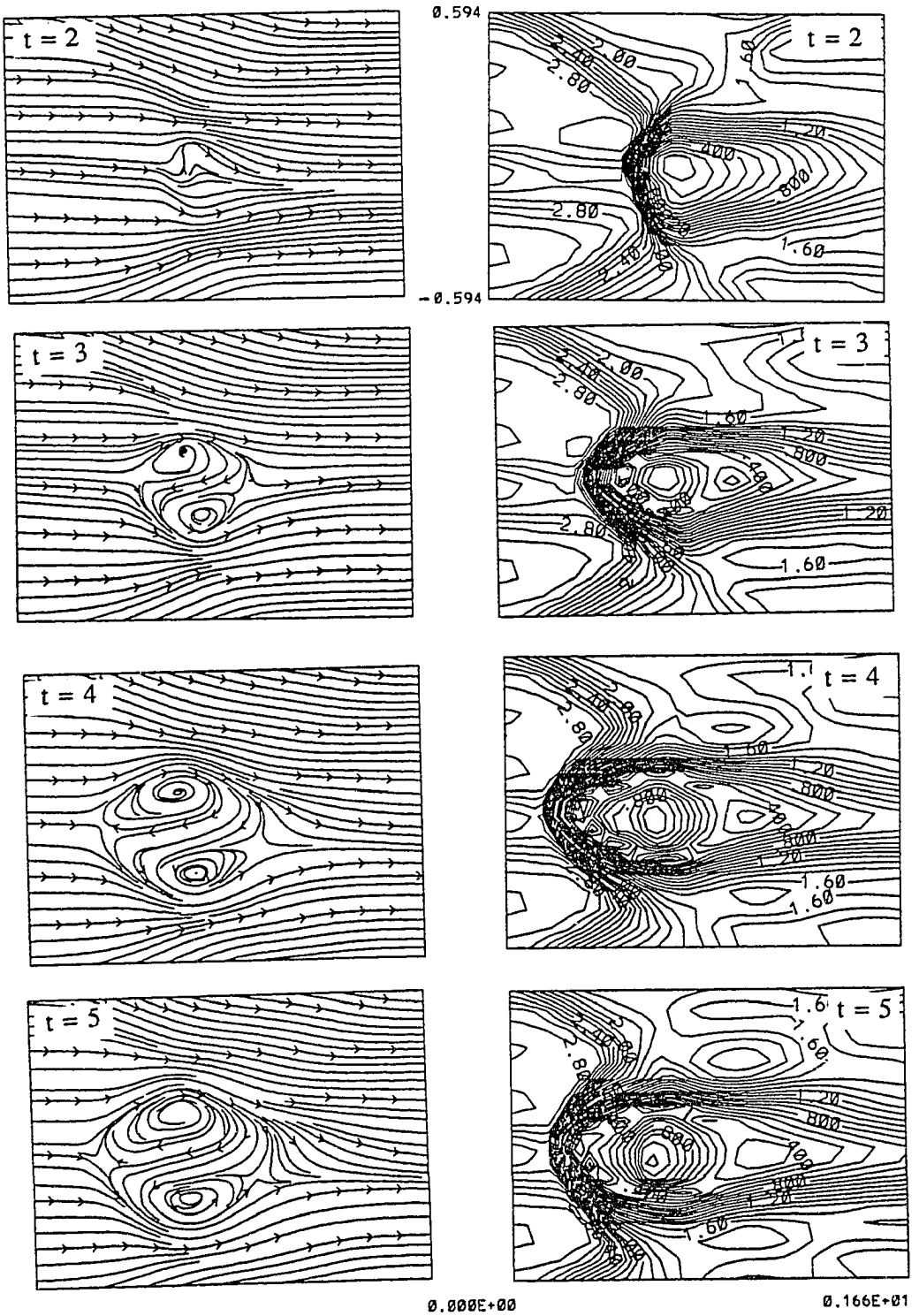

Figure 9.5 Streamlines and Mach contours in a horizontal plane for a supersonic swirling jet using grid number 1, $M_j = 3.0$, $M_\infty = 2.0$ and $R_e = 296,000$.

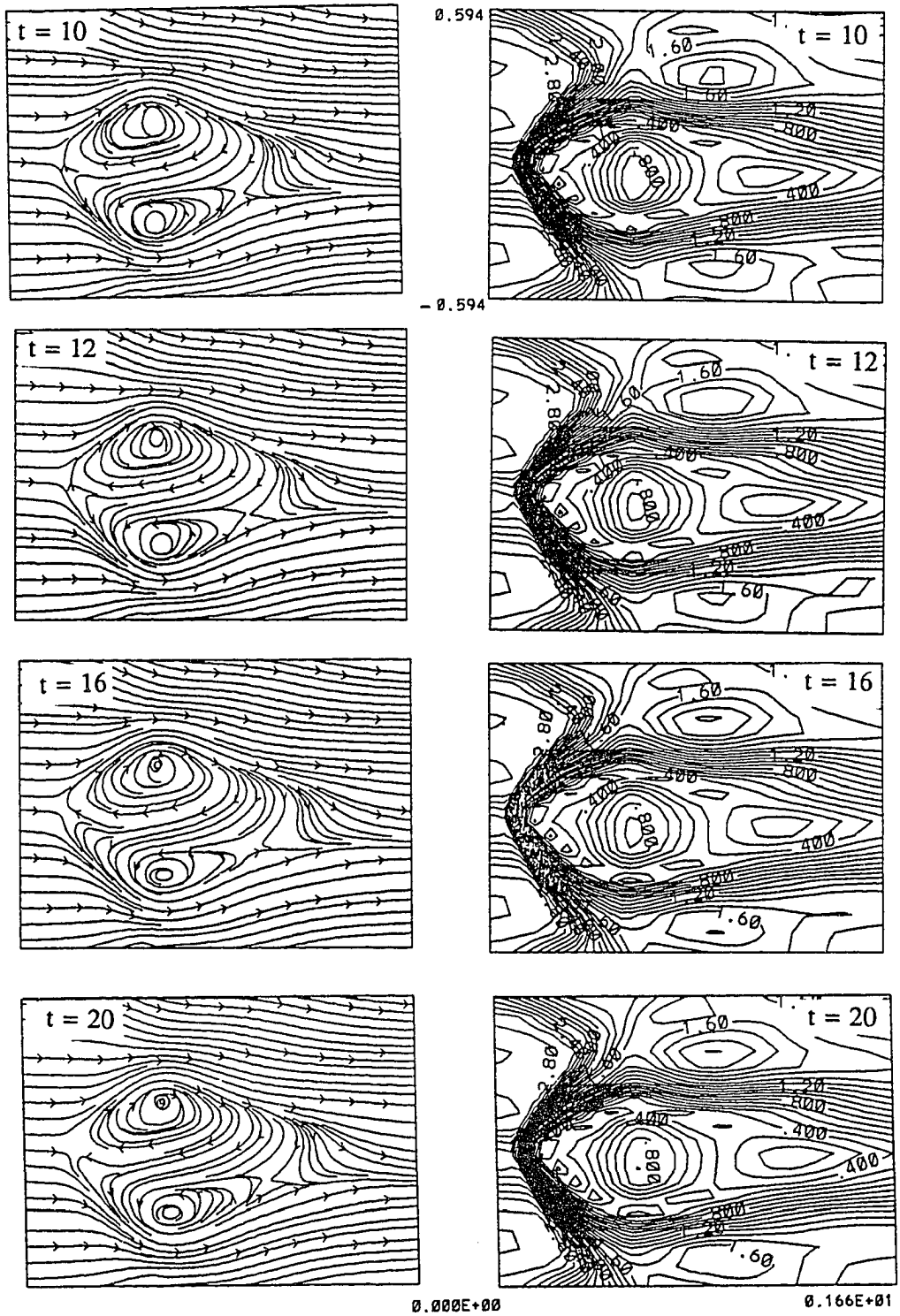

Figure 9.5: Cont'd

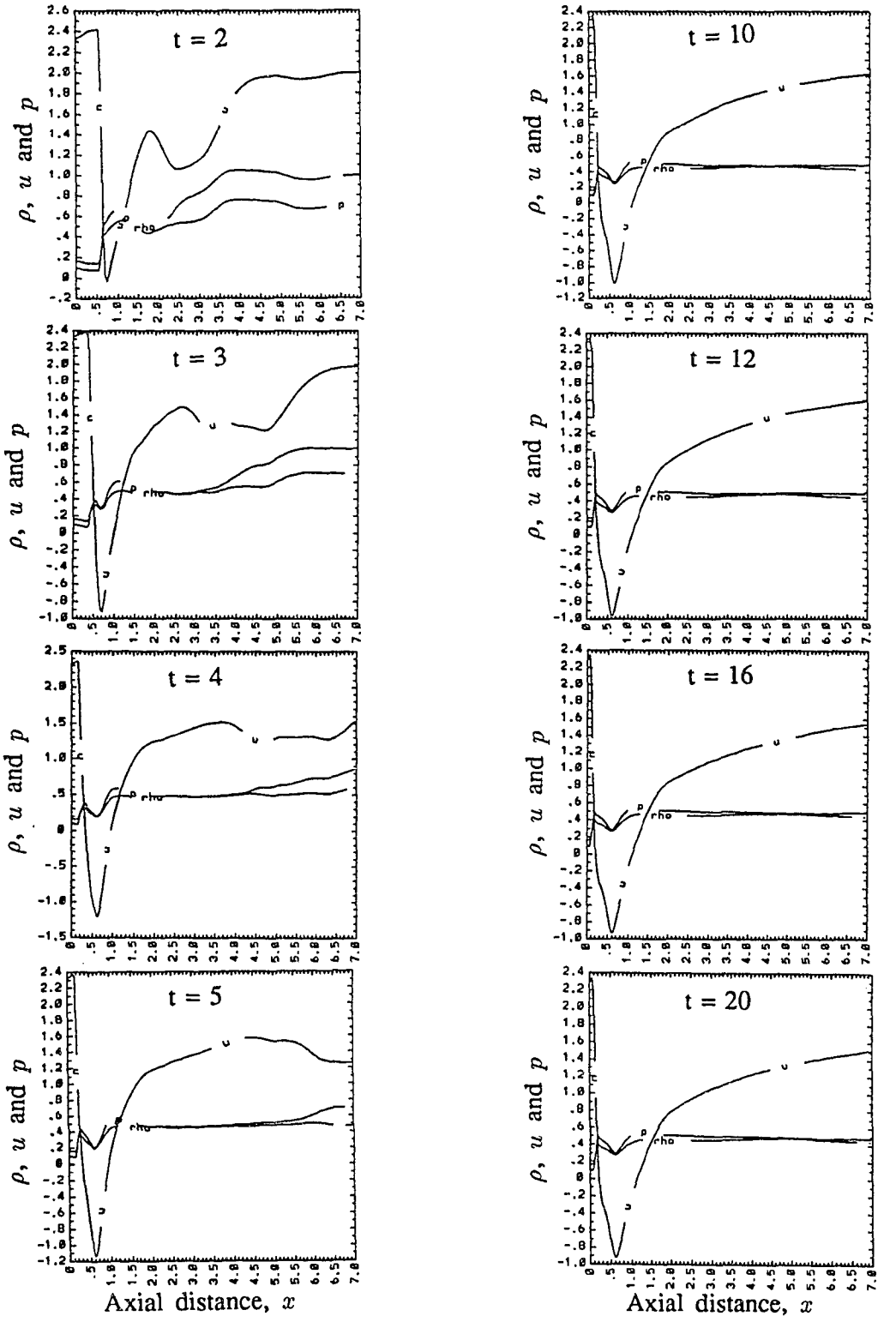

Figure 9.6 Axial distributions of the axial velocity, u, density, ρ and pressure, p, for a supersonic swirling jet using grid number 1, $M_j = 3.0, M_\infty = 2.0$ and $R_e = 296,000$.

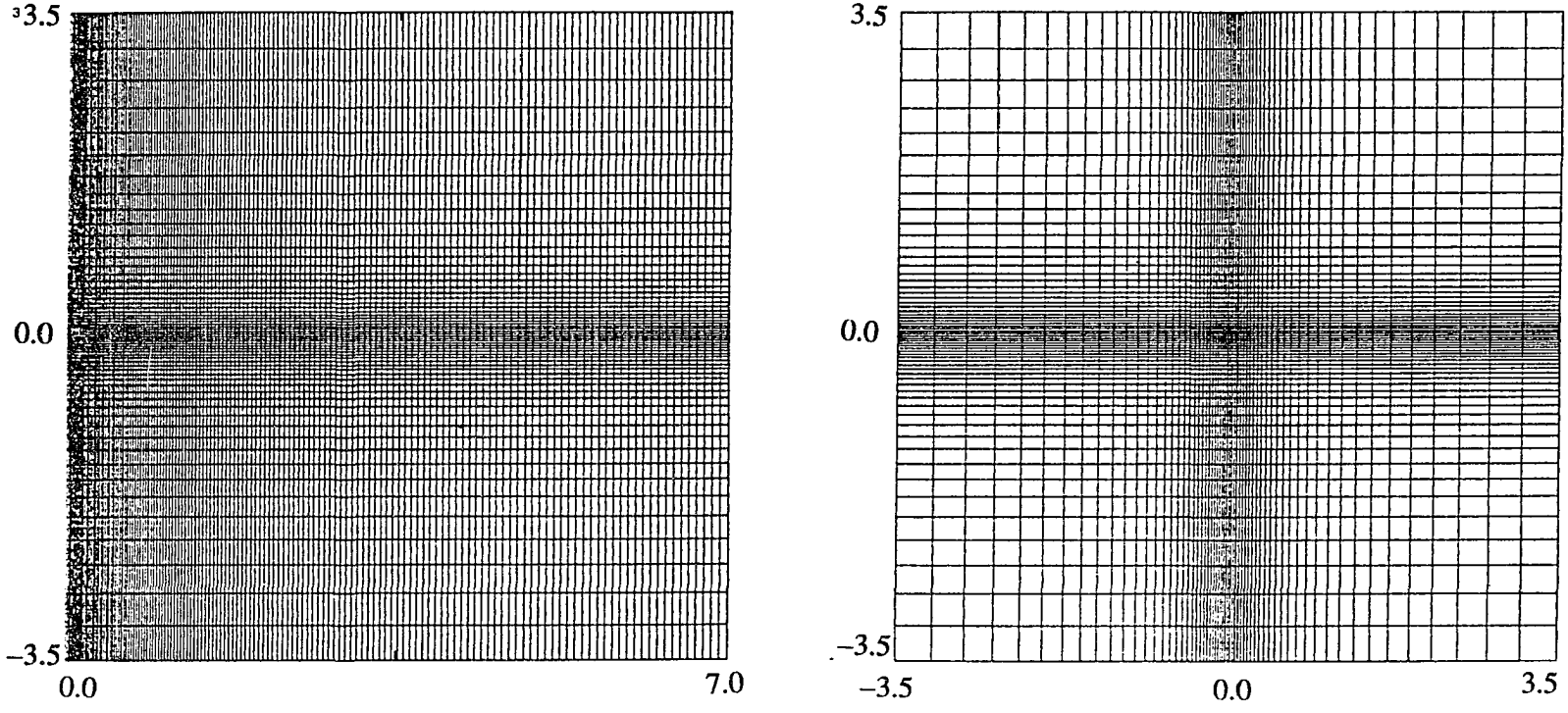

a- Axial plane

b- Cross-flow plane

Figure 9.7 Grid number 2 (rectangular fine grid in the cross-flow plane), 145x61x61 grid points in the axial and cross-flow plane, respectively.

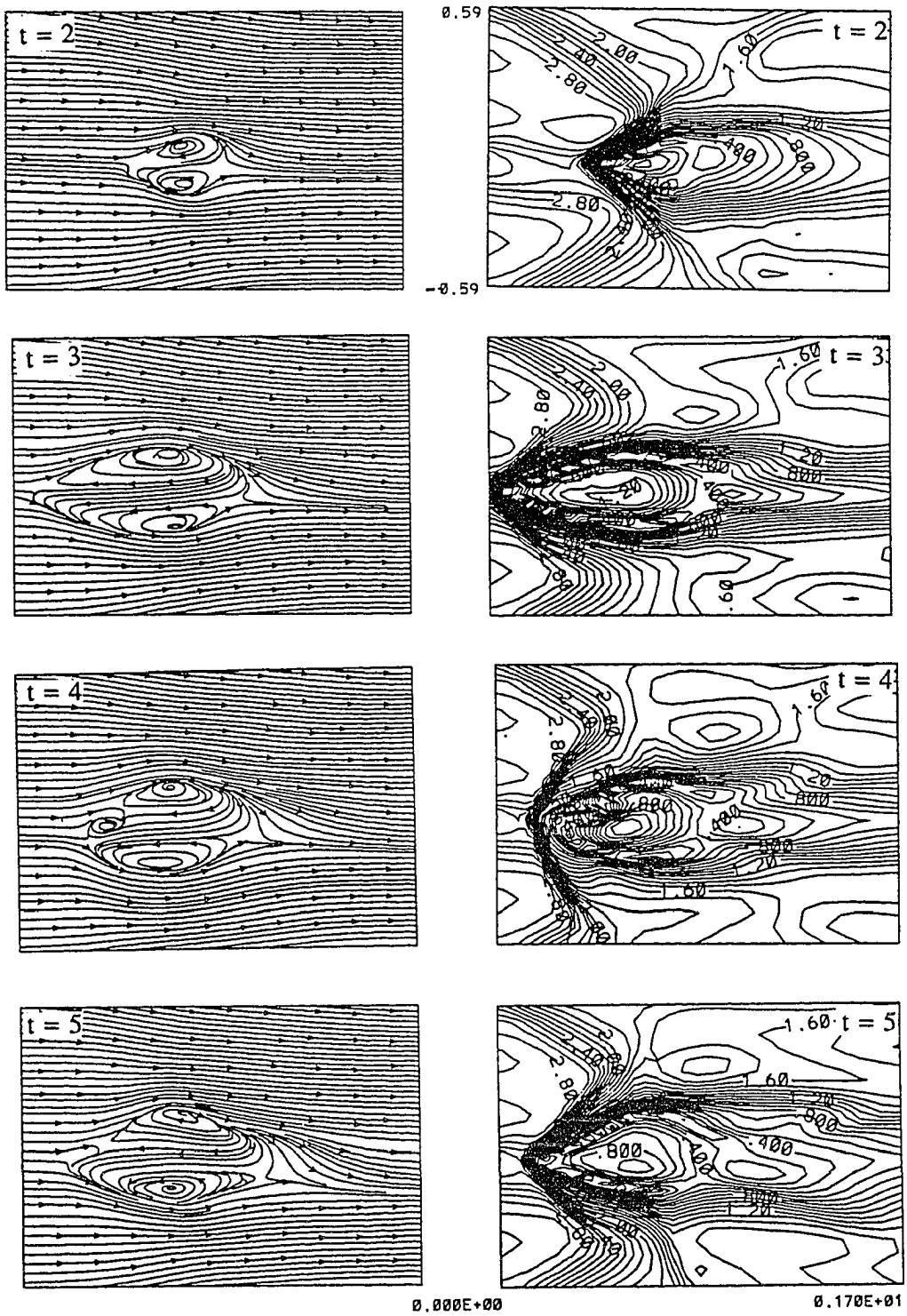

Figure 9.8 Streamlines and Mach contours in a horizontal plane for a supersonic swirling jet using grid number 2, $M_j = 3.0$, $M_\infty = 2.0$ and $R_e = 296,000$.

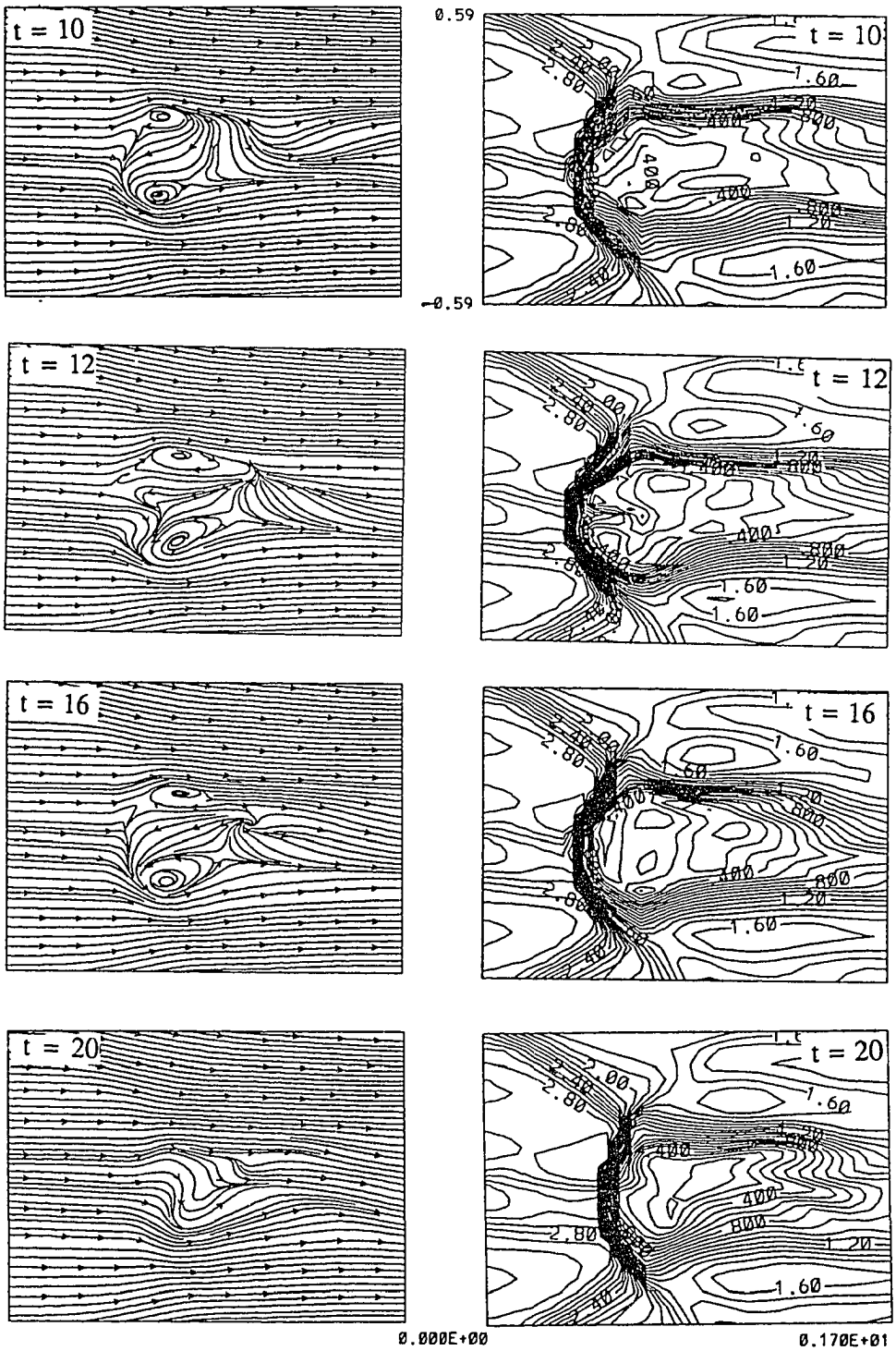

Figure 9.8: Cont'd

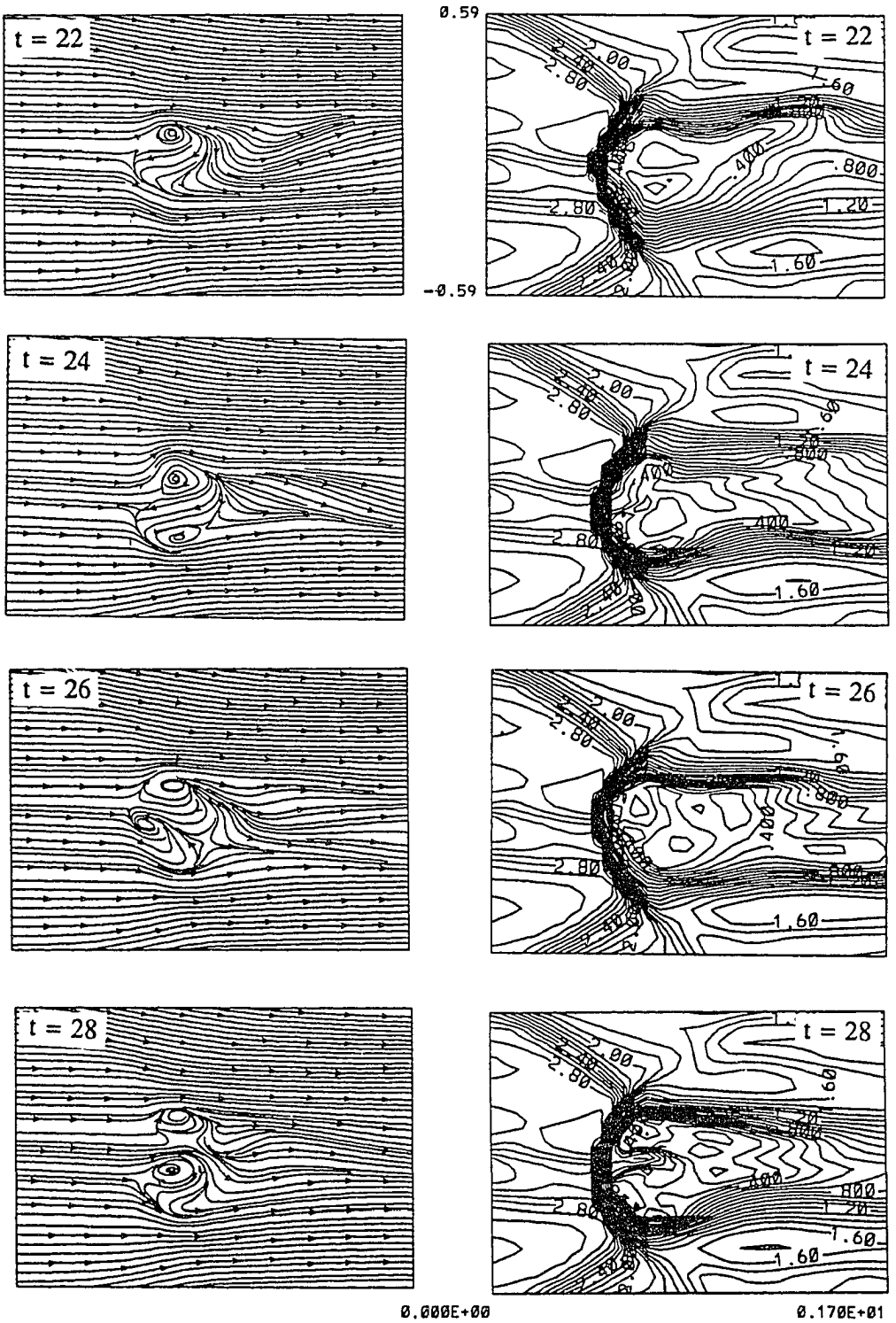

Figure 9.8: Cont'd

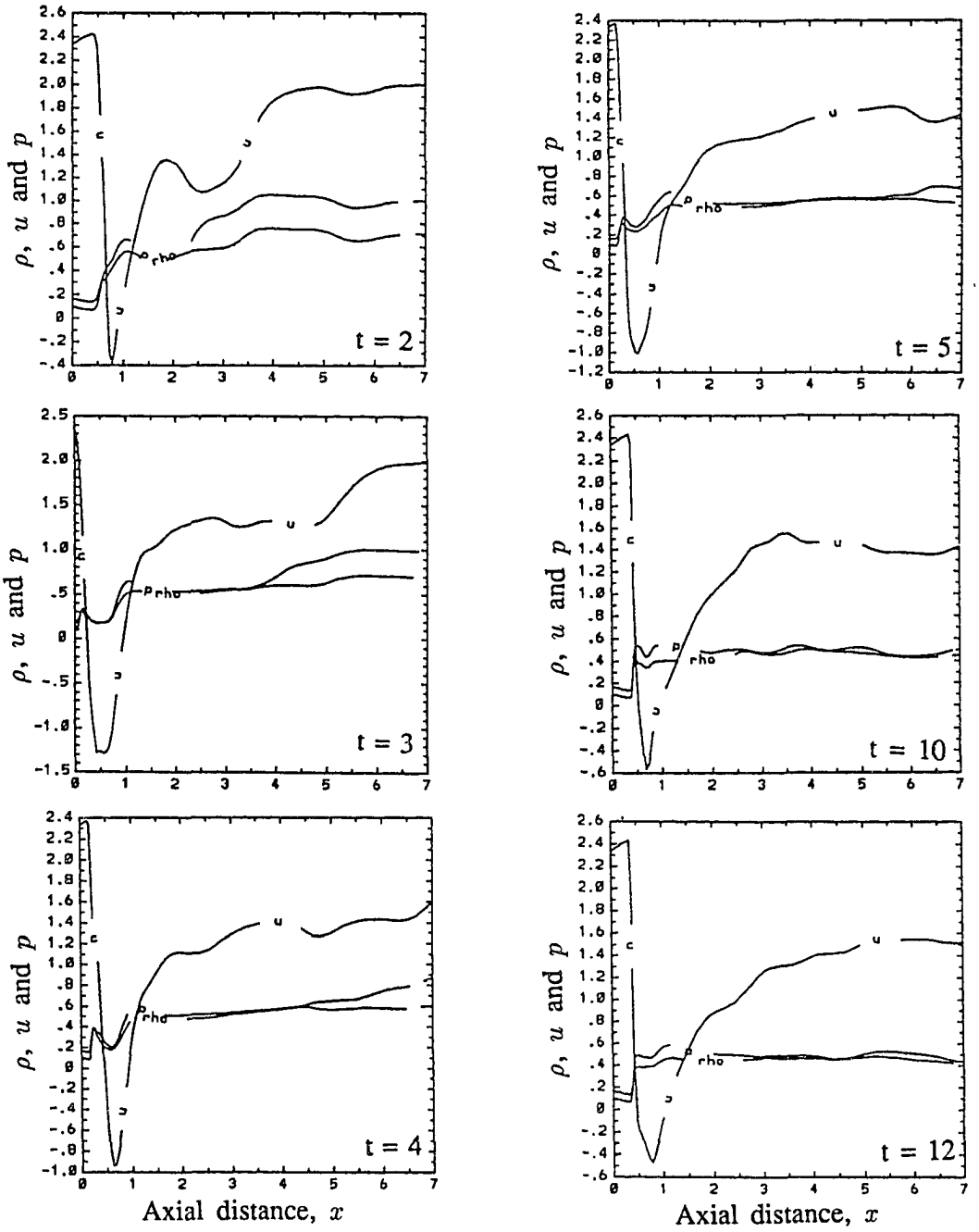

Figure 9.9 Axial distributions of the axial velocity, u, density, ρ and pressure, p, for a supersonic swirling jet using grid number 2, $M_j = 3.0$, $M_\infty = 2.0$ and $R_e = 296,000$.

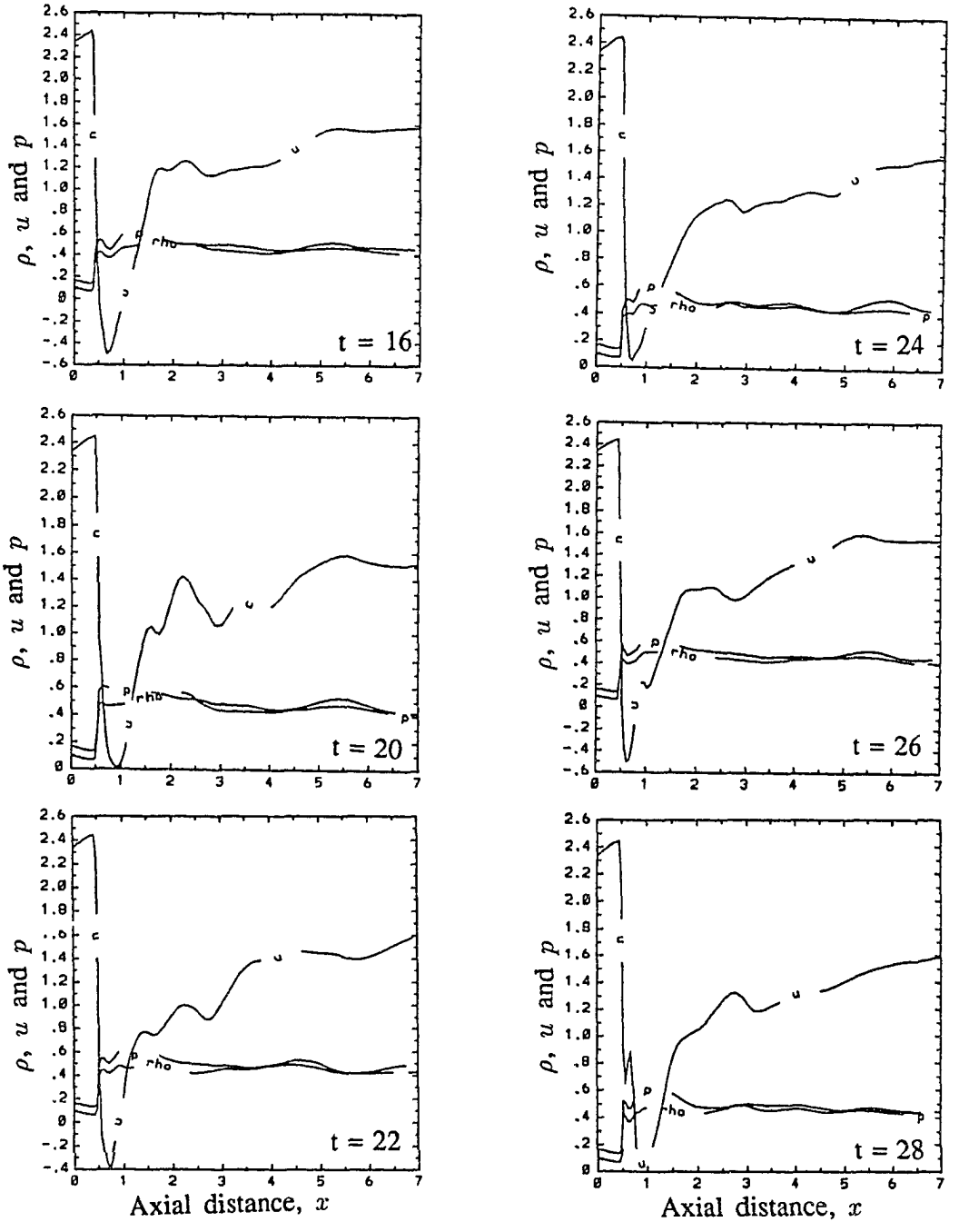

Figure 9.9: Cont'd

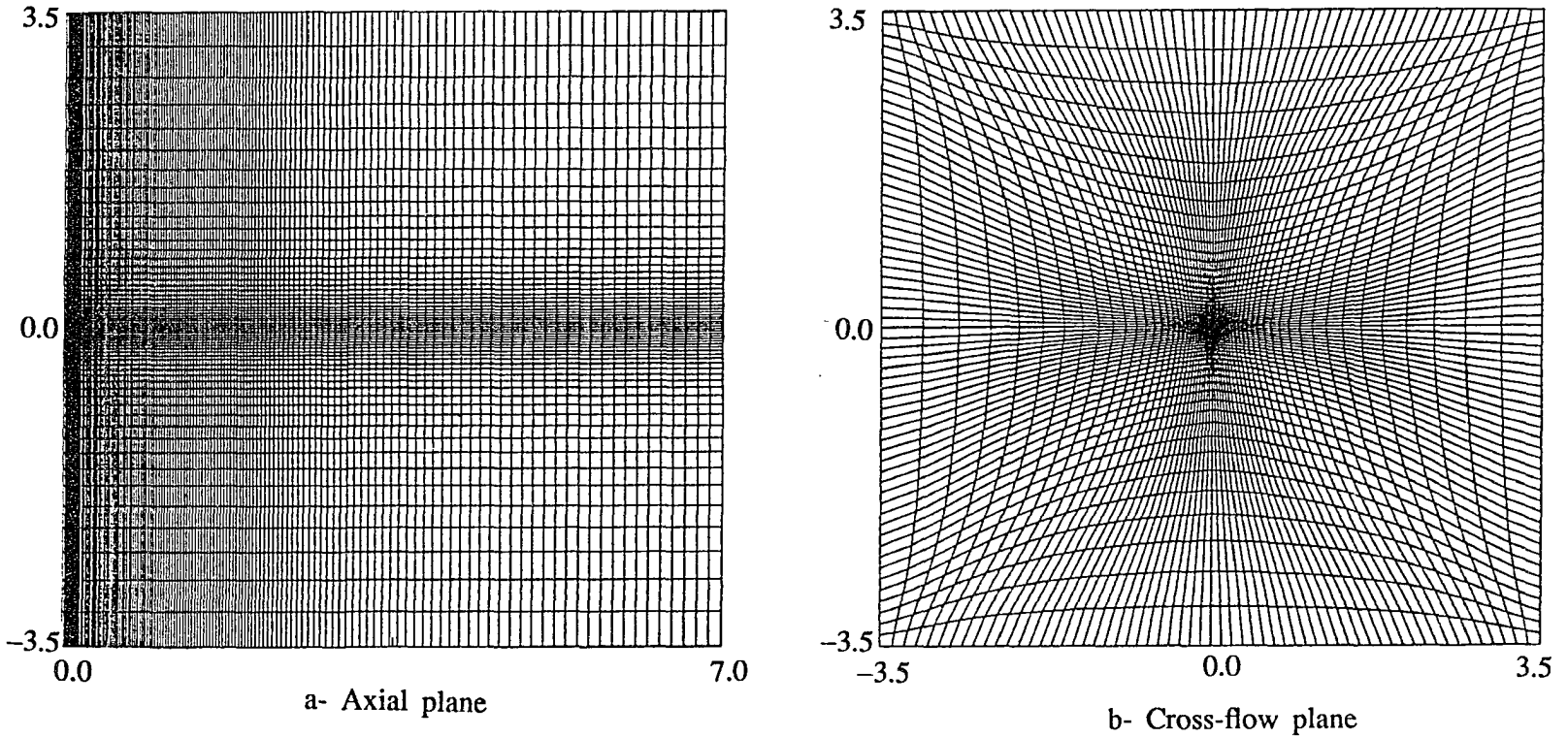

Figure 9.10 Grid number 3 (rectangular fine grid), 145x61x61 grid points in the axial and cross-flow plane, respectively.

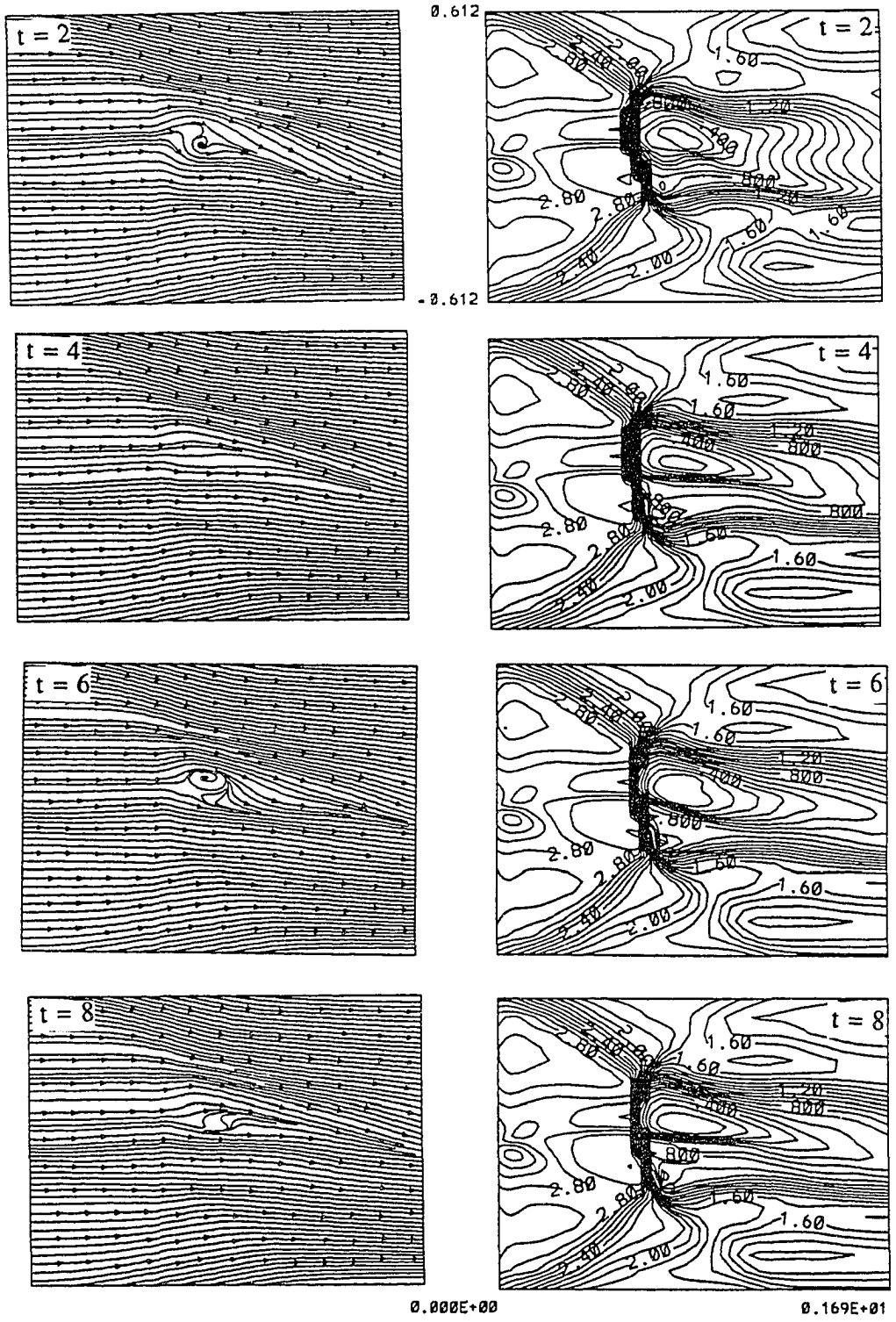

Figure 9.11 Streamlines and Mach contours in a horizontal plane for a supersonic swirling jet using grid number 3 with asymmetric initial flow profiles, $M_j = 3.0$, $M_\infty = 2.0$ and $R_e = 296,000$.

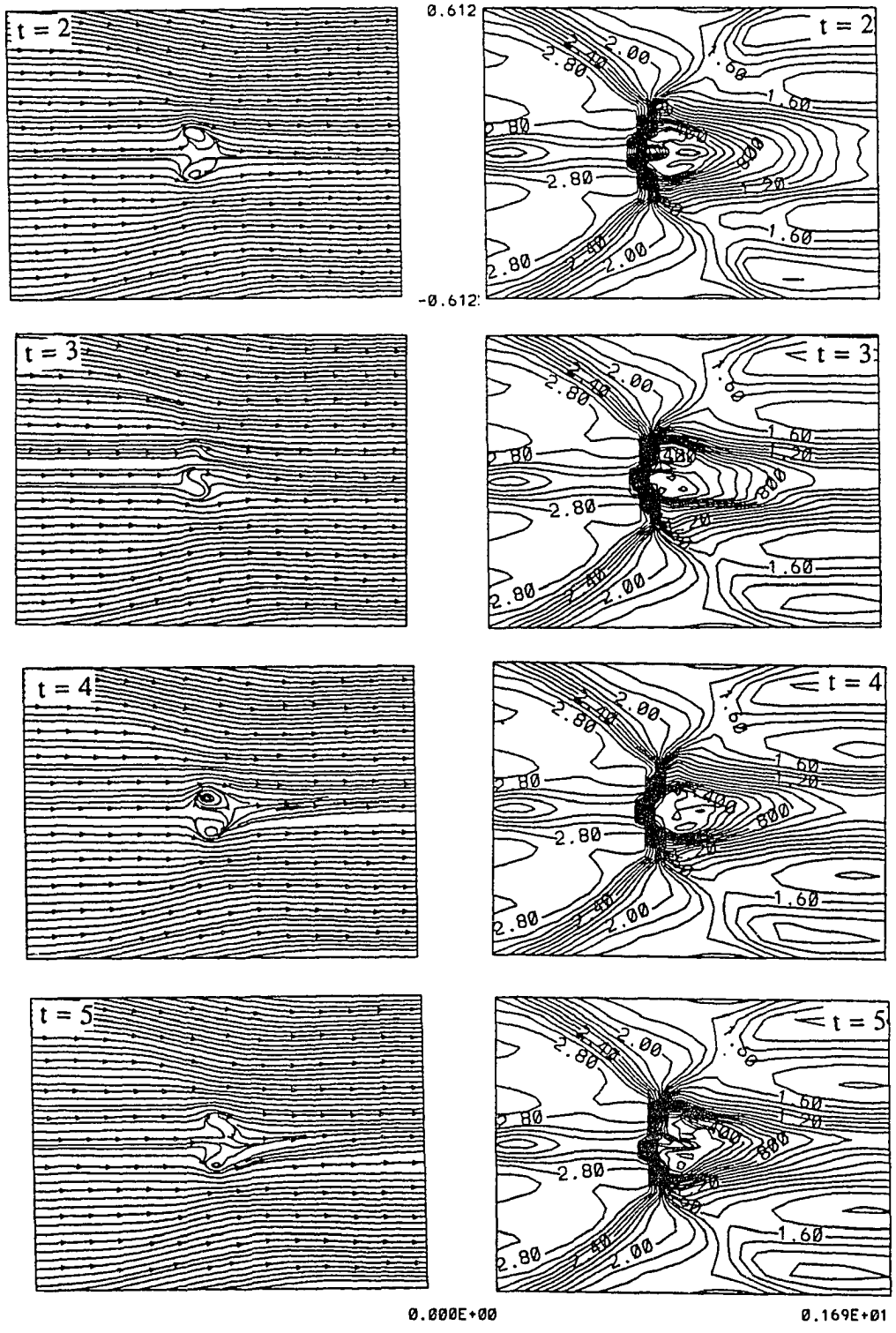

Figure 9.12 Streamlines and Mach contours in a horizontal plane for a supersonic swirling jet using grid number 3, $M_j = 3.0$, $M_\infty = 2.0$ and $R_e = 296,000$.

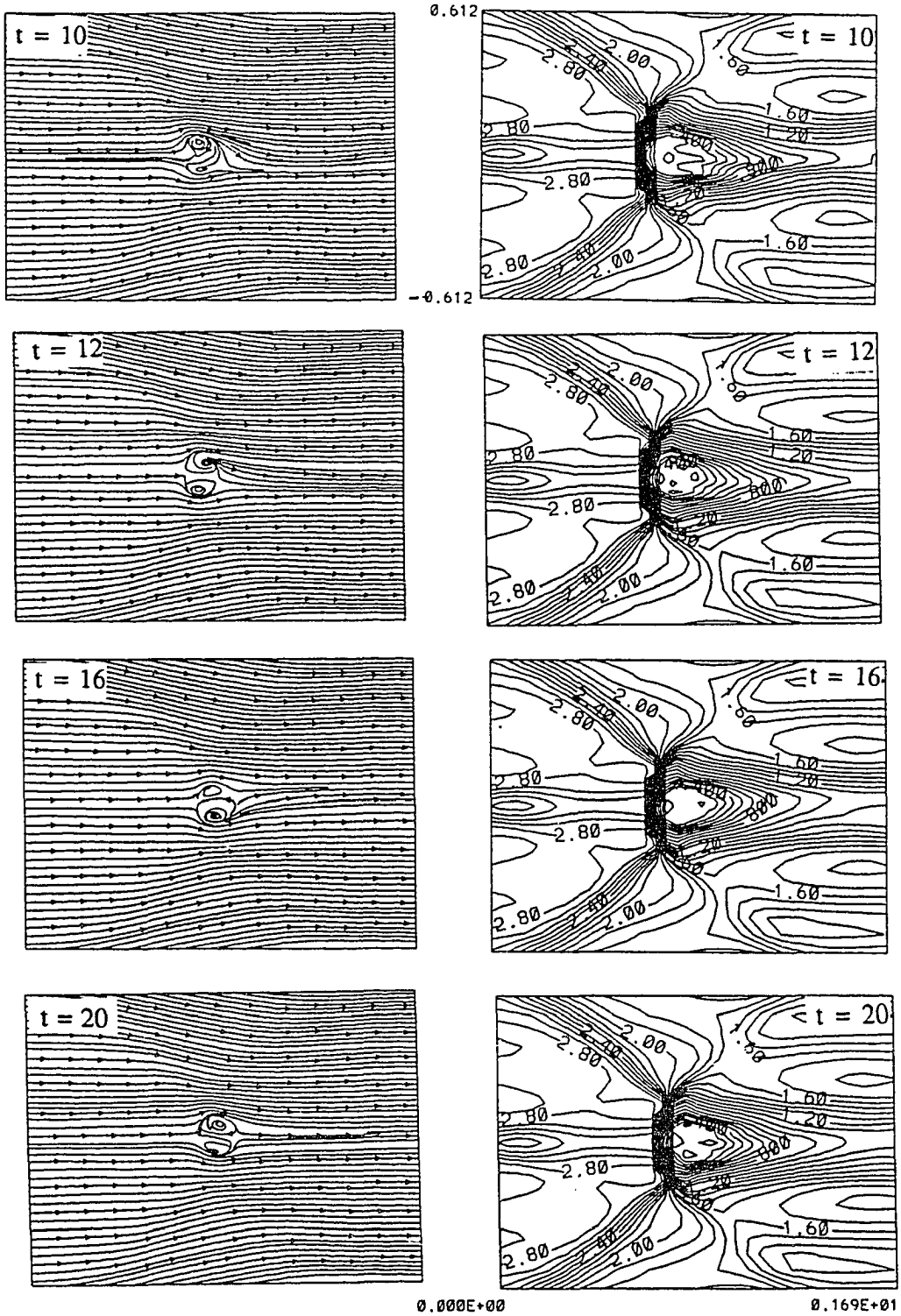

Figure 9.12: Cont'd

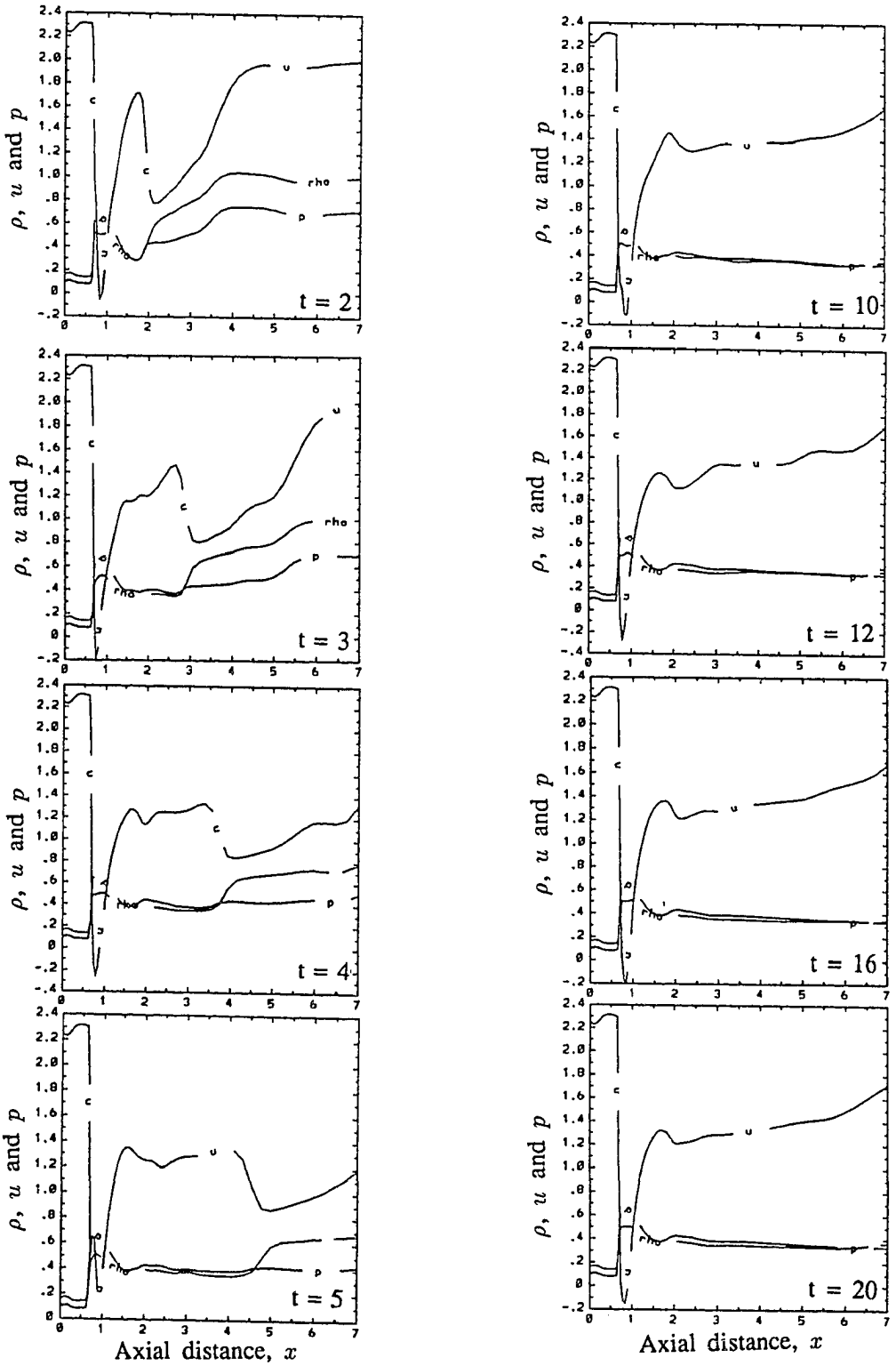

Figure 9.13 Axial distributions of the axial velocity, u, density, ρ and pressure, p, for a supersonic swirling jet using grid number 3, $M_j = 3.0$, $M_\infty = 2.0$ and $R_e = 296,000$.

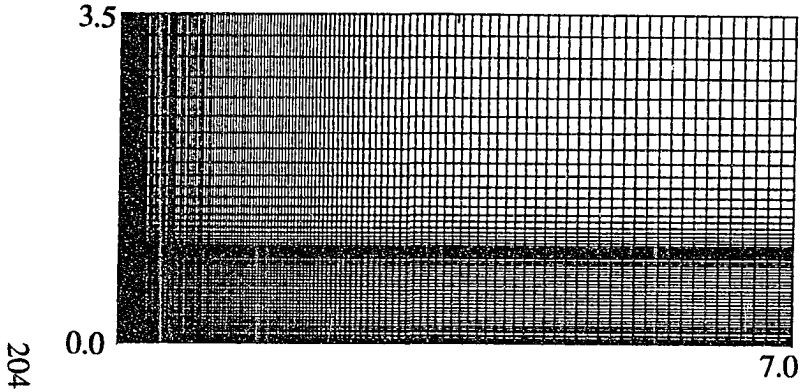

a- Meridian plane

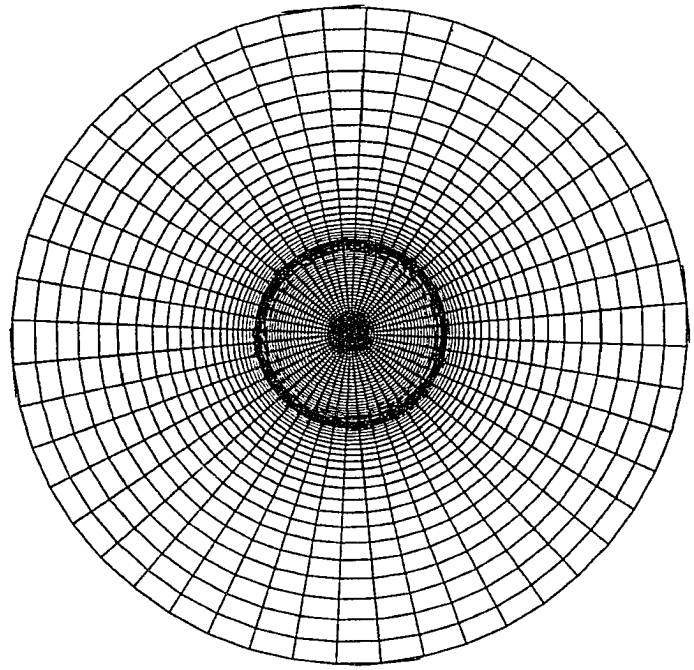

b- Cross-flow plane

Figure 9.14 Grid number 4 (circular fine grid), 145x61x61 grid points in the axial and cross-flow plane, respectively.

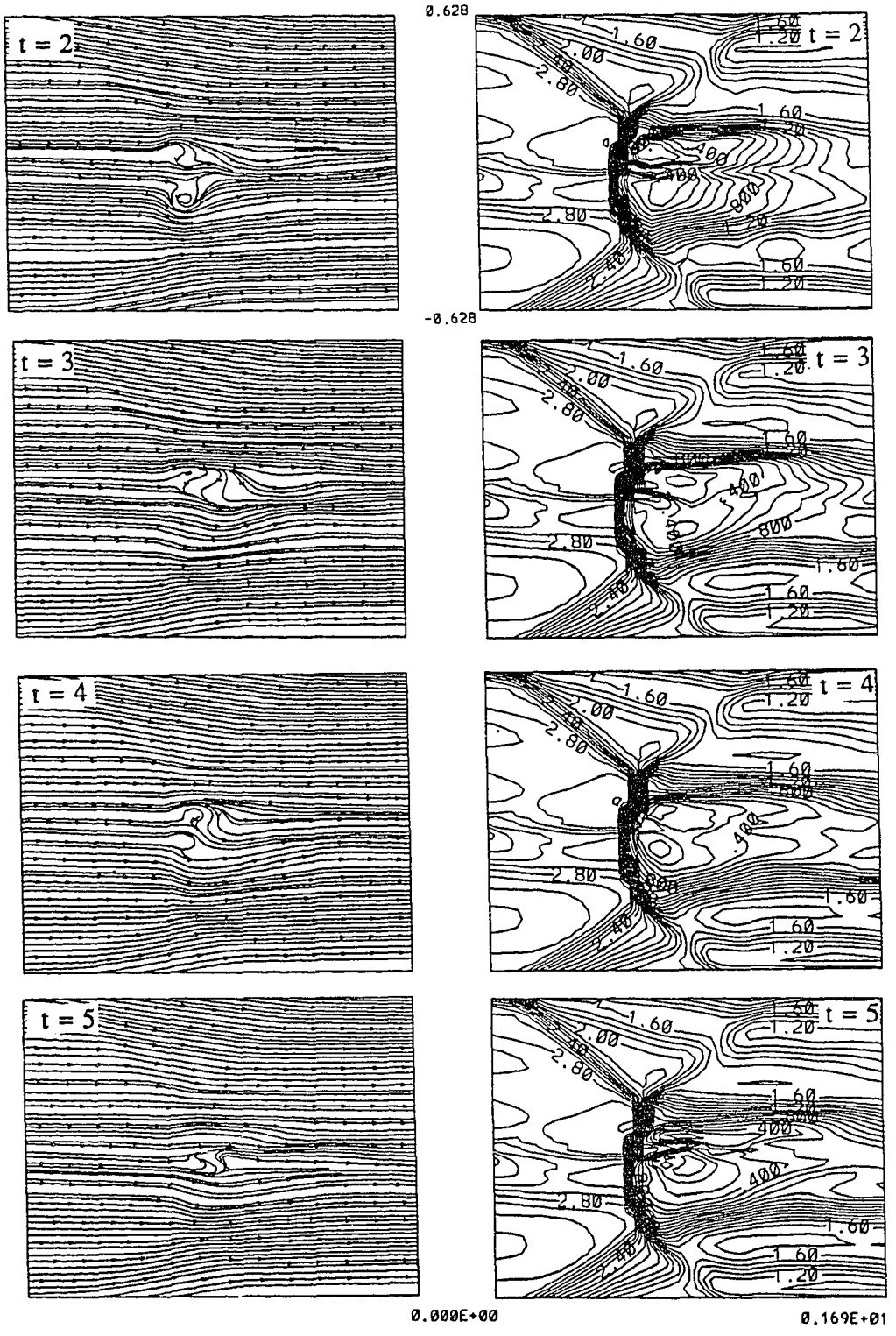

Figure 9.15 Streamlines and Mach contours in a horizontal plane for a supersonic swirling jet using grid number 4 with asymmetric initial flow profiles, $M_j = 3.0$, $M_\infty = 2.0$ and $R_e = 296,000$.

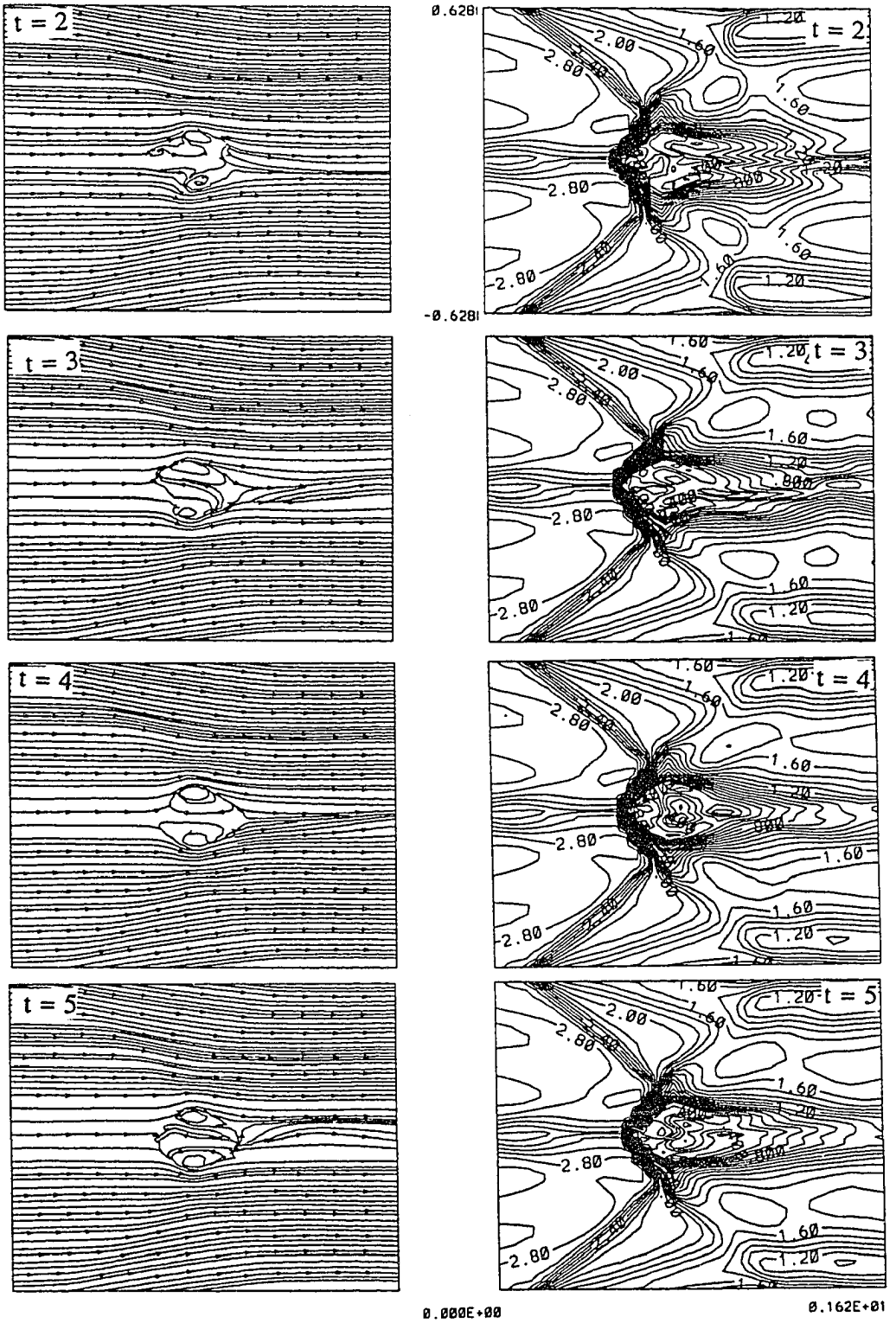

Figure 9.16 Streamlines and Mach contours in a horizontal plane for a supersonic swirling jet using grid number 4, $M_j = 3.0$, $M_\infty = 2.0$ and $R_e = 296,000$.

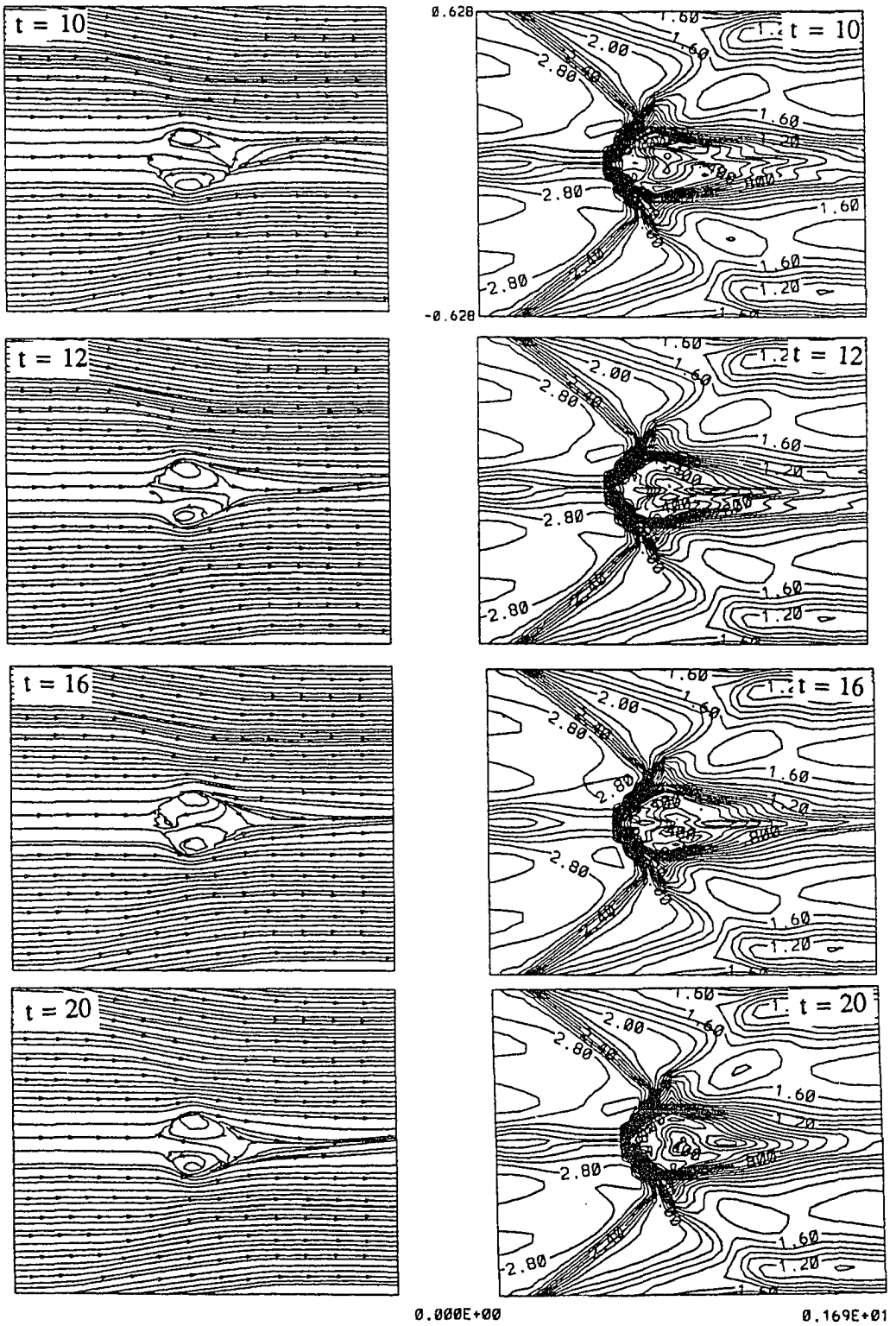

Figure 9.16: Cont'd

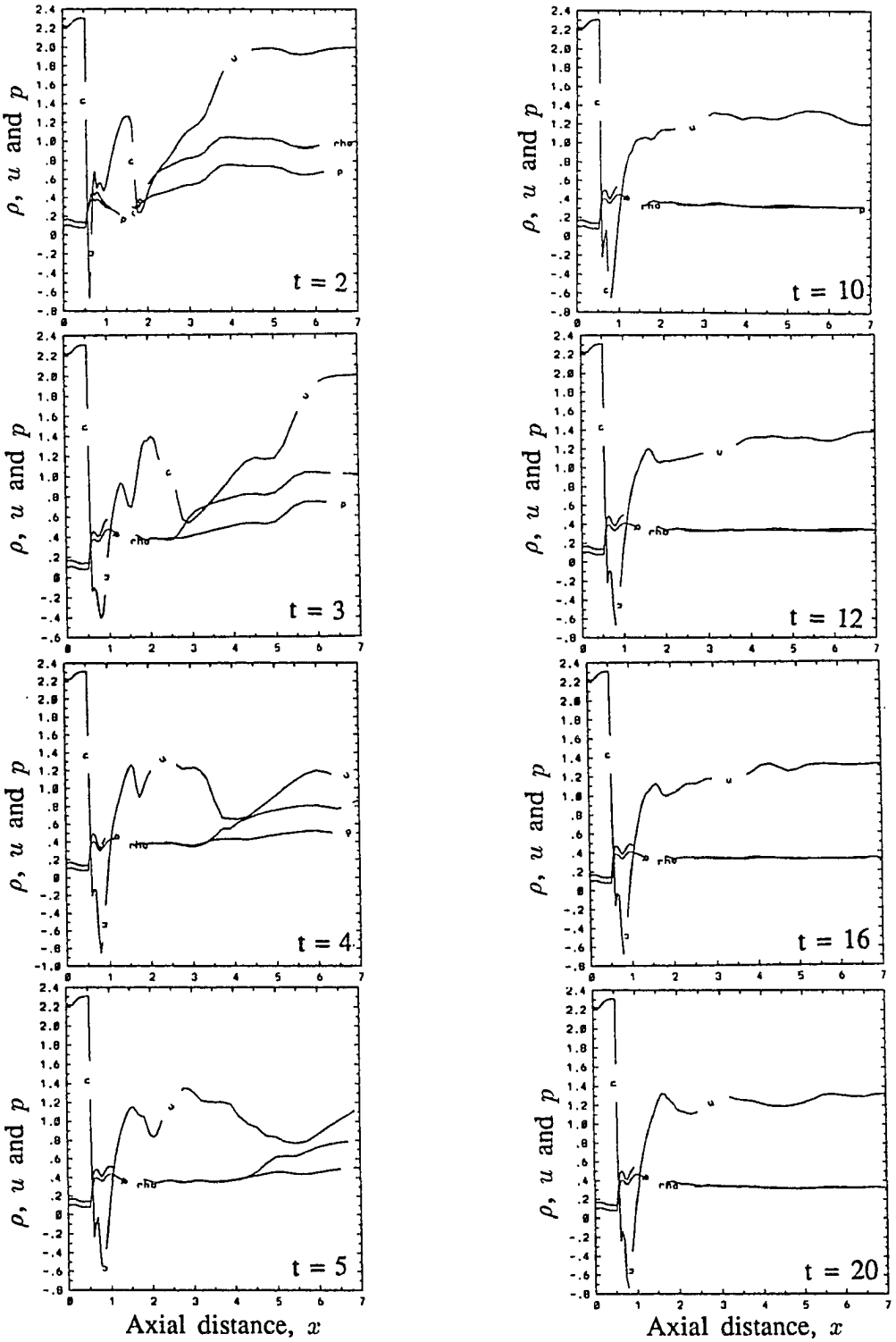

Figure 9.17 Axial distributions of the axial velocity, u, density, ρ and pressure, p, for a supersonic swirling jet using grid number 4, $M_j = 3.0$, $M_\infty = 2.0$ and $R_e = 296,000$.

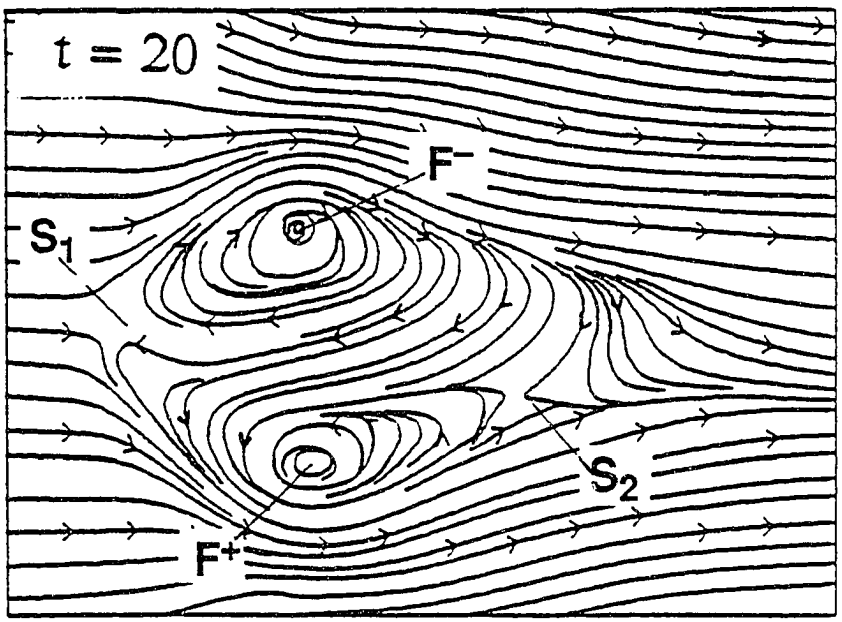

Figure 9.18 Streamline patterns on a horizontal plane for a supersonic vortex breakdown (grid number 1) at t = 20, $M_j = 3.0$, $M_\infty = 2.0$ and $R_e = 296,000$.

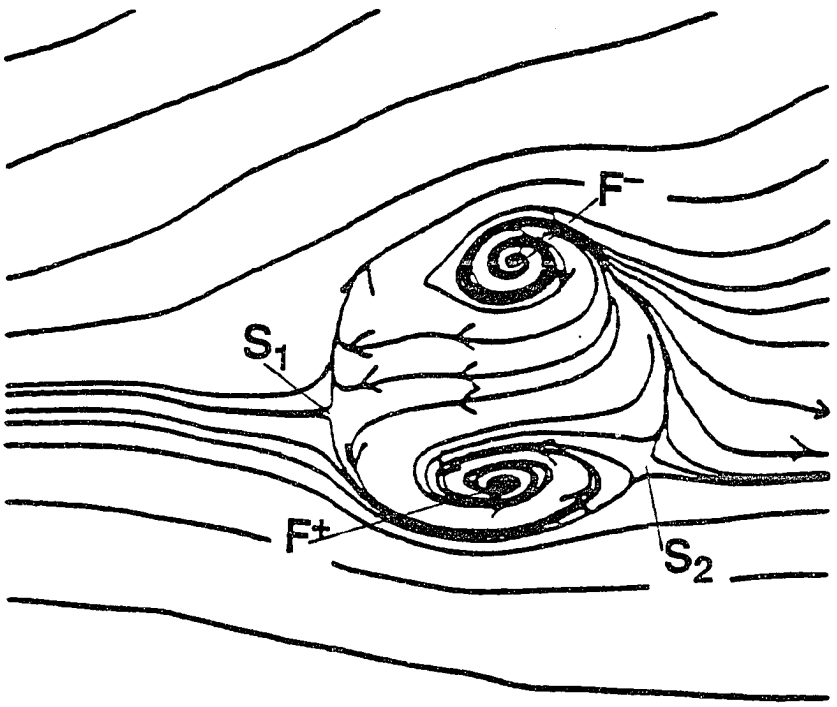

Figure 9.19 Experimental streamline patterns on a vertical plane for an incompressible vortex breakdown on a delta wing at high angle of attack, [113].

CHAPTER 10
CONCLUDING REMARKS AND RECOMMENDATIONS FOR FUTURE WORK

An extensive computational investigation of vortex-breakdown phenomena in compressible flows has been presented in this study. The applications included swirling supersonic flows in both bounded and unbounded domains. The literature survey presented in Chapter 2 showed the importance of the vortex-breakdown phenomena and the need to develop computational schemes to study, predict and control vortex flows including vortex breakdown. The formulation and computational schemes used in this study have been presented in Chapters 3 and 4. The results have been presented in Chapters 5-9.

In this Chapter, a summary of the findings of the computational investigation is presented. At the end of the Chapter, some recommendations for future research work are suggested.

10.1 Concluding Remarks

In this study, the full Navier-Stokes equations were used to study compressible vortex flows and shock-vortex interactions including vortex breakdowns. The solution of the unsteady full Navier-Stokes equations needs large computational resources. Therefore, simplifying assumptions were used to reduce the compressible full Navier-Stokes equations to a simpler set of equations or to reduce the computational domain to a smaller domain which consisted only of two meridian planes.

In the first simplified case, a slender vortex core was considered and the flow was assumed to be quasi-axisymmetric and steady. The full Navier-Stokes equations were reduced to a simple set of parabolic equations which were solved using a type-differencing scheme. The results were presented in Chapter 5. Only subsonic and transonic flows were studied using this method. The results are in good agreement with those of the full Navier-Stokes equations for the case of a stable vortex flow with no vortex breakdown. Because of the parabolic nature of the governing equations, this scheme is not capable of studying the effects of the downstream conditions and computing for the reversed flow region. This method can be used to predict if the vortex breakdown will take place and its approximate location. The scheme is a fast tool to study the effect of flow parameters on the vortex breakdown since it requires the solution of a simple set of equations and does not need large memory or computational time.

Next, the quasi-axisymmetric assumption was used for a supersonic swirling flow in a configured circular duct to reduce the required computer time and memory by an order of magnitude in comparison with those requirements for three-dimensional flow. The experimental data for flows in axisymmetric combustion chambers showed the quasi-axisymmetric assumption to be acceptable in axisymmetric geometries. The present applications included the effects of the Reynolds number, Mach number, swirl ratio and duct-wall and downstream boundary conditions on the development and behavior of vortex breakdown. The results were presented in Chapter 6. It was shown that increasing the Reynolds number, Mach number and/or swirl ratio increased the size and number of vortex-breakdown bubbles. As a result of increasing the Reynolds number from 2,000 to 100,000, the flow changed from a stable vortex flow to a flow with a transient single-bubble vortex breakdown to a flow with transient multi-bubble vortex breakdown to a flow with unsteady multi-frequency multi-bubble vortex breakdown. It was noticed that

the boundary layer on the duct wall may separate because of the shock-boundary layer interaction and the pressure field generated by the presence of the vortex breakdown bubble. The effects of boundary-layer separation were isolated by assuming the flow at the duct wall to be inviscid. The results showed the substantial effects of a separated boundary layer on the behavior of the vortex-breakdown bubbles. The effects of the exit-boundary conditions were studied using five types of exit conditions, and the results showed that it was possible to control the vortex-breakdown mode by controlling the downstream boundary conditions. The streamline patterns inside the breakdown bubble were discussed in view of the experimental results of Faler and Leibovich (FL) [38] and Escudier [12] of incompressible flows in divergent ducts. The computational results at certain time levels were in good qualitative agreement with the experimental results. It was found that the FL mode was a transient mode which was obtained several times during the development and shedding of the breakdown bubbles. Escudier's mode was a stable mode which was obtained as a limiting case of increasing the swirl ratio or the Reynolds number to high values.

In Chapter 7, the problem of a shock/vortex interaction in an unbounded domain was considered. A supersonic swirling jet was issued from a nozzle into a uniform supersonic flow at a lower Mach number. The mismatch between the pressure fields of the nozzle flow and the external flow generated a conical shock outside the nozzle. The flow was assumed to be quasi-axisymmetric. The results showed the effects of downstream boundary conditions on the vortex breakdown behind the shock wave. Extrapolation and Riemann-type boundary conditions were used and the results were compared. In the case of Riemann-type boundary conditions, the flow reached a nearly steady-state condition, while in the case of extrapolation boundary conditions, the vortex-breakdown bubbles were continuously oscillating while their sizes were changing. The effects of

the Reynolds number were also investigated. It was shown that using small Reynolds numbers resulted in the production of vortex-breakdown bubbles of smaller sizes.

In Chapters 8 and 9, the three–dimensional solutions of the unsteady, full Navier-Stokes equations were presented where the flow in a circular duct was considered in Chapter 8 and the interaction of a supersonic swirling jet with a normal shock wave in an unbounded domain was considered in Chapter 9. The results of Chapter 8 showed the three-dimensional features of vortex breakdown. Several types of three-dimensional vortex-breakdown modes were captured including the bubble type and the spiral type. The quasi-axisymmetric analysis of Chapter 6 was not capable of capturing several structures of the three-dimensional vortex breakdown. The effects of boundary-layer separation were isolated by assuming the flow at the duct wall to be inviscid, which resulted in significant changes in the vortex-breakdown-bubble shape and behavior. The location of the shock wave in the duct entrance region was fixed and the flow reached a quasi-steady state.

In Chapter 9, the effects of the grid fineness and grid-point distribution were studied. The results showed the flow to be highly dependent upon the grid fineness and mesh distribution. It is concluded that, using coarser grids has the same effect as simulating flows with higher Reynolds numbers. The results with fine grids showed the development of small or transient small vortex-breakdown bubbles which explains the difficulty in capturing those bubbles experimentally. The streamline patterns on a horizontal plane passing through the vortex-breakdown bubble was investigated and compared with experimental results of an incompressible vortex breakdown on a delta wing at high angle of attack. Similar topology was observed, where both the computed and experimental streamline patterns display the same number and type of critical points. The streamline pattern were different from the axisymmetric patterns discussed in Chapter 6.

10.2 Recommendations for Future Work

The studies presented in this work need to be extended to cover more parameters. For internal flow applications, the effect of changing the duct length on the development, structure and behavior of vortex breakdown needs to be investigated. The heat transfer through the duct wall is an important parameter that affects the boundary-layer flow and separation and hence it has a significant effect on the vortex breakdown. This effect should be considered by using isothermal boundary conditions on the duct wall. More grids with different shape and fineness need to be used in order to select optimum grids that accurately simulate certain experimental measurements.

The computational scheme used in this study is first-order accurate in time which requires the use of very small time steps in order to achieve an acceptable accuracy of the computational results. The accuracy of the scheme in time needs to be increased to second order to gain higher accuracy and to make it possible to study the stability of the flow and trace the disturbance waves.

Different types of the computational-scheme errors such as phase and dispersive errors and their effects on the computed flow field need to be investigated.

Topological studies have been used for three-dimensional boundary-layer flows to identify and classify critical points in the domain under consideration. Similar studies might be used for vortex-breakdown flows for better physical understanding of the breakdown mechanisms.

Adaptive grids need to be used for better resolution of the highly complex vortex-breakdown and vortex-shock-interaction regions. These schemes will allow local-grid refinement according to flow gradients of the solution and effectively will make use of the grid points.

The experimental measurements showed the vortex-breakdown flow to be turbulent especially downstream of the reversed flow region. Unfortunately, no turbulence model is available that can handle such a complex flow and take into account three-dimensional and compressibility effects. The development of such models is very important in order to simulate real physical problems.

If the computational resources and capabilities are available, further efforts with very fine grids and higher-order schemes have to be focused on fully resolving the complex flow regions. Using such techniques will minimize the effects of truncation errors and artificial dissipation on numerical solutions and allow a better judgement of flow physics.

No detailed experimental measurements for supersonic vortex breakdown were available during the course of this study. It is recommended that more experimental investigations be carried out and be focused on the vortex/shock interaction and supersonic vortex-breakdown applications for both internal and external flow applications. Such experimental measurements are needed for the validation of the computational results. The experimental investigations might be guided by the present computational studies.

The applications in this study included only isolated vortex flows where the inflow profiles were obtained analytically or from experimental measurements. The next step is to consider practical applications where supersonic vortex breakdown occurs. The transonic flow around a delta wing in the moderate to high angle-of-attack range is a typical application, where vortex breakdown usually occurs behind a transverse shock wave, which is called a "terminating shock". This problem is currently being investigated. Such a breakdown is undesirable since it results in a loss of lift and may cause tail buffeting for high-performance aircrafts such as F/A 18.

Computational research is needed for the vortex flow and breakdown in actual combustion chambers' geometries, where vortex breakdown may be induced to enhance

fuel-air mixing and improve the combustion efficiency. The flow of real gases with chemical reactions is another important application for future work.

In both external and internal flow applications, computational studies are needed to study, predict and control vortex-shock interaction flows, including vortex breakdown.

REFERENCES

[1] Hall, M. G., "Vortex Breakdown," *Annual Review of Fluid Mechanics*, vol. 4, 1972, pp. 195–218.

[2] Leibovich, S., "The Structure of Vortex Breakdown," *Annual Review of Fluid Mechanics*, vol. 10, 1978, pp. 221–246.

[3] Leibovich, S. and Stewartson, K., "A Sufficient Condition for the Instability of Columnar Vortices," *Journal of Fluid Mechanics*, vol. 126, 1983, pp. 335–356.

[4] Newsome, R. W. and Kandil, O. A., "Vortical Flow Aerodynamics-Physical Aspects and Numerical Simulation," AIAA Paper No. 87–0205, Jan. 1987.

[5] Escudier, M., "Vortex Breakdown: Observations and Explanations," *Progress in Aerospace Sciences*, vol. 25, no. 2, 1988, pp. 189-229.

[6] Peckham, D. H. and Atkinson, S. A., "Preliminary results of low speed wind tunnel tests on a gothic wing of aspect ratio 1.0," TN No. Aero. 2504, Report C. P. No. 508, Aeronautical Research Council, April 1957.

[7] Elle, B. J., "An investigation at low speed of the flow near the apex of thin delta wings with sharp leading edges," arc 19,780–perf. 1621–f.m. 2629, Aeronautical Research Council, Jan. 1958.

[8] Werlé, H., "Sur l'éclatement des tourbillons d'apex d'une aile delta aux faibles vitesses," *La Rechreche Aéronautique*, no. 74, Jan./Feb. 1960, pp. 23–30.

[9] Lambourne, N. C. and Bryer, D. W., "The Bursting of Leading-Edge Vortices — Some Observations and Discussion of the Phenomenon," Reports and Memoranda No. 3282, Aeronautical Research Council, April 1961.

[10] Harvey, J. K., "Some Observations of the Vortex Breakdown Phenomenon," *Journal of Fluid Mechanics*, vol. 14, 1962, pp. 585–592.

[11] Lowson, M. V., "Some Experiments With Vortex Breakdown," *Journal of the Royal Aeronautical Society*, vol. 68, May 1964, pp. 343–346.

[12] Escudier, M., "Vortex Breakdown in Technology and Nature," Lecture Series No. 1986–08, Introduction to Vortex Dynamics, von Karman Institute for Fluid Mechanics, May 1986.

[13] Squire, H. B., "Analysis of the 'Vortex Breakdown' Phenomenon, Part I," Tech. Rep. No. 102, Aeronautic Department, Imperial College of Science and Technology, London, 1960.

[14] Sarpkaya, T., "On Stationary and Travelling Vortex Breakdowns," *Journal of Fluid Mechanics*, vol. 45, Part 3, 1971, pp. 545–559.

[15] Benjamin, T. B., "Theory of the Vortex Breakdown Phenomenon," *Journal of Fluid Mechanics*, vol. 14, Part 4, 1962, pp. 593–629.

[16] Benjamin, T. B., "Significance of the Vortex Breakdown Phenomenon," *Journal of Basic Engineering, Trans. ASME, Series D*, vol. 87, 1965, pp. 518–524, 1091–1092.

[17] Benjamin, T. B., "Some Development in the Theory of Vortex Breakdown," *Journal of Fluid Mechanics*, vol. 28, Part 1, 1967, pp. 65–84.

[18] Grabowski, W. J. and Berger, S. A., "Solutions of the Navier-Stokes Equations for Vortex Breakdown," *Journal of Fluid Mechanics*, vol. 75, 1976, pp. 525–544.

[19] Bossel, H. H., "Vortex Breakdown Flowfield," *Physics of Fluids*, vol. 12, no. 3, March 1969, pp. 498–508.

[20] Ludwieg, H., "An Explanation of the Instability of the Free Vortex Cores Occurring over Delta Wing with Raised Edges," *Zeitschrift für Flugweissenschaften*, vol. 10, no. 6, June 1962, pp. 242–249.

[21] Howard, L. N. and Gupta, A. S., "On the Hydrodynamic and Hydromagnetic Stability of Swirling Flows," *Journal of Fluid Mechanics*, vol. 14, 1962, pp. 463–476.

[22] Jones, J. P., "The Breakdown of Vortices in Separated Flow," Tech. Rep. No. 140, USAA Report, University of Southampton, 1960.

[23] Lessen, M., Singh, P. J., and Paillet, F., "The Stability of a Trailing Line Vortex, Part I," *Journal of Fluid Mechanics*, vol. 63, no. 4, 1974, pp. 753–763.

[24] Lessen, M. and Paillet, F., "The Stability of a Trailing Line Vortex, Part 2," *Journal of Fluid Mechanics*, vol. 65, no. 4, 1974, pp. 769–779.

[25] Hall, M. G., "The Structure of Concentrated Vortex Cores," *Progress in Aeronautical Sciences*, vol. 7, 1966.

[26] Hall, M. G., "A New Approach to Vortex Breakdown," *Proc. Heat Transfer Fluid Mechanics Institute*, 1967, pp. 314–340.

[27] Kirkpatrick, D. L. I., "Experimental investigation of the breakdown of a vortex in a tube," Current Papers C.P. No. 821, Aeronautical Res. Council, 1964.

[28] Bossel, H. H., "Vortex Computation by the Method of weighted Residuals using Exponentials," *AIAA Journal*, vol. 9, no. 10, Oct. 1971, pp. 2027–2034.

[29] Mager, A., "Dissipation and Breakdown of a Wing-Tip Vortex," *Journal of Fluid Mechanics*, vol. 55, Part 4, 1972, pp. 609–628.

[30] Kandil, O. A. and Balakrishnan, L., "Recent Improvements in the Prediction of Leading and Trailing Edge Vortex Cores of Delta Wings," AIAA Paper No. 81–1263, 1981.

[31] Krause, E., Shi, X. G., and Hartwich, P. M., "Computation of Leading Edge Vortices," AIAA Paper No. 83–1907, 1983.

[32] Krause, E., "Pressure Variation in Axially Symmetric Breakdown," in *Proceedings Colloquium on Vortex Breakdown, Rheinisch-Westälischen Technischen Hochschule, Aachen*, Feb. 1985, pp. 49–68.

[33] Menne, S., *Rotationssymmetrische Wirbel in Achsparalleler Strömung*. PhD thesis, Rheinisch-Westfälischen Technischen Hochschule, Aachen, Dec. 1986.

[34] Kandil, O. A. and Kandil, H. A., "Computation of Compressible Quasi-Axisymmetric Slender Vortex Flow and Breakdown," *Computer Physics Communications*, vol. 65, March 1991.

[35] Stuart, J. T., "A critical review of vortex-breakdown theory," in *Proceedings of the Second International Colloquium on Vortex Flows, Brown Boveri Research Center*, April 1987, pp. 131–154.

[36] Sarpkaya, T., "Vortex Breakdown in Swirling Conical Flows," *AIAA Journal*, vol. 9, no. 9, Sept. 1971, pp. 1792–1799.

[37] Sarpkaya, T., "Effect of the Adverse Pressure Gradient on Vortex Breakdown," *AIAA Journal*, vol. 12, no. 5, May 1974, pp. 602–607.

[38] Faler, J. H. and Leibovich, S., "Disrupted States of Vortex Flow and Vortex Breakdown," *The Physics of Fluids*, vol. 20, no. 9, Sept. 1977, pp. 1385–1400.

[39] Faler, J. H. and Leibovich, S., "An Experimental Map of the Internal Structure of a Vortex Breakdown," *Journal of Fluid Mechanics*, vol. 86, Part 2, 1978, pp. 313–335.

[40] Garg, A. K. and Leibovich, S., "Spectral Characteristics of Vortex Breakdown Flowfield," *The Physics of Fluids*, vol. 22, no. 11, Nov. 1979, pp. 2053–2064.

[41] Uchida, S., Nakamura, Y., and Ohawa, M., "Experiments on the Axisymmetric Vortex Breakdown in a Swirling Air Flow ," *Transactions of the Japan Society for Aeronautical and Space Sciences*, vol. 27, no. 78, Feb. 1985.

[42] Uchida, S., Nakamura, Y., Zhang, J. Z., and Sagawa, N., "An Experiment on a Spiral Type of Vortex Breakdown of a Swirling Flow in a Pipe," *Transactions of the Japan Society for Aeronautical and Space Sciences*, vol. 30, no. 87, May 1987.

[43] Chanaud, R. C., "Observations of Oscillatory Motion in Certain Swirling Flows," *Journal of Fluid Mechanics*, vol. 21, Part 1, 1965, pp. 111–127.

[44] Cassidy, J. J. and Falvey, H. T., "Observations of Unsteady Flow arising after Vortex Breakdown," *Journal of Fluid Mechanics*, vol. 41, Part 4, 1970, pp. 727–736.

[45] Lambourne, N. C., "The Breakdown of Certain Types of Vortex," N.P.L. Aero. Report 1166– A.R.C. No. 27200, 1965.

[46] Granger, R. A., "Speed of Surge in a Bathtub Vortex," *Journal of Fluid Mechanics*, vol. 34, Part 4, 1968, pp. 651–656.

[47] Escudier, M. and Zehnder, N., "Vortex Flow Regimes," *Journal of Fluid Mechanics*, vol. 115, 1982, pp. 105–122.

[48] Hummel, D. and Srinivasan, P. S., "Vortex Breakdown Effects on the Low-Speed Aerodynamic Characteristics of Slender Delta Wings in Symmetrical Flow," *Journal of the Royal Aeronautical Society*, vol. 71, April 1967, pp. 319–322.

[49] Wentz, W. H. and Kahlman, D. L., "Vortex Breakdown on Slender Sharp-Edged Wings," in *AIAA Aircraft Design & Operations Meeting*, (Los Angeles), AIAA Paper No. 69–778, 1969.

[50] Hall, M. G., "A Numerical Method for Solving the Equations for a Vortex Core," ARC 27150, R.&M. No. 3467, A.R.C., 1965. RAE Technical Report No. 65106.

[51] Lavan, Z., Hielsen, H., and Fajer, A. A., "Separation and Flow Reversal in Swirling Flows in Circular Ducts," *The Physics of Fluids*, vol. 12, no. 9, Sept. 1969, pp. 1747–1757.

[52] Torrance, K. E. and Kopecky, R. M., "Numerical Study of Axisymmetric Vortex Breakdown," NASA Contractor Report No. CR–1865, NASA, August 1971.

[53] Kopecky, R. M. and torrance, K. E., "Initiation and Structure of Axisymmetric Eddies in Rotating Stream," *Computers and Fluids*, vol. 1, 1973, pp. 289–300.

[54] Narain, J. P., "Numerical Prediction of Confined Swirling Jets," *Computers and Fluids*, vol. 5, 1977, pp. 115–125.

[55] Hafez, M., Kuruvila, G., and Salas, M. D., "Numerical Study of Vortex Breakdown," *Applied Numerical Mathematics*, vol. 2, 1986, pp. 291–302.

[56] Salas, M. D. and Kuruvila, G., "Vortex Breakdown Simulation: A Circumspect Study of the Steady, Laminar, Axisymmetric Model," *Computers and Fluids*, vol. 17, no. 1, 1989, pp. 247–262.

[57] Salas, M. D. and Kuruvila, G., "Study of Three-Dimensional Effects on Vortex Breakdown," in *presented at the 16th ICAS Congress, Jerusalem, Israel*, Aug. 28–Sept. 2 1988.

[58] Hafez, M., Ahmed, J., Kuruvila, G., and Salas, M. D., "Vortex Breakdown Simulation, Part I," AIAA Paper No. 87–1343, 1987.

[59] Beran, P. S., "Numerical Simulation of Trailing Vortex Bursting," AIAA Paper No. 87–1313, 1987.

[60] Hafez, M. and Ahmed, J., "Vortex Breakdown Simulation, Part II," AIAA Paper No. 88–0508, 1988.

[61] Shi, X., "Numerical Simulation of Vortex Breakdown," *Acta Aerodynamica Sinica*, no. 1, 1985, pp. 22–29.

[62] Shi, X., "Numerical Simulation of Vortex Breakdown," in *Proceedings Colloquium on Vortex Breakdown, Rheinisch-Westälischen Technischen Hochschule, Aachen*, Feb. 1985, pp. 69–80.

[63] Benay, R., "Numerical Modeling of a Vortex Breakdown in a Laminar Flow of Revolution," *La Recherche Aérospatiale, English Edition*, no. 1984–4, 1984, pp. 15–27.

[64] Pagan, D. and Benay, R., "Vortex Breakdown Induced by an Adverse Pressure Gradient," AIAA Paper No. 87–2478, 1987.

[65] Pagan, D. and Solignac, J. L., "Experimental Study of the Breakdown of a Vortex Generated by a Delta Wing," *La Recherche Aérospatiale, English Edition*, no. 1986–3, 1986.

[66] Pagan, D. and Benay, R., "Numerical Analysis of Vortex Breakdowns under Pressure Gradients," *La Recherche Aérospatiale, English Edition*, no. 1988–1, 1988, pp. 15–27.

[67] Menne, S., "Vortex Breakdown in an Axisymmetric Flow," AIAA Paper No. 88–0506, 1988.

[68] Wu, J. C. and Hwang, S., "Computational Study of Vortex Breakdown in Circular Tube," AIAA Paper No. 91–1820, 1991.

[69] Nakamura, Y., leonard, A., and Spalart, P. R., "Numerical Simulation of Vortex Breakdown by the Vortex-Filament Method," in *AGARD CP No. 342*, 1983.

[70] Nakamura, Y., leonard, A., and Spalart, P. R., "Vortex Breakdown Simulation," AIAA Paper No. 85–1581, July 1985.

[71] Nakamura, Y., leonard, A., and Spalart, P. R., "Internal Structure of a Vortex Breakdown," AIAA Paper No. 86–1074, May 1986.

[72] Spall, R. E., *A Numerical Study of Three-Dimensional Vortex Breakdown.* PhD thesis, Old Dominion University, May 1987.

[73] Spall, R. E., Gatski, T. B., and Ash, R. L., "The Structure and Dynamics of Bubble-Type Vortex Breakdown," *Proc. Poyal Society, London*, no. A 429, 1990, pp. 613–637.

[74] Spall, R. E. and Gatski, T. B., "A Computational Study of the Taxonomy of Vortex Breakdown ," AIAA Paper No. 90–1624, 1990.

[75] Liu, C. and Menne, S., "Simulation of a Three-Dimensional Vortex Breakdown," AIAA Paper No. 89–1806, 1989.

[76] Liu, C. and Menne, S., "Numerical Investigation of a Three-Dimensional Vortex Breakdown," Presented at the Fourth Asian Congress of Fluid Mechanics, Hong Kong, Aug. 1989, pp. 21–25.

[77] Menne, S. and Liu, C. H., "Numerical Simulation of a Three-Dimensional Vortex Breakdown," *Z. Flugwiss. Weltraumforsch (ZFW)*, vol. 14, 1990, pp. 301–308.

[78] Breuer, M. and Hänel, D., "Solution of 3–D Incompressible Navier-Stokes Equations for the Simulation of Vortex Breakdown," in *8th GAMM Conference on Numerical Methods in Fluid Mechanics*, Sept. 1989. Delft.

[79] Hsu, C. H., Chen, Y. M., and Liu, C. H., "Time-Marching Methods for Three-dimensional Steady and Unsteady Viscous Incompressible Flows," AIAA Paper No. 91–0024, 1991.

[80] Elle, B. J., "On the Breakdown of High Incidences of the Leading Edge Vortices on Delta Wings," *Journal of the Royal Aeronautical Society*, vol. 64, Aug. 1960, pp. 491–493.

[81] Craven, A. H. and Alexander, A. J., "An Investigation of Vortex Breakdown at Mach 2," CoA Note Aero-158, The College of Aeronautics, Department of Aerodynamics, Cranfield, Nov. 1963.

[82] Zatoloka, V. V., Ivanyushkin, A. K., and Nikolayev, A. V., "Interference of Vortexes with Shocks in Airscoops. Dissipation of Vortexes," *Fluid Mechanics — Soviet Research*, vol. 7, no. 4, July-August 1978, pp. 153–158.

[83] Délery, J. and Horowitz, E., "Interaction Between a Shock-Wave and a Vortex Flow," in *Aerodynamics of Vortical Type Flows in Three Dimensions*, AGARD-CP–342 Paper No. 5, 1983. In French.

[84] Schrader, K. F., Reynolds, G. A., and Novak, C. J., "Effects of Mach Number and Reynolds Number on Leading-edge Vortices at High Angle-of-attack," AIAA Paper No. 88–0122, 1988.

[85] Glotov, G. F., "Interference of Vortex Braid with Free-stream Shock Waves and Nonisobaric Jets," *Uchenyye Zapiski TsAGI*, vol. XX, no. 5, 1989, pp. 21–32.

[86] Bannink, W. J., "Some Recent Results on Vortex Bursting on a Delta Wing at High Subsonic Speeds," in *AGARD Symposium on Validation of Computational Fluid Dynamics, Lisbon, Portugal*, Paper No. 9, May 1988, pp. 9–21–9–23.

[87] Erickson, G. E., "Wind Tunnel Investigation of the Interaction and Breakdown Characteristics of slender-Wing Vortices at Subsonic, Transonic and Supersonic Speeds," NASA Technical Paper No. 3114, Nov. 1991.

[88] Metwally, O., Settles, G., and Horstman, C., "An Experimental Study of Shock/Vortex Interaction," AIAA Paper No. 89–0082, Jan. 1989.

[89] Cattafesta, L. N. and Settles, G., " Experiments on Shock/Vortex Interaction ," AIAA Paper No. 92–0315, Jan. 1992.

[90] Delery, J., Horowitz, E., Leuchter, O., and Solignac, J. L., "Fundamental Studies of Vortex Flows," *La Recherche Aérospatiale, English Edition*, no. 1984–2, 1984, pp. 1–24.

[91] Cutler, A. D. and Levey, B. S., "Vortex Breakdown in a Supersonic Jet," AIAA Paper No. 91–1815, June 1991.

[92] Kalkhoran, I. M., Sforza, P. M., and Wang, F. Y., " Experimental Study of Shock-Vortex Interaction in a Mach 3 Stream," AIAA Paper No. 91–3270–CP, Sept. 1991.

[93] Kalkhoran, I. M. and Sforza, P. M., " Airfoil Pressure Measurements During Oblique Shock Wave-Vortex Interaction in a Mach 3 Stream," AIAA Paper No. 92-2631–CP, June 1992.

[94] Liu, C., Krause, E., and Menne, S., "Admissible Upstream Conditions for Slender Compressible Vortices," AIAA Paper No. 86–1093, May 1986.

[95] Copening, G. and Anderson, J., "Numerical Solutions to Three-Dimensional Shock/Vortex Interaction at Hypersonic Speeds," AIAA Paper No. 89–0674, Jan. 1989.

[96] Kandil, O. A., Kandil, H. A., and Liu, C. H., "Computation of Steady and Unsteady Compressible Quasi-Axisymmetric Vortex Flow and Breakdown," AIAA Paper No. 91–0752, Jan. 1991.

[97] Kandil, O. A., Kandil, H. A., and Liu, C. H., "Supersonic Quasi-Axisymmetric Vortex Breakdown," AIAA Paper No. 91–3311–CP, Sept. 1991.

[98] Kandil, O. A., Kandil, H. A., and Liu, C. H., "Critical Effects of Downstream Boundary Conditions on Vortex Breakdown," AIAA Paper No. 92–2601–CP, June 1992.

[99] Kandil, O. A., Kandil, H. A., and Liu, C. H., "Shock/Vortex Interaction and Vortex-Breakdown Modes," in *IUTAM Symposium of Fluid Dynamics of High Angle of Attack*, no. T.1.3, (Tokyo, Japan), Sept. 1992.

[100] Kandil, O. A., Kandil, H. A., and Liu, C. H., "Thee-Dimensional Supersonic Vortex Breakdown," AIAA Paper No. 93–0526, Jan. 1993.

[101] Beam, R. M. and Warming, R. F., "An Implicit Factored Scheme for the Compressible Navier-Stokes Equations," *AIAA Journal*, vol. 16, April 1978, pp. 393–402.

[102] Anderson, W. K., Thomas, J. L., and van Leer, B., "Comparison of Finite Volume Flux Vector Splitting for the Euler Equations," *AIAA Journal*, vol. 24, no. 9, Sept. 1986.

[103] Vatsa, V. N., Thomas, J. L., and Wedan, B. W., "Navier-Stokes Computations of prolate Spheroids at Angle-of-Attack," AIAA Paper No. 87–2627–CP, August 1987.

[104] Thomas, J. L., Van Leer, B., and Walters, R. W., "Implicit Flux-Split Schemes for the Euler Equations," *AIAA Journal*, vol. 28, no. 6, June 1990, pp. 973–974.

[105] Thomas, J. L. and Walters, R. W., "Upwind Relaxation Algorithms for the Navier-Stokes Equations," *AIAA Journal*, vol. 25, no. 4, April 1987.

[106] Roe, P. L., "Approximate Riemann Solvers, Parameter Vectors, and Difference Schemes," *Journal of Computational Physics*, vol. 43, 1981, pp. 357–372.

[107] Walters, R. M. and Thomas, J. L., "Advances in Upwind Relaxation Methods," in *State-of-the-art Surveys on Computational Mechanics* (Noor, A. K., ed.), pp. 145–183.

[108] Altgeld, H., Jones, W. P., and Wilhelmi, J., "Velocity Measurements in a Confined Swirl Driven Recirculating Flow," *Experiments in fluids*, vol. 1, 1983, pp. 73–78.

[109] Chao, Y. C., Hung, Y. F., and Lin, C. K., "The Downstream Boundary Effects on the Spectral Characteristics of the Combuster Swirling Flowfield," AIAA Paper No. 88–0735, Jan. 1988.

[110] Drummond, J. P., "Mixing Enhancement of Reacting Parallel Fuel Jets in a Supersonic Flow Field," (University of California, Davis, California), Presented at the Fourth International Symposium on Computational Fluid Dynamics, Sept. 1991.

[111] Anderson, D. A., Tannehill, J. C., and Pletcher, R. H., *Computational Fluid Mechanics and Heat Transfer*. McGraw-Hill, 1984.

[112] Metwally, O. M., *The Interaction of a Supersonic Vortex and a Normal Shock Wave*. PhD thesis, Pennsylvania State University, Feb. 1989.

[113] Lin, J. C. and Rockwell, D., "Transient Structure of Vortex Breakdown on a Delta Wing at High Angle of Attack," manuscript in preparation, 1992.

[114] Chong, M. S., Perry, A. E., and Contwell, B. J., "A General Classification of Three-Dimensional Flow Fields," *Physics of Fluids A*, vol. 2, no. 5, May 1990, pp. 765–777.

[115] Perry, A. E. and Chong, M. S., "A Description of Eddying Motions and Flow Patterns using Critical-Point Concepts," *Annual Review of Fluid Mechanics*, vol. 19, 1987, pp. 125–155.

[116] Tobak, M. and Peake, D., "Topology of 3D Separated Flows," *Annual Review of Fluid Mechanics*, vol. 14, 1982, pp. 61–85.

APPENDIX A
COMPATIBILITY EQUATION

In order to ensure that the vortex is slender, a compatibility condition which must be satisfied for the ratio between the radial velocity and axial velocity components, v/u, at any axial station is used. To derive the compatibility equation we follow the procedure obtained by Liu et al. [94]. The axial momentum equation is differentiated with respect to η and the radial momentum equation with respect to ξ. The resulting equations are added, and the circumferential momentum equation, the energy equation and the equation of state are used to eliminate all the ξ derivatives. A second-order equation for (v/u) is obtained. The compatibility equation is given by:

$$\frac{\partial^2}{\partial\eta^2}\left(\frac{v}{u}\right) + G_1^*\frac{\partial}{\partial\eta}\left(\frac{v}{u}\right) + G_2^*\left(\frac{v}{u}\right) + G_3^* = 0 \tag{A.1}$$

where

$$\begin{aligned} G_1^* &= G_1\frac{\rho}{\lambda} - \frac{1}{\rho}\frac{\partial\rho}{\partial\eta} \\ G_2^* &= \frac{\rho^2}{\lambda^2}\,G_2 \\ G_3^* &= \frac{\rho^2}{\lambda^2}\,G_3 \end{aligned} \tag{A.2}$$

and

$$G_1 = \frac{1}{r} + \frac{1}{1-\frac{u^2}{a^2}}\left(\frac{2}{u}\frac{\lambda}{\rho}\frac{\partial u}{\partial\eta} - \frac{1}{T}\frac{\lambda}{\rho}\frac{\partial T}{\partial\eta}\right) + \frac{\gamma}{a^2}\frac{w^2}{r} \tag{A.3}$$

$$\begin{aligned} G_2 = \frac{w^2}{u^2 r}\left(\frac{2}{w}\frac{\lambda}{\rho}\frac{\partial w}{\partial\eta} - \frac{1}{T}\frac{\lambda}{\rho}\frac{\partial T}{\partial\eta}\right) + \frac{w^2}{u^2 r^2}\left(1-\frac{u^2}{a^2}\right)\left[2+(\gamma-1)\frac{w^2}{a^2}\right] \\ - \frac{1}{r}\left(1+\frac{w^2}{a^2}\right)\left[\frac{1}{r} + \frac{1}{r}\left(1+\frac{w^2}{a^2}\right) - G_1\right] \end{aligned} \tag{A.4}$$

$$G_3 = \frac{w^2}{ru^2}\left(1-\frac{u^2}{a^2}\right)(K-2Q) - \frac{\lambda}{\rho}\frac{\partial}{\partial\eta}(K-P) + (K-P)\left(\frac{w^2}{ra^2} + \frac{1}{r} - G_1\right) \tag{A.5}$$

In the above equations, K, P and Q are given by

$$K = \frac{\mu M}{\rho u C_p T r}\left\{\frac{\lambda}{\mu}\left[\left(1+\frac{r}{\mu}\frac{\lambda}{\rho}\frac{\partial \mu}{\partial \eta}\right)\frac{\lambda}{\rho}\frac{\partial T}{\partial \eta}+r\left(\frac{\lambda^2}{\rho^2}\frac{\partial^2 T}{\partial \eta^2}-\frac{\lambda^2}{\rho^3}\frac{\partial \rho}{\partial \eta}\frac{\partial T}{\partial \eta}\right)\right]\right.$$
$$\left.+r\left[\left(r\frac{\lambda}{\rho}\frac{\partial}{\partial \eta}\left(\frac{w}{r}\right)\right)^2+\left(\frac{\lambda}{\rho}\frac{\partial u}{\partial \eta}\right)^2\right]\right\}, \tag{A.6}$$

$$P = \frac{\mu M}{\rho u^2 r}\left[\left(1+\frac{r}{\mu}\frac{\lambda}{\rho}\frac{\partial \mu}{\partial \eta}\right)\frac{\lambda}{\rho}\frac{\partial u}{\partial \eta}+r\left(\frac{\lambda^2}{\rho^2}\frac{\partial^2 u}{\partial \eta^2}-\frac{\lambda^2}{\rho^3}\frac{\partial \rho}{\partial \eta}\frac{\partial u}{\partial \eta}\right)\right], \tag{A.7}$$

and

$$Q = \frac{\mu M}{\rho u w r}\left[\left(1+\frac{r}{\mu}\frac{\lambda}{\rho}\frac{\partial \mu}{\partial \eta}\right)r\frac{\lambda}{\rho}\frac{\partial}{\partial \eta}\left(\frac{w}{r}\right)+r\left(\frac{\lambda^2}{\rho^2}\frac{\partial^2 w}{\partial \eta^2}-\frac{\lambda^2}{\rho^3}\frac{\partial \rho}{\partial \eta}\frac{\partial w}{\partial \eta}\right)\right] \tag{A.8}$$

The radial distance, r, is obtained from the integral equation:

$$r = \int_0^{\eta} \frac{\lambda}{\rho} \quad d\eta. \tag{A.9}$$

The value of (v/u) at the axis of symmetry, $r = 0$, is given by:

$$v/u = 0. \tag{A.10}$$